Politecnico di Torino

1859

CIRA

Centro Italiano Ricerche Aerospaziali

POLITECNICO DI TORINO

Master's degree course in Aerospace Engineering

July 2021

Master Thesis

Shape Memory Alloy torsional actuators for aerospace applications: a preliminary design procedure

Supervisor:
Prof. Enrico Cestino

Candidate:
Mario Sansone

Company Supervisors:
Dr. Antonio Concilio
Dr. Salvatore Ameduri

ACADEMIC YEAR 2020-2021

Abstract

Shape Memory Alloys (SMAs) are metal alloys capable of undergoing large deformations and recovering their original shape upon thermal or mechanical loading. This work is a systematic effort to help researchers and designers in developing SMA torsional actuators with a particular focus on aeronautical applications. The intent is to critically review the fundamental aspects of SMAs involved during torsional actuation, warning about unexpected and unwanted behaviours. Experimental results, phase diagrams and patents are discussed to provide a wide overview on this topic. Furthermore, this thesis reports all the steps toward the preliminary design of such devices, using a state-of-the-art commercially available FEM software. Simple aerodynamic load predictions are performed using Xfoil for three classes of aircraft (medium size UAV, Four-Seat Aircraft and Regional Transport Aircraft). Also, the SMA rods behaviour under mechanical and thermal loading is thoroughly examined, monitoring stress, temperature, torque and martensite evolution simultaneously, thus providing a holistic vision of the macroscopic phenomena involved during phase transformations.

To my parents,
Antonella and Salvatore

Acknowledgements

I wrote this section in my mother tongue to appropriately thank all the people who supported me during this journey, and as a tribute to my nearest and dearest. To anyone who will be reading this thesis that does not speak Italian, I apologise.

Prima di tutto vorrei ringraziare il Prof. Enrico Cestino, mio relatore, per la guida e il supporto che mi ha fornito durante questo intenso lavoro di ricerca; ma anche per tutti gli insegnamenti che ho ricevuto negli anni della specializzazione in Aerostrutture, in particolar modo per quelli acquisiti durante il corso di "Analisi di strutture aerospaziali con l'impiego di codici FEM", che hanno costituito un presupposto indispensabile per lo sviluppo di questa tesi. Vorrei inoltre ringraziarlo per la fiducia che ha manifestato nei miei confronti fin dai primi momenti, per la sua disponibilità e per avermi offerto l'opportunità di collaborare con un ente prestigioso come il CIRA.

Per lo stesso motivo, non posso che ringraziare la Dott.ssa Nunzia Favaloro, senza la quale questa cooperazione non sarebbe mai nata.

Sono sinceramente grato ai miei correlatori aziendali: il Dr. Antonio Concilio e il Dr. Salvatore Ameduri, per avermi guidato nell' insidioso e sorprendente mondo delle Leghe a Memoria di Forma. Ogni incontro è stato un indispensabile momento di apprendimento e un balzo in avanti nell' avanzamento dei lavori. Sono loro grato per l'incredibile opportunità di crescita professionale e per avermi permesso di guardare da vicino il lavoro del ricercatore. Non di meno, vorrei ringraziarli per la professionalità e la gentilezza che hanno sempre dimostrato nei miei confronti: l'ho apprezzato molto. Devo inoltre un ringraziamento speciale al Dr. Ameduri per avermi costantemente seguito nella modellazione agli elementi finiti.

A tal proposito, ringrazio sinceramente l'Ing. Mauro Linari, per avermi suggerito degli interessantissimi aspetti sulla modellazione. Sono grato anche al Dr. Giorgio Capovilla e all'Ing. Daniele Catelani per l'assistenza tecnica legata all'utilizzo dei software MSC.

Durante il mio percorso di studi universitari e il lavoro svolto per questa tesi, ho costantemente fatto affidamento sulla logica e sul mio pensiero scientifico, la cui formazione è stata opera di un grandissimo numero di docenti. Meriterebbero di essere citati tutti, ma in questa sede il mio pensiero si rivolge in particolar modo alla Prof.ssa Maria di Santo, tra le altre cose, per gli insegnamenti di geometria euclidea, e alla Prof.ssa Maria Santoro, per aver soffiato sul fuoco della mia passione per la fisica e averne costruito delle solide fondamenta. Non posso non citare il Prof. Paolo Cortese per le preziose nozioni di Analisi Matematica e per avermi trasmesso insegnamenti che trascendono la tecnica; nonché il Prof. Dario Daghero, per le appassionanti lezioni di Fisica I e le lunghe chiacchierate dopo le lezioni. La lista dei docenti da ringraziare sarebbe ben più lunga e mi scuso con coloro che non sono stati citati: sono sinceramente grato

a tutti gli insegnati che mi hanno trasmesso con passione un frammento della loro conoscenza.

Di fianco agli aspetti legati alla mia formazione accademica esiste un mondo parallelo di importanza inestimabile. È il mondo di coloro che mi hanno sostenuto emotivamente, materialmente e affettivamente. A loro vanno i miei ringraziamenti più sentiti.

Grazie ad Alessio, con il quale ho trascorso i bellissimi anni del liceo e convissuto come un fratello negli anni universitari. Grazie per aver condiviso la stessa stanza per quattro anni e mezzo senza mai farmi sentire fuori posto, per la coerenza, per la lealtà, per avermi ascoltato, per aver capito tanto di me con naturalezza, e aver cercato sempre il mio bene con l'esatta dose di persuasione. Grazie, semplicemente, per esserci stato.

Grazie a Paola, per aver portato brio (e spesso cibo) nella nostra casa, ma grazie soprattutto per avermi mostrato sempre il tuo lato più vero e sincero. La quotidianità della vita a Torino non sarebbe stata la stessa senza di te. Ad entrambi, grazie per avermi fatto sentire parte di una seconda famiglia, non lo dimenticherò mai.

Grazie a Piera, per avere sempre a cuore le mie vicende personali in modo sincero ed empatico. Grazie per mostrarmi punti di vista esotici, e per farmi guardare con occhi diversi aspetti che magari non avrei neanche considerato. Se è vero che siamo la media delle cinque persone che frequentiamo di più, tu sei l'elemento fondamentale che sbilancia delle certezze altrimenti immote, ed inneschi spesso quell'equilibrio dinamico necessario per ogni evoluzione. Grazie, perché dopo più di dieci anni ci ascoltiamo ancora nel trambusto di questa strana danza della vita.

Grazie a tutti i miei colleghi e amici del Politecnico, in particolare ad Alessandro, Fabio, Ludovico, Samuel, Pietro, Andrea, Beatrice, Elisa, Antonio, Matteo e Nicholas. L'immagine dell'università sarà per me indissolubilmente legata ai vostri volti.

In generale, grazie a tutti coloro che hanno reso Torino una città tanto magica.

Grazie a tutti i membri del team Icarus Polito, in particolare ai ragazzi della divisione Air Cargo Challenge. Grazie per avermi introdotto, ormai più di tre anni fa, alla modellazione agli elementi finiti, grazie per le interminabili riunioni, per le grigliate, per l'emozione di vedere Vega in volo dopo un anno di progettazione e costruzione. Insieme abbiamo imparato il vero significato del lavoro di squadra, condiviso momenti di tensione, di gioia, di fatica e di profonda soddisfazione. Non c'è stato un singolo giorno in cui mi sia chiesto se ne valesse la pena. Non di meno, grazie per essere stati degli amici oltre che dei colleghi.

Grazie a tutti i miei amici di sempre, soprattutto grazie a Mauro, Luca e Andrea B., per essere la migliore compagnia che avessi mai potuto desiderare; chi dall'asilo, chi dalle scuole elementari e chi dalle medie, avete sempre reso la mia vita più felice. Grazie per la pazienza con la quale ascoltate i miei "no" e per la tenacia con la quel cercate i miei "sì". Sappiate che sono poche le cose che mi rendono orgoglioso quanto la vostra presenza nella mia vita.

Grazie di cuore a tutti i miei zii e cugini, per l'incondizionata fiducia che avete sempre mostrato nei miei confronti, per l'affetto gratuito e l'interessamento verso le mie attività. Sebbene la distanza e gli impegni ci abbiano tenuti lontani, il vostro pensiero è stato spesso fonte di incoraggiamento negli anni universitari.

Grazie ai miei nonni, per aver sempre assecondato la mia curiosità e tollerato i miei pasticci quando ero bambino. Grazie a mia nonna Mena, per essere sempre profondamente coinvolta durante le mie prove ed esserne fiera a prescindere dall'esito. Grazie a mio nonno Mario, di cui porto con orgoglio il nome e dal quale mi piace credere di aver ricevuto la propensione alla manualità e all'ingegno. A entrambi, grazie per il costante sostegno e affetto.

Grazie a mio fratello Raffaele, per aver rappresentato prima una figura di riferimento, poi un modello, poi una fonte di ispirazione, dai miei primi anni di vita e per tutta la mia crescita. A sua insaputa mi ha introdotto alla propensione verso l'obiettività, al giudizio critico e alla consapevolezza della necessità del duro lavoro per inseguire le proprie passioni.

Grazie ai miei genitori, per tutto. Grazie per avermi portato sulle spalle come facevate quando ero bambino, ma questa volta per farmi guardare molto più in là di quanto avrei potuto fare altrimenti. Grazie per avermi sostenuto ancor prima che nascessi e per non avere mai smesso di farlo, nemmeno per un giorno. Grazie per essere riusciti nel difficilissimo compito di essere genitori. Se sono felice della persona che sono oggi lo devo soprattutto a voi. Grazie per l'amore smisurato che mi avete dato e per tutti i sacrifici e le prove che avete affrontato per il bene mio e di Raffaele. Un giorno, forse, comprenderò a pieno la portata inquantificabile della vostra forza d'animo e capirò quanto debba esservi grato davvero.

Contents

List of Tables

List of Figures

Chapter 1

Introduction

1.1 Shape memory alloys

Shape memory alloys are a class of metallic materials that exhibit particular properties like the shape memory effect (SME) and the pseudoelastic effect (PE). These phenomena are actually two sides of the same coin, as shown later in this chapter. Since the discovery of the SME in Ni-Ti based alloys by Buehler in 1961 [19], different elements were combined to reproduce this behaviour. Although the promising overall characteristic of Copper-Aluminum-Nickel (CuZnAl) and Copper-Zinc-Aluminium (CuAlNi) shape memory alloys [54], NiTi based alloy, also known as Nitinol, remains the most performing choice for most engineering applications. Their behaviour is the macroscopic outcome of internal lattice swap and crystalographic reorientation during a solid-state transformation. Indeed, Nitinol has two stable phases depending on temperature and applied stress. The high-temperature phase is called austenite (A) and exhibits a high symmetry cubic crystal lattice. In contrast, the low-temperature one, called martensite (M) has a low symmetry monoclinic lattice as shown in figure 1.1.

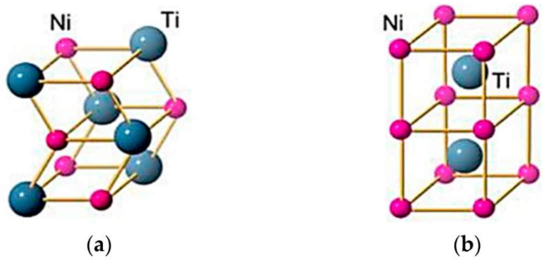

Figure 1.1: a) Martenste monoclinic crystallattice b) Austenite cucic crystal lattice [20].

The SME and the PE are only possible thanks to the existence of what is known as *single-variant martensite*, also known as *detwinned martensite*, and the *multiple-variant martensite*, or *twinned martensite*. Unlike its detwinned counterpart, the transformation between twinned martensite and austenite does not involve any macroscopic change in the component shape.

To further clarify the concepts below, it is useful to keep in mind the stress-strain-temperature graph in figure 1.2.

It is possible to obtain multiple-variant martensite upon heating and subsequently cooling a stress-free specimen through a specific range of temperatures (points 1-2 of figure 1.2). This way the overall shape of the specimen will remain the same as the austenite-parent phase, that is why twinned martensite is also referred to as *self-accommodated martensite*.

As stress is applied to twinned martensite, the specimen undergoes a reorientation transformation leading to detwinned martensite and macroscopic change in shape (points 2-3). Removing the applied load will make the specimen recover only the elastic part of deformation [1] (points 3-4). At this point, heating the alloy will restore the austenite-parent lattice and its associated initial macroscopic shape: this is what is known as the shape memory effect (points 4-1). An overview of the crystal lattice transformation is shown in figure 1.3.

Detwinned martensite can be obtained not only from twinned martensite but also directly from austenite. This is possible by applying a sufficient load to the specimen; it follows that this phenomenon is often referred to as *stress-induced martensitic transformation*. In the absence of any temperature change, unloading the component will bring it back to its original austenite-parent lattice and its related shape. This is known as the pseudoelastic or hyperelastic effect; in fact, during the stress-induced martensitic transformation, the material undergoes large recoverable deformations up to 10% strain [19].

[1] At point 3, strain can be divided into three components: elastic strain, plastic strain and transformation strain, which generally is an order of magnitude greater than the others. Only transformation strain is recovered upon heating, hence its name.

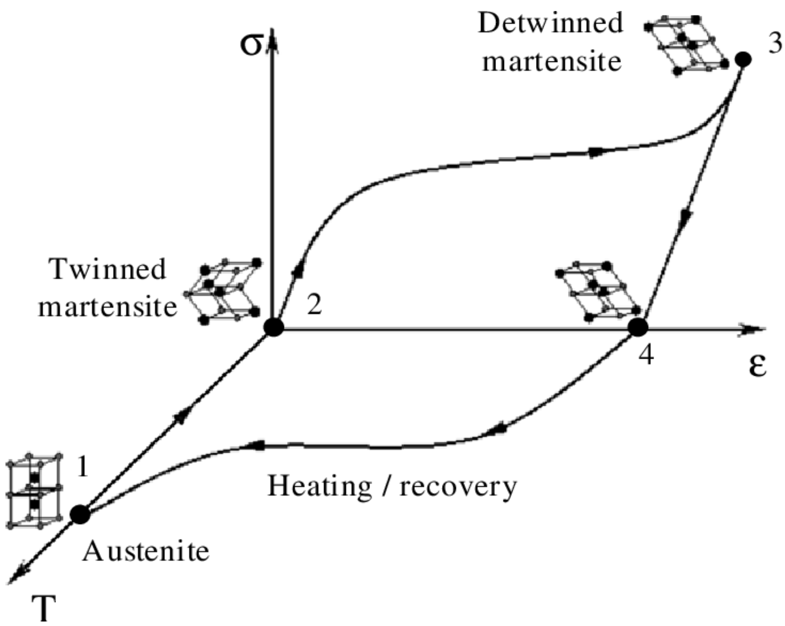

Figure 1.2: Stress-Strain-Temperature schematic of the crystallographic changes involved in the Shape Memory Effect [44].

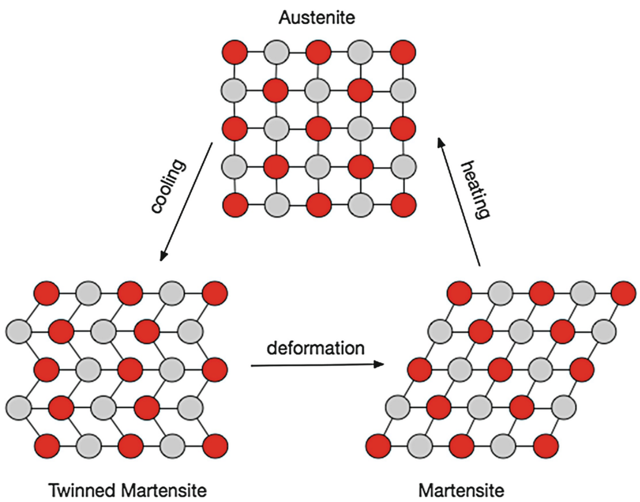

Figure 1.3: A schematic illustrating the shape memory effect of NiTi alloys [12].

To better understand the governing principles of shape memory alloys it is useful to introduce three crucial charts that will be considered several times in this work:

- Stress-strain
- Strain-temperature
- Stress-temperature

Figure 1.4 shows a typical pseudoelastic alloy loading and unloading cycle at a constant temperature. In the stress-free condition, the specimen is in the austenite phase. After a first linear part, stress-induced martensitic transformation begins at σ_{M_s} and completes reaching σ_{M_f}.Further loading the component entails a linear response until reaching the plastic limit of the martensite phase. Removing the load, the specimen discharges linearly until σ_{A_s} and completes its transformation from martensite to austenite at σ_{A_f}. Note that the order of σ_{A_s} and σ_{M_s} depends on the particular alloy under examination. As it appears clearly from the chart, during the phase transformation, the effective stiffness of the material is far lower than the pure phase ones. Moreover, austenite is always stiffer than martensite.

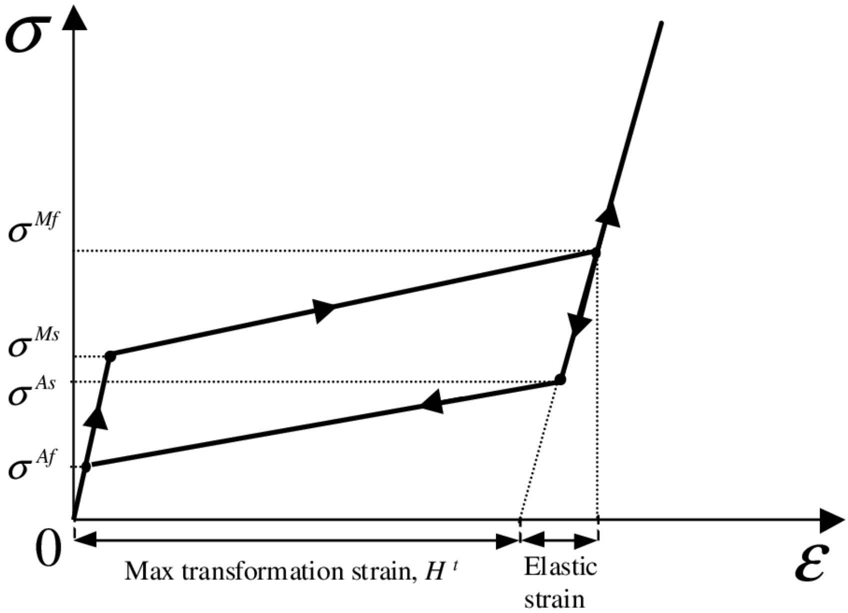

Figure 1.4: Schematic of isothermal, pseudoelastic stress-strain curve showing the critical stresses σ_{M_s}, σ_{M_f}, σ_{A_s} and σ_{A_f} required for initiation and completion of the forward and reverse transformation. The maximum uniaxial transformation strain H^t is also shown [44].

Another remarkable chart is illustrated in figure 1.5 showing the relation between strain and temperature at constant load.

Starting from a high-strain and low-temperature condition, recalling the shape memory effect, it is possible to recover the transformation strain and the related original shape heating the SMA. The transformation begins at A_s and completes at A_f. Because of the constant force applied during the subsequent cooling, the specimen will return to the martensite shape in the temperature interval $M_s - M_f$. It is also possible to obtain a similar result in absence of any recalling force in different measures, depending on the particular alloy and its undergone training cycles. The recovery of the martensitic associated shape in absence of recalling loads or either with an opposing force is known as *two-way shape memory effect* (TWSME).

As mentioned above, SME and PE are two sides of the same coin. To clarify this idea it is possible to observe figure 1.6.

As temperature rises, the typical stress-strain chart of the shape memory effect converters to that of a pseudoelastic effect. A way of seeing the phenomenon is that the pseudoelastic effect is nothing but the behaviour of a shape memory alloy that is always maintained at a higher temperature than A_f, and consequently, the transformation strain is immediately recovered as the load is exited. The same idea is summarized in figure 1.7 in a stress-strain-temperature field.

In order to identify which phase is present at a given thermomechanical condition, a stress-temperature chart is required such that illustrated in figure 1.8. In addition, to help designers during the preliminary phases of the development of SMA structures, it represents a crucial starting element for the formulation of phenomenological mathematical SMA models. In the simplified version shown, one can recognise the activation temperature at given stress, the transformation tensions at fixed temperature and the different phase regions.

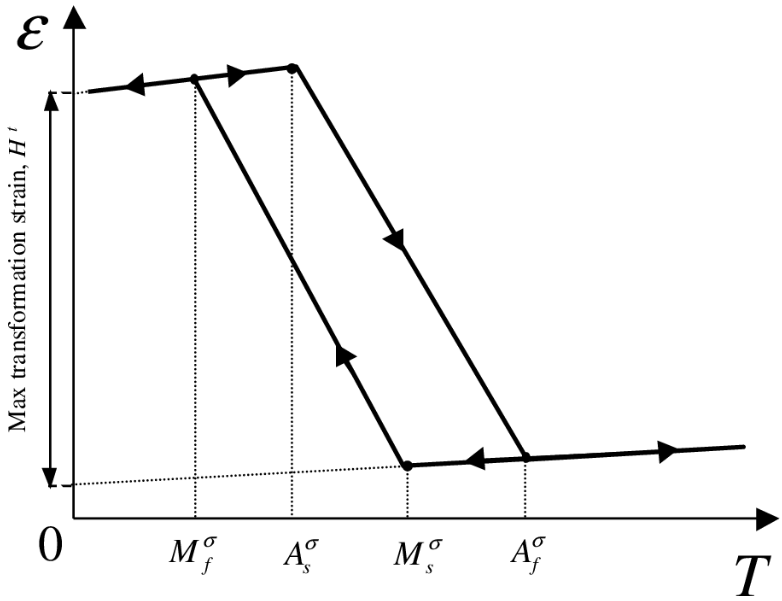

Figure 1.5: Schematic of isobaric, cooling/heating cycle showing the critical temperatures A_s^σ, A_f^σ, M_s^σ and M_f^σ required for initiation and completion of the forward and reverse transformation [44].

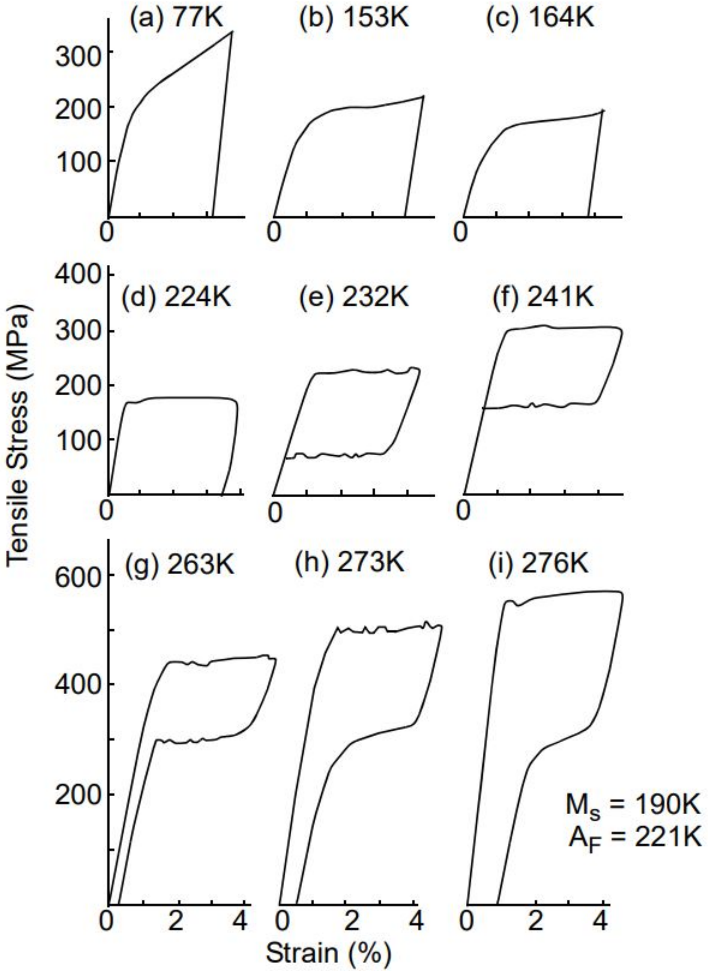

Figure 1.6: Stress-strain curves for a Nitinol alloy showing shape memory effect (a-d) and presudoelastic effect (e-i) [40].

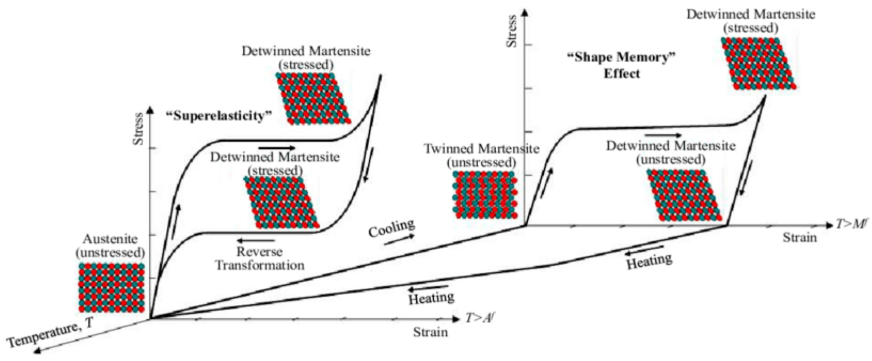

Figure 1.7: Behavior of pseudoelastic shape memory alloy materials according to phase transformation at different temperatures [49].

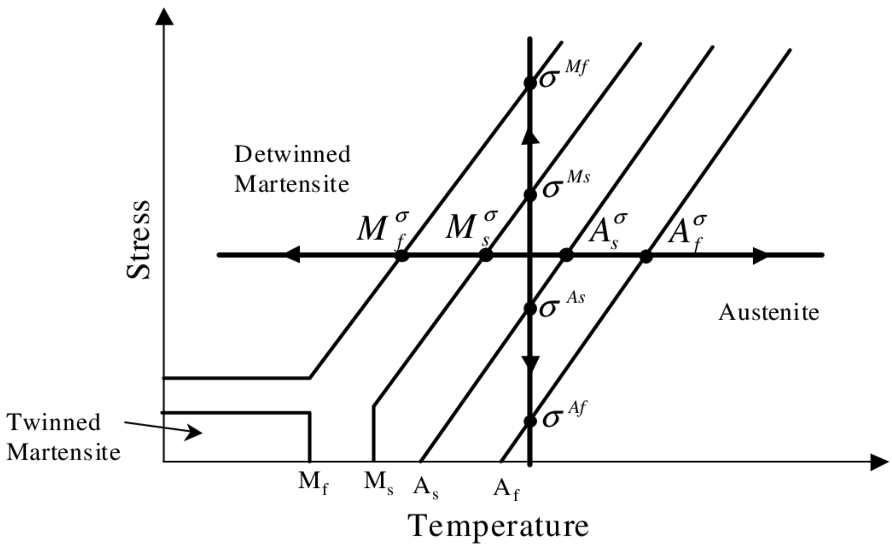

Figure 1.8: Isothermal and isobaric pseudoelastic loading paths. The two most commonly encountered pseudoelasticity loading paths - and isothermal and isobaric one. For clarity, the initial loading from austenite to achieve the required constant stress for the isobaric path is not shown [44].

1.2 SMA actuators

Designer and researcher saw in SMA's unique capability to recover their original shape under load the potential to craft revolutionary devices soon after discovering Nitinol.

In biomedical applications, shape memory alloys represent the state of the art material for, among the others, endovascular stents, vena cava filters, dental files, and archwires [52]. In addition, complex devices like the ankle-foot orthotic (AFO) have been developed by leveraging the pseudoelastic effect [53].

Shape memory alloys have also been used in the automotive industry to craft minor components for engine control, brake ventilation, climate control and also for side mirrors automatic adjustment [52]. However, the benefits obtained seems not to justify the high related costs; this explains why only a few commercial applications can be found within the products of the last thirty years.

Notwithstanding the vital importance of biomedical applications and the exciting outcomes from the automotive sector, this work addresses SMA actuators in aerospace. The main remarkable advantage of such devices is the reduced part number, the lower maintenance required, and consequently, they result very simple, efficient and reliable. Indeed, used as stressed components, they can be integrated into structures reducing the added weight. Moreover, due to their solid-state nature and compactness, SMA actuators promise to open the way to the morphing wing technologies spreading a distributed array of actuators along the aerodynamic surfaces. Another essential aspect is SMA energy density, which is over $1000J/kg$ [19].

Considering these appealing characteristics, in 1980s, The Boeing Company has begun a ponderous research program in the field of shape memory actuators, leading to the deposition of numerous patents [19].

One decade later, the Shape Memory Alloy Consortium (SMAC) was founded under the Defence Advanced Research Projects Agency (DARPA) Smart Materials and Structures program [32]. SMAC program included several Universities, organizations and enterprises with the aim of characterise materials, design actuators and test them to further understand the behaviour of these alloys, enabling the development of methods, tools and processes to successfull design a new class of devices. An overview of the overall SMAC program organisation and roles can be found in [32]. Again, The Boeing Company was among the enterprises involved in this challenge to further pushing the cutting edge for these technologies.

Always in the 1990s, the US government founded the Smart Aircraft and Marine Project System Demonstration (SAMPSON), which led to the design, development and test of the SAMPSON Smart Inlet shown in figure 1.9. Thanks to the bundle of SMA wires illustrated in figure 1.10 , it was possible to actuate a variable geometry F-15 inlet. In order to give an idea of the forces involved, a bungle of sixty Ni-Ti wires provides over $90000N$ of axial force [19].

Variable geometry Chevrons (VGC) were designed to increase engine performance and decrease noise level, particularly during the landing phase, where civil agencies restrictions are pretty strict. Chevrons are deputed to engine flow mixing, and their design is always a compromise result. By applying SMA beam components as shown in figure 1.12 from [30], it is possible to vary the overall geometry of the device to fit the specific operation requirements better. The real world application is shown in figure 1.11.

A similar idea was implemented with the Variable Area Fan Nozzle (VAFN) in figure 1.13. In this case, shape memory alloy flexure actuators are used to expand and contract the nozzle to adapt to the flight condition and engine operations. Similarly to the VGC, the heat generated from the engine is employed to actuate the SMA components beside thermocouples deputed to obtain a refined control over the actuation.

Even the space industry found a place for SMA active devices.

A remarkable example is the Micro Sep Nut shown in figure 1.14, a very compact release mechanism that employs the SME to be activated, overcoming the problem of low-shock release. Moreover, such devices are an order of magnitude smaller than their conventional counterpart[30].

Another fascinating original work was born from the collaboration between Lockheed Martin

Figure 1.9: The SAMPSON F-15 inlet cowl as installed in the NASA Langley Transonic Wind Tunnel [30].

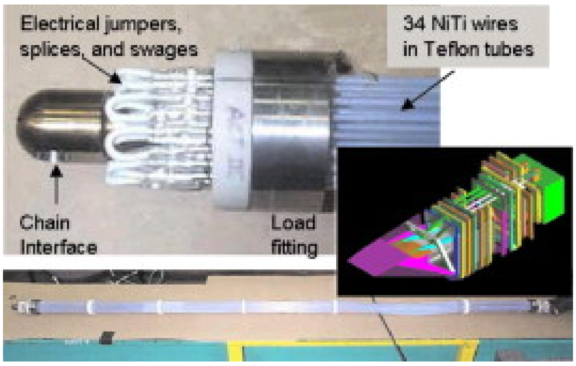

Figure 1.10: SAMPSON Smart Inlet cowl rotation actuation system, SMA wire bundle actuator, with inset design schematic [19].

and NASA-Goddard and is called lightweight flexible solar array (LFSA). This device incorporates an SMA hinge able to deploy the solar array in its open configuration, saving both weight and space. An overview of the design is presented in figure 1.15.

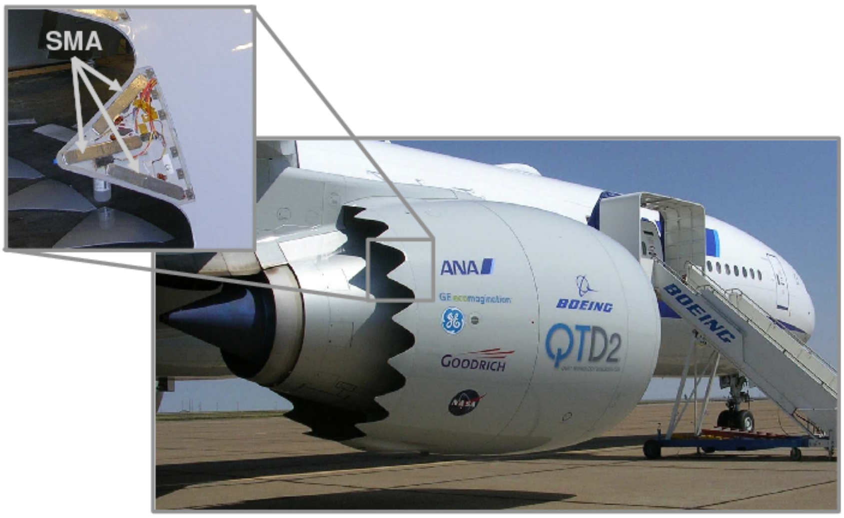

Figure 1.11: Boeing variable geometry chevron, flight testing [30].

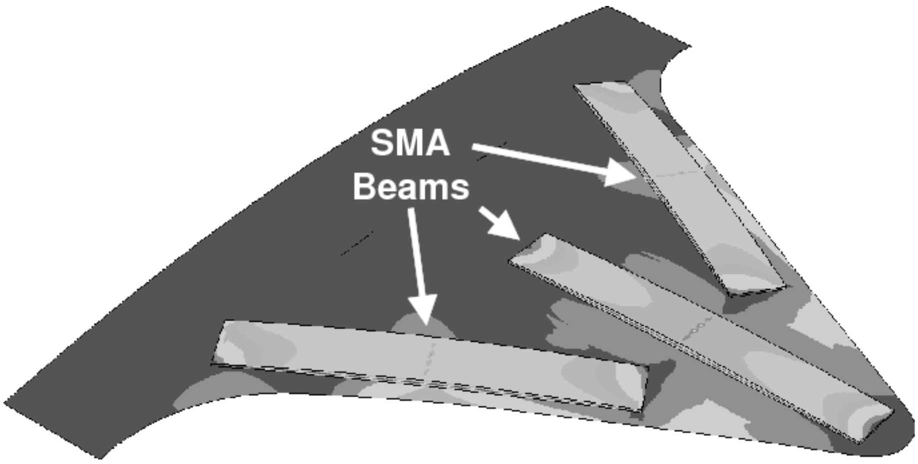

Figure 1.12: SMA beams position of Boeing VGC [30].

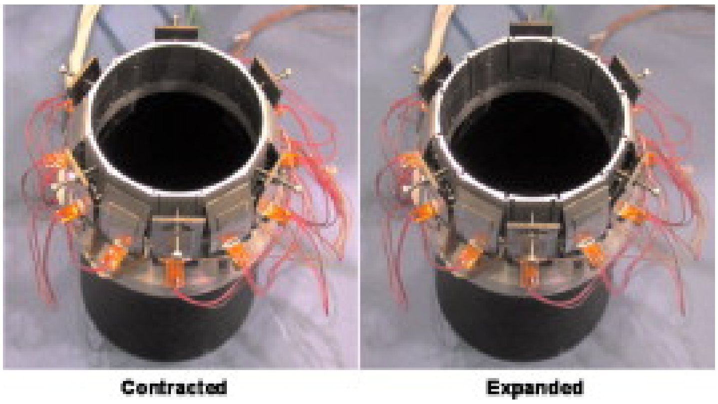

(a) Scale model variable area nozzle contracted and expanded

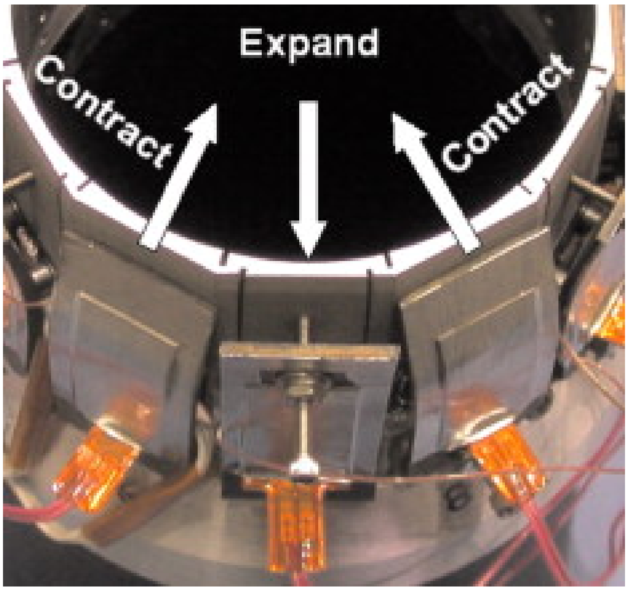

(b) Variable area nozzle configuration

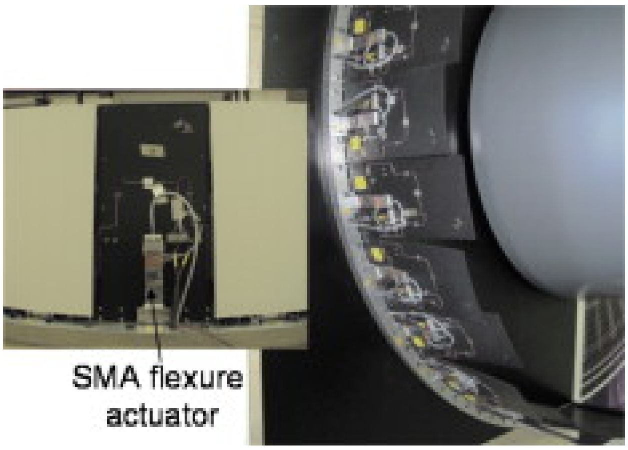

(c) VAFN panel showing flexure actuator and display with covers off showing SMA flexure actuator

Figure 1.13: Variable Area Fan Nozzle (VAFN) [19].

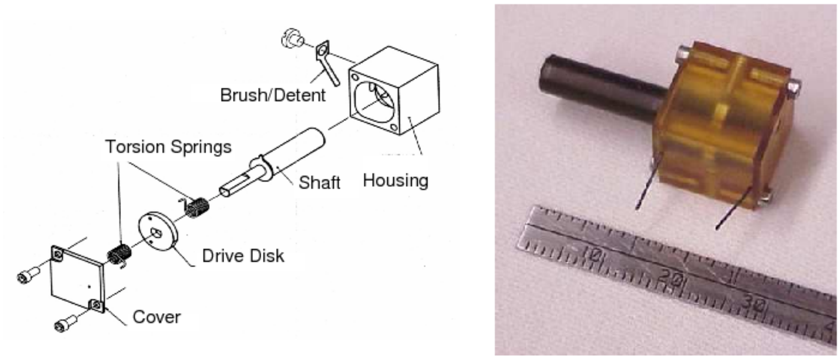

Figure 1.14: The rotary latch as design and tested at the Applied Physics Laboratory [30].

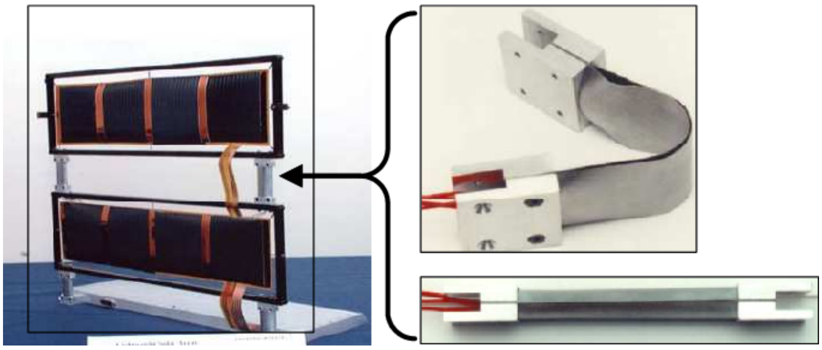

Figure 1.15: LFSA and detail of hinges, folded and deployed configurations [30].

1.3 SMA torsional actuators

The main idea underneath the functioning of shape memory alloy torsional actuators is fearly straightforward. Consider an SMA rod or tube deformed under torque in a way to rotate its free edge to a certain angle, ensuring to bring it in the martensitic phase. Simply heating the specimen will bring it back to its original undeformed shape, supplying rotary actuation. The martensite to austenite transformation induced by heating will generate the macroscopic effect of rotation as simplified in figure 1.16 from [52]. To give an order of magnitude of the quantities involved, the torque tube illustrated in figure 1.17 is able to produce over $70Nm$ of torque over 90 degrees of rotation [52].

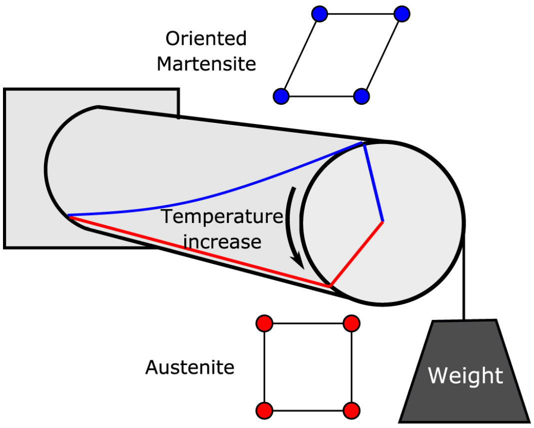

Figure 1.16: Schematic of torque rod and tube actuation mechanism [52].

Figure 1.17: Example shape memory alloy torque tube actuator. Ends are splined for connection to components being driven[52].

Despite the simplicity of their working principle, SMA torque tubes and rods exhibit complex behaviour that, to date, are not fully understood.

Since the 1990s, SMAC put its efforts to further investigate the mechanisms underneath shape memory alloys under torque deformation. Indeed, the development of new and functional actuators was bounded by the models' accuracy, which in turn was limited by the sma understanding of the time. This is why modelisation, design and experimental test go hand in hand.

Torque tube manufacturing is explained in [34]. Because of the inherent difficulty in machining SMA material, SMA tubes are manufactured in a multistep process. Rods are usually extruded, cut by length by saw and eventually undergone Electro-Discharge Machining (EDM).

Holes can be simply gun-drilled and refined by EDM. Beyond typical heat treating such as annealing, SMA undergoes different thermomechanical cycles depending on the final desired alloy property. This process, known as *training*, is also described in [34] as follows:

- The device is first annealed, heating it up and maintaining that temperature for a certain time;
- The device is cooled down, and rotational stress is applied in its cold state, causing permanent deformation;
- Upon further heating, the device "remembers" or return to its annealed, untwisted state.The above sequence is repeated several times until the device is fully trained.

A simple SMA torque tube training apparatus is shown in figure 1.18.

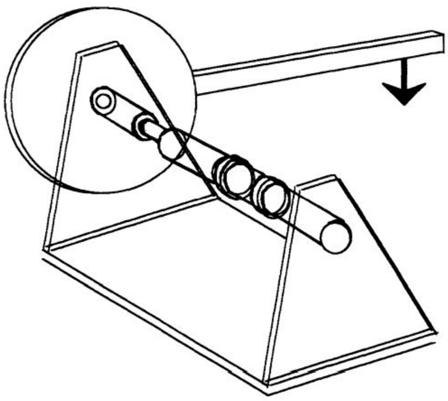

Figure 1.18: SMA Torque Tube Training Apparatus [34].

Further insights on training process will be reported in chapter 2.

The steps forward required to obtain an SMA torsional actuator are well described in figure 1.19 from [32]. This particular design was developed under the "Smart Structure for rotorcraft control" (SSRC) program, which also involved the Boeing Helicopters division (Philadelphia). The baseline actuator displays a heating resisting element as well as a locking mechanism and the more expected housings and attachment components. It is remarkable that already at that time, crucial aspects like locks and brakes were investigated. Generally speaking, locks exhibit a limited angular resolution but often offer a more reliable and effective performance; on the other hand, brakes, operating through friction, features infinite resolution but suffer wear. Both devices help control the actuation and, depending on the particular application, can dramatically reduce the power budget of the actuator. A timeline of the early development of these devices is illustrated in figure 1.20.

During the same years, the Smart Wing Program[2] was born to develop and demonstrate smart materials potentiality to improve the performance of lifting bodies and as a bench test for the new discoveries in SMAs field. The initial design was implemented on a 16% scaled F-18 wing section, representing one of the earliest attempts to use an SMA torque tube actuator in a real-life operation. As it is shown in figure 1.21, the actuation system included two SMA torque tubes to provide a spanwise variable twist. Several tests were carried out in different configuration with one or two torque tubes. Although the results were satisfactory for the downscaled model, it was

[2]Smart wing Program was developed within the framework of DARPA, in collaboration with Northrop Grumman and monitored by the US Air Force Research Lab (AFRL) [30].

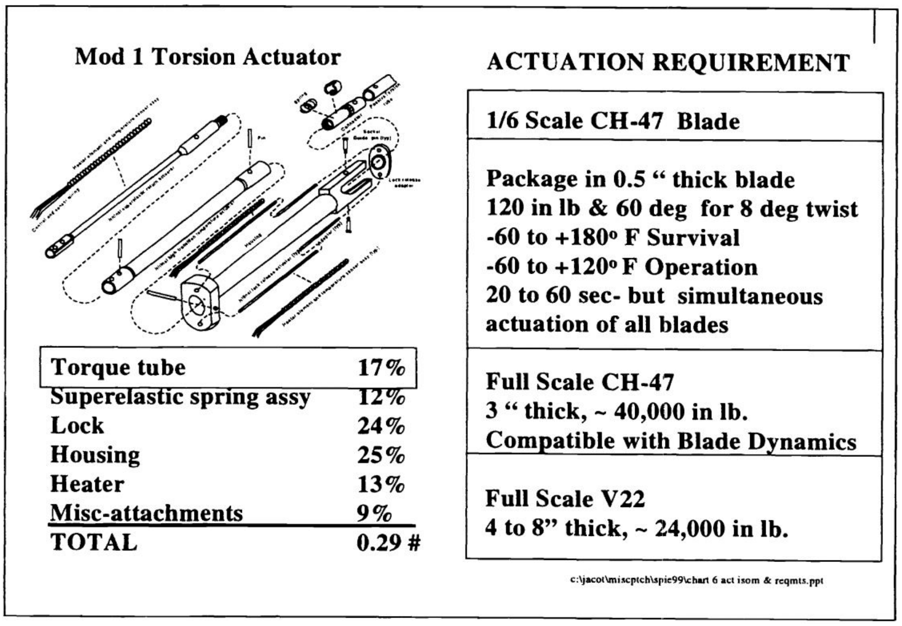

Figure 1.19: Actuator Isometric & Requirements [32].

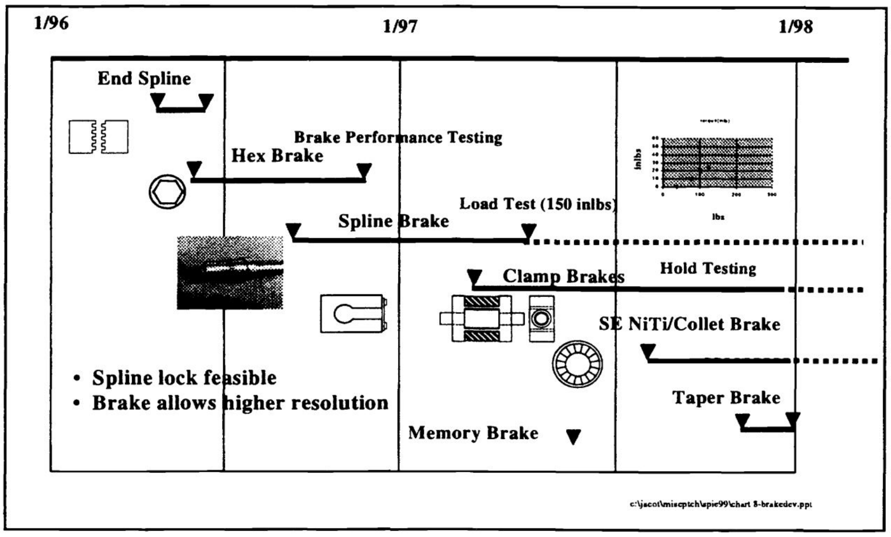

Figure 1.20: Lock & Brake early developments [32].

found that the material adopted was not suitable for the real size application, so the program continued exploring other configurations in Phase II [30], [52].

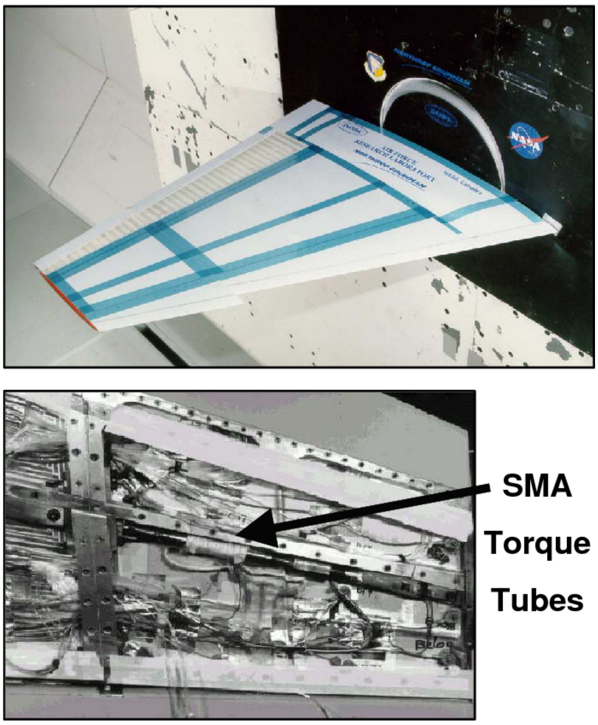

Figure 1.21: Total and cut-away view of the SMA torque tube as installed in the model wing during phase I of the SMART Wing project [30].

1.4 CIRA

CIRA, the Italian Aerospace Research Centre, is a company mainly of public ownership created in 1984 to perform research in the fields of space and aeronautics.

With headquarters in Capua, the Centre was founded by the Italian State itself to promote research and technological development in the aerospace field according to the standards of other European countries and contribute to the country's socio-economic development. Today CIRA has the most extensive research facilities in the field of aerospace in Italy, with testing facilities unique in the world and state-of-the-art laboratories available to national and international enterprises.

The company is involved in the most advanced themes of aerospace research: from the study of aircraft and spacecraft able to fly autonomously and at very high speeds; to the development of innovative systems that can reduce the environmental footprint of aircrafts, increase flight safety, and improve the management of air traffic; always looking forward to the space transportation systems of tomorrow. CIRA participates in the main European and International research programmes and collaborates with top Universities and aeronautical and space companies in Italy and other countries [1].

This work was developed within the framework of the CIRA Adaptive Structure Department. Among the others, a major mission is developing and implementing theoretical and numerical models to design sensing and actuation systems based on so-called "Smart" materials such as SMAs. These models contribute to the sizing and the parametrisation of the systems mentioned above, characterised by peculiar issues like non-linear constitutive laws and involving multiple aspects of the design process. The Adaptive Structure Department is also responsible for the detailed design, manufacture and integration of these systems. Moreover, it manages all the operations related to prototypes manufacturing, testing and characterisation required to validate the models, following the projects in all its stages [2].

1.5 Outline of current research

The work presented in this thesis aims to help researchers and designers in developing SMA torsional actuators with a particular focus on aeronautical applications.

In the latest thirty years, many designs have been presented, and several mathematical models were developed in response to the increasing demand for accuracy in predicting SMA behaviour. Research groups around the world have partially completed this daunting task, despite open issues still remains as will be presented in the next chapters.

The main focus of this thesis is double:

- to provide a critical review of the fundamental aspects of SMA involved during torsional actuation, warning engineers from unexpected and unwanted behaviours;
- to provide all the steps toward the preliminary design of an SMA torsional actuator using state of the art commercially available FEM software.

Consequently, this work is intended to provide an of-the-shelf engineered solution to design SMA torsional actuators, pointing out both its potential and its limits.

Chapter 2

State of the art

2.1 Phase diagrams

Phase diagram of shape memory alloys is fundamental for understanding their behaviour and represent the foundation of a solid phenomenological mathematical model. Although phase diagrams are based on experimental results, modelisation enables researchers to simulate multiple conditions that eventually suggest insight for a deeper understanding of the phenomena under investigation. However, the principal reason that underlies modelisation is often to give designer practical tools to develop their concepts. For this reason, it is crucial to understand the assumptions, the potential and the limits of a mathematical model, which has its roots in the physical behaviour of what it describes.

Accordingly, this section presents a brief review of the primary phase diagrams describing shape memory alloys behaving.

A simple phase diagram is presented in [11] related to the model by Souza et al. [51], which admits only austenite ad single-variant martensite as shown in figure 2.1.

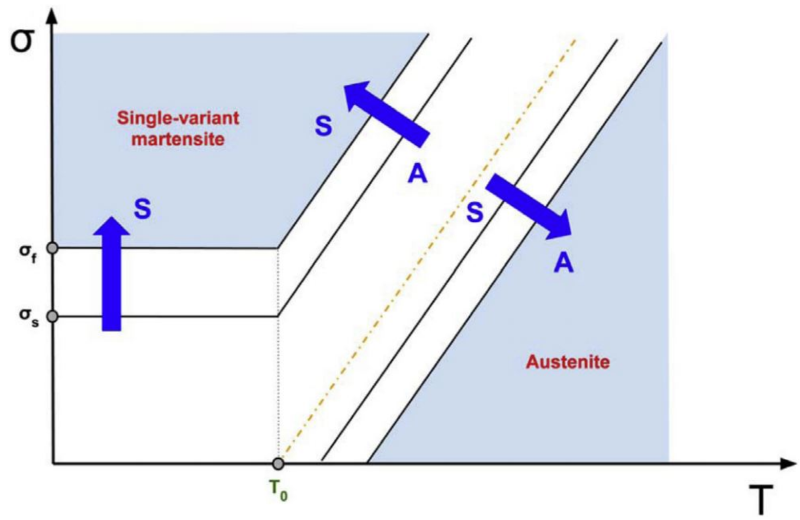

Figure 2.1: 1D phase diagrams generated by Souza model, in terms of stress and temperature [11].

Early in 1993, Brison et al. [16] presented a constitutive model that admits the existence of both twinned and detwinned martensite as shown in figure 2.2.

Consistently with the presented phase diagram, twinned martensite can only exist for temperature and stress levels below M_s and σ_f.

Below M_s, the critical stresses inducing transformation between multi-variant and single-variant martensite don't change with temperature. On the other hand, the critical stress - temperature curve pattern above M_s is assumed to be linear in good accordance with experimental data. Similarly, for temperature-induced transformation, temperature thresholds don't vary with applied stress below σ_s^{cr}.

It is important to note that no distinction is made between threshold temperatures involved in austenite to twinned martensite and austenite to detwinned martensite transformations. The same can be said for the respective reverse conversions. This assumption is coherent with the experimental data available at that time.

Starting from the work of Brinson [16], Popov and Lagoudas [45] further investigate the behaviour of shape memory alloys aiming to create a phase diagram able to predict all the possible mechanical and thermal loading paths. Despite the great performace offered by Brinson phase diagram based models in describing shape memory effect and pseudoelastic effect, a complex

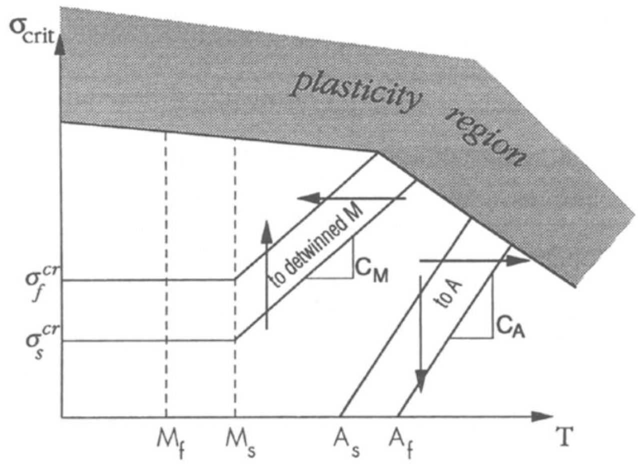

Figure 2.2: Critical stresses for transformation or martensite twin conversion as functions of temperature. Plasticity region indicated [16].

path can lead to unphysical outcomes. Figure 2.3 shows some examples of time history in the stress temperature field.

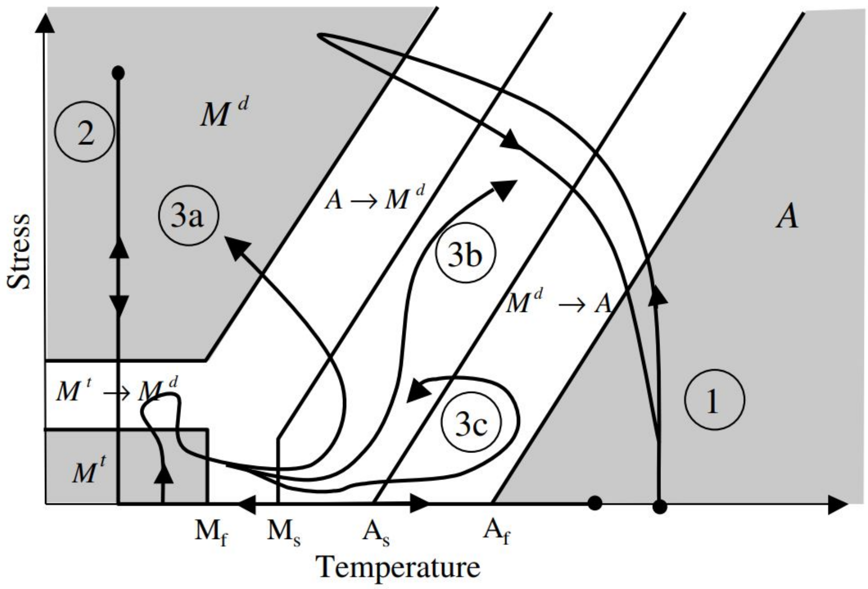

Figure 2.3: A typical phase diagram for SMA materials showing different load paths [45].

While paths 1 and 2 (describing the PE and the SME respectively) are physically coherent, path 3b leads, for example, to a state in which twinned martensite is present above σ_f, which would represent a paradox. In order to solve these issues and according to experimental results, Popov and Lagoudas introduced three main improvements regarding the following aspects:

- Austenite to martensite transformation ($A \rightarrow M^t, A \rightarrow M^d$)
- Detwinning of multi-phase martensite ($M^t \rightarrow M^d$)
- Combined austenite to detwinned martensite ($A \rightarrow M^d$) at low stresses

Based on experimental results, Popov and Lagoudas conclude that $M^t \rightarrow A$ and $M^d \rightarrow A$ transformation temperatures at zero stress are generally different[1]. Consequently, their representations appear as the green and blue lines in figure 2.4.

Moreover, the delimiting lines of the transformation region between twinned and detwinned martensite assume a slight negative slope, indicated by k^d, and are extended to A_f^t. This adjustment better defines the martensite twinned to martensite detwinned region, excluding irrealistic behaviour such as that illustrated in path 3b of figure 2.3. As shown in the next chapters, it is remarkable that, according to the established literature, it is impossible that a loading path may lead to the existence of twinned martensite at high-temperature and high-stress regions of the phase diagram [45].

Finally, the low-stress region is described differently, depending on sample composition, heat treatment, manufacturing process, etc. For example, it is common to find a critical stress level below which detwinned martensite cannot form, leading to the assumption that the M^d surface is temperature-independent for $T < Ms$. However, thinking of a specimen exhibiting PE, it is clear that the development of transformation strain at zero stress level implies that the $M^d \rightarrow A$ surface should extend to zero stress. Accordingly, in figure 2.4 these aspects lead to different possible lines referred to as "trained" and "untrained."

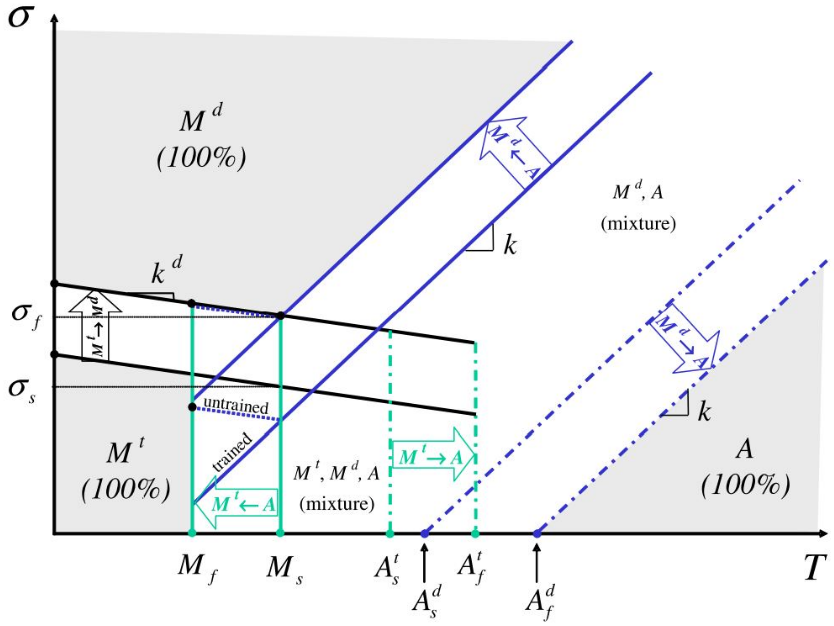

Figure 2.4: The SMA phase diagram used in Popov and Lagoudas model. All the three pure phase regions (A, M^d and M^t) are enclosed by transformation strips. The diagram is completely defined by the respective transformation temperatures $Ms, M_f, A_s^t, A_f^t, A_s^d, Ad_f$, the critical stresses for detwinning σ_s and σ_f and the slopes k and k^d [45].

Although there is no unambiguous definition of how some zones of the phase diagram should look like, the work proposed by Popov and Lagoudas [45] can be considered the state of the art. Another model at the cutting edge has been developed by Auricchio et al. [11]. As for Popov

[1] "A qualitative explanation for this result can be done as follows: the twinned martensite requires some energy input to transform back to austenite. The detwinned martensite, also requires this energy input, but in addition it also needs more energy in order to reverse the inelastic strains which are present (note this always happens in the presence of a local stress field, even when its macroscopic average is zero)" [45].

and Lagoudas model, figure 2.5 [2] shows the five possible phase transformations, indicated by the blue arrows, and the possible phase existing in different regions. In the three light-blue shaded zones, only pure phases can exist. These regions are separated by strips labelled according to the transformations that occur, and where more strips overlap, multiple conversions are possible. As a consequence, the non-shaded region admits the existence of various mixtures [11].

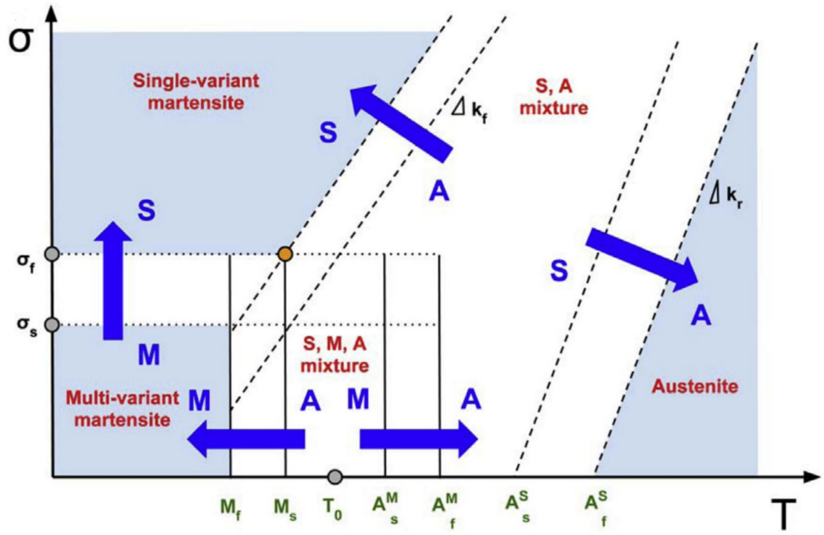

Figure 2.5: 1D phase diagrams generated by Auricchio's model [11].

Two main aspects of the Auricchio et al. phase diagram are worth mentioning for the purposes of this dissertation:

- The strips representing the austenite to single-variant martensite ($A \to S$) transformation and its reverse counterpart ($S \to A$) exhibit different slopes and widths. This allows the consequent model to be more flexible. This way it better predicts different kinetics between forward and reverse transformations, the increasing hysteresis width for low applied stresses in thermal-cycling test at constant load, and the decreasing width of the hysteresis loop in superelasticity with increasing temperatures.
- For the austenite to single-variant martensite transformation ($A \to S$) at temperature and stress below M_s and σ_s respectively, it is assumed to extend the $A \to S$ strip to zero-stress level.

Figure 2.6 and 2.7 are reported in order to clarify some aspect related to temperature-induced and stress-induced transformations respectively.

[2] In figure 2.5 all the temperature are presented except for S_s and S_f which are respectively the start and finish temperature for austenite to single variant martensite transformation at zero stress level.

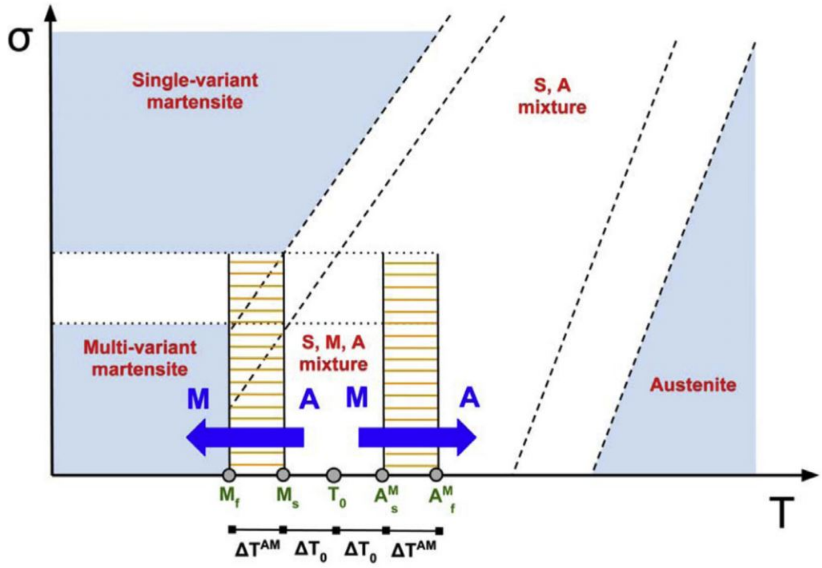

Figure 2.6: Temperature-induced transformation from Auricchio's model [11].

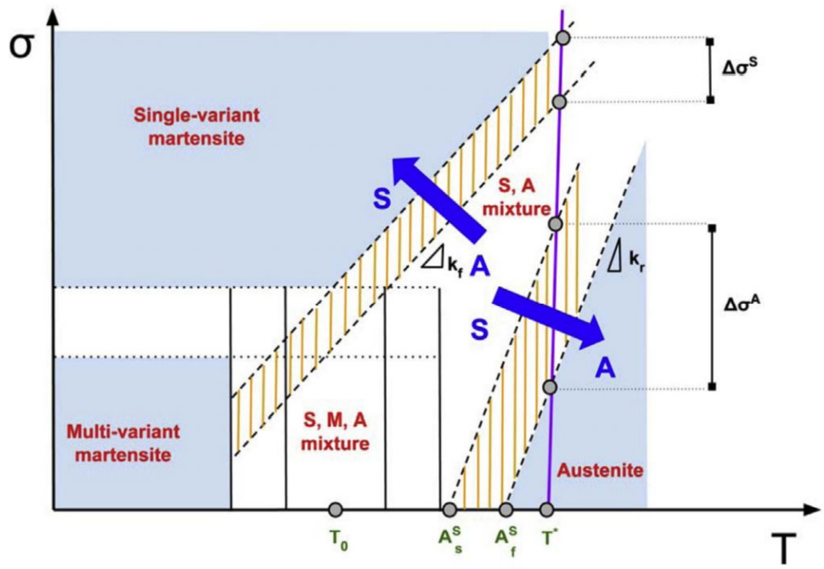

Figure 2.7: Stress-induced transformation from Auricchio's model [11].

2.2 SMA torque tubes and rods simplified models

In current literature, two main formulations have been established aiming to the modelisation of shape memory alloys behaviour. The Brinson model and the Auricchio model are both based on Helmholtz free energy; meanwhile, the Lagoudas model relies upon Gibbs free energy [52] [9]. A detailed overview of Auricchio's formulation will be provided in chapter 4. On the other hand, this section is focused on two simplified models based on Boyd and Lagoudas formulation [15].

Mirzaeifar et al. [39] found an exact solution for pure torsion of shape memory alloy circular rods and tubes. After considering the general constitutive model based on Gibbs free energy, it is assumed that all the material properties vary with martensitic volume fraction. A hardening function is introduced to define the transformation strain behaviour typical of SMA material. To complete the model, an additional constraint is included obtained from the Second Law of Thermodynamics. All the steps mentioned above for the definition of the general 3D constitutive model are exactly the same adopted by Taheri Andani et al. [53]. Mirzaeifar et al. subsequently reduce the system for pure torsion, taking into account only the shear stress, shear strain and transformation shear strain. This way the resultant quartic equation can be solved analytically using Ferrari's method, avoiding approximations deriving from the model resolution and thus resulting in an exact solution. Consequently, one of this model's main strengths is that the closed-form solution doesn't involve a massive iterative computational process. Besides the shear stress, the equations found can also predict the martensitic volume fraction continuously with the radius both in loading and unloading paths. The numerical data provided are not trivial. First of all, the rod can be divided into three regions along the radius depending on the phase composition, as shown in figure 2.8.

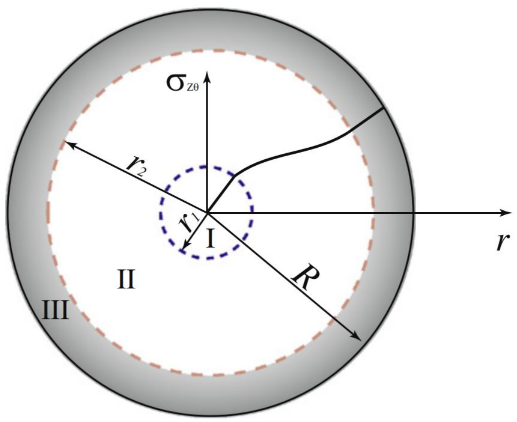

Figure 2.8: Schematic of stress distribution in a circular bar. Regions I, II, and III are the austenite core, transition region, and the martensite outer layer, respectively [39].

In the torsion load case, in fact, the stress generated in the outer radius is greater than inside. This leads to different torque required to activate the stress-induced transformation in the SMA rod along the radius. For isotropic material[3], assuming a simple kinematic[4] and elasticity equations for cylindrical rods or tubes, the following relations between torque and shear stress can be obtained:

$$\tau(r) = \frac{Tr}{J}$$

[3]For isotropic materials, effective shear modulus G can be simply expressed as $G = \tau/\gamma$

[4]For cylindrical rods and tubes, the shear strain γ can be expressed in terms of the twist angle θ and the overall length L as $\gamma(r) = \theta * r/L$

where T is the applied torque, r is the radius, and J is the second moment of area of the cross-section, which, in the case of circular geometry, is expressed as

$$J = \frac{\pi}{2}(R_0^4 - R_i^4)$$

Where R_0 and R_i and represent the outer and inner radius, respectively.

Differently, shape memory alloys don't exhibit a linear stress-radius law as for linear elastic materials, but the overall trend is influenced by phase transformation and phase stiffness. Consequently, figure 2.9 and 2.10 highlight the peculiar behaviour of SMA rods under torque loads.

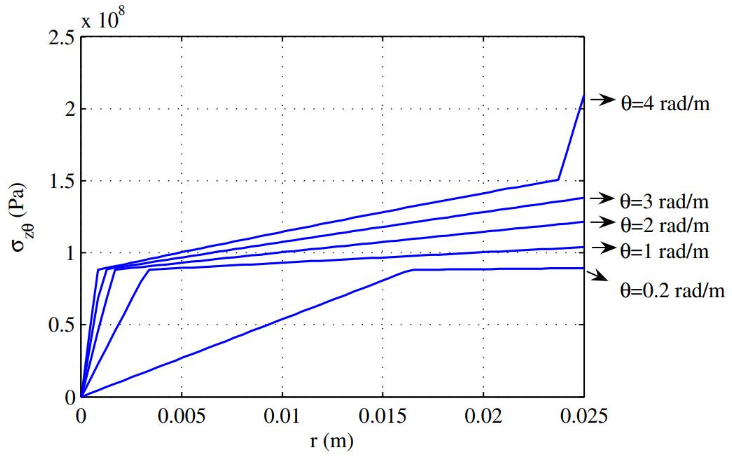

Figure 2.9: Shear stress for various twist angels in loading [39].

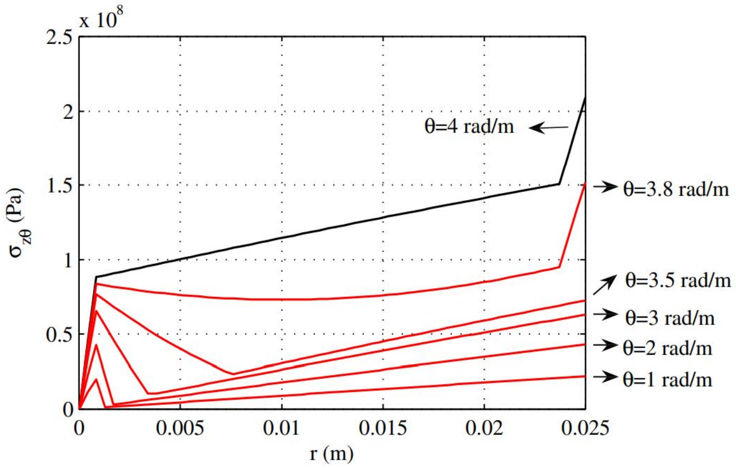

Figure 2.10: Shear stress for various twist angels in unloading [39].

In order to understand this phenomenon, it is helpful to consider the martensitic volume evolution during the loading path as shown in figure 2.11 and 2.12.

Further considerations on this behaviour are reported in chapter 5.

Probably the main weakness of the model from Mirzaeifar et al. is its inability to predict the response of a cylinder under combined stress loads. In order to improve this model performance, including combined tension-torsion behaviour, Taheri Andani et al. [53] developed a

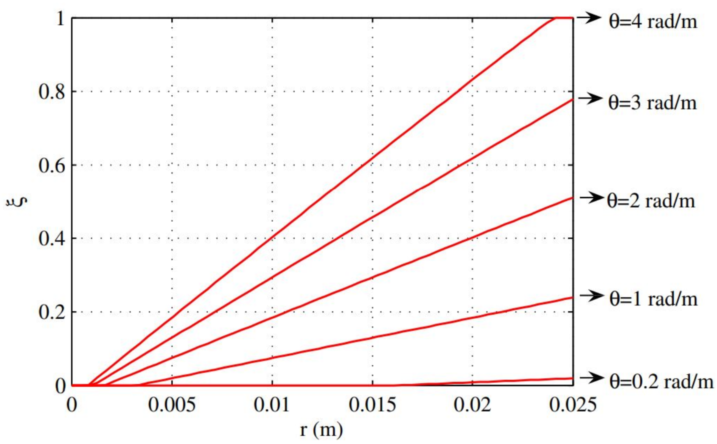

Figure 2.11: Martensitic volume fraction for various twist angels in loading [39].

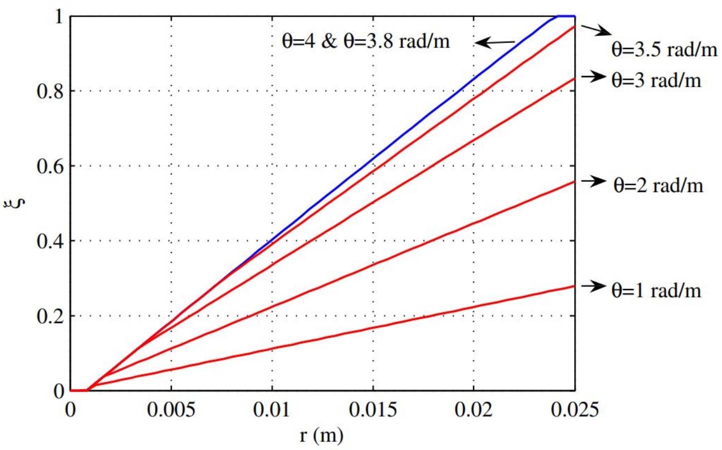

Figure 2.12: Martensitic volume fraction for various twist angels in unloading [39].

semi-analytical approach based on the same general 3D constitutive model used by Mirzaeifar et al.. In this case, however, axial stress, axial strain and axial transformation strain are not neglected. Also, other terms are included to meet mass conservation, but they are not considered in the further steps. The non-linear governing equations obtained are solved using an iterative method for which the rod is discretised into a finite number of narrow annular regions, while the total twist and axial displacement are partitioned into multiple steps. The solution algorithm considers the discretised generalised displacements as loading inputs, resulting less computationally expensive than an implicit scheme. The model predictions are reasonably accurate for simple load cases and are in good accordance with experimental data. However, during non-proportional loading tests, maximum errors of 43% are observed, probably because the model neglects martensitic reorientation.

2.3 Experimental results

The section below attempts to collect remarkable observation about SMA torsional actuators from experimental results upon SMA tubes and rods. The aim is to further illustrate the unique characteristics of these alloys and warn designers of critical issues they could face while dealing with them.

An extensive collection of data was performed by Mabe at al [36] involving 29 torque tubes from two different suppliers with different composition, sizes and manufacturing process. Most of the observation presented below are deducted by their results.

As mentioned in previous chapters, SMAs usually undergo a training process in order to develop SME and PE. However, one of the most important reasons for this procedure is stabilising the overall SMA behaviour. Of course, even for a stabilised material, the strain response varies depending on applied torque and the consequent induced stress, as shown in figure 2.13. This means that in a pure phase configuration (100% austenite or 100% martensite) the angular displacement achieved changes with applied torque as in the case of variable force actuators. Moreover, this is remarkable because many advantages derived from having a complete transformation cycle during the actuation.

In fact, as shown in experimental results by Befan et al. [13], for specimens that undergo a partial transformation loop, retained (or untransformed) martensite generates, which is no longer contributes to shape recovery and thus reduces transformation strain. Concerning that, figure 2.14 shows the stress-cycle profile and its consequent transformation shear strain. Moreover, Befan et al. demonstrated that different training could maximise SMAs property like:

- Required number of cycles to stabilise the material
- Reduction in the hysteresis width
- Total amount and stability of transformation strain
- Development of two-way shape memory effect (TWSME)

Partial reverse transformation and the TWSME were further investigated by Wada et al. [55] which concluded that “the generation of maximum TWME and SATWME [Stress-Assisted Two Way Memory effect] does not result particularly from the retention of martensite but rather predominantly determined by the favourable dislocations and internal stress field created during martensite pre-deformation and under constrained thermal cycling”.

Stabilization of the material response should always be considered extremely carefully, being strongly influenced by the material composition and training process. As an example, NiTiHf specimen tested by Befan et al. [13] under descending torque cycle achieved stability after around 50 cycles, as shown in figure 2.15. At the same time, NiTi specimens examined by Mabe et al. [36] required around 1000 cycles, as shown in figure 2.16 in which transformation strain can be calculated as the difference between martensite and austenite strain. It is essential to highlight that long term stability can only be caught with a high number of cycles, necessary to account for creep. The creep effect is relevant because even completing the transformation cycle at each actuation (therefore preserving the overall transformation strain and the related actuator excursion) the minimum and maximum actuator deflection change following the trend of martensite and austenite strain, as shown in figure 2.17.

Similarly to the stabilisation process, the two-way shape memory effect requires a certain training to develop ad stabilise. Figure 2.18 shows that 1000-1500 cycles are needed to achieve a constant transformation strain for most tested specimens. For the sake of clarity, figure 2.19 gives a great overview of the TWSE in terms of shear stress and strain. Note that even with an adverse torque that generates negative stress, austenite is able to recover the martensitic shape upon cooling.

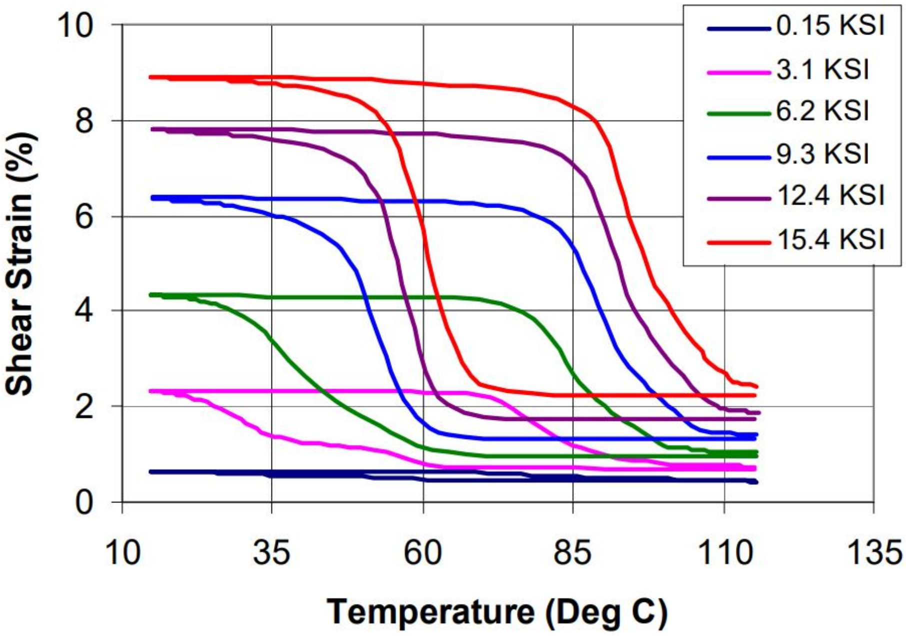

(a) Initial Hysteresis Curves

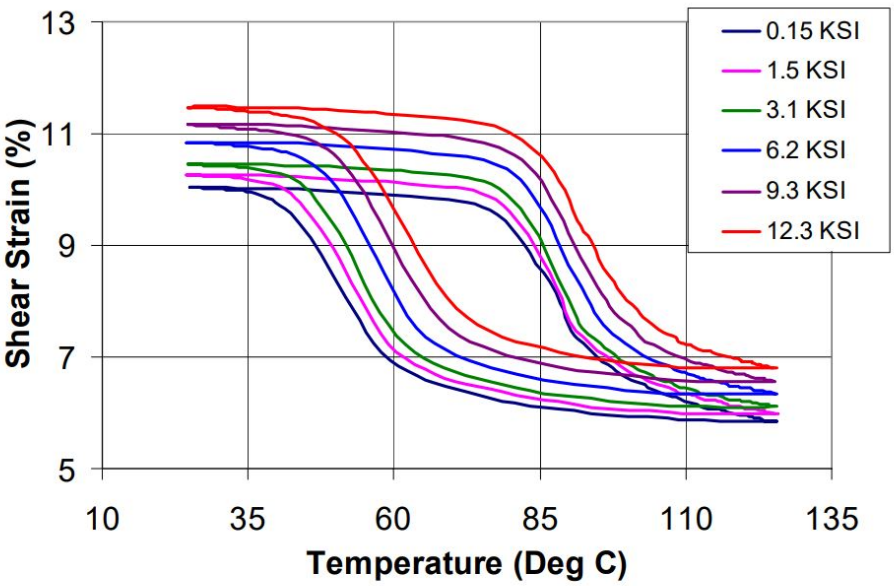

(b) Hysteresis Curves After Cycling

Figure 2.13: Stress-Temperature Hysteresis Curves [36].

Thermal aspects are of fundamental importance for SMA actuators design. However, due to its breadth, this topic is not addressed in depth within the current work. Still, some basic concepts are presented here to give some interesting insights.

As with most SMA properties, transition temperatures at zero-stress are influenced by material composition. It was found that the presence of Hafnium increases these temperatures and generally provides better performance with respect to basic NiTi alloys [14].

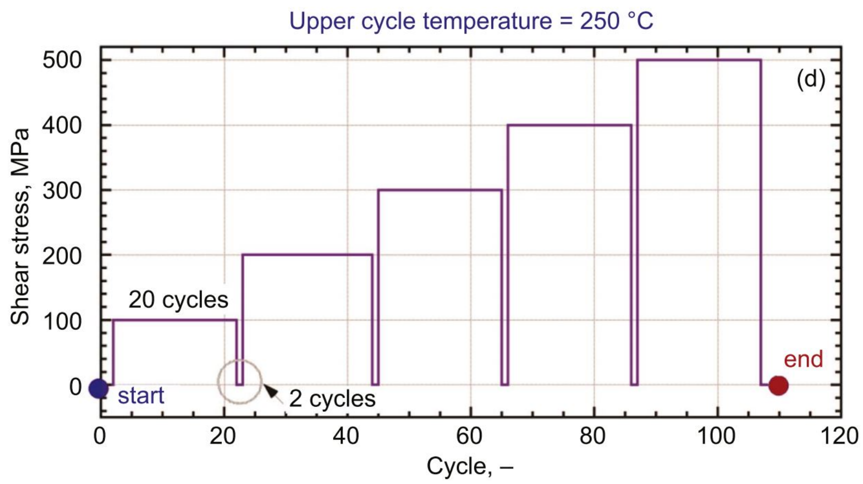

(a) Stress-cycle profile corresponding to constant-torque thermal cycling experiments for series of ascending stress levels from 0 to 500 MPa using lower upper cycle temperature of 250 °C.

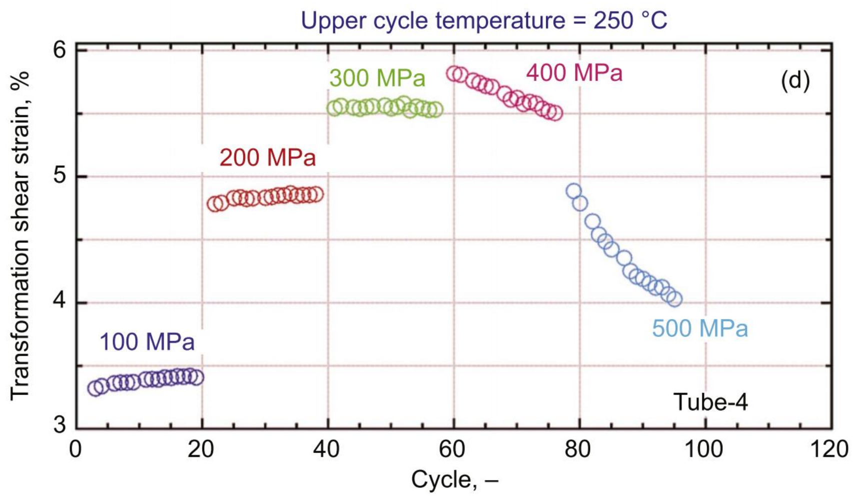

(b) Transformation shear strains as function of cycle number for 20 constant-torque thermal cycles at each stress level.

Figure 2.14: Stress-cycle profile and corresponding transformation shear strains [13].

Due to creep effects, induced stress generated by a constant torque varies with thermal cycles; consequently, transformation temperature may change as well, as shown in figure 2.20. This means that, considering the actuator control logic, activation temperature cannot be assumed as constant for long-term applications.

It is well known that actuation frequency is one of the greatest weaknesses of SMA actuators. The main reason is related to the alloy nature itself in being activated by temperature change, and so constrained by thermal conduction laws. As example, figure 2.21 shows typical strain-time thermal cycling data. In this case, four thermoelectric modules were used for heating and cooling the specimen, and, in order to maximise conductivity, the gaps between the TEMs and the tube were filled with thermal grease and Carbon Fiber Brush [36]. The great advantage of using TEMs is that they provide active cooling, dramatically reducing actuation time.

In addition to this, Saunders et al. [48] demonstrated that induction heating could reduce

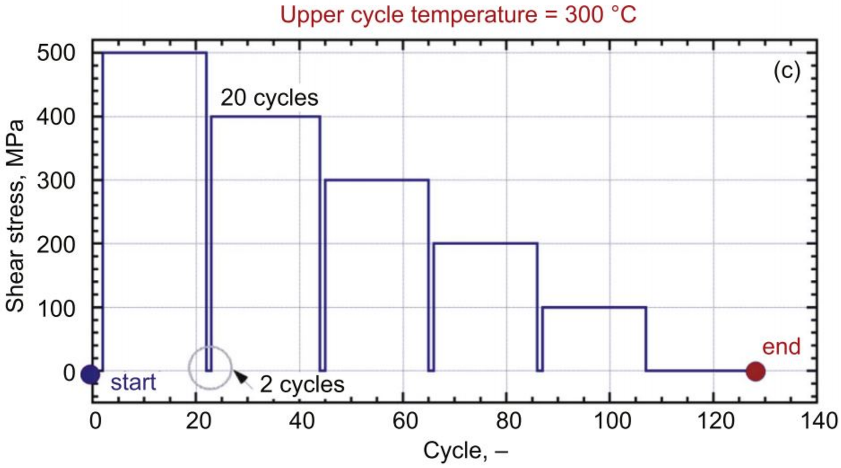

(a) Stress-cycle profile corresponding to constant-torque thermal cycling experiments for series of descending stress levels from 500 to 0 MPa.

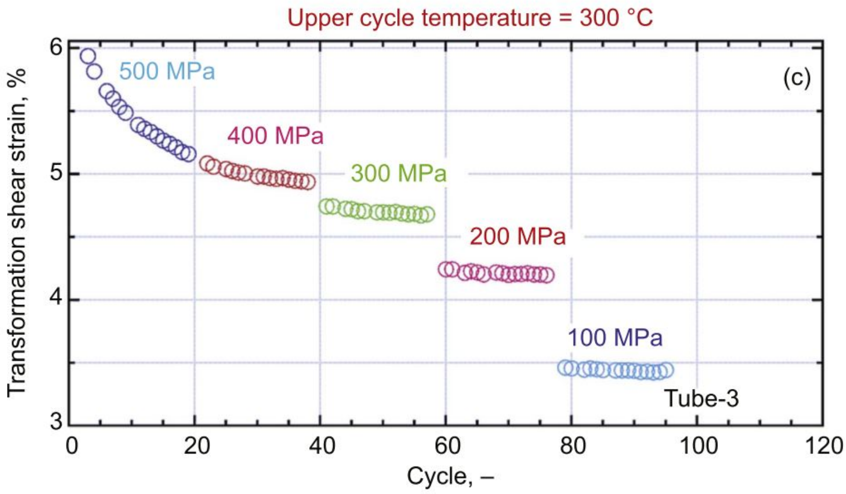

(b) Transformation shear strains as function of cycle number for 20 constant-torque thermal cycles at each stress level.

Figure 2.15: Stress-cycle profile and corresponding transformation shear strains [13].

cycling time by an order of magnitude compared with cartridge heating, which is the simplest off-the-shelf solution generally adopted. Figure 2.22 shows results comparing cartridge heating to induction heating for their specific application.

One last aspect which is worth recalling is the connection and integration of the tubes. In the specimens tested by Mabe et al. [36], all the failures initiated at the end of the fitting pinholes illustrated in figure 2.23. A better solution is using a splined end as that shown in figure 1.17 or a tapered spline coupled with a crimp as that illustrated in figure 2.24, with the additional benefit that radial force prevents the tube from slippage [34].

Certainly, SMA properties widely vary for each specimen. For example, as mentioned in chapter 1, in some instances, M_s temperature is higher than A_s, as for the material studied in [53] and [52]. Outright, in some isolated cases, SMAs even show anisotropic properties, as shown in figure 2.25.

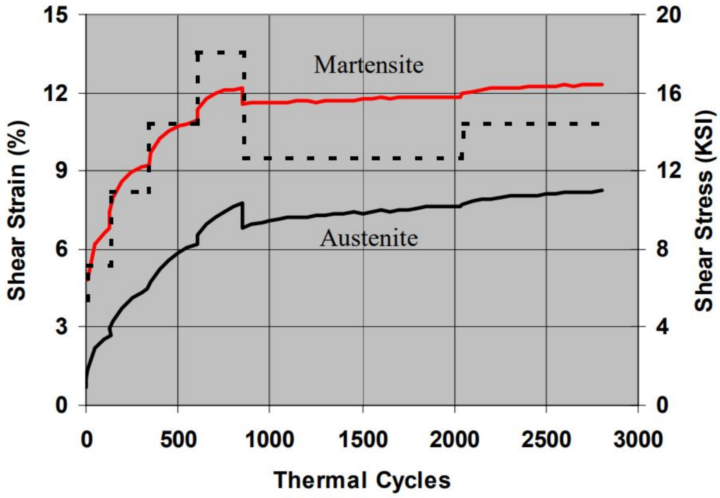

Figure 2.16: Shear stress and strain as a function of thermal cycles under constant loading [36].

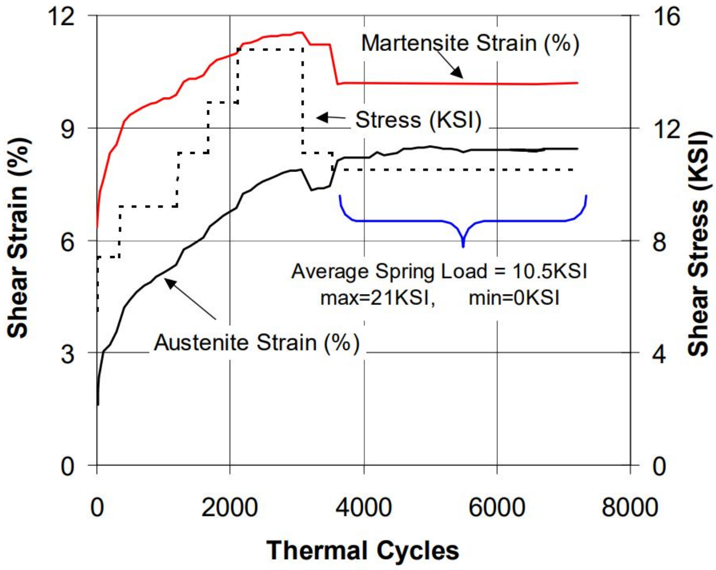

Figure 2.17: Shear stress and strain as a function of thermal cycles under spring loading [36].

Based on most of the consideration presented above, Mabe et al. [36] proposed a procedure to design SMA torsional actuators based on the following steps:

1. " Develop a desired load line. Force and deflection curve for the load.

2. Specify the maximum number of thermal cycles the actuator must perform.

3. Develop a maximum working stress for NiTinol. This stress level usually is based on the maximum acceptable creep level.

4. Develop a stress-strain curve for the NiTinol load from the data obtained in steps 1 and 3.

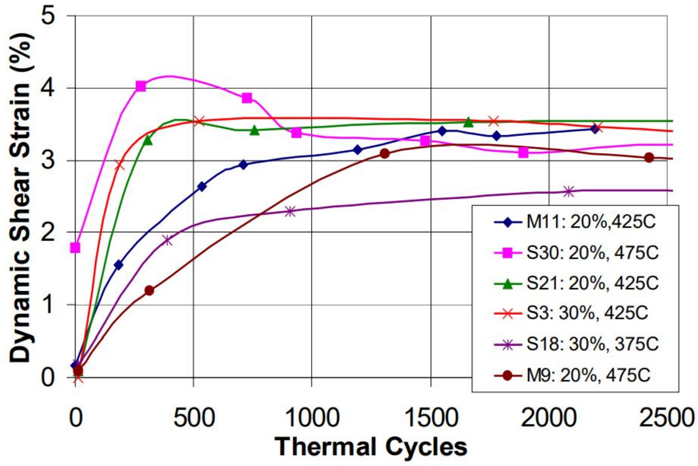

Figure 2.18: Tw-way memory development [36].

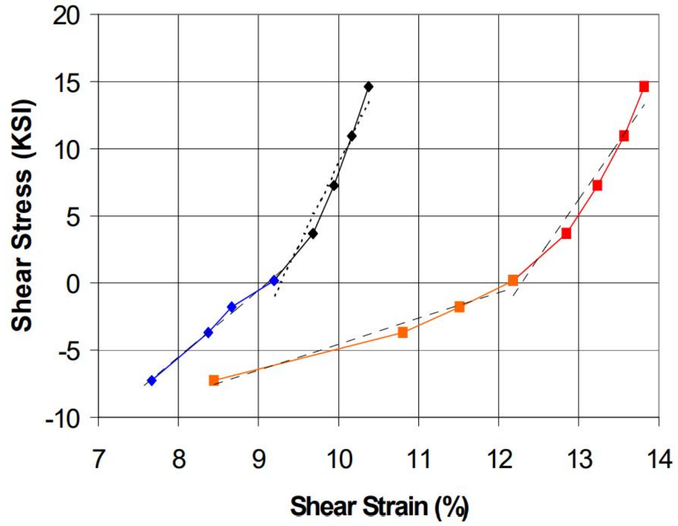

Figure 2.19: Austenite and martensite stress vs. strain curves after TWSME development [36].

5. Develop the dynamic stress-strain curves for Austenitic and Martensitic NiTinol by testing under scaled loading of the same type as in step 1. (Note 1: These curves are initially strong functions of the number of thermal cycles. Therefore, testing should be conducted over sufficient cycles to reliably predict the performance at the cycle requirement specified in step 2.) (Note 2: Typically 2-way effect will develop as a part of this procedure. Two-way effect is an important feature of the dynamic stress-strain performance, and is a function of thermal cycles and stress level.)

6. Based on the data developed in step 5, design a full-scale actuator that meets the load and displacement requirements of the application.

7. Develop a control procedure that anticipates creep and 2-way growth, and minimizes their effect on load.

8. Optimize the system design. Usually this means minimizing weight and activation time for a given input power and available cooling.

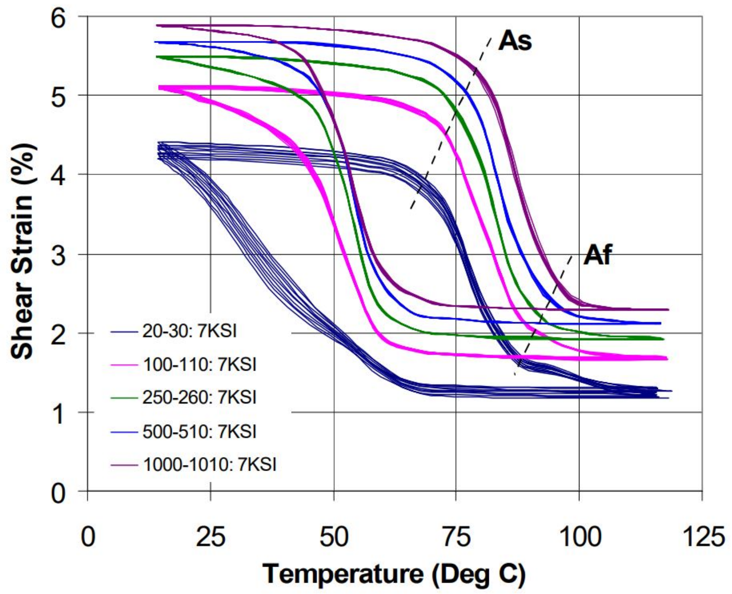

Figure 2.20: Cycling effects on transition temperature [36].

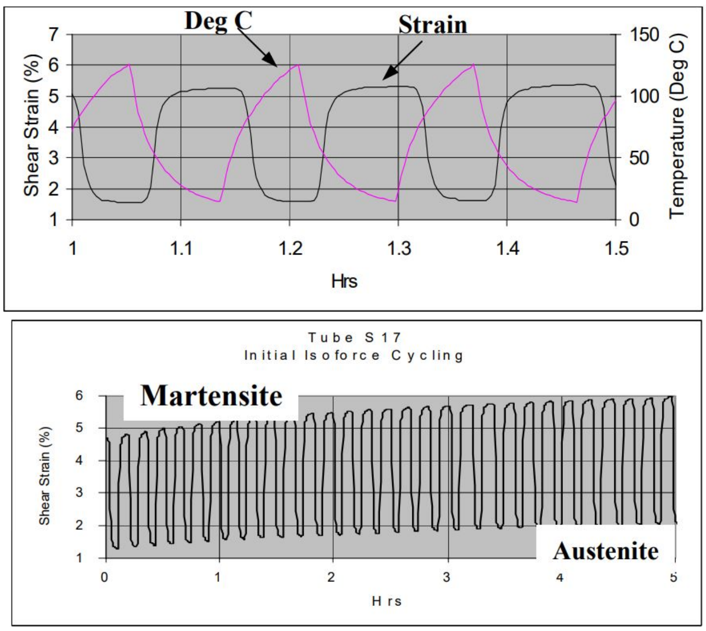

Figure 2.21: Typical thermal cycling data [36].

9. Construct a scale system, and operate it at design stress, under scaled loads, to determine the creep and lifetime performance of the actuator."

This procedure, which includes several experimental tests, probably offers the best results in terms of accuracy and method robustness; however, it turns out to be expensive and time-consuming. Although the steps reported above are mandatory to define the final draft of an SMA actuator, a leaner approach can be followed for the preliminary design, as shown in the following chapters.

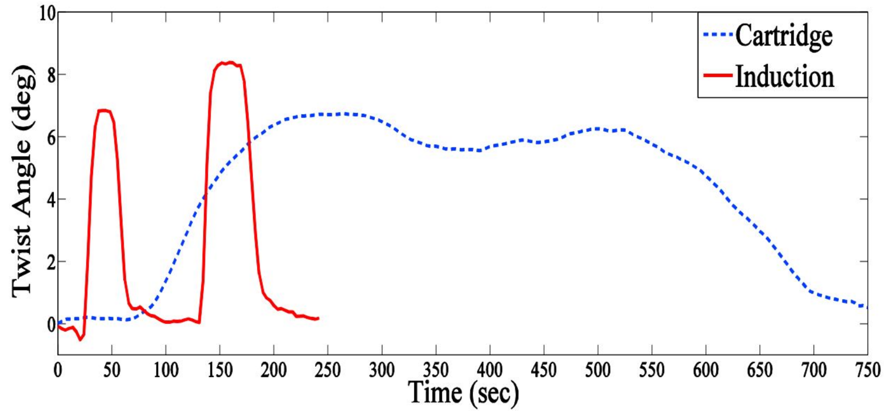

Figure 2.22: Cartridge heating compared to induction heating of the SMA tube in the twisting wing [48].

Figure 2.23: NiTinol finished torque tube [36].

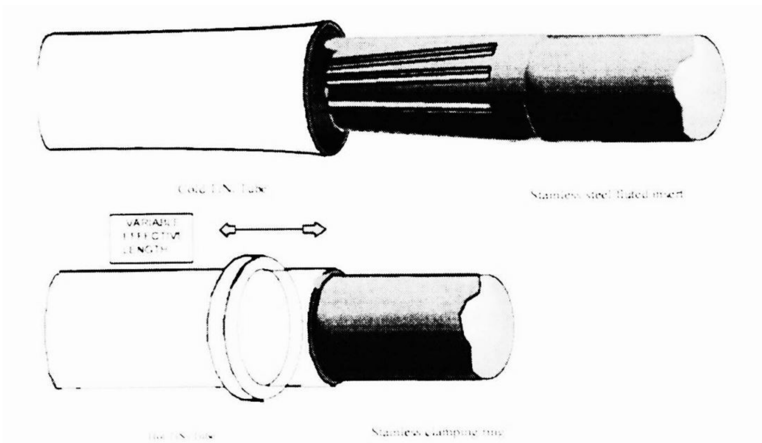

Figure 2.24: Torque tube connection scheme [34].

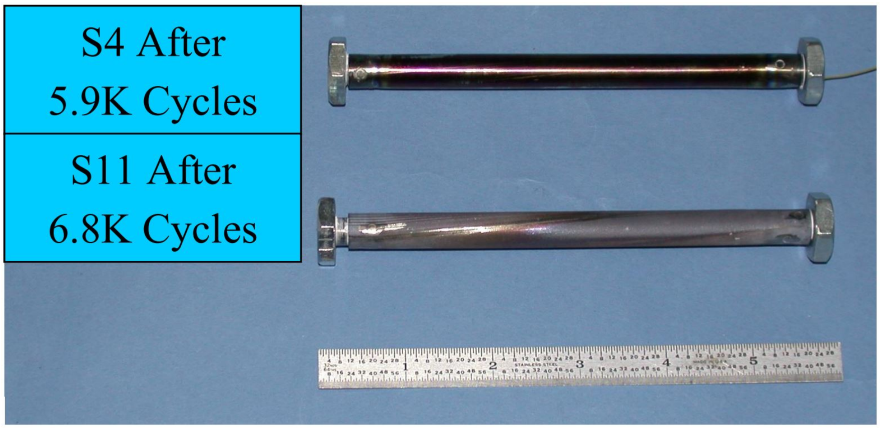

Figure 2.25: Torque tubes after Cycling [36].

2.4 Patents

This section presents several examples of relevant actuators based on shape memory torque tubes, collected from both papers and patents. This collection aims to provide a general idea of the state-of-the-art, suggest methodologies and design solution.

2.4.1 Mabe et al. Shape Memory Alloy Actuator

Mabe et al. patented an SMA torsional actuator differentiated in different configurations [37]. One of those consists of a double hinge flap that employs a rotary actuator to drive two surfaces synchronised using a pinion gear as shown in figure 2.26. This device also includes a spring and a locking mechanism, which can work together as a fast actuation device, precedently loaded by two SMA torque tubes. Moreover, the locking mechanism enables the SMA to cool down soon after the flap reaches the target position, resulting in remarkable energy saving. Figure 2.27 shows the locking operation, as well as the spline, numbered 738, which allow the SMA torque tube to drive the device in only one direction. This is a brilliant yet simple idea to overcome the necessity to have a clutch during the SMA cooling.

Another remarkable claim of this patent, related to another device, is the introduction of a clutch that can be engaged and disengaged according to the desired flap position. Moreover, it allows to employ only the range of temperatures in which the SMA response is quicker, thus reducing the actuation time. Figure 2.28 shows the overall idea of this concept.

2.4.2 Jacot et al. Shape Memory Alloy device and control method

Jacot et al. designed and tested a brilliant device deputed to control a morphing rotor blade [17] [8]. Figure 2.29 shows a down-scaled version of the device. The actuator can maintain two stable position thanks to a strain energy shuttle apparatus, as shown in figure 2.30.

Further insights about this kind of device are reported in [21] as shown in figure 2.31.

The active part of the actuator is composed of two parallel SMA torque tubes that activate simultaneously during each actuation. Thus, leveraging on two-way SME, it is possible to overcome the necessity of a return spring needed for those configurations in which stress-assisted SME is required. What is even more remarkable is the incredibly advanced thermal management, which operates three TEMs to redirect thermal fluxes, and a thermosyphon to dissipate excessive heat. Indeed, being mounted in opposite directions, for both tubes to turn clockwise, one must be heated, while the other is cooled. This way, both the SMA tubes provide torque at each actuation even if they undergo an opposite transformation. Figure 2.32 and figure 2.33 present an overview of the actuator and the heat transfer dynamics. Further insights about this kind of device are reported in [33].

Research on morphing rotor blades still continues nowadays. The European programme “Shape Adaptive Blades for Rotorcraft Efficiency” (SABRE), within the framework of Horizon 2020, also aimed to develop SMA based actuators. In this context, a great contribution comes from CIRA researchers as evidenced by [43].

2.4.3 Gunter et al. Remotely Actuated wind tunnel model rudder using shape memory alloy

Gunter et al. designed a torsional actuator with two collinear SMA tubes having an antagonistic reaction about a control temperature point [29]. This application specifically addresses controlling wind tunnel model rudder remotely; consequently, the general architecture of this device is straightforward and doesn’t aim to minimise power consumption. The SMA torque tubes are trained to develop an opposite twist direction. This way, the actuation is obtained by differentially heating the tubes using cartridge heaters. Figure 2.34 shows an overview of the aforementioned design.

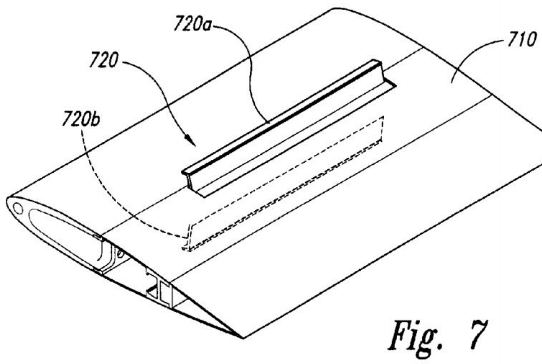

(a) Illustration of a rotor blade that includes multiple deployable devices.

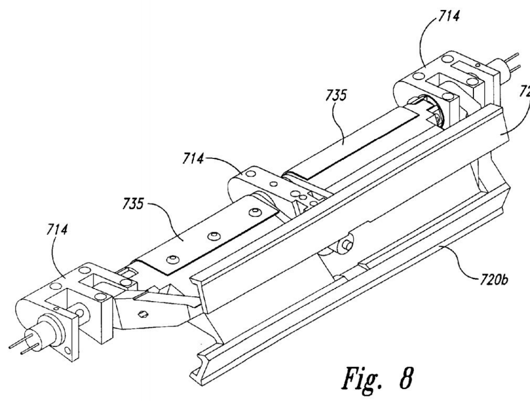

(b) Illustration of the deployable devices.

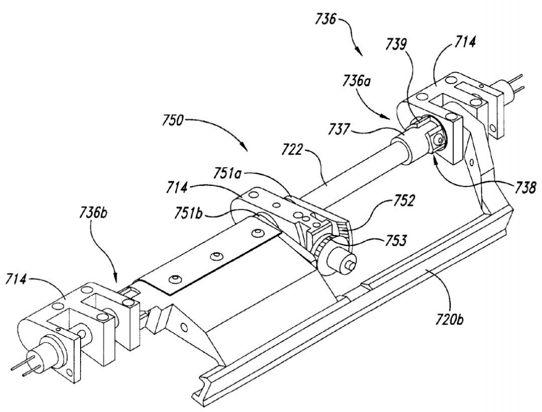

(c) Illustration of an SMA actuator and associated connections with the deployable devices.

Figure 2.26: Overview of SMA torsional actuator device from [37].

2.4.4 Spanwise Adaptive Wing (SAW)

The Spanwise Adaptive Wing project has been developed to articulate outboard wing sections using SMA torsional actuators. The program aim is twofold: saving aeroplanes planform space for specific applications as aircraft carrier missions, and augmenting lateral-directional stability. While static actuation was performed on a full-scale F18 wing, flight tests have been carried on a UAV platform denominated Area-I PTERA in 2017 [52], as shown in figure 2.35. A similar concept is presented in the patent of "Controllable Winglets" by Mithra et al. [47].

2.4.5 Boeing Adaptive Trailing Edge (ATE)

The Adaptive Trailing Edge program represents one of the most significant milestones in SMA torsional actuators development. Indeed in 2012, for the first time, these devices were tested in flight on a Boeing 737-800, leading to maturation from TRL4 to TRL7 [18]. The actuation system was intended to deflect a little split-flap of 2% of the local chord in a range between 30 degrees up and 60 degrees down, as shown in figure 2.36. The overall apparatus was redundant for safety reasons and included secondary components that also provided a locking and damping function. Despite it appears relatively cumbersome, the SMA actuating core is straightforward as shown in figures 2.37 and 2.38. Indeed, a dual-tube design was adopted in order to control the flap motion through martensite to austenite transformation for both deployment and retraction via heating. A simple cartridge heater supplied thermal energy.

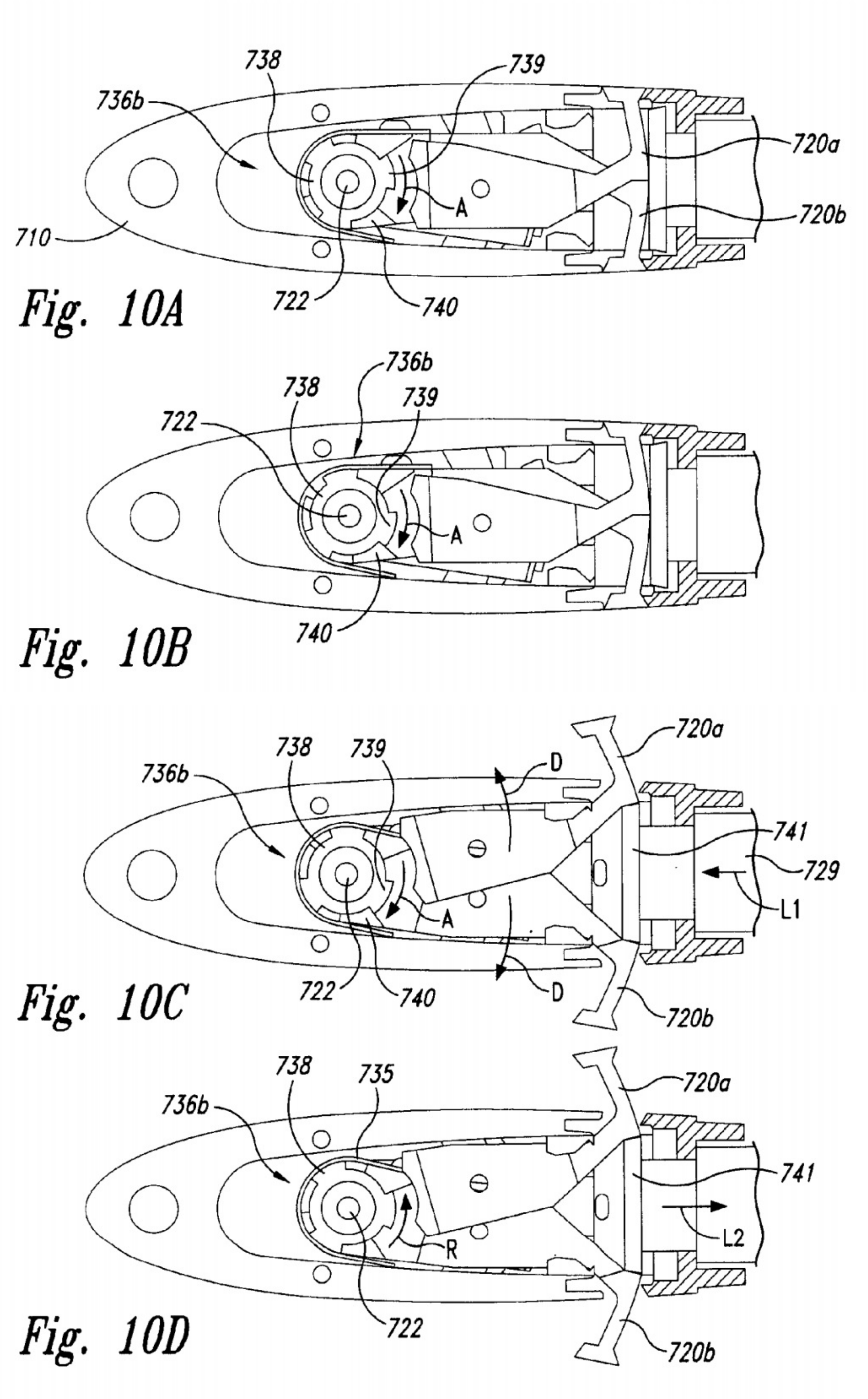

Figure 2.27: Illustration of actuator operation phases from [37].

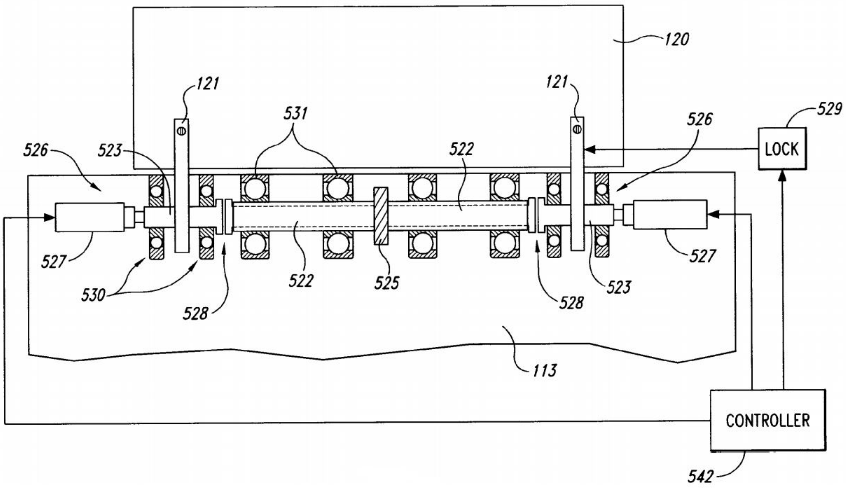

Figure 2.28: Schematic plan view illustration of an SMA actuator coupled to a deployable device with an activatable link [37].

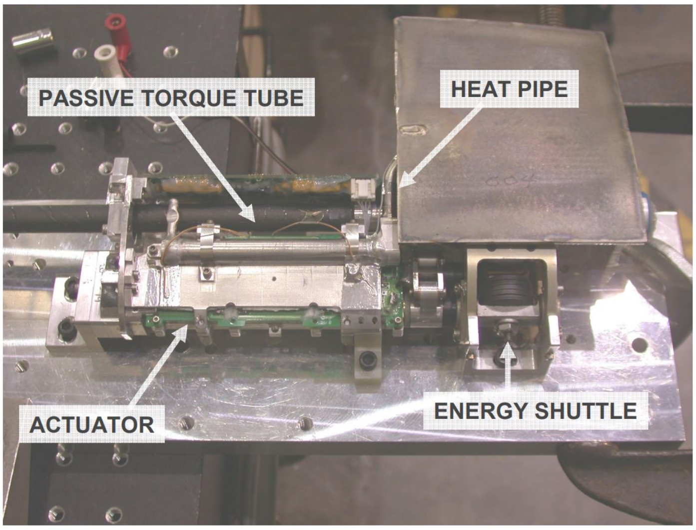

Figure 2.29: Quarter-scale actuator and cooler on laboratory bench top [8].

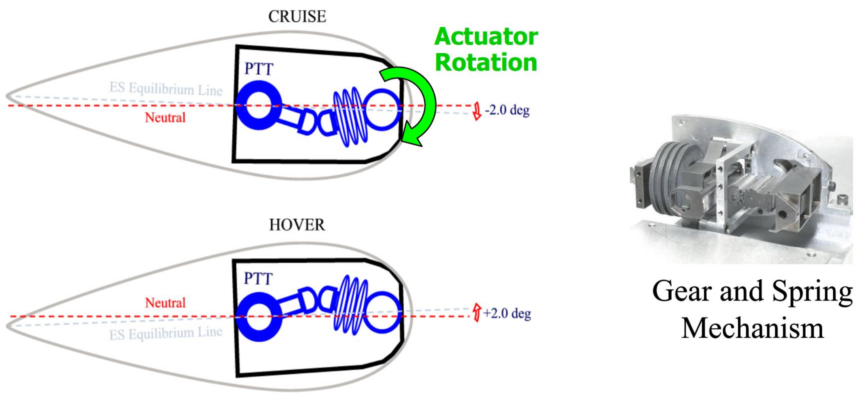

Figure 2.30: Spring mechanism and illustration of operation [17].

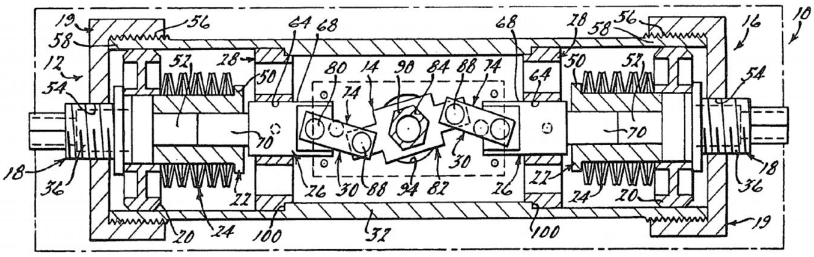

Figure 2.31: Strain energy shuttle apparatus from [21].

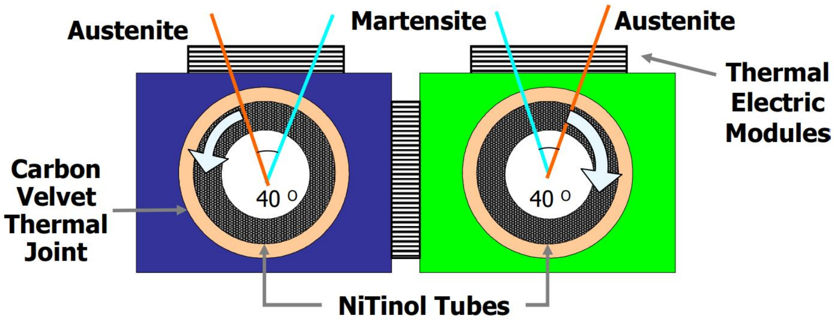

Figure 2.32: NiTi tube arrangement in an actuator [8].

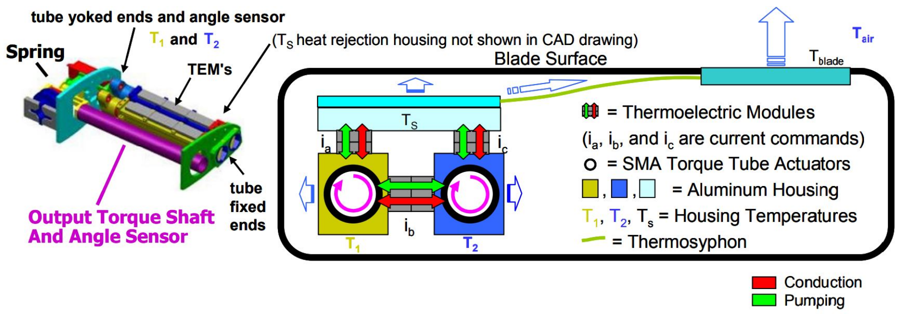

Figure 2.33: Actuator model and heat transfer illustration [17].

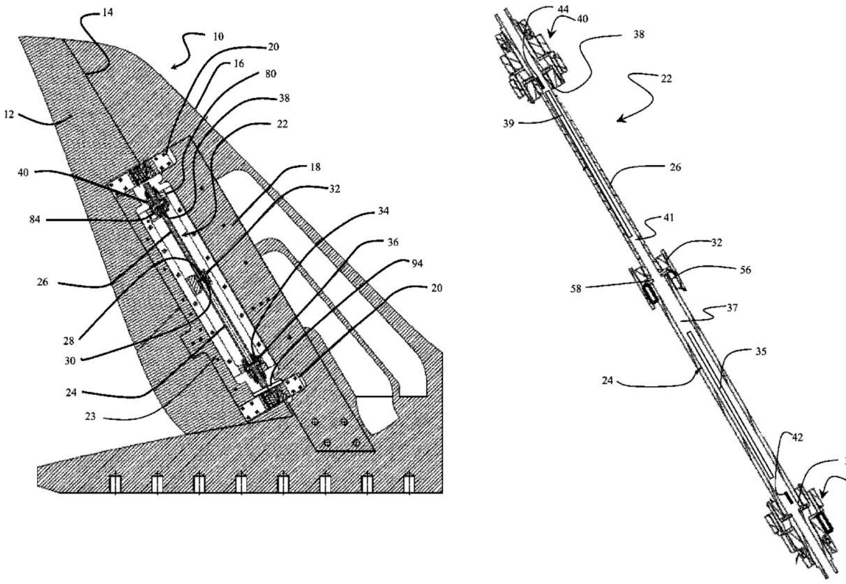

Figure 2.34: Side section view of a wind tunnel model rudder and actuator assembly showing the actuation tubes and support structure [29].

Figure 2.35: NASA Spanwise Adaptive Wing incorporating torsional actuators; flight tested on an Area-I PTERA UAV. SMA torque tubes are mounted in the chord-wise direction along the hinge-line to control the articulation of the outboard wing section [52].

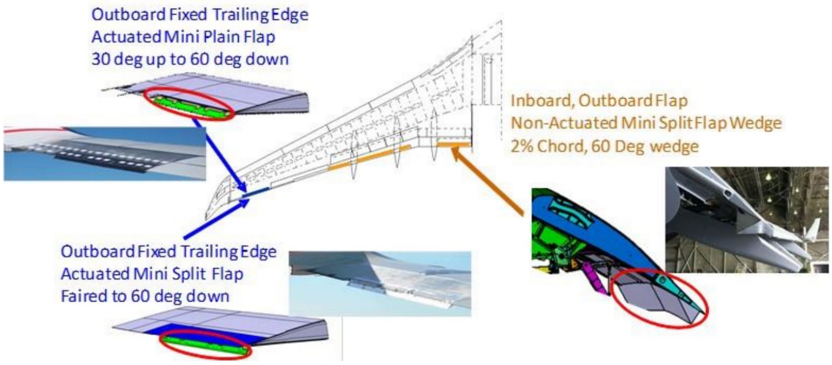

Figure 2.36: ATE Flight-Test Elements: Outboard Wing Actuated Mini Split Flap and Mini Plain Flap, and One Fixed Wedge (2% of local chord 60-deg deflection) on Inboard and Outboard Aft Flap [18].

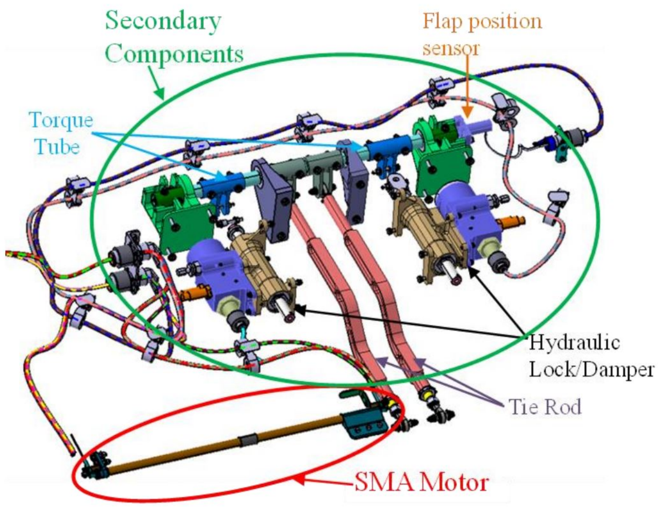

Figure 2.37: Mini Flap actuation system components [18].

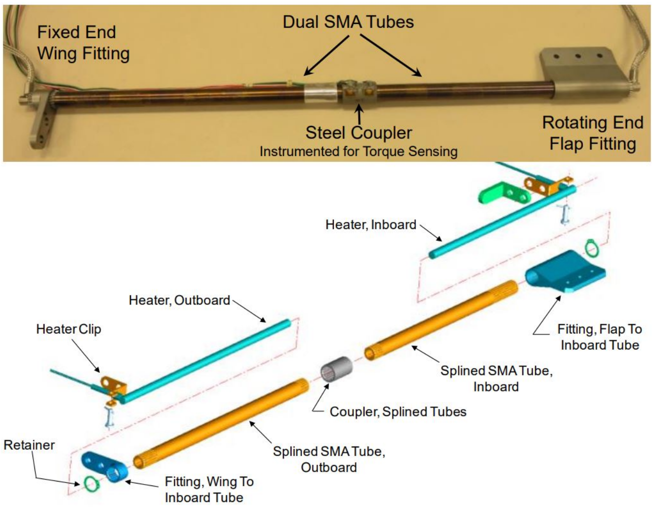

Figure 2.38: Dual NiTi tube actuator assembled and exploded view [18].

Chapter 3

Conceptual design

3.1 Basis for the interpretation of actuator diagram

This section illustrates some ideas that, despite their simplicity, are worth mentioning to understand deeply the general charts describing SMA actuators thermomechanical response. It is crucial to consider these aspects to avoid mistakes during the conceptual design phase. The following approach consists of a series of steps in which classical torque-angle charts are manipulated to represent SMA actuators' behaviour more directly. Figure 3.1 represents the torque-angle characteristic (C and θ respectively) for two different components in the same reference frame. In particular, the red and orange lines show a simplified SMA exhibiting pseudoelastic effect at temperature T_1. In particular, red segments represent the loading path, while the orange ones the unloading path. The blue line, instead, shows a linear elastic response such as that of a torsional spring. For the couple of deflection angles, θ_1 and θ_2 the reaction torque of the two components is equal and opposite so that $C_1 = |C_2|$.

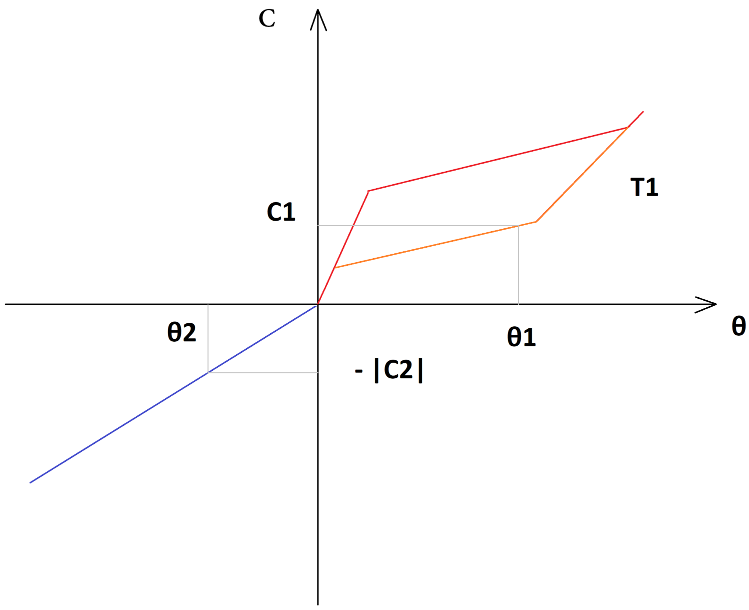

Figure 3.1: Actuator diagram - Step 1

A graphical representation of these components is presented in figure 3.2, in which, moreover, the torsional spring torque is substituted by its modulus. This representation aims to get immediately that the reaction torque of the components is equal in absolute values.

A step forward is done in figure 3.3. Indeed the origin of the θ axis related to the torsional spring is translated rightward overlapping θ_1 and θ_2 in their respective reference frame.

Despite having two θ axis could appear less intuitive, the advantage of this representation method is that any change of the equilibrium position θ_1, θ_2 is immediately recognised for both the SMA and the linear elastic spring.

Indeed, as shown in figure 3.4, the coupling of the two preloaded components constrains both of them to rotate by the same angle about the original equilibrium position upon a perturbation.

At this point, thermal-induced transformation comes into play. As temperature rises, martensite to austenite transformation occurs. This leads to a modification in the torque-angle SMA characteristic that can be visualised as an upward and rightward translation of the hysteresis loop. Consequently, at a given temperature $T_2 > T_1$, a new equilibrium point is established, as shown in figure 3.5. The recovery of austenitic shape leads to an angular actuation of $\Delta\theta$ under a variable load. This representation immediately shows how the SMA component returns toward

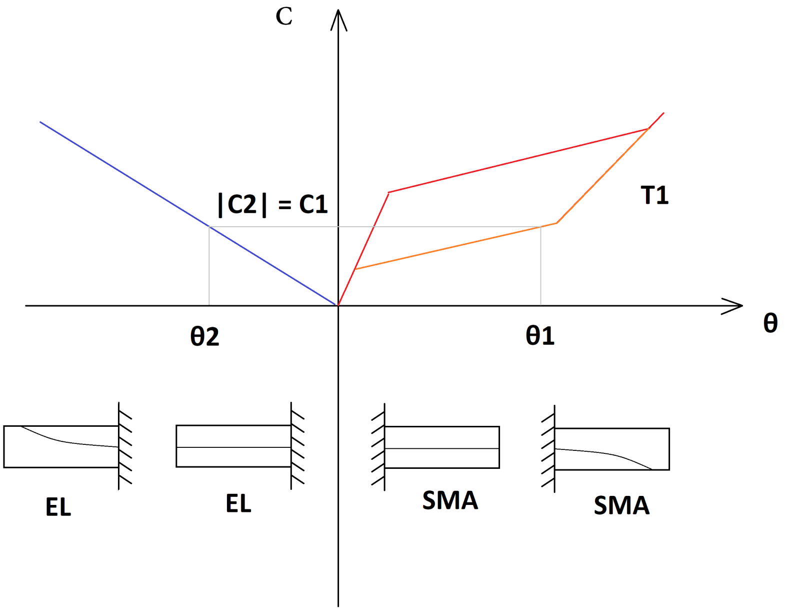

Figure 3.2: Actuator diagram - Step 2

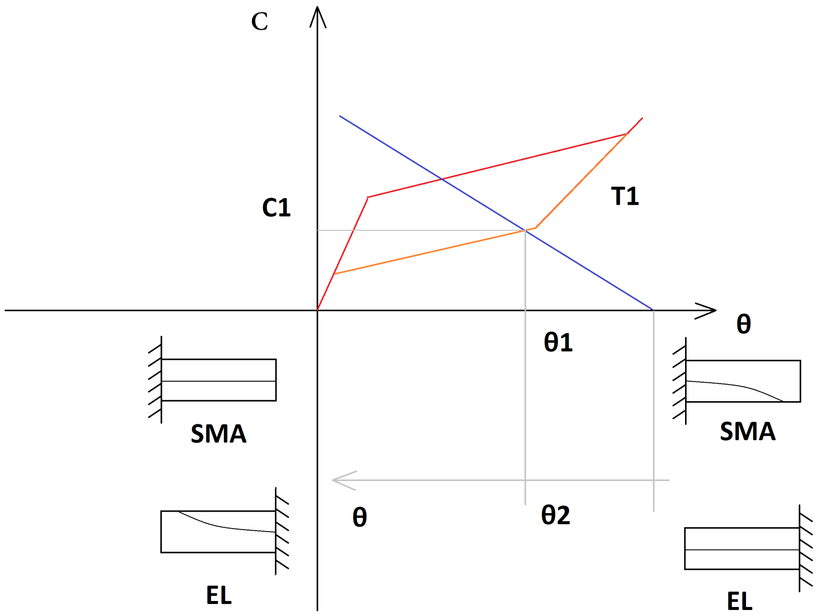

Figure 3.3: Actuator diagram - Step 3

its undeformed configuration while the torsional spring increases its deformation[1]. Consequently,

[1]Note that a rigorous representation of $\Delta\theta$ sign has been sacrificed to greater clarity.

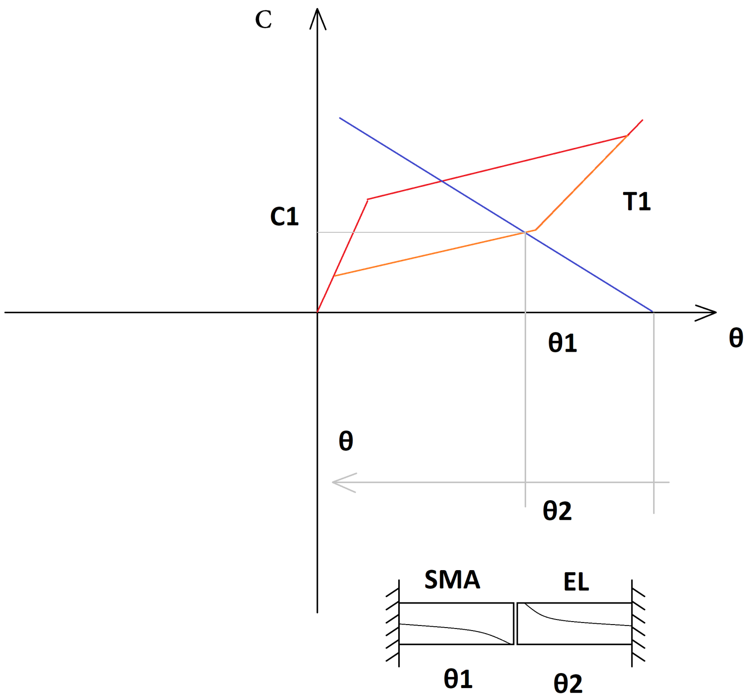

Figure 3.4: Actuator diagram - Step 4

during the forward actuation, the SMA is heating and unloading; meanwhile, in the reverse actuation, the SMA undergoes cooling and loading. This consideration is crucial to understand that upon heating and shape recovery, the equilibrium point is obtained from the intersection of the load line with the unloading segment of the SMA loop ($M \rightarrow A$ segment), while during cooling, the loading section ($A \rightarrow M$) has to be considered. It is clear at this point that aspects from either thermal-induced and stress-induced transformation are involved.

The aspects described above, are further illustrated in [23] as shown in figure 3.6.

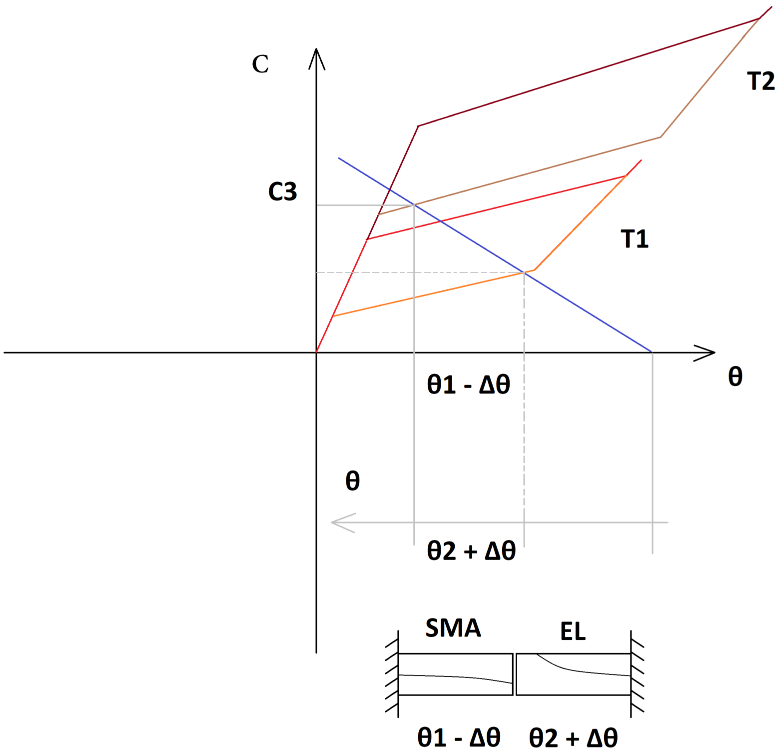

Figure 3.5: Actuator diagram - Step 5

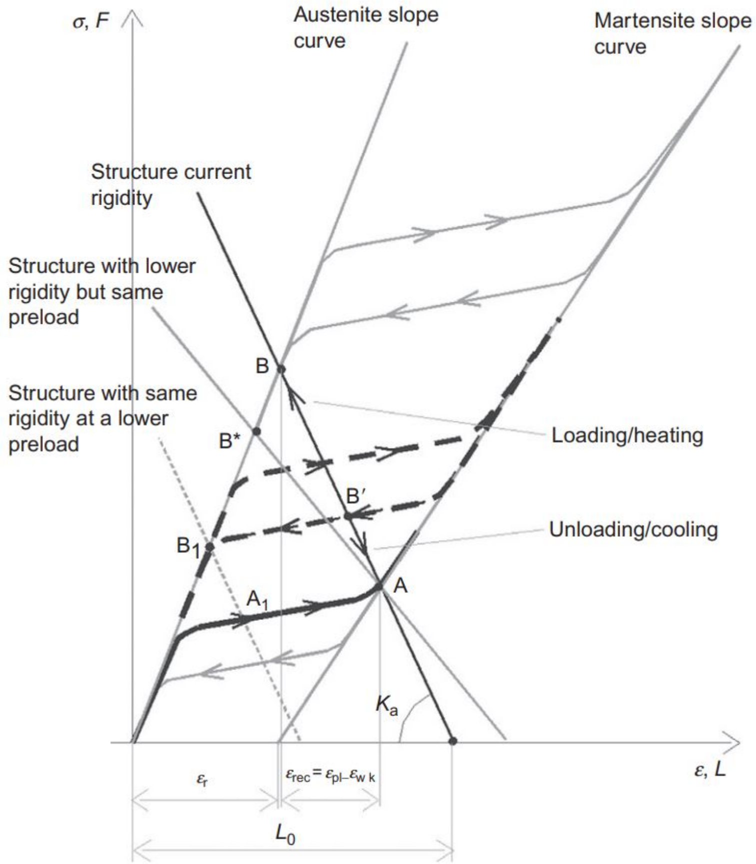

Figure 3.6: SMA and structure material curves: design steps (Austenite - Martensite path). Axes are stress-strain and force-displacement domains [23].

3.2 Architecture choice

In this section, the overall SMA torsional actuator design of this work is presented. As shown in previous chapters, state of the art actuators usually employ two torque tubes avoiding using a contrast spring and thus optimizing the system weight. Moreover, leveraging on two-way shape memory effect, both tubes can provide torque in both direct and reverse motion. However, aiming to provide a general procedure, and to keep the general architecture as simple as possible, the architecture proposed here includes an SMA torque rod and a return torque spring collinearly coupled. This way, the forward actuation exploits direct transformation ($M \rightarrow A$), while the backward phase transformation is assisted by the contrast element applied force (stress assisted two-way memory effect). In the case of a constantly powered actuator such as that presented in [29] these components, joined by a thermal control system, are sufficient to accomplish the operations required. The current work does a step forward by including a blocking mechanism that enables to cool down the SMA component once the desired position is reached. The principal advantage of this choice is the resulting energy saving, however, even being a simple upgrade, the resulting consequents are not trivial. Examples of the utilisation of this kind of devices can be found in flap or adaptive trailing edge. Still with the intention of keeping operations simple, the actuator is designed to provide movement only in the forward direction, while a further damped return spring system controls the backward motion. A similar solution was implemented in [37]. In order to deactivate the SMA tube while maintaining the control surface position unaltered, a spline coupling system or a clutch is required. These components are essential to decouple the driving SMA rod rotation from that of the driven shaft during cool down. This way, upon cooling, the SMA can recover the shape associated with its martensitic phase, while the driven shaft keyed with the control surface, maintains its angular position thanks to the locking mechanism. Upon locking release, the driven shaft recovers its original position. In the case of an ATE, in which also upward deflection is needed, the equilibrium position of the return mechanism can be set with a certain offset with respect to the hinge zero angular displacement, so that the actuator can provide either negative and positive deflections despite operating always in the same direction.

A spline assembly similar to that presented in [37] and its working scheme is illustrated in figure 3.7, while figure 3.8 shows a schematic image of the architecture described above.

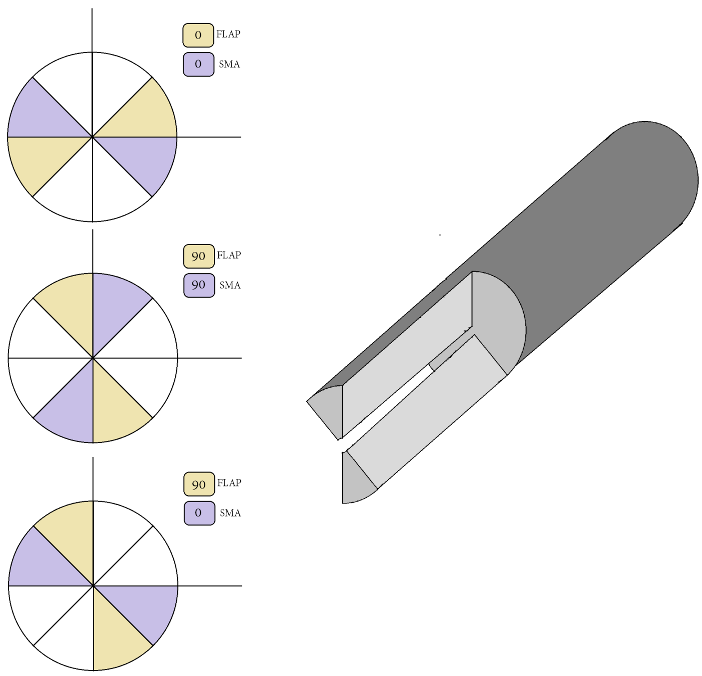

Figure 3.7: Spline coupling working principle.

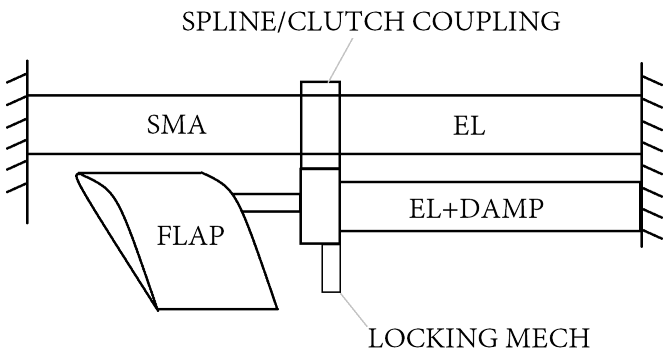

Figure 3.8: Outline of the SMA actuator under investigation.

3.3 Graphical analysis

3.3.1 Method

This section presents a very helpful method to predict the overall behaviour of SMA components during actuation, based on graphical analysis. In chapter 1, stress-strain, stress-temperature and strain-temperature fileds were introduced depending on the need. These diagrams are fundamental to describe several aspects of SMAs, however even a more powerful tool can be obtained by their combination, monitoring the specimen evolution on each graph at the same time. Indeed, the stress-strain field alone, cannot appreciate any change in the state of the SMA for certain temperature ranges. On the other hand, stress-temperature and strain-temperature fields on their own don't supply an easy view of the load-lines. Figure 3.9 illustrates an overview of the simplified diagrams used in this work to predict the overall behaviour of SMA torque tubes. Note that, at this level, stress and strain can interchangeably represent torque and angular displacement respectively. In the stress-strain diagram, two SMA hysteresis loop for different temperatures are illustrated, as well as two load-lines. In particular, one load line varies with the SMA deformation, while the other is strain-independent. The first load line represents the summation effect of return springs and aerodynamic forces, while the second one represents that of an ideally constant return torque[2]. As part of the current description, all the possible load-lines can be placed between the two depicted. Indeed, during the cool down, aerodynamic forces are not applied to the SMA rod, so that the unloading path is different with respect to the loading path, which is considered strain-invariant (and so angular-displacement-invariant) to simplify the following discussion. Operating at high stress and temperature condition, a simplified version of the stress-temperature diagram is reported in figure 3.9. Finally, the shear-temperature graph represents the SMA response under the maximum and the minimum applied torque during the working cycle in red and blue respectively. This means the loops shown in the fourth quadrant of figure 3.9 can be obtained experimentally upon temperature change at constant torque.

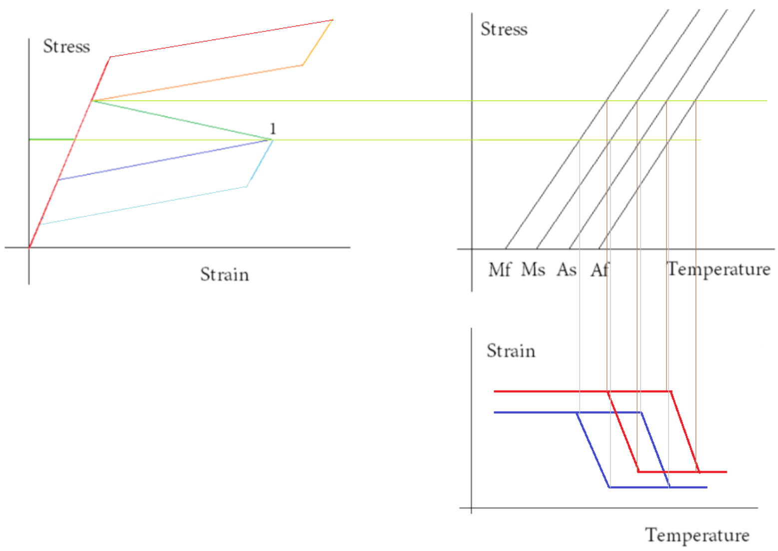

Figure 3.9: Diagrams considered for the graphical analysis.

[2]In a laboratory test, the constant stress load line can be reproduced by means of weight hanging to a pulley coupled with the SMA rod, so applying a constant torque.

3.3.2 Actuator with clutch

At this point, it is possible to examine the working scheme and the expected response of the SMA rod during the actuation. All the steps are enumerated coherently in figure 3.10 and figure 3.11 which represent a simplified schematic of the actuator. Note that the numbers presented on the top of each box represent a hypothetical angle of deflection for the related assembly, while the red and green dots represent an activated or de-activated locking mechanism, respectively. Moreover, a continuous rectangle between the "SMA+EL box" and the rest of the system represents a disengaged clutch (the systems are coupled); meanwhile, a discontinuity between the two of them represent that the clutch is engaged (the systems are decoupled).

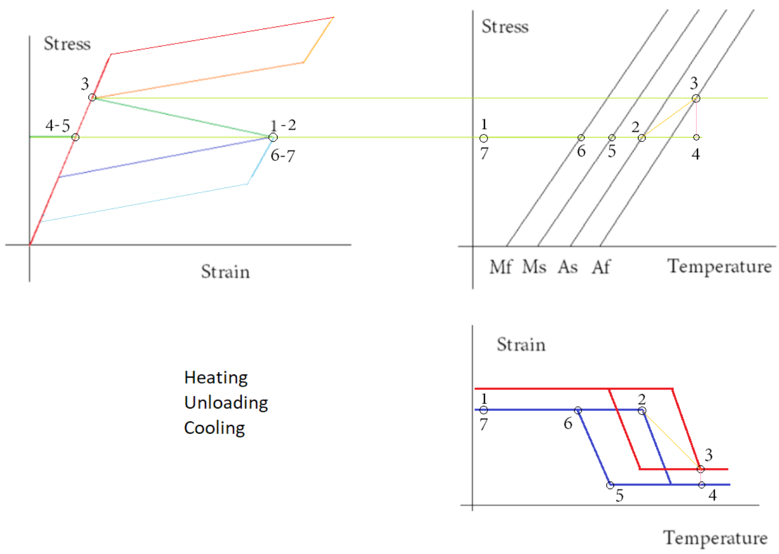

Figure 3.10: Graphical analysis - Actuator with clutch.

Point 1 represents the initial equilibrium condition between the SMA rod and the driven system, represented by the dark green line. Upon heating, before reaching A_s^σ [3], no significant changes can be appreciated on the stress-strain diagram (Point 2). Further temperature increasing, beyond A_s^σ induce the martensite to austenite transformation, resulting in the original shape recovery. Consequently, from point 2 to 3, the SMA rod angle and strain decrease following the load line equilibrium condition. This means that the 2 $\rightarrow$ 3 transformation induced by temperature rise undergo a variable load. The yellow shaded lines in stress-temperature and strain-temperature diagrams are hypothetical paths based on the expected starting and finishing equilibrium points. Note that point 3 also represents the SMA rod's angular position at the end of the forward actuation. At this step, the locking system is activated to hold the flap in position, and the clutch is engaged, enabling the SMA rod to cool down and return to its martensitic phase. As the driver and driven systems are decoupled, the overall torque applied to the SMA drops down to the horizontal load line, as shown in points 3 and 4. Simultaneously monitoring all three charts, it is evident that temperatures remain constant, stress decreases as well as strain, following the high-temperature SMA characteristic. Again, 3 $\rightarrow$ 4 loading path on stress-strain and strain-temperature diagrams are based on starting end finishing equilibrium points. Cooling the SMA rod down to M_s^σ doesn't involve any macroscopic stress-strain change as shown in points 4 and 5. Further temperature decreasing triggers the stress-assisted shape

[3] A_s^σ indicates the temperature intercepted on the A_s line for a given stress σ. This kind of notation will be reported often hereafter.

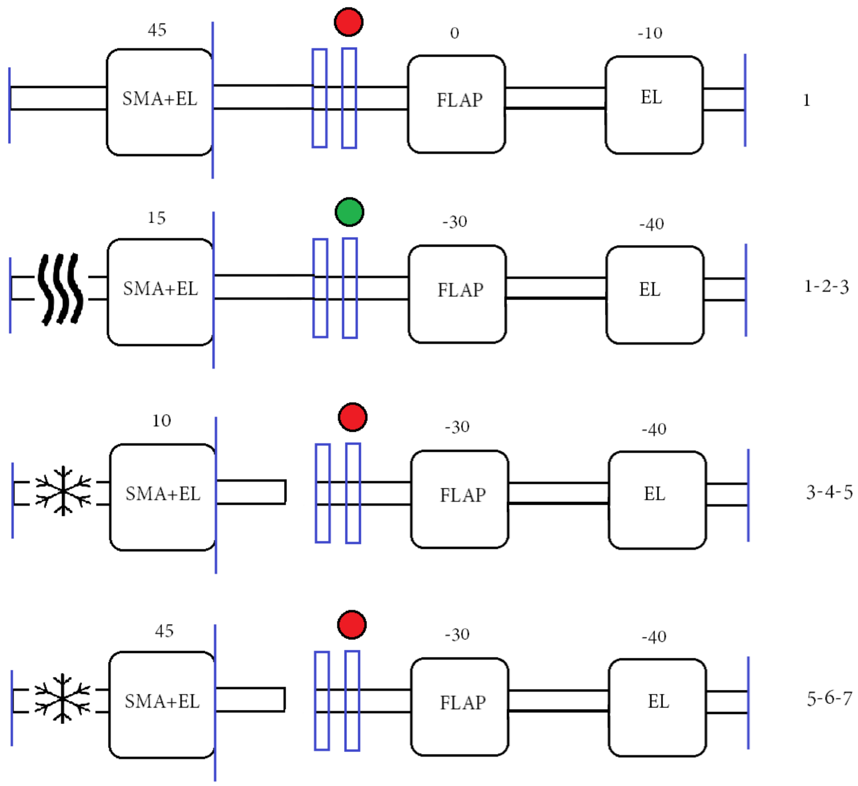

Figure 3.11: Functioning scheme - Actuator with clutch.

memory effect. The transformation ends on Point 6 as M_s^σ is reached. Strictly speaking, cooling down the SMA from point 6 to 7 under constant torque should induce a further increase in the rod strain, moving on the 100% martensite characteristic. Still, to simplify the dissertation, it can be assumed that Points 1 and 7 are sufficiently close to M_f^σ so that no macroscopical effects can be observed.

3.3.3 Actuator without clutch

The working scheme and the graphical analysis of the actuator without clutch are reported in figure 3.12 and figure 3.13.

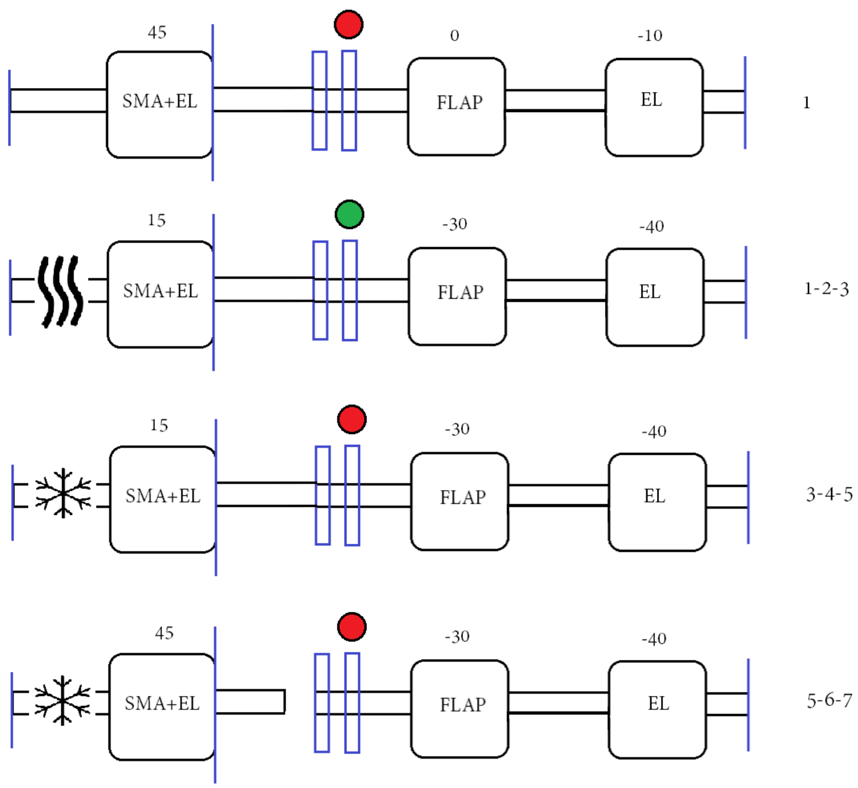

Figure 3.12: Functioning scheme - Actuator without clutch.

Most of the transformations involved in an actuator without a clutch are the same as illustrated in the previous section. Indeed, nothing changes up to Point 3. The spline coupling allows to decouple the SMA rod backward motion from that of the driven system, however, the forward motion still remains constrained. Differently from the case presented above, upon cooling the SMA rod cannot undergo strain decreasing since the lower angular position is imposed by the flap position. Consequently, as A_s^σ for the point 3 stress level is reached, $A \rightarrow M$ transformation begins but no strain changes can occur, since the returning force at this step is not high enough. Further temperature drop increases the martensitic volume fraction, lowering the component stiffness. As a result, stress must decrease, while strains remain constant during the 4 to 5 transformation. At step 5, the returning force is sufficient to trigger the stress-assisted two-way memory effect, so that the original shape is recovered at point 6. The following steps are not different with respect to the clutch provided actuator.

In the light of this working sequence, a big concern emerges. During the transformation $4 \rightarrow 5$ according to established literature, as mentioned in chapter 2 , austenite to twinned martensite transformation cannot occur in a high-stress, high-temperature region of the phase diagram as in this case. On the other hand, $4 \rightarrow 5$ transformations doesn't involve any macroscopic shape recovery, thus suggesting that detwinned martensite, which is associated with macroscopic shape deformation, is not forming.

Consequently, two possibilities can be found:

- The $4 \rightarrow 5$ transformation generates twinned martensite, eventually decaying the SMA

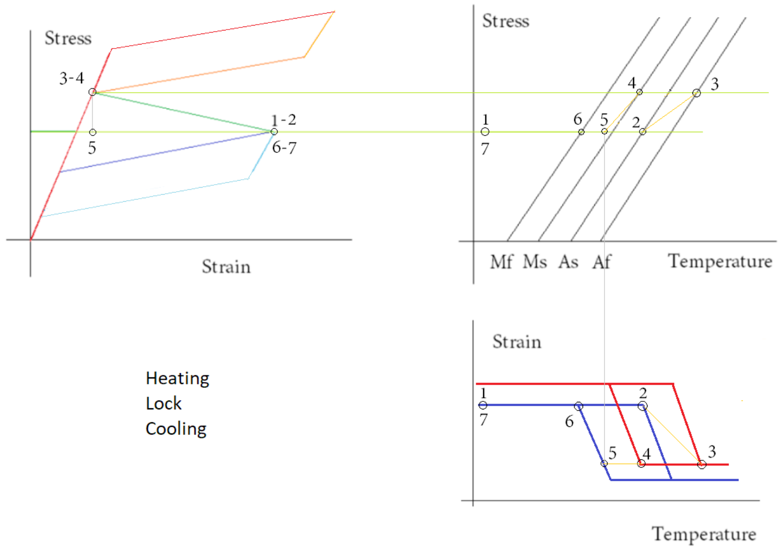

Figure 3.13: Graphical analysis - Actuator without clutch.

actuator performance due to retained martensite and the consequent decreasing of transformation strain with time. On the other hand, this would open a new region in the phase diagram never considered before.

- The 4 → 5 transformation generates detwinned martensite even without macroscopic shape change, thus preserving the transformation strain and the SMA performance with time.

In this context, Popov and Lagoudas [45] examined a similar situation obtaining the response predicted by their model as shown in fiugure 3.14. For simplicity, they considered a rod in a uniaxial stress state. From high stress and temperature condition with 100% austenite phase, the specimen is constrained and then gradually cooled. “At first, a thermoelastic contraction of the rod slightly increases the stress. When the $A \rightarrow M_d$ transformation surface is reached, transformation strains begin to develop. Now, as the transformation strains becomes nonnegative it will relax the stress state. Observe that the maximum possible value of the transformation strain H is an order of magnitude larger than the elastic strain ϵ_0 (which is kept fixed during the cooling). Therefore, very little phase transformation is required to produce transformation strains comparable with ϵ_0 and, thus to drastically reduce the stress.” [45].

In view of this consideration, the second possibility appears to be more realistic, however, it is worth mentioning that the results presented above are not experimental data, but model-predicted, moreover, it would be a good measure to perform an experimental test on long term response dispelling any slightest doubt.

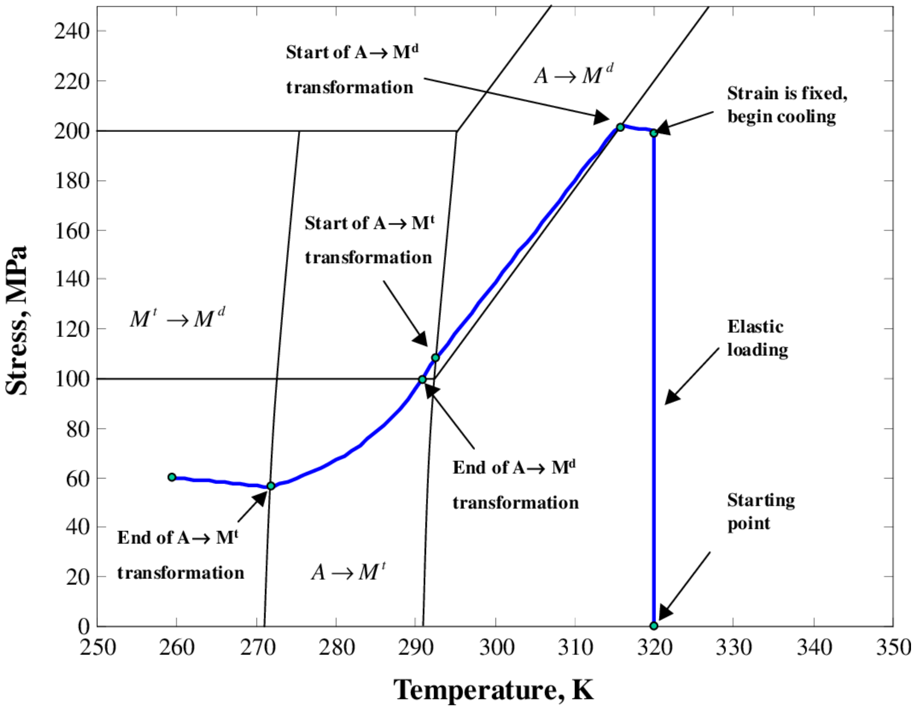

Figure 3.14: A constrained cooling path in stress–temperature space. The rod is loaded in tension at the austenitic phase to a stress lower than required for phase transformation. The strain is then fixed and the rod is cooled. The rapid drop of the stress during the phase transformation is caused by the development of inelastic strains. Since the total achievable inelastic strain is an order of magnitude larger than the initial elastic strain, very little $A \rightarrow M^d$ transformation occurs. For clarity, only the $A \rightarrow M^d$, $A \rightarrow M^t$ and $M^t \rightarrow M^d$ transformation strips are shown [45].

3.3.4 Actuation behaviour for SMA with $A_s < M_s$

This section presents the same observation mentioned above but in the case of an SMA with austenite start temperature lower than martensite start. Note that the rod's behaviour should be very responsive in the interval between these temperatures since both direct and reverse transformation are immediately activated upon temperature changes. Figure 3.15, 3.16 and 3.17 show the results of graphical analysis.

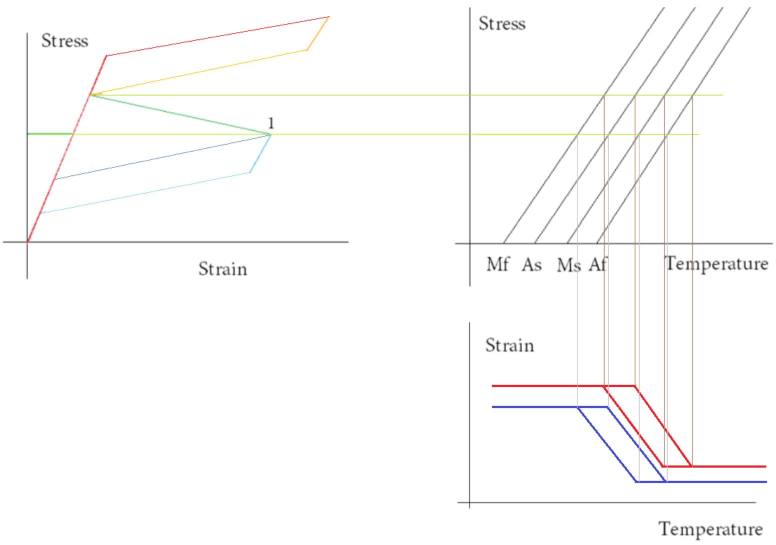

Figure 3.15: Diagrams considered for the graphical analysis ($A_s < M_s$).

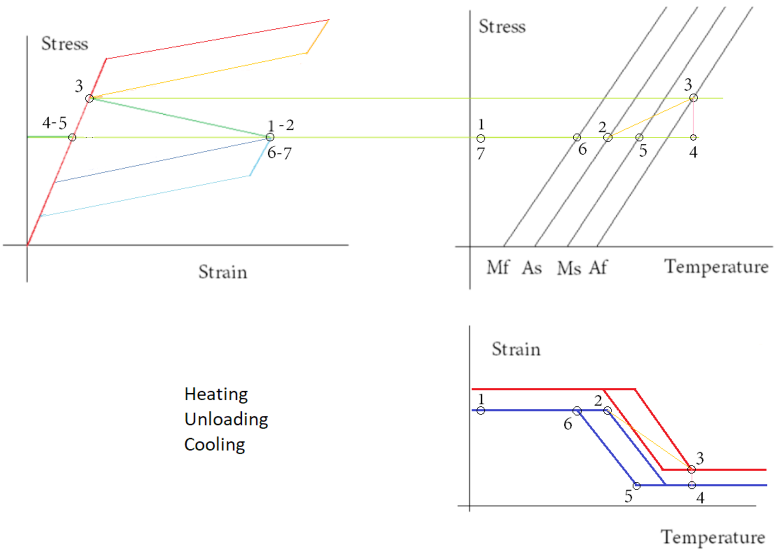

Figure 3.16: Graphical analysis - Actuator with clutch ($A_s < M_s$).

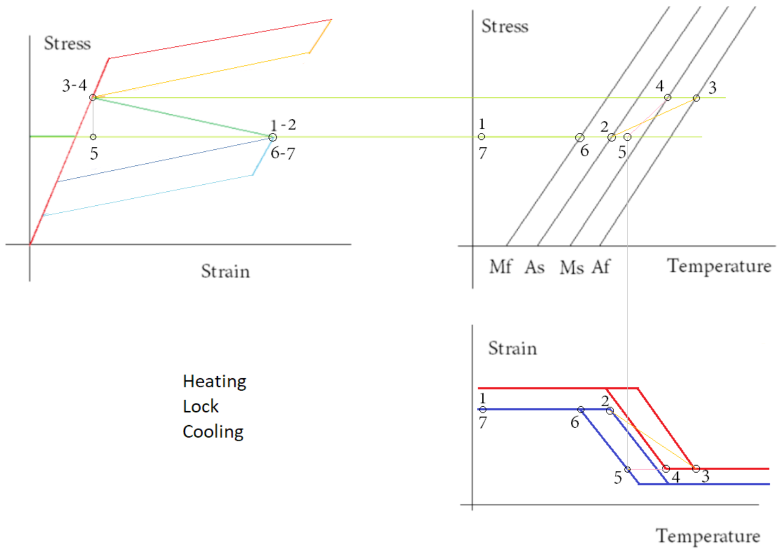

Figure 3.17: Graphical analysis - Actuator without clutch ($A_s < M_s$).

3.4 Further insights

3.4.1 Constant-torque joint mechanisms

In the previous section, the stress-strain diagram exhibit a constant load-line in order to simplify the dissertation. However, many researchers tried to design a structural components that exhibit a nearly deformation-invariant torque output within a determined range of angular displacement. Such devices, also known as *constant-torque joint mechanisms* (CTJM), would improve the actuator performance since the driven system would lose the incrementing resistance from the linear elastic returning element necessary to the stress-assisted two-way memory effect. Despite different ways are viable to achieve this result, one of the most promising ones, for the aim of this work, was presented by Hou et al. [31]. Leveraging on distributed-compliance models, they produced a very simple solid-state CTJM, compatible with SMA actuators design philosophy. A similar approach, implemented using different materials, could maybe meet the output torque requirements for the applications studied in this work.

3.4.2 Actuator with mechanical energy accumulator

Hereafter, a different actuator architecture is considered introducing an additional elastic element. This component has the function to accumulate, store and deploy mechanical energy to achieve quick actuation and to submit the SMA rod to constant loading cycles independently of the point in the flight envelope. The main drawbacks of this configuration are the necessity of more significant bumper systems and the overall system complication in contrast to the SMA actuator philosophy. Figure 3.18 and figure 3.19 shows the overall operation scheme during the forward and reverse transformation, respectively. As in the previous sections, the green and red dots represent activation and deactivation of the locking systems (three locks are present in this case), while the clutch, placed between the accumulator ("ACC box") and the flap is represented as engaged and disengaged by a brown and green square respectively. The SMA driving subsystem and the mechanical accumulator are coupled via a spline.

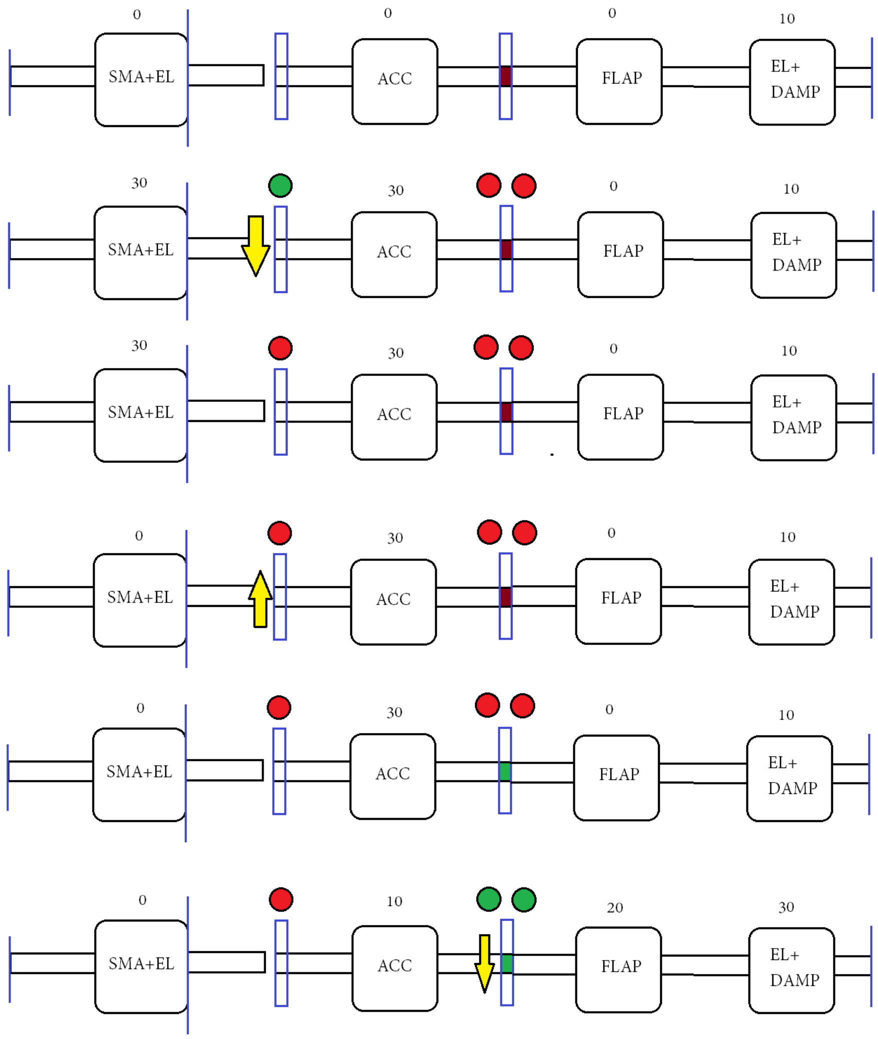

Figure 3.18: Forward transformation functioning scheme - Actuator with mechanical energy accumulator.

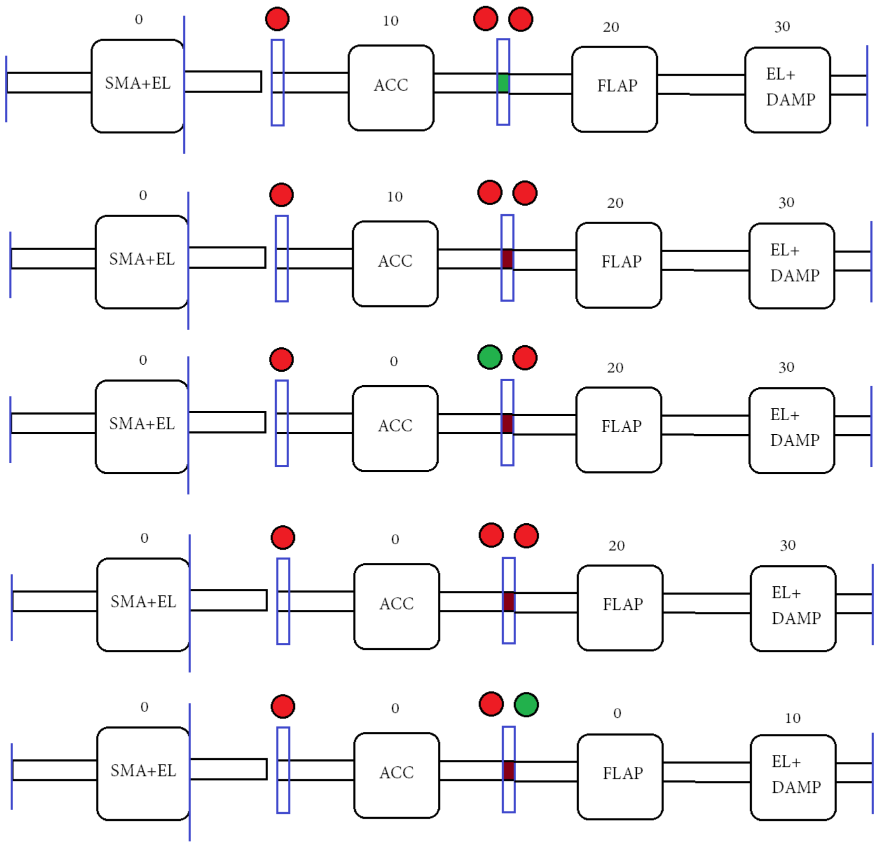

Figure 3.19: Reverse transformation functioning scheme - Actuator with mechanical energy accumulator.

3.5 Loads estimation

This section aims to estimate the torque involved during some secondary control surfaces actuation for three classes of aircraft. The method adopted can be used for a large variety of cases, constituting a helpful tool to obtain approximation values of the torque needed, which is a crucial design specification to develop an actuator. The aircrafts chosen in this work are the medium size UAV RQ7 Shadow, the Cessna 172 Skyhawk and the ATR 42-600. Indeed, in order to examine the possibility and implications of scaling up SMA torsional actuators technology, the aircraft mentioned above belong to three distinct categories. The specific model choice, instead, is based on data availability in literature and on the web. Indeed most of the required data presented hereafter were collected from manufacturer websites, brochures, factsheets and documentation, along with minor details found on other websites.

The case study considered here aims to predict the aerodynamic hinge moment applied to the flap during take-off and landing. Moreover, only for the ATR 42 an Adaptive Trailing Edge as that presented in [18] is considered.

The required geometric data were extrapolated directly form the technical drawings shown in figure 3.20, 3.21 and 3.22.

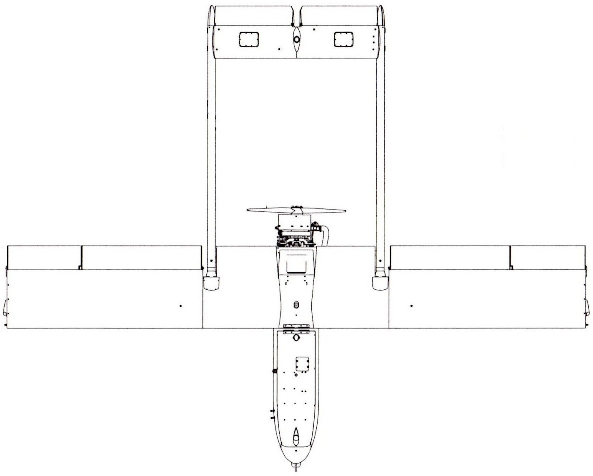

Figure 3.20: RQ-7 Shadow - top view [3] .

The RQ7and Cessna 172 airfoils were found on the web [6] [7] , while the ATR 42 airfoil was assumed to be a NACA 23015 based on the observations from [35]. Note that at this level of accuracy, this approximation is assumed to be adequate. Take-off and landing speeds were determined based on manufacturer data and certification specification. Referring to the UAV and the four-seats aircraft, EASA CS-23 [24] was adopted, while CS-25 [25] prescriptions were followed in the case of the ATR 42. At this step, considering sea-level standard air condition, it is possible to calculate Reynolds and Mach numbers. Table 3.1 resumes the properties of sea-level standard air of interest in this case study. The last unknown to be determined is the hinge moment coefficient, which is found using Xfoil, and its embedded functions “flap” and “hinc”. The airfoils mentioned above are already stored in the programme database. Using the geometric definition function, it is possible to modify the airfoil geometry deflecting the trailing edge about a user-defined point. The obtained shape is subsequently re-panelized and considered as a new custom airfoil. The hinge moment coefficient provided by Xfoil is defined as follow:

$$\frac{HingeMoment}{Span} = C_{HingeMoment}\frac{1}{2}\rho V^2 c^2 \tag{3.1}$$

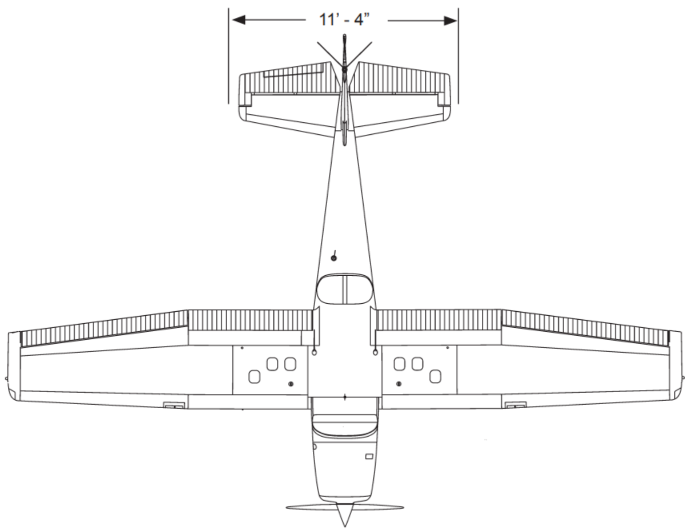

Figure 3.21: Cessna 172 Skyhawk - top view [4] .

Figure 3.22: ATR 42-600 - top view [5] .

where the hinge moment is calculated as a result of the aerodynamic forces with respect to the user-defined hinge location. The analysis had been run via a MATLAB script to obtain data at different flight conditions, accounting for several flap angle deflections with respect to the angle of attack. Figure 3.23, 3.24 and 3.25 provide an overview of the most demanding condition for the RQ7, Cessna 172 and ATR 42 respectively.

In order to confirm the consistency of the coefficient obtained, several data were collected from the literature. As shown in figures 3.26, 3.27, 3.28,3.29 and tables in figure 3.30, the absolute values and the trends of the curves are compatible with those found using Xfoil.

All the data required to determine the hinge moment are summarised in table 3.2.

Hereafter, as previously said, an adaptive trailing edge device for the ATR 42 is assessed. As in [18] it is assumed a moving surface of 2% of the local chord. Moreover, a typical cruise condition for regional aircraft was considered. As a compromise between medium and short-haul flights, an altitude of around 13000 feet (or 4 kilometres) was selected for this investigation. Table 3.3 reassumes the data required for the analysis at this flight level.

ρ_{SL}	1.225	kg/m^3
ν_{SL}	1.44e-5	m^2/s
$V_{sound,SL}$	343	m/s

Table 3.1: Standard air at sea level

	RQ7 Shadow		Cessna 172 Skyhawk		ATR 42 600	
Gross weight	170	kg	1111	kg	18600	kg
Wingspan	3.87	m	11	m	24.57	m
Airfoil	NACA 4415		NACA 2412		NACA 23015	
Root chord	0.42	m	1.63	m	2.624	m
Flap chord	0.114	m	0.491	m	0.75	m
Flap span	1.012	m	2.043	m	3.498	m
$x_{hinge}\%$	73%		70%		71%	
δ_{max}	40	°	30	°	30	°
Stall speed (V_{s1})	17.5	m/s	24.2	m/s	50.99	m/s
Cruise speed	36	m/s	62.8	m/s	154.4	m/s
Max speed	55.5	m/s	80	m/s		
V_2	21	m/s	29	m/s	57	m/s
V_3	22.75	m/s	31.46	m/s	62.72	m/s
V_{LND}	34.12	m/s	47.19	m/s	94.08	m/s
Re_{LND}	9.95e+5		5.34e+6		1.71e+7	
M_{LND}	0.099		0.138		0.274	
V_{TO}	22.75	m/s	31.46	m/s	62.72	m/s
Re_{TO}	9.19e+5		4.93e+6		1.57e+7	
M_{TO}	0.092		0.127		0.252	
$C_{hinge,max}$	0.34		0.38		0.37	
$M_{hinge,max}$	3.19	Nm	255.28	Nm	3946.69	Nm
$M_{hinge,max}/span$	3.15	N	124.95	N	1128.27	N

Table 3.2: Data summary - Flap

Figures 3.31, 3.32 and 3.33 show the modified NACA 23015 airfoils and their related diagrams showing hinge moment coefficient versus angle of attack, referred to an upward deflection of 5 degrees, and a downward deflection of 10 and 20 degrees respectively.

Given the hinge moment coefficients, the torque and the data required to their determination in the most demanding condition are summarised in table 3.4.

To sum up, the maximum hinge moment obtained for the RQ7 shadow is about $3.2Nm$, compatible with the torque output of commercially available UAV actuators. The hinge moment calculated for the Cessna 172 is $225Nm$, close to the values achieved by the refined optimisation performed by Florjancic in [26] for the same aricraft (ranging from $332Nm$ to $267Nm$). The maximum ATR 42 hinge moment was found to be about $3950Nm$. Although no reference was found to reasonably validate this data, as a means of comparison, a rotary actuator adopted for the motion of the Boeing 777 outboard flap develops a max torque of $12.1kNm$ [57]. Finally, a hinge moment of $9.4Nm$ was found in the ATE case, which is probably the less accurate result. However, knowing the SMA torque actuator size used in [18] and its related average torque performance, a value of the same magnitude is also expected in this case.

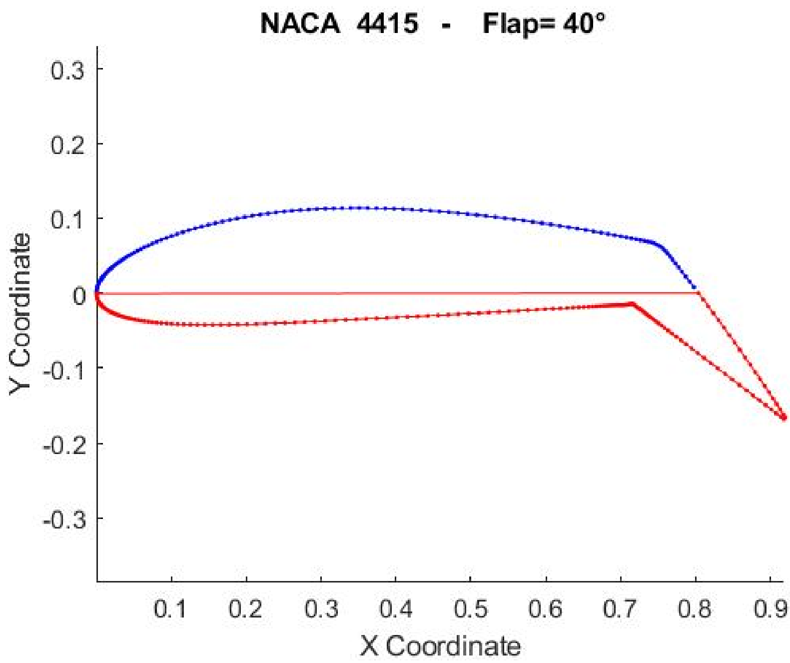

(a)

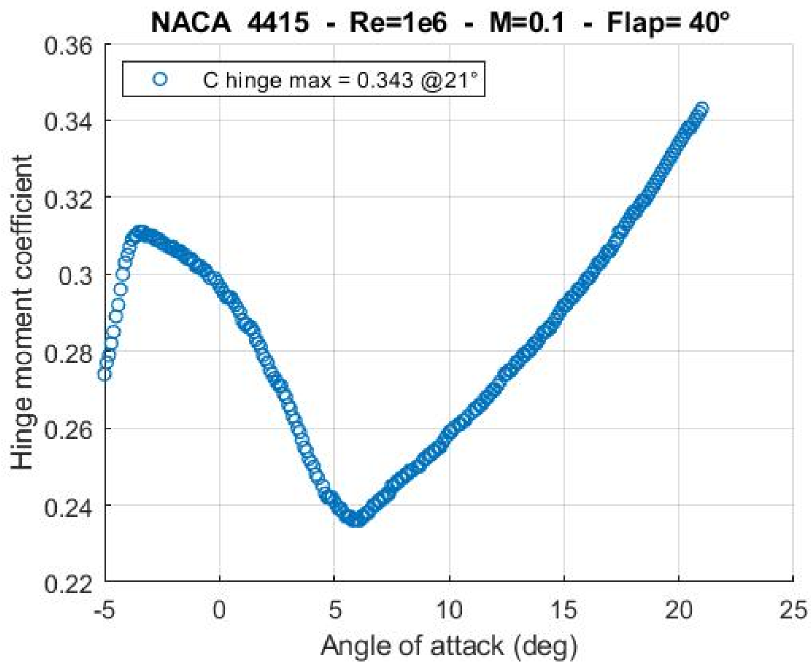

(b)

Figure 3.23: RQ-7 Shadow - Worst case scenario.

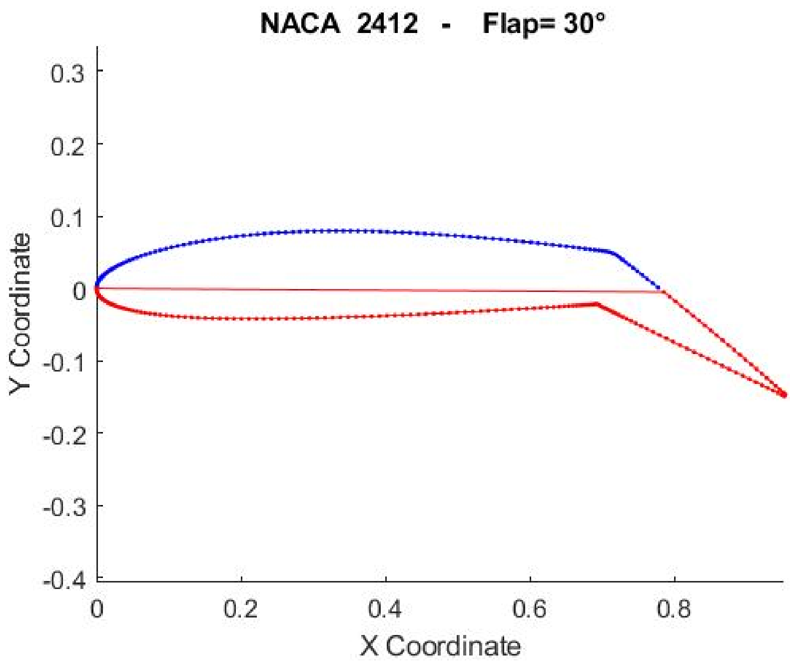

(a)

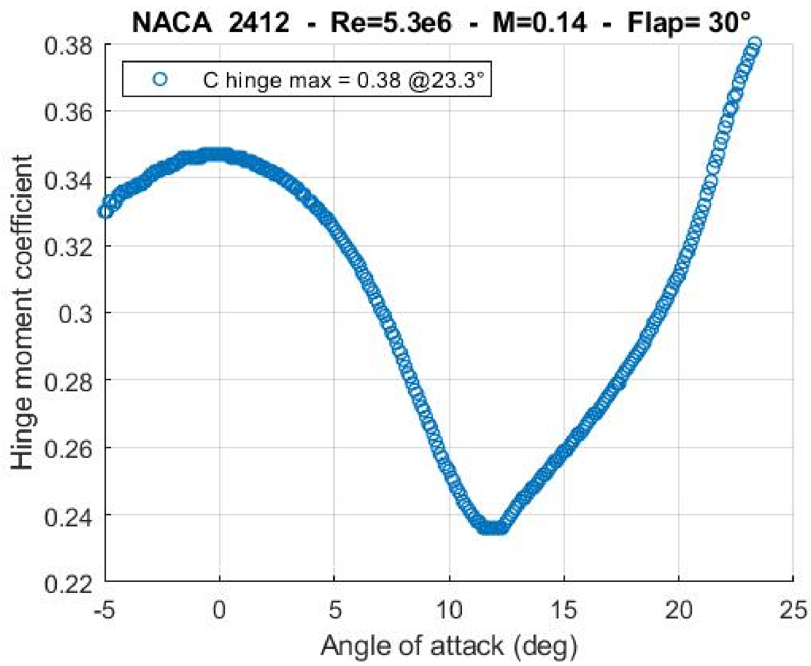

(b)

Figure 3.24: Cessna 172 Skyhawk - Worst case scenario.

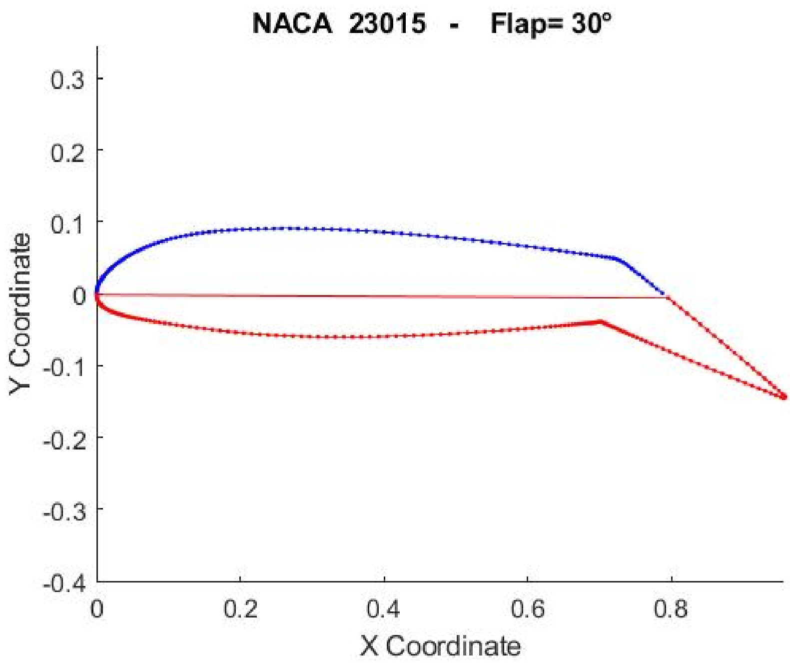

(a)

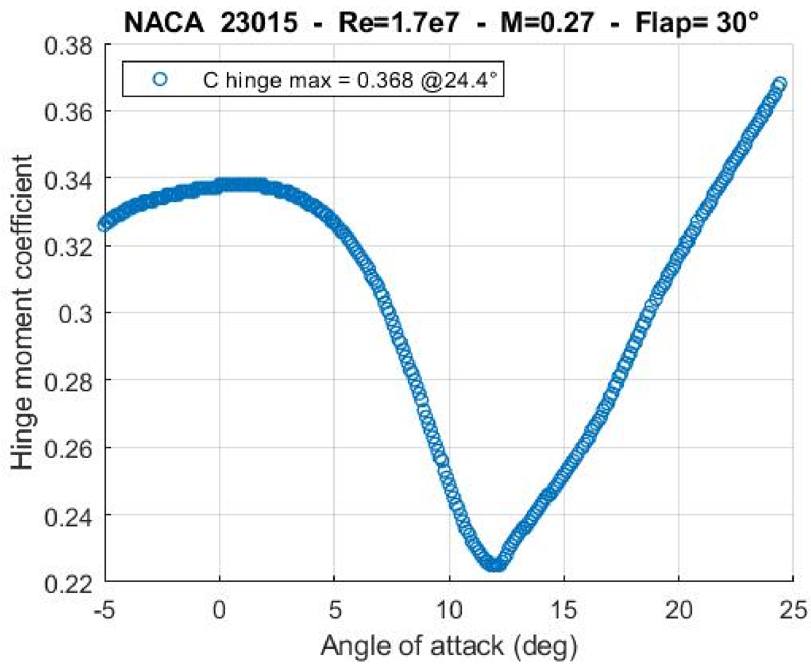

(b)

Figure 3.25: ATR42-600 - Worst case scenario.

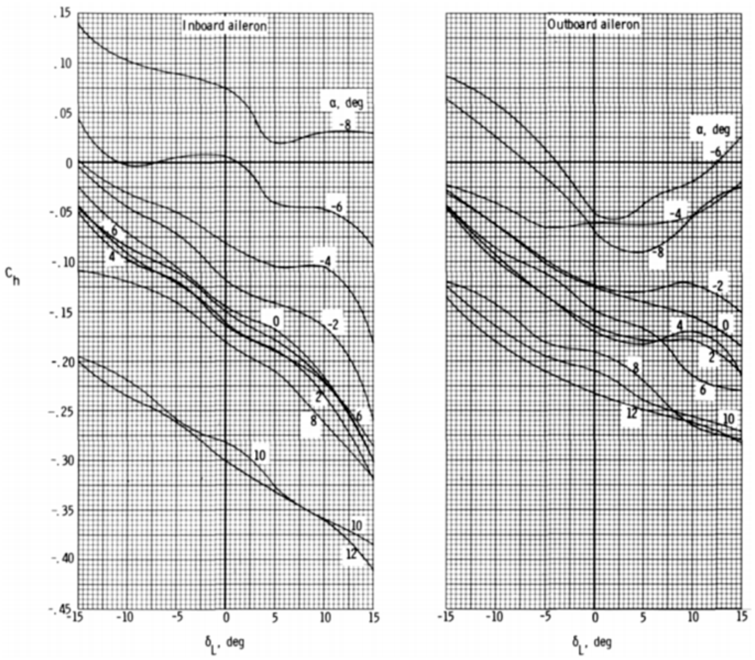

Figure 3.26: Hinge moment of a supercritical-wing wind tunnel model, $M = 0.9$ [46].

ρ_{4k}	0.819	kg/m^3
ν_{4k}	2.03e-5	m^2/s
$V_{sound,4k}$	324	m/s

Table 3.3: Standard air at 4000 m

	ATR 42 600	
Airfoil	NACA 23015	
Root chord	2.624	m
Flap chord	0.75	m
Flap span	3.498	m
$x_{hinge}\%$	98%	
δ_{max}	20	°
Cruise speed	154.4	m/s
Re_{cruise}	2.00e+7	
M_{cruise}	0.467	
$C_{hinge,max}$	0.1	
$M_{hinge,max}$	9.4	Nm
$M_{hinge,max}/span$	2.7	N

Table 3.4: Data summary - ATE

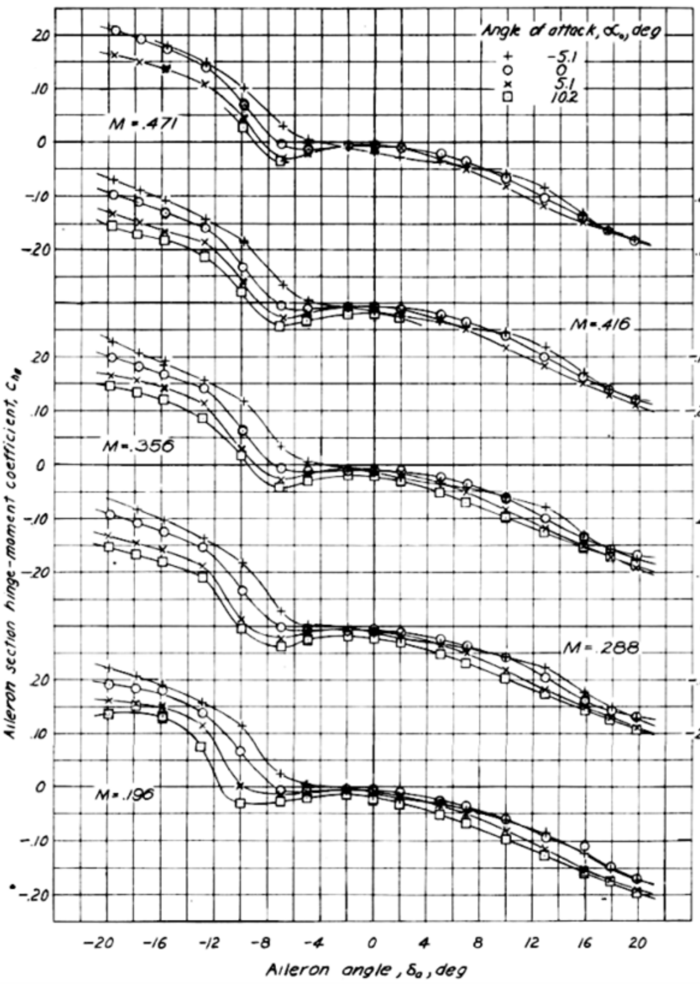

Figure 3.27: An example of Frise aileron hinge moment [22].

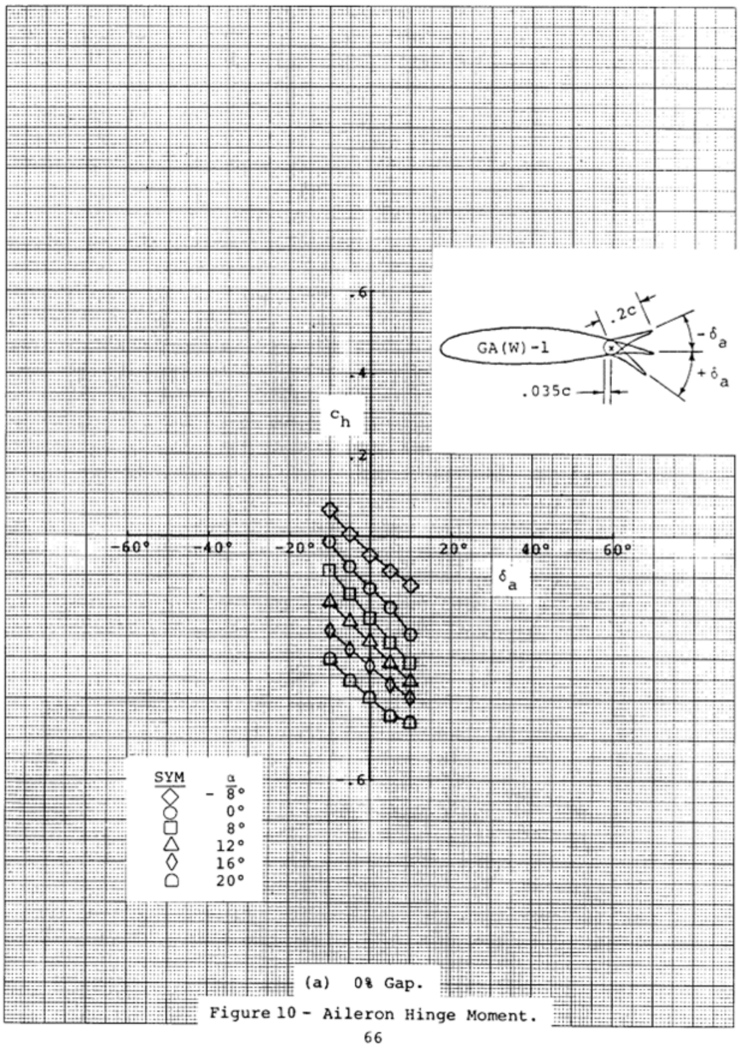

Figure 3.28: Control surface hinge moment coefficient, section moment/(dynamic pressure x control surface reference chord^2)(a)[56].

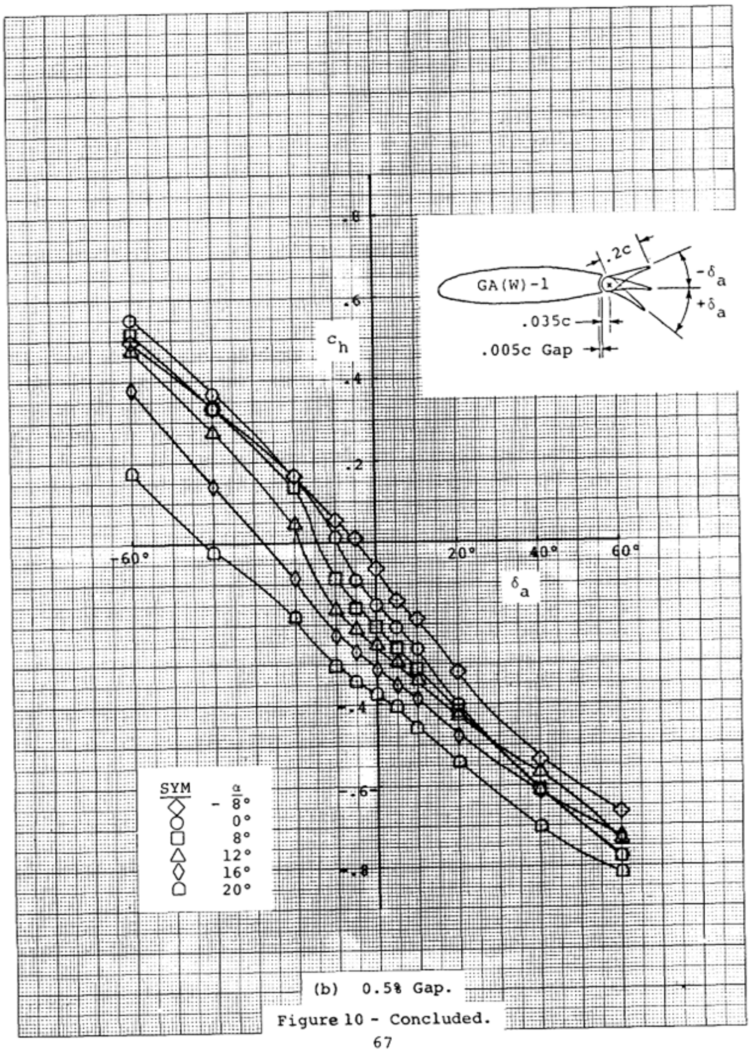

Figure 3.29: Control surface hinge moment coefficient, section moment/(dynamic pressure x control surface reference chord^2)(b)[56].

Table 3.1: GA(W)-1 reference quantities

Quantity	Symbol	Value
Airfoil chord	c	24 in
Airfoil thickness-to-chord ratio	t/c	0.17
Control surface chord ratio	c_f/c	0.20
Hinge axis x-coordinate	x_h/c	0.80
Hinge axis z-coordinate	z_h/c	0.03443
Reynolds number	Re	2.2×10^6
Mach number	M	0.13

Table 3.8: Comparison of GA(W)-1 hinge moment results, $\alpha = 0°$

δ	Reference	Datcom + C_{h_0}	XFOIL	Steady FUN3D
-40	0.3653	0.3885	0.2892	0.3312
-20	0.1631	0.1167	0.1100	0.1442
-10	0.0106	-0.0192	-0.0410	0.0245
-5	-0.0949	-0.0871	-0.1161	-0.0840
0	-0.1551	-0.1551	-0.1859	-0.1450
5	-0.2106	-0.2231	-0.2476	-0.1930
10	-0.2652	-0.2910	-0.2623	-0.2392
20	-0.4007	-0.4269	-0.3334	-0.3423
40	-0.6114	-0.6988	-0.4431	-0.4963

Table 3.12: Comparison of GA(W)-1 hinge moment results, $\alpha = 20°$

δ	Reference	Datcom + C_{h_0}	XFOIL	Steady FUN3D
-40	-0.0222	0.1689	0.0347	-0.0582
-20	-0.1820	-0.1030	-0.0226	-0.0884
-10	-0.3034	-0.2389	-0.2045	-0.2355
-5	-0.3429	-0.3068	-0.2496	-0.2731
0	-0.3748	-0.3748	-0.2915	-0.3126
5	-0.4039	-0.4427	-0.3286	-0.3531
10	-0.4575	-0.5107	-0.3667	-0.3937
20	-0.5431	-0.6466	-0.4431	-0.4752
40	-0.7029	-0.9184	-0.5825	-0.6106

Figure 3.30: Reference data from [50].

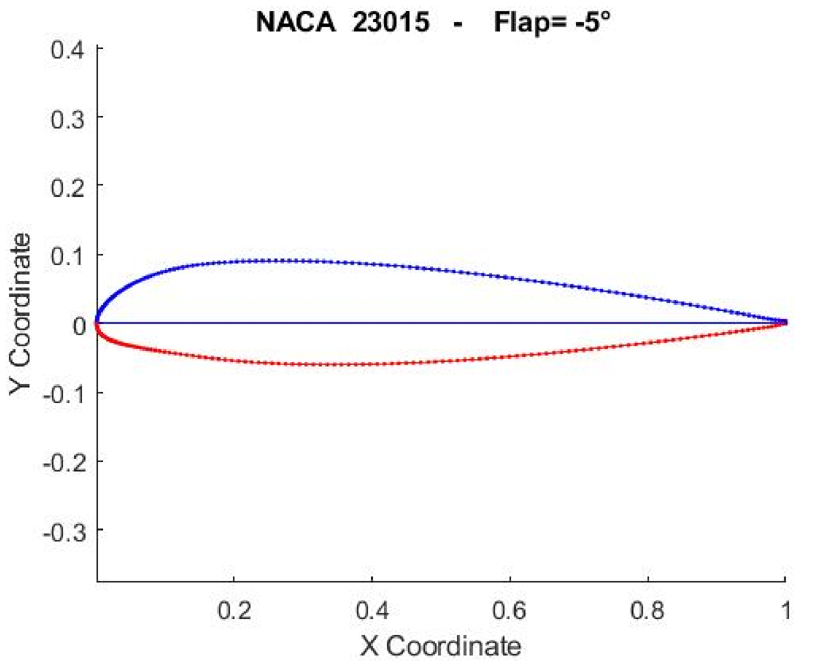

(a)

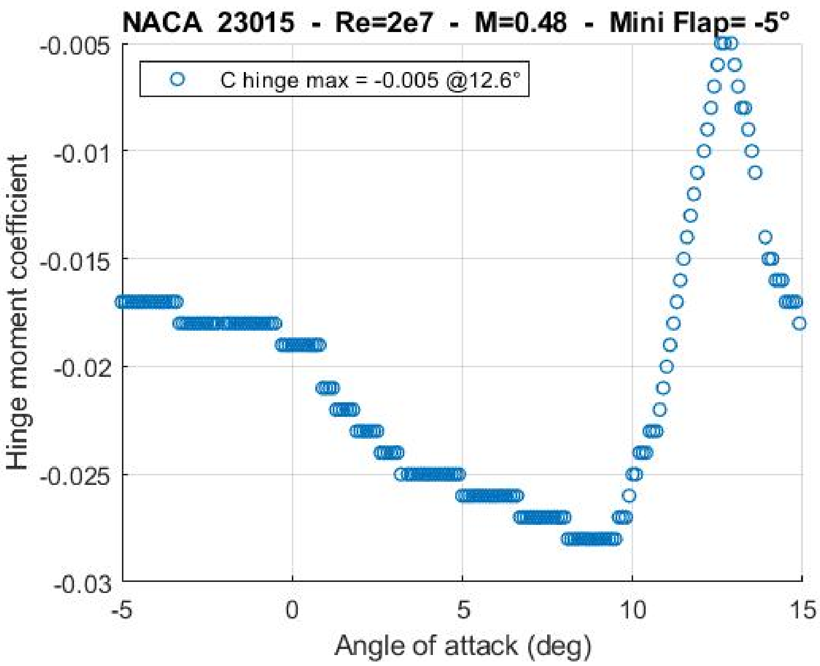

(b)

Figure 3.31: ATE - 5° upward

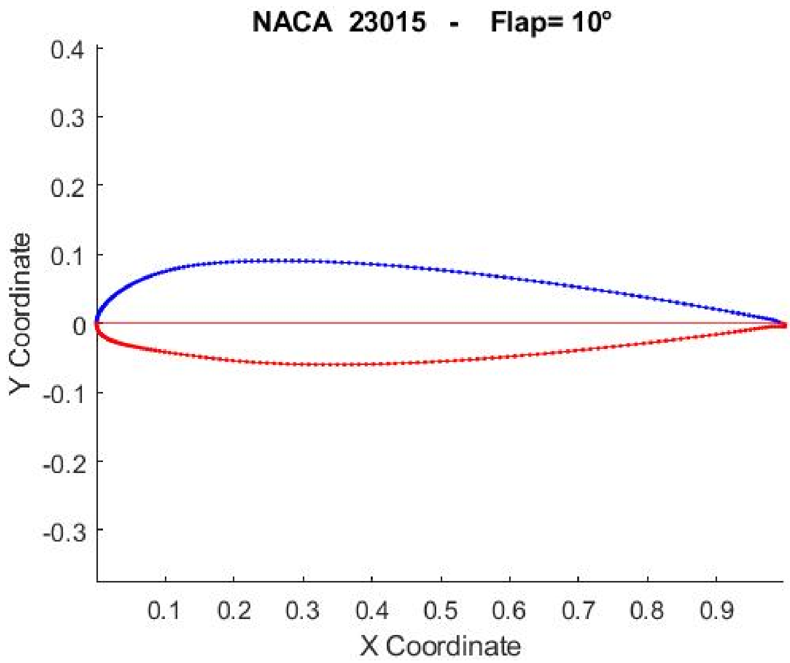

(a)

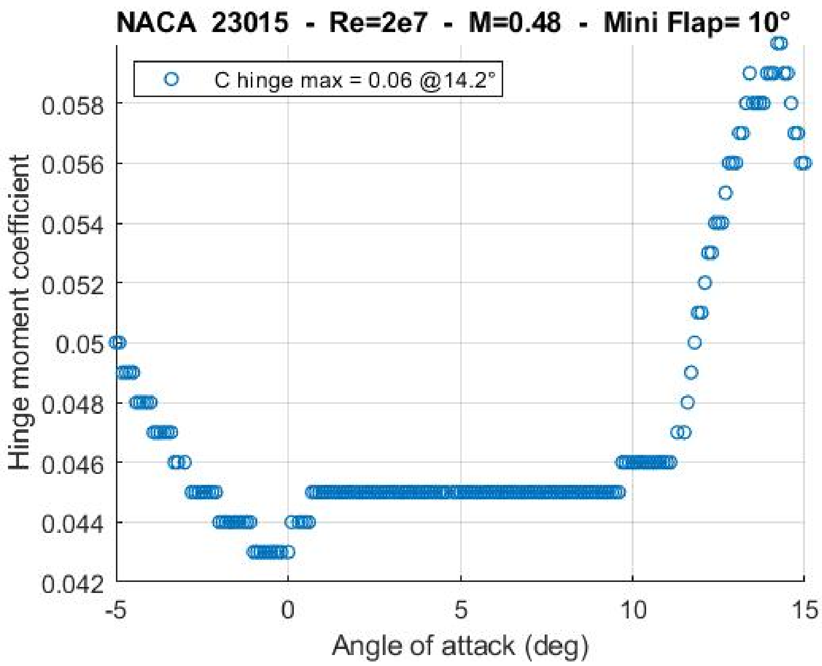

(b)

Figure 3.32: ATE - 10° downward

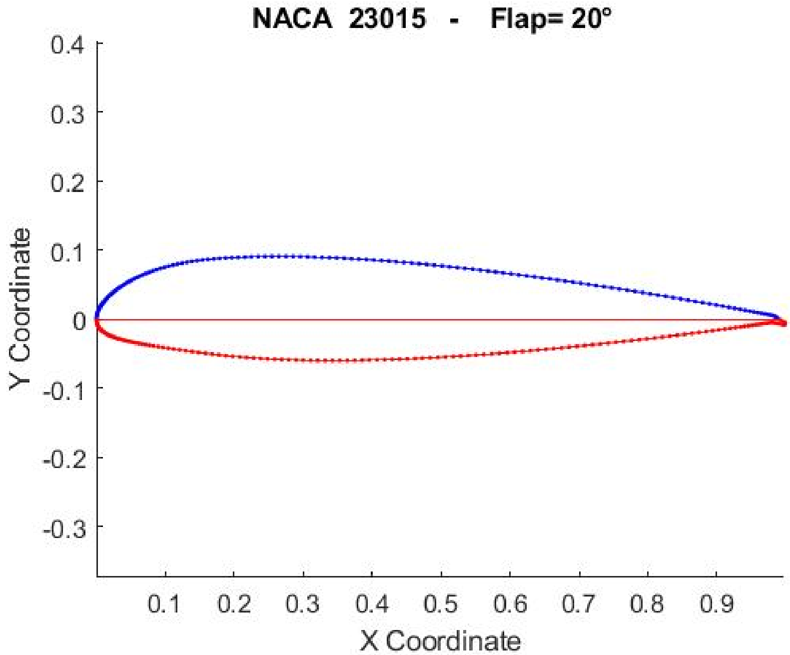

(a)

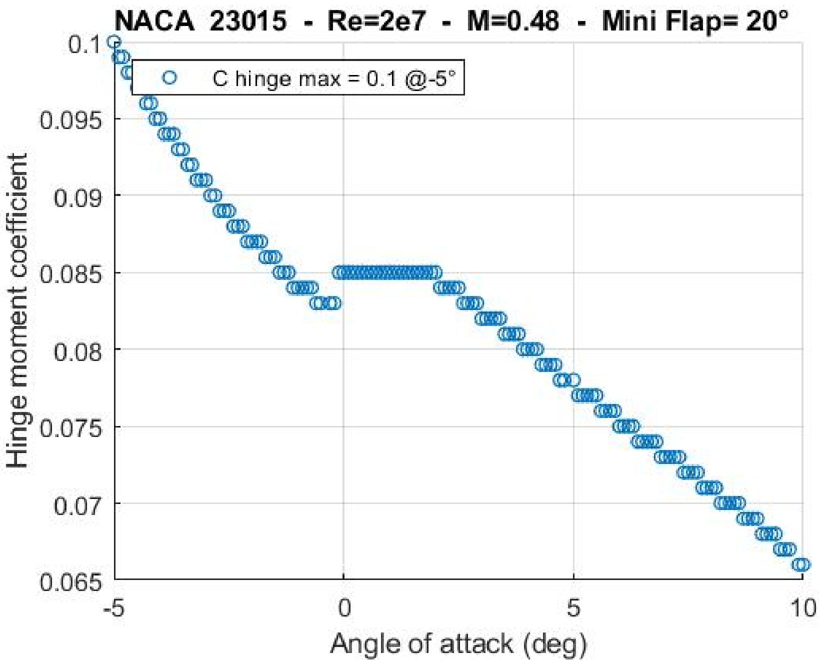

(b)

Figure 3.33: ATE - 20° downward

Chapter 4

Preliminary design - FEM approach

This section aims to present the preliminary design of an SMA torsional actuator according to the architecture choice and the working scheme illustrated in chapter 3. In order to do that, the commercial software MSC Patran and Nastran have been adopted, along with the related SMA prediction capability based on Auricchio's model [9] [10]. After validating results from simple loading conditions with those presented in the literature, design-assisting diagrams have been computed. Finally, different actuation cases simulations have been performed as described in the previous chapter.

4.1 Auricchio's formulation

4.1.1 Constitutive equations

MSC Nastran supports a mechanical shape memory alloy model originally implemented in MSC Marc, based on Auricchio's formulation [9], [10]. The model was developed in the framework of multiplicative decomposition. It is assumed the deformation gradient $\boldsymbol{F}$, as the control variable, and the martensite fraction ξ_S, as the only scalar internal variable. The deformation gradient transforms a vector from an undeformed body to that of a deformed one. Like any invertible second-order tensor, it can be decomposed using the polar decomposition theorem, which, in this case, leads to the product of the elastic and phase transformation part. At this point, the elastic left Cauchy-Green tensor $\boldsymbol{b}^e$ is introduced. Indeed, applying polar decomposition again on the elastic part of the deformation gradient, it is divided into the pure rotation and stretch components. The remarkable result is that by multiplying the deformation gradient by its transpose, the rotation matrix is eliminated, which is crucial because only deformation is of interest to compute the stress state. The same procedure is executed on the transformation part of the deformation gradient. Assuming an isotropic response, the Kirchhoff stress $\boldsymbol{\tau}$ [1] and the elastic left Cauchy-Green tensor share the same principal directions. Accordingly, the following spectral decomposition can be introduced:

$$\boldsymbol{\tau} = \sum_{A=1}^{3} \tau_A \boldsymbol{n}^a \otimes \boldsymbol{n}^a \tag{4.1}$$

$$\boldsymbol{t} = \sum_{A=1}^{3} t_A \boldsymbol{n}^a \otimes \boldsymbol{n}^a \tag{4.2}$$

$$\boldsymbol{b^e} = \sum_{A=1}^{3} (\lambda_A^e)^2 \boldsymbol{n}^a \otimes \boldsymbol{n}^a \tag{4.3}$$

With λ_A^e the elastic principal stretches and $\boldsymbol{t}$ the deviatoric part, according to the relation:

$$\boldsymbol{\tau} = p\boldsymbol{I} + \boldsymbol{t} \tag{4.4}$$

Where $\boldsymbol{I}$ is the second-order identity tensor, p is the pressure, defined as $p = tr(\boldsymbol{\tau})/3$, and is $tr(\cdot)$ the trace operator [38].

Remembering that $\boldsymbol{\tau} = \boldsymbol{FSF^T}$, where $\boldsymbol{S}$ is the 2^{nd} Piola-Kirchhoff stress tensor; and the 2^{nd} Piola-Kirchhoff stress is the partial derivative of the Helmholtz free energy (Ψ) with respect to the Green strain tensor, equation 4.1 can be written in the following component form:

$$\tau_a = p + t_a \tag{4.5}$$

With

[1] The Kirchhoff stress tensor is related to the Cauchy stress tensor through multiplication by the Jacobian (the determinant of the deformation gradient $\boldsymbol{F}$)

$$p = K\theta^e \tag{4.6}$$

$$t_a = 2Ge_A^e \tag{4.7}$$

Note that e_A and θ can be decomposed into elastic and transformation components. The final constitutive equation can be summarised as follows:

$$p = K(\theta - 2\alpha\epsilon_L\xi_s) \tag{4.8}$$

$$\boldsymbol{t} = 2G(\boldsymbol{e} - \epsilon_L\xi_s\boldsymbol{d}) \tag{4.9}$$

$$\boldsymbol{d} = \frac{\boldsymbol{e}}{\|\boldsymbol{e}\|} \tag{4.10}$$

4.1.2 Phase transformation and activation conditions

Two phase transformations are considered in the model: the conversion of austenite into martensite ($A \rightarrow S$) and the conversion of martensite into austenite ($S \rightarrow A$). To model the possible phase-transformation pressure-dependence, a Drucker-Prager-type loading function is introduced, defined as follows:

$$F(\boldsymbol{\tau}) = \|\boldsymbol{t}\| + 3\alpha p \tag{4.11}$$

Where α is a material parameter and $\|\cdot\|$ indicates the Euclidean norm. Indicating variants in time with a superposed dot, the following linear form for the evolution of ξ_s during ($A \rightarrow S$) transformation is assumed:

$$\dot{\xi_S} = H^{AS}(1 - \xi_S)\frac{\dot{F}}{F - R_f^{AS}} \tag{4.12}$$

While ($S \rightarrow A$) evolution equation is not reported for brevity. In equation 4.12 R_f^{AS} is a scalar depending on material, while H^{AS} assumes 0 or 1 value depending on phase transformation state.

4.1.3 Time-discrete model

The time-discrete model is obtained by integrating the time-continuous model over the time interval $[t_n, t]$. In particular a backward-Euler integration formula is adopted for the rate-equations evaluating all the nonrate equations at time t. Written in residual form the time-discrete evolutionary equation for ($A \rightarrow S$) transformation specializes to :

$$R^{AS} = (F - R_f^{AS})\lambda_s + H^{AS}(1 - \xi_s)(F - F_n) = 0 \tag{4.13}$$

where

$$\lambda_S = \int_{t_n}^{t} \dot{\xi_S} dt = \xi_S - \xi_{S,n} \tag{4.14}$$

The quantity λ_S can be computed expressing F as a function of λ_S and requiring the satisfaction of the discrete equation relative to the corresponding active phase transition.

An iterative procedure based on trial solutions, indicated by superscription "TR", is performed in order to calculate λ_S, starting from the beginning assumption that no transformation occurs. Note that at this point, $\boldsymbol{F}$, $\boldsymbol{F}_n$ and $\xi_{S,n}$ are assumed to be known. Also, the parameter

β, valuing 1 or -1 depending on the transformation direction, is introduced. If phase transformation conditions are satisfied, martensite increment, martensite fraction and stress are updated. At this point, the algorithmic tangent modulus is computed. Indeed, within the framework of non-linear implicit equations, as in the case under examination, Newton's method, is used in conjunction with an incremental-iterative solution procedure which, at each time or load step, reduces the nonlinear problem to a sequence of linearized problems (called iterations). Thus, at every iteration, a linearized incremental problem is solved, which requires the tangent stiffness matrix of the structure. The consistent tangent preserves the quadratic convergence of Newton method, adopted for the incremental solution of the finite element scheme [9]. In fact, "two types of material tangent moduli can be selected to form the structure stiffness matrix: continuum tangent moduli and consistent tangent moduli. Consistent tangent moduli (also called algorithmic tangent moduli) are obtained through differentiation of the incremental constitutive equations ($\Delta\sigma = \Delta\sigma(\Delta\epsilon)$) with respect to the total incremental strains, $\Delta\epsilon$, while the continuum tangent moduli are defined as the differentiation of the rate constitutive equations $\dot{\sigma} = \dot{\sigma}(\dot{\epsilon})$ with respect to the strain rate $\dot{\epsilon}$" [27].

Table shown in figure 4.1 resumes the solution algorithm for the time discrete model, while figure 4.2 illustrates the main steps followed in the model definition. Also a schematic representation of Newton's method is provided in figure 4.3.

Solution algorithm for the time-discrete model

---

1. Spectral decomposition
Compute spectral decomposition of b
Compute $\mathbf{n}^{\mathrm{A}}$, d_{A} and λ_{A}
Compute ϵ_{A}, θ and e_{A}

2. Compute β
Compute $||\mathbf{e}||$
Depending on $\|e\| - \epsilon_L \xi_{S,n}$ set β

3. Compute trial state
Assume no phase transformations ($\lambda_{\mathrm{S}} = 0$)
Compute p^{TR}, $\mathbf{t}^{\mathrm{TR}}$, $\mathrm{F}^{\mathrm{AS,TR}}$

4. Check phase transformations
if (PT conditions satisfied) then
    compute martensite increment
    update martensite fraction
    update stress
end if

5. Compute algorithmic tangent

Figure 4.1: Solution algorithm for the time-discrete model [9].

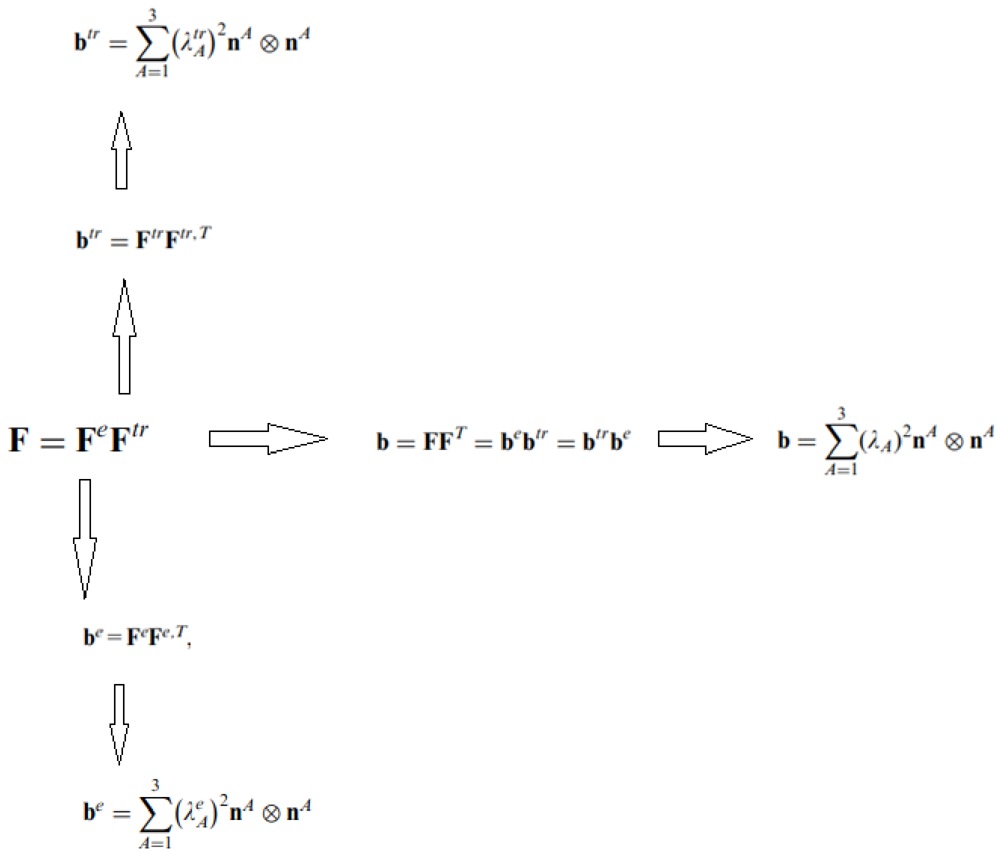

(a)

Figure 4.2: Auricchio's Formulation graphical summary.

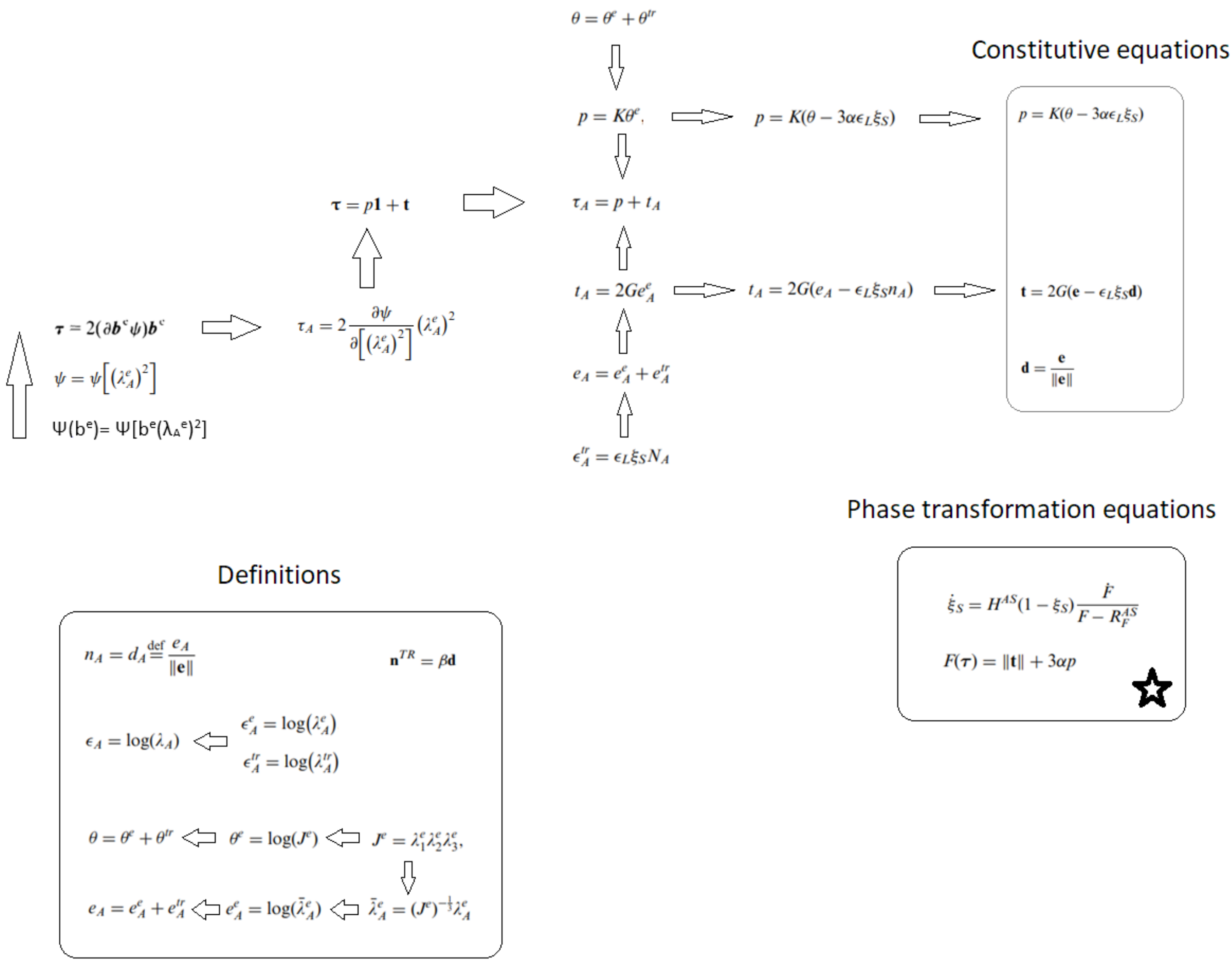

(b)

Figure 4.2: Auricchio's Formulation graphical summary.

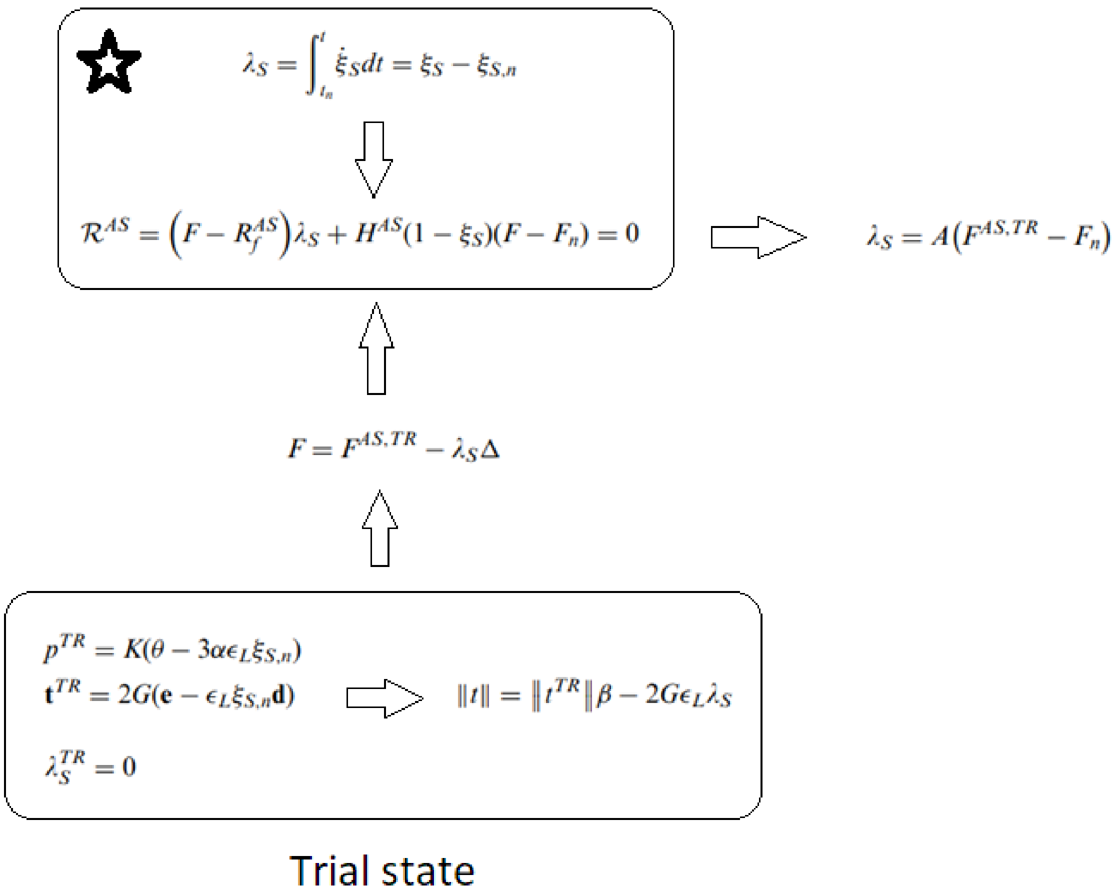

(c)

Figure 4.2: Auricchio's Formulation graphical summary.

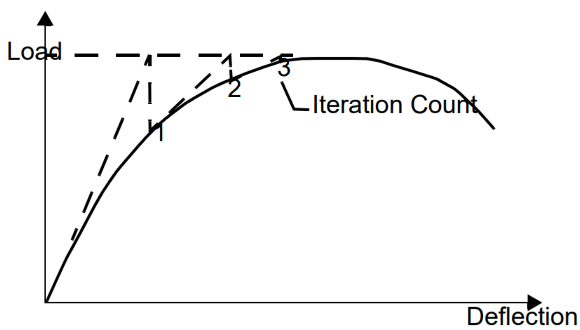

Figure 4.3: Schematics of Newton-Raphson method [28].

4.2 Finite element model definition

The subject of the finite element analysis executed in MSC Patran and Nastran is an SMA rod $200mm$ long and with a radius of $5mm$, which expected performance is compatible with the UAV flap actuator device. Despite a tube offers higher torque outputs for the same weight, rods are less susceptible to buckling effects; moreover, it is interesting for the aim of this work to find out the SMA behaviour in the inner radial parts, as the lower stress generated should lead to partial transformations.

Shape memory alloys are defined using MATSMA material property [41] originally designated for MSC Marc and compatible with Nastran SOL400 (implicit non-linear solution). The mechanical model, defined by Auricchio's formulation, requires the following parameters:

- T_0: Reference temperature used to measure stresses.
- L: Maximum deformation, obtainable by detwinning of multiple-variant martensite.
- E_a : Austenite young's modulus of elasticity
- ν_a : Austenite poisson's ratio
- α_a: Austenite coefficient of thermal expansion
- ρ_a: Austenite mass density
- σ_s^{AS} : Stress at the beginning of Austenite to Martensite transformation at T_0
- σ_f^{AS}: Final stress of Austenite to Martensite transformation at T_0
- C_a : Slope of the stress-dependence of austenite finish and start temperatures in the stress-temperature diagram
- E_m : Martensite young's modulus of elasticity
- ν_m : Martensitepoisson's ratio
- α_m: Martensitecoefficient of thermal expansion
- ρ_m: Martensitemass density
- σ_s^{SA} : Stress at the beginning of Martensite to Austenite transformation at T_0
- σ_f^{SA}: Final stress of Martensite to Austenite transformation at T_0
- C_m : Slope of the stress-dependence of martensite finish and start temperatures in the stress-temperature diagram

The material parameters for the model under examination were extrapolated from Taheri et al. [53] and summarized in table 4.1.

Due to the material and deformation non-linearities, added to the non-linear nature of Auricchio's formulation itself, SOL 400 was adopted. Furthermore, a non-linear static analysis was preferred at this level since the heating method is not examined in this work. Consequently, a non-linear transient analysis would have resulted in useless over-accuracy considering the time domain, but without having the necessary data concerning thermal aspects. Shape memory alloys modelisation is only supported for nonlinear element with property extensions [41]. Moreover, at least three elements within the radius are necessary to predict the transformation regions evolution during mechanical and thermal loading. For the reasons mentioned above, solid elements CHEXA and CPENTA have been adopted for the specimen discretisation. These are modified isoparametric elements that use selective integration points for different components of strain [42]. In particular, CPENTA-15 are adopted for the rod's core and CHEXA-20 for the

1	2	3	4	5	6	7	8	9	10
MATSMA	MID	MODEL	T_0	L					
	E_a	ν_a			ρ_a	σ_s^{AS}	σ_f^{AS}	C_a	
	E_m	ν_m			ρ_m	σ_s^{SA}	σ_f^{SA}	C_m	
MATSMA	1	1	24.	0.023					
	$25.e+03$	0.330			$6.5e-9$	150.	325.	6.8	
	$15.e+03$	0.330			$6.5e-9$	175.	45.	7.6	

Table 4.1: MATSMA entries (N,mm,ton).

outer region. The CPENTA-15 is a 15 nodes element with 21 integration points and a quadratic integration type. The CHEXA-20 is a 20 nodes element with only 8 integration points and a quadratic reduced integration type, aiming to reduce the overall element stiffness. Reduced integration also results in lower computational costs; however, unlike full integration, virtual work is not integrated exactly [2]. Both the elements are associated with quadratic interpolation (shape) functions which describe both the coordinate position and displacements. Such elements, referred to as isoparametric, can exactly represent the rigid body modes and the homogeneous modes; a necessary condition for convergence to the exact solution as the mesh is refined [28]. Figure 4.4 and figure 4.5 represent the CPENTA-15 and the CHEXA-20 elements respectively.

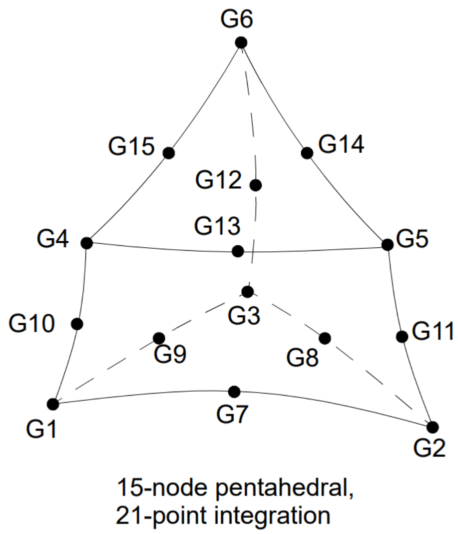

Figure 4.4: CPENTA-15 element [28].

The model under investigation presents 27772 nodes ad 6840 elements. Moreover, in order to achieve simple outputs, two RBE2 spider elements were connected at either end respectively to apply loads and constraints. Figure 4.6 shows an overview of the model.

[2]Full integration implies that if the displacement varies over the element consistently with the interpolation function, then the virtual work expression is integrated exactly [28].

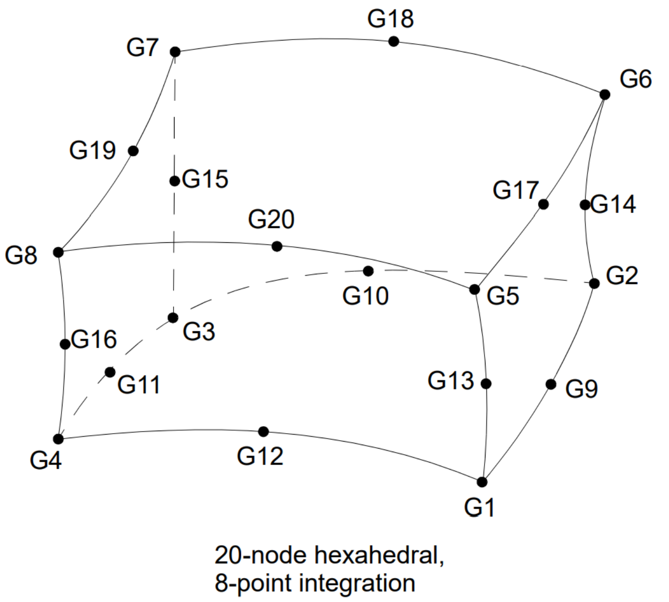

Figure 4.5: CHEXA-20 element [28].

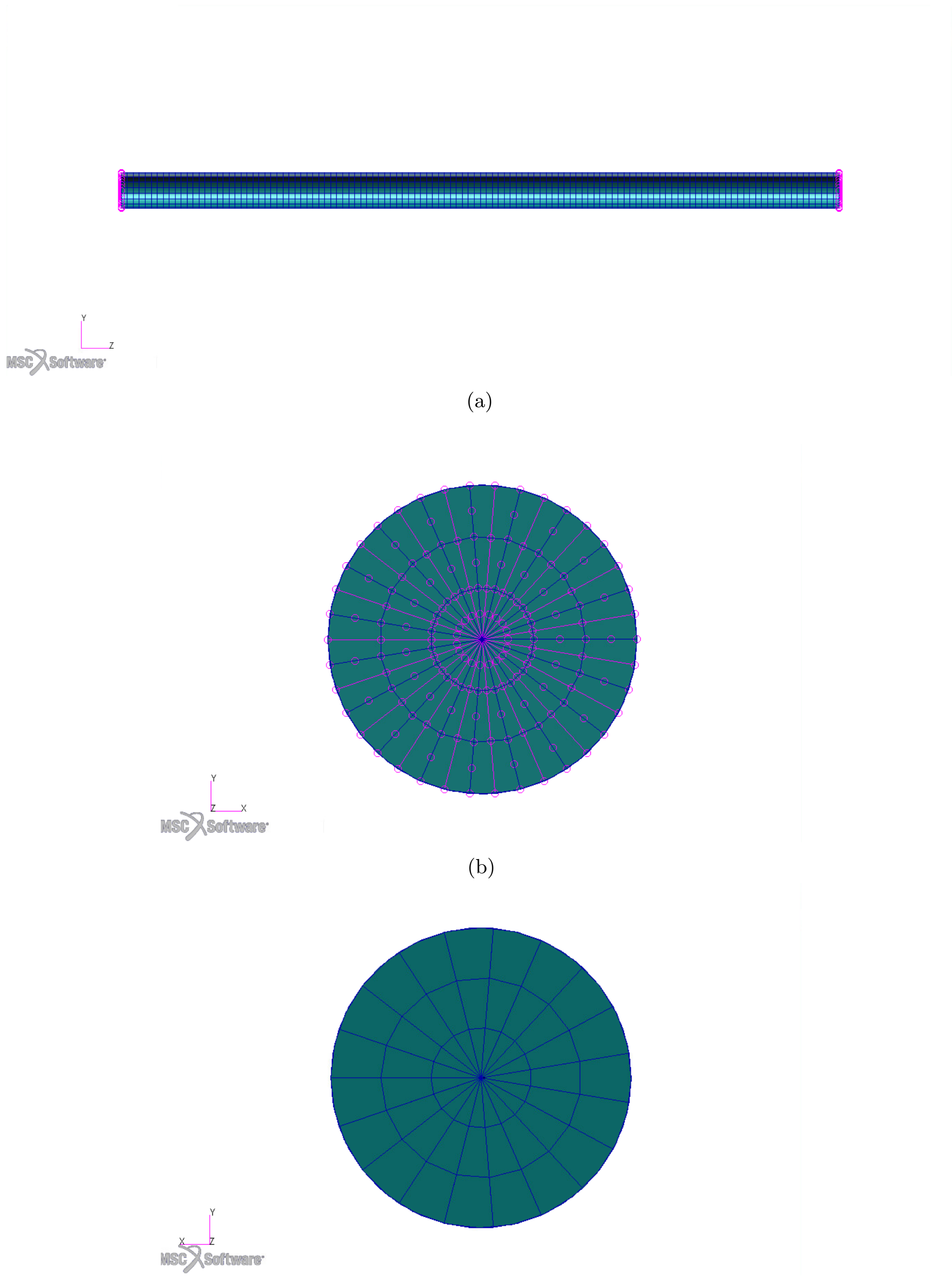

(a)

(b)

(c)

Figure 4.6: FEM model of SMA rod

4.3 Model validation

This paragraph presents the data obtained from the FEM analysis discussed in the section above, considering either uniaxial and torsional loading. The aim is to assess the accuracy of this method by comparing results with experimental data from Taheri et al. [53].

4.3.1 Uniaxial loading

In the case of uniaxial loading, three temperatures were considered: 297K, 313K and 323K as shown in figueres 4.7, 4.8 and 4.9 respectively.

As expected, the transformation stresses are accurately predicted. At the same time, the strain seems to be over-estimated with respect to experimental data and the model by Taheri et al., which predicts the overall behaviour very well. It is thought that the reasons behind these differences can derive from the following aspects:

- The reduced integration method adopted for the CHEXA element could underestimate the element stiffness.
- A different ξ evolution law between Auricchio's and Taheri et al. formulations is assumed.
- Differences can be generated from the definition of effective stiffness, defined as $E = E^A(1-\xi) + E^M(\xi)$ in Auricchio's formulation, and effective compliance, defined as $S = S^A(1-\xi) + S^M\xi$ in Taheri et al. model.
- Different variational principles are adopted by Auricchio's and Taheri et al. formulation, derived from Helmholtz and Gibbs free energy, respectively.

Furthermore, tables 4.2, 4.3 and 4.4 compares the theoretical stranformation stresses with those obtained from the FEM model.

	Th	FEM	Err%
$\sigma_{M_f}(MPa)$	325	314.5	3.2
$\sigma_{M_s}(MPa)$	150	147	2.0
$\sigma_{A_f}(MPa)$	175	173.8	0.7
$\sigma_{A_f}(MPa)$	45	41.4	8.0

Table 4.2: Theoretical vs FEM analysis transformation stresses at 24°C.

	Th	FEM	Err%
$\sigma_{M_f}(MPa)$	433.8	426.5	1.68
$\sigma_{M_s}(MPa)$	258.8	267	-3.17
$\sigma_{A_f}(MPa)$	296.6	274.7	7.38
$\sigma_{A_f}(MPa)$	166.6	150.6	9.6

Table 4.3: Theoretical vs FEM analysis transformation stresses at 40°C.

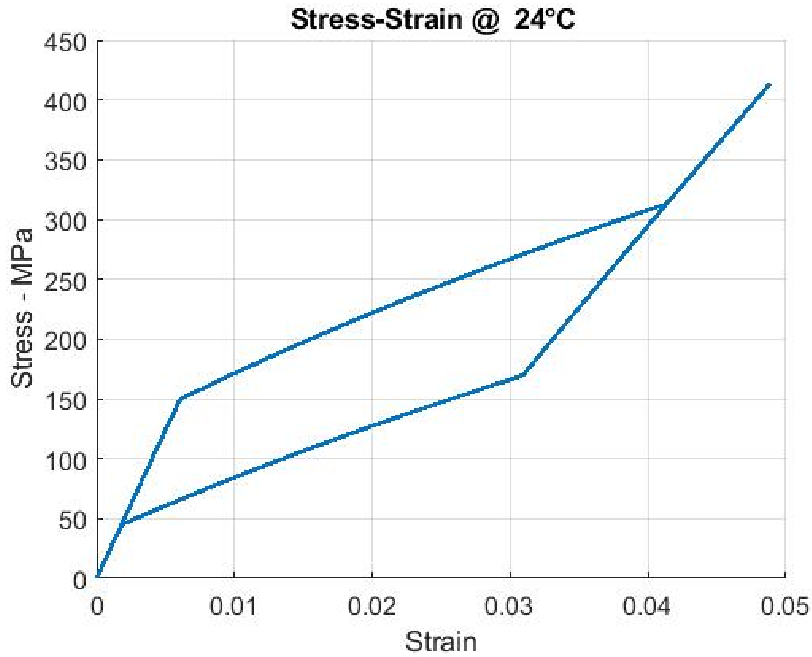

(a) Uniaxial stress-strain response at $24°C$ - FEM results (Auricchio's formulation).

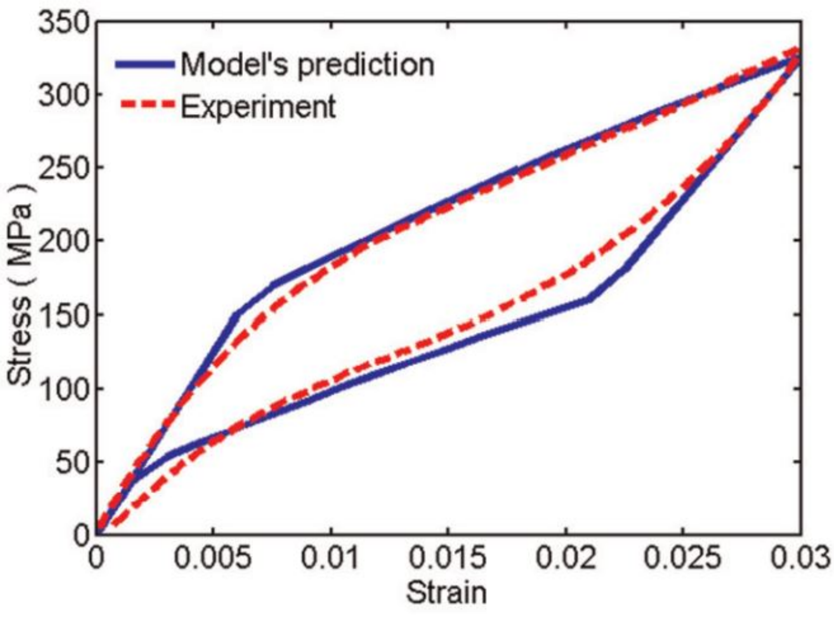

(b) Uniaxial stress-strain response at $24°C$ - Experimenatl data and Taheri et al. model's prediction [53].

Figure 4.7: Model validation - Uniaxial loadig case at $24°C$.

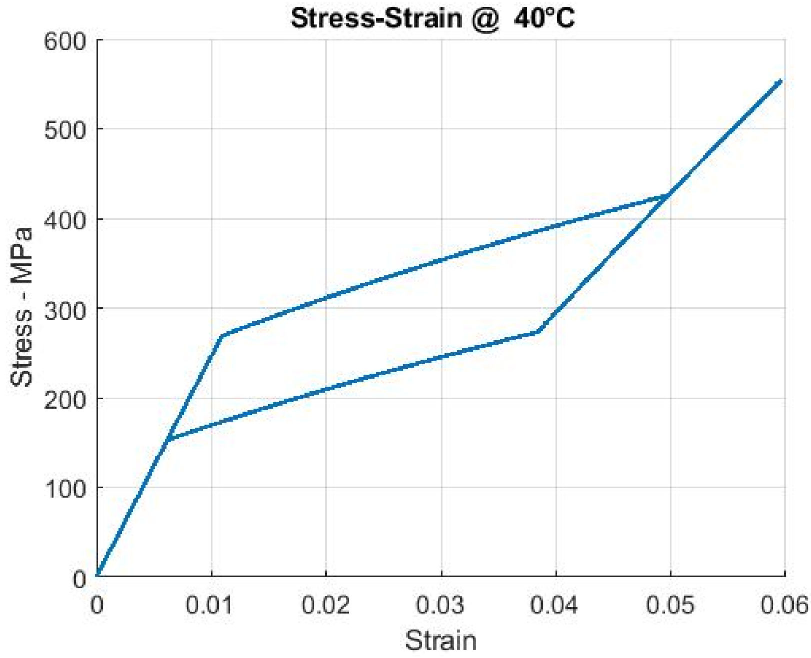

(a) Uniaxial stress-strain response at 40°C - FEM results (Auricchio's formulation).

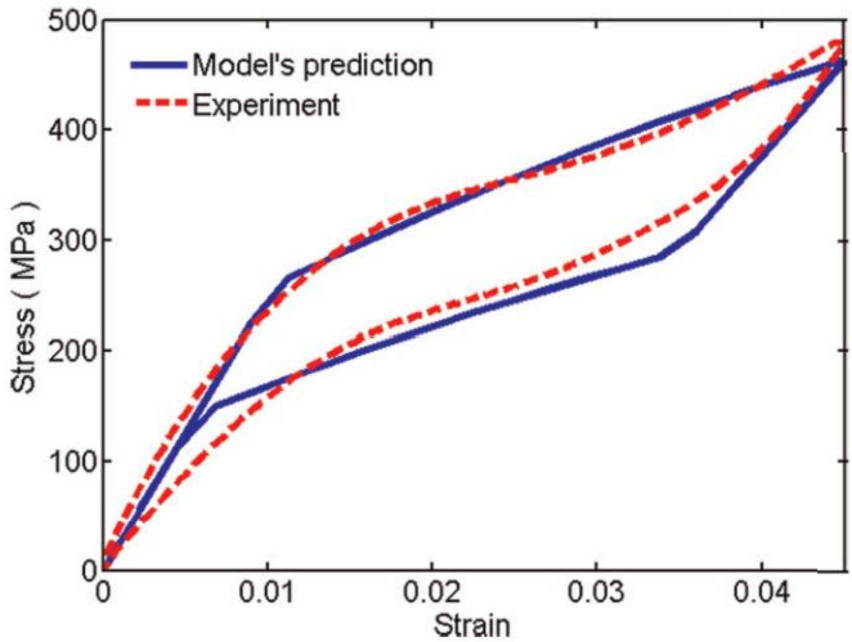

(b) Uniaxial stress-strain response at 40°C - Experimenatl data and Taheri et al. model's prediction [53].

Figure 4.8: Model validation - Uniaxial loading case at 40°C.

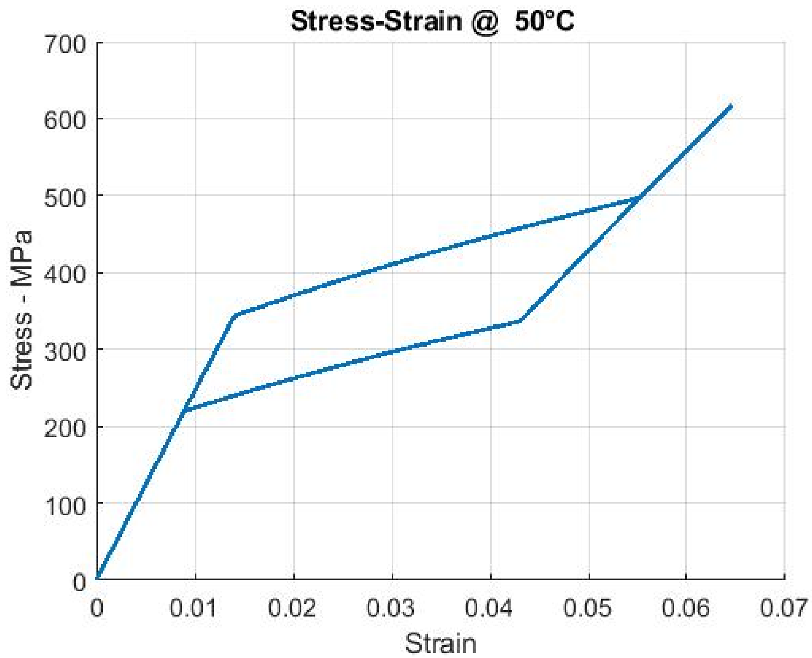

(a) Uniaxial stress-strain response at 50°C - FEM results (Auricchio's formulation).

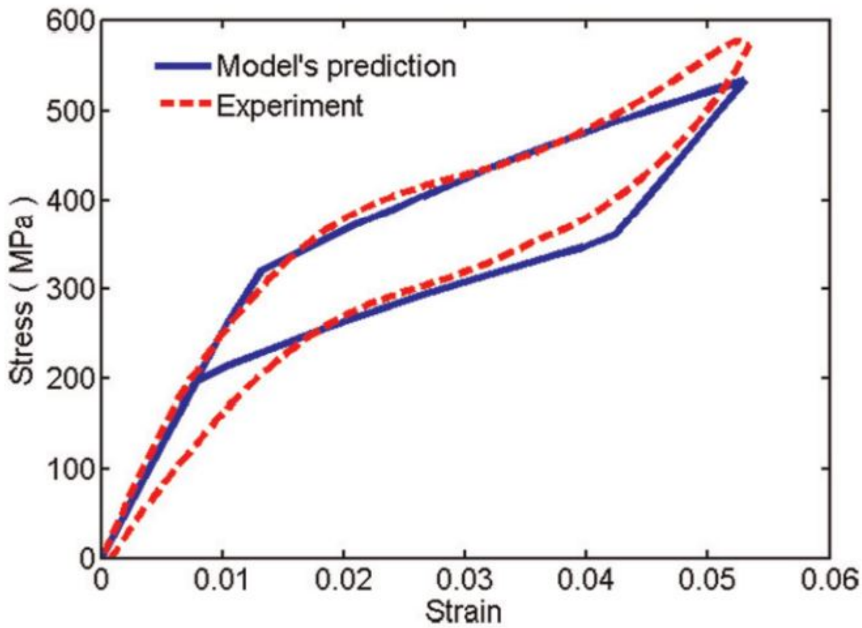

(b) Uniaxial stress-strain response at 50°C - Experimenatl data and Taheri et al. model's prediction [53].

Figure 4.9: Model validation - Uniaxial loading case at 50°C.

	Th	FEM	Err%
$\sigma_{M_f}(MPa)$	501.8	503.3	-0.3
$\sigma_{M_s}(MPa)$	326.8	339.6	-3.92
$\sigma_{A_f}(MPa)$	372.6	339.6	8.86
$\sigma_{A_f}(MPa)$	242.6	219.2	9.65

Table 4.4: Theoretical vs FEM analysis transformation stresses at $50^{\circ}C$.

4.3.2 Torsional loading

The torsional loading case has been examined on a reduced model, representing a section of the SMA tube tested by Taheri et al.. In this case the diameter, thickness and length of the specimen are $D_{ext} = 4.5mm$, $t = 0.3mm$ and $L = 20mm$ respectively. In order to reduce the computational cost, only a portion of the entire component was simulated, and torque-angle characteristic was reconducted to those of a full-size specimen assuming a homogeneous behaviour along the length. Also, RBE2s have been set to reduce spurious effects related to warpage. Figure 4.10 illustrates the FEM model discussed above. The results comparison, shown in figure 4.11, leads to the same consideration reported for the uniaxial loading case.

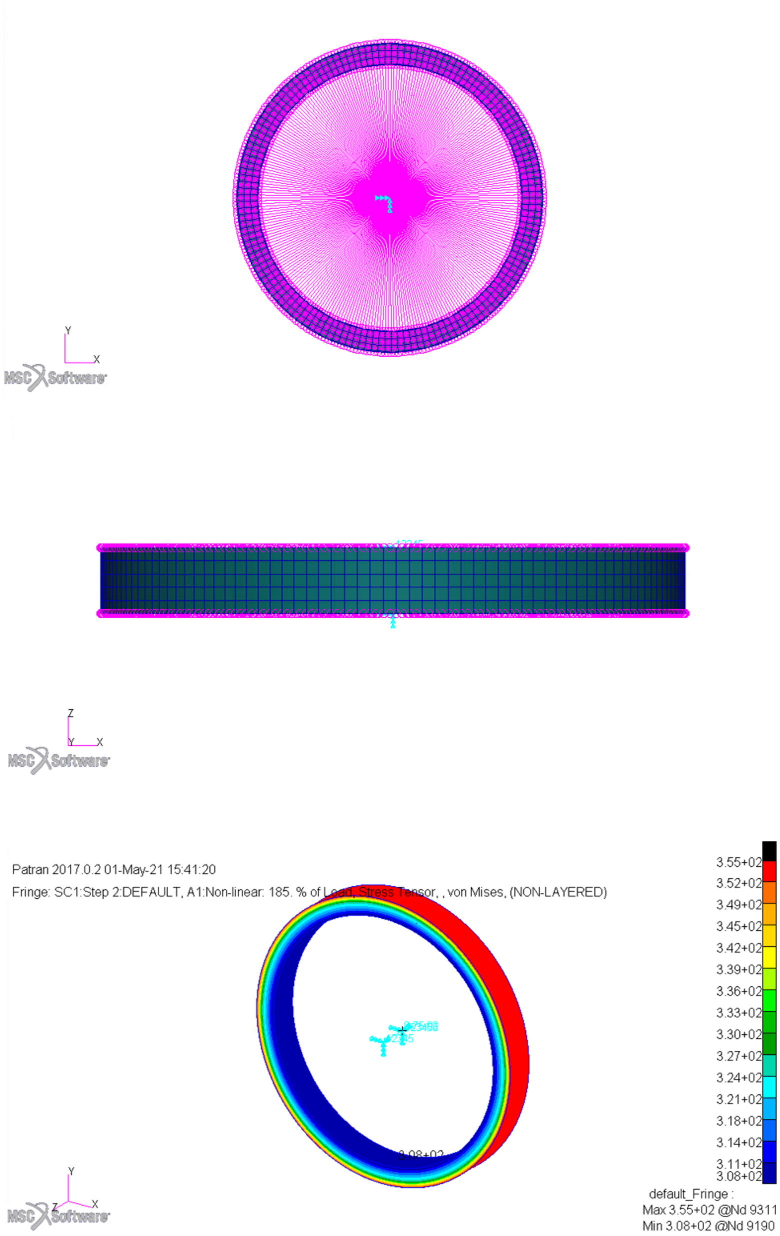

Figure 4.10: FEM model of a section of the tube considered by Taheri et al. [53] for the experimental torque test.

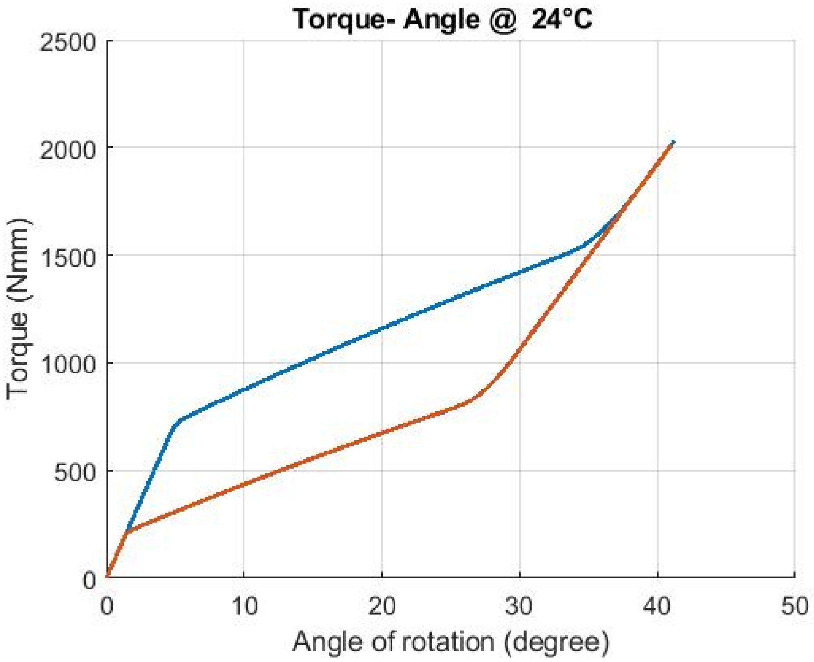

(a) Torque-angle response at 24°C - FEM results (Auricchio's formulation).

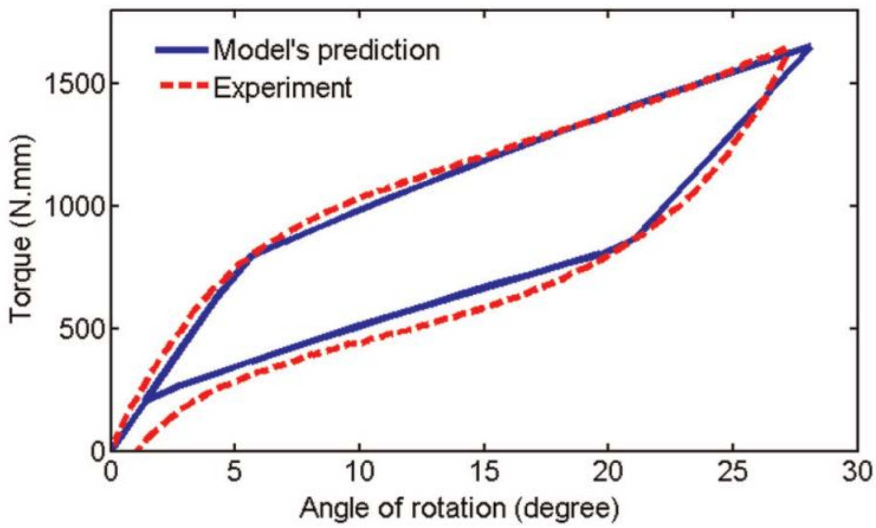

(b) Torque-angle response at 24°C - Experimenatl data and Taheri et al. model's prediction [53].

Figure 4.11: Model validation - Torsional loading case at 24°C.

4.4 Characteristic diagrams

4.4.1 Torque-angle diagrams

As discussed in the conceptual design section, torque-angle diagrams are of great use to estimate the SMA actuator mechanical capabilities. Moreover, loading cycles simulation also allows getting a sense of the required temperature range. For these reasons, the SMA rod studied in this work has been analysed at different temperatures under torque conditions. In particular, one end of the specimen was constrained, while a moment or an angular displacement was applied to the other end. No differences have been appreciated in these two cases. Figure 4.12, 4.13 ad 4.14 show torque-angle, shear stress-strain and tangential stiffness at $24°C$. Note that the shear stress τ is conventionally defined as $\tau(r) = Tr/J$ where T is the applied torque and r is the rod's radius. On the other hand, tangential stiffness refers to the incremental ratio of stress-strain function, thus figure 4.14 plots the quantity $\Delta\tau/\Delta\gamma$ with repect to τ. Figures 4.15, 4.16 and 4.17 show the aforementioned charts at $40°C$ condition, while figures 4.18, 4.19 and 4.20 refer to $50°C$.

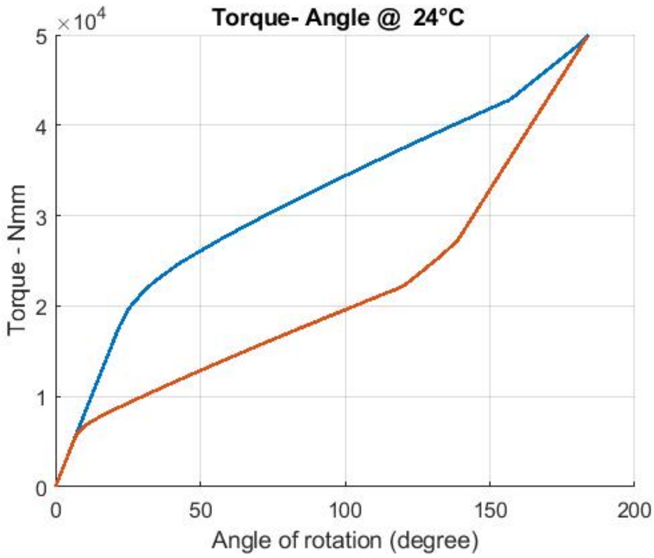

Figure 4.12: Torque-Angle diagram at $24°C$.

Finally, figure 4.21 and figure 4.22 show the specimen behaviour at the temperatures mentioned above superimposed in a single diagram in torque-angle and stress-strain fields, respectively.

At this step, it is possible to estimate $35Nm$ of torque over $50°$ of rotation, activated by a $25°C$ temperature increase. Note that the total amount of torque also has to drive the return spring devices.

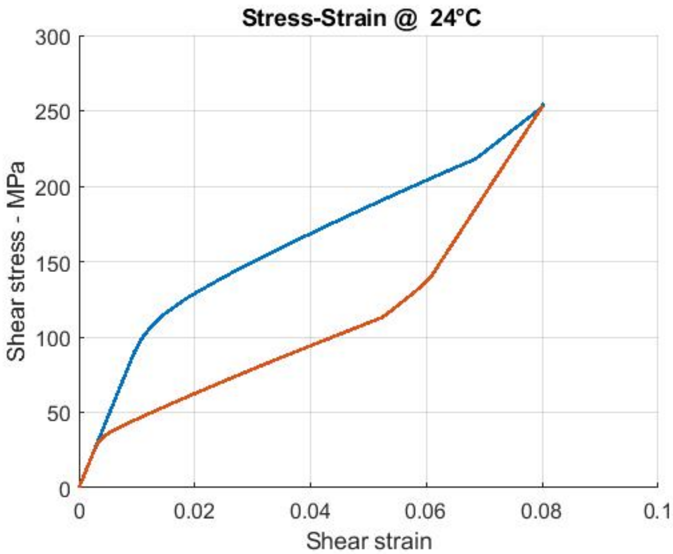

Figure 4.13: Shear stress-strain diagram at 24°C.

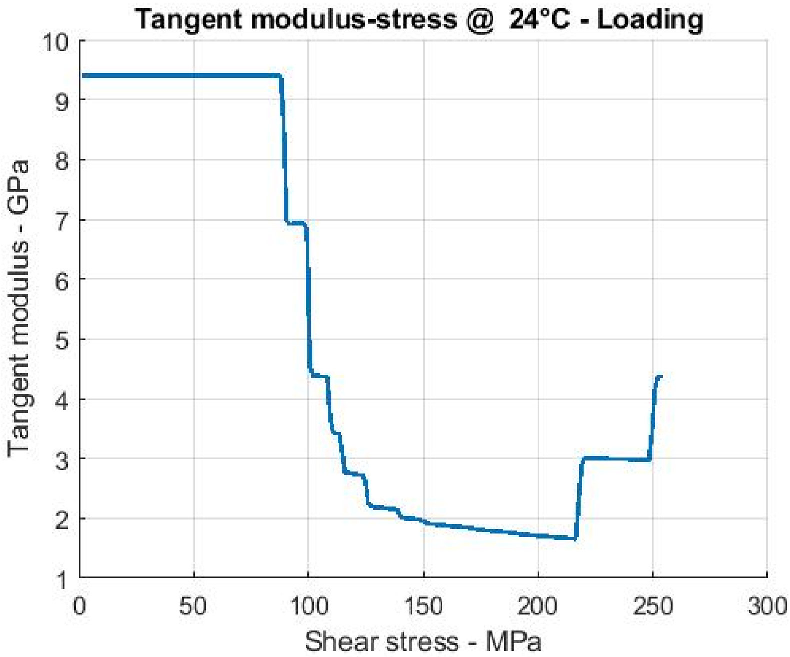

(a)

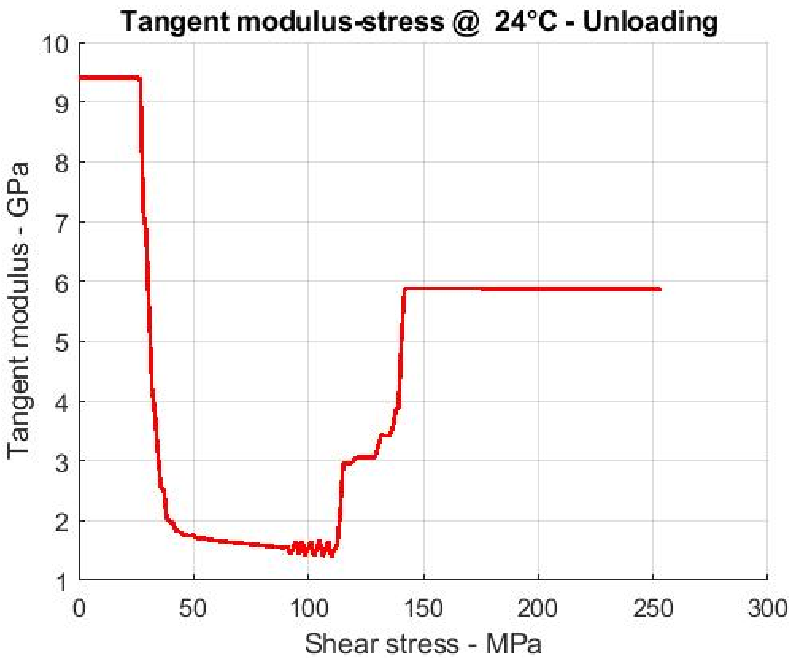

(b)

Figure 4.14: Tangent modulus ($\Delta(stress)/\Delta(strain)$) at 24°$C$.

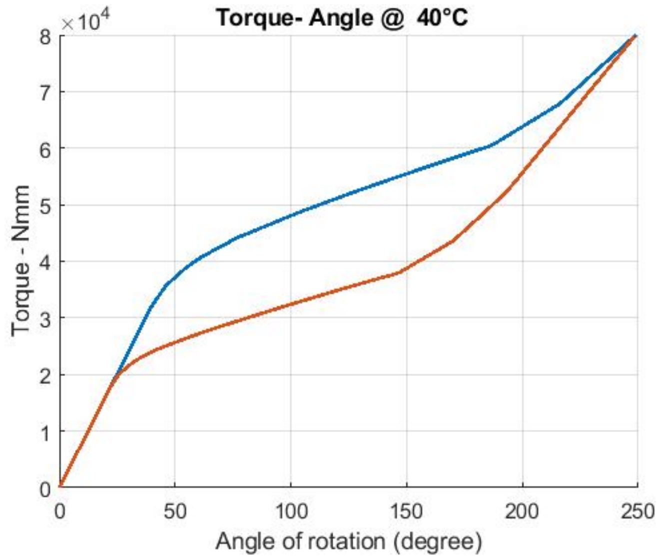

Figure 4.15: Torque-Angle diagram at 40°C.

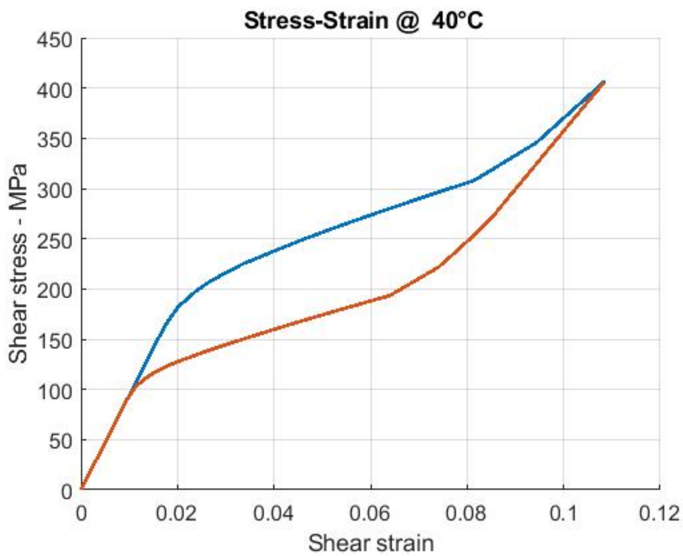

Figure 4.16: Shear stress-strain diagram at 40°C.

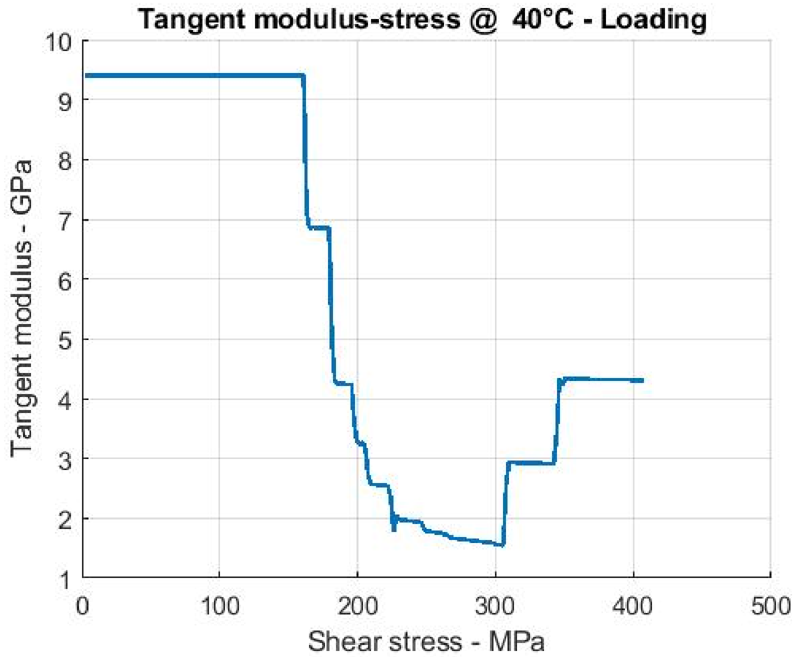

(a)

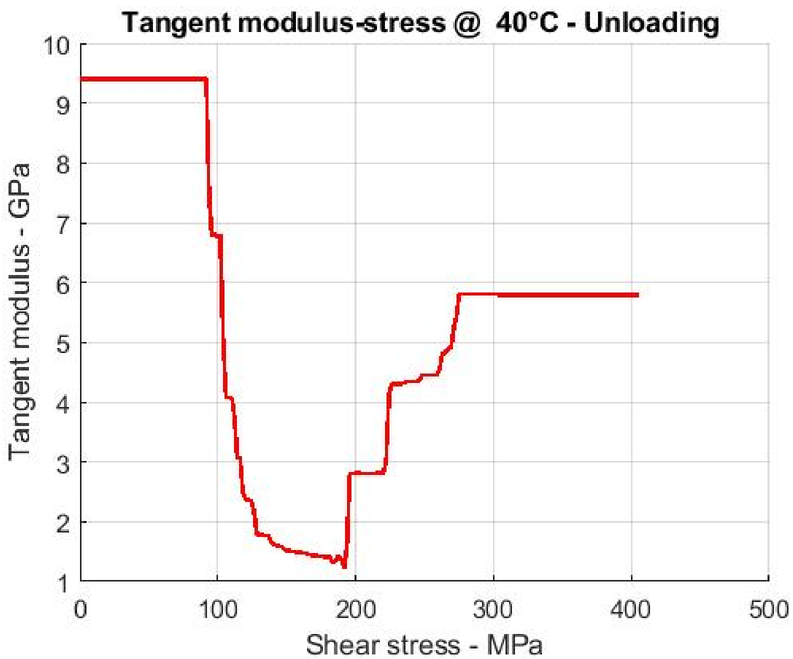

(b)

Figure 4.17: Tangent modulus ($\Delta(stress)/\Delta(strain)$) at 40°$C$.

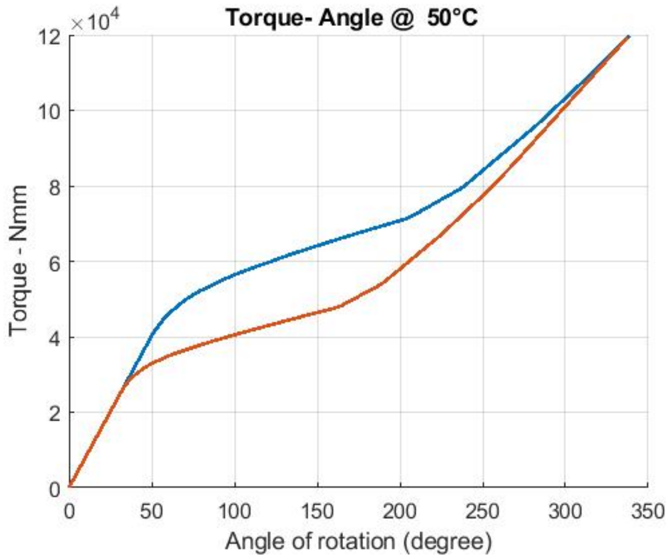

Figure 4.18: Torque-Angle diagram at $50°C$.

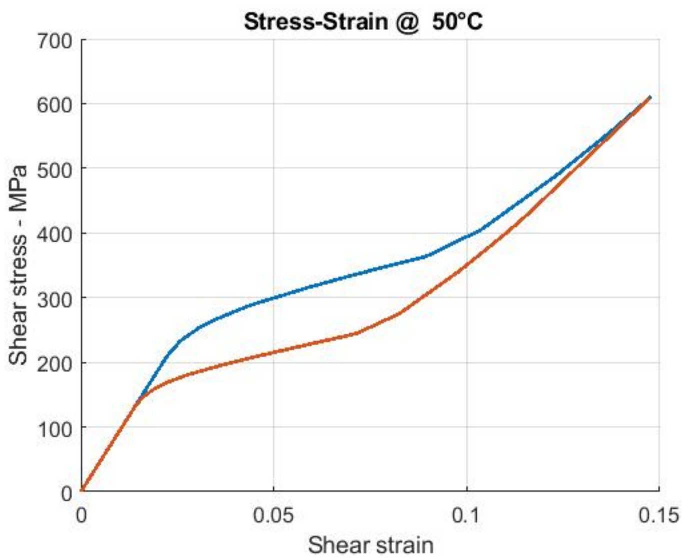

Figure 4.19: Shear stress-strain diagram at $50°C$.

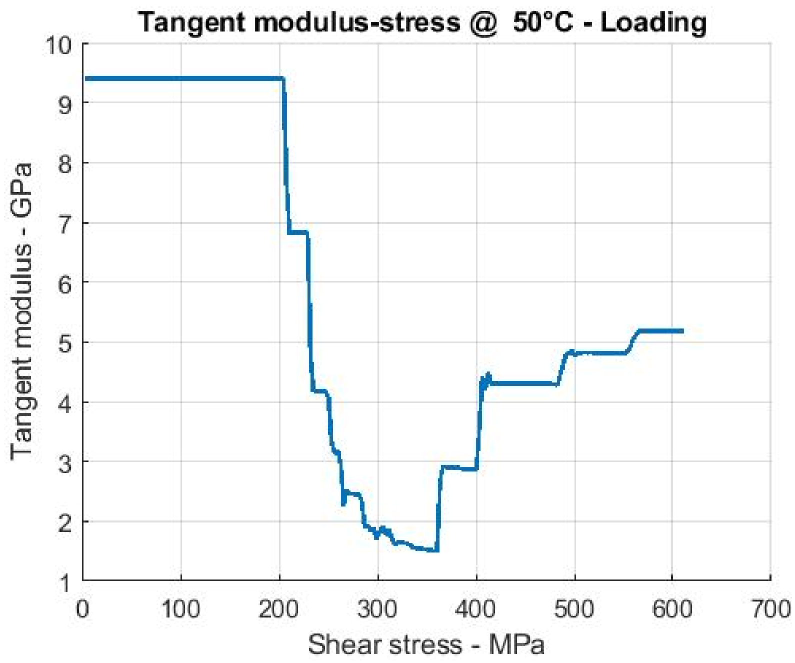

(a)

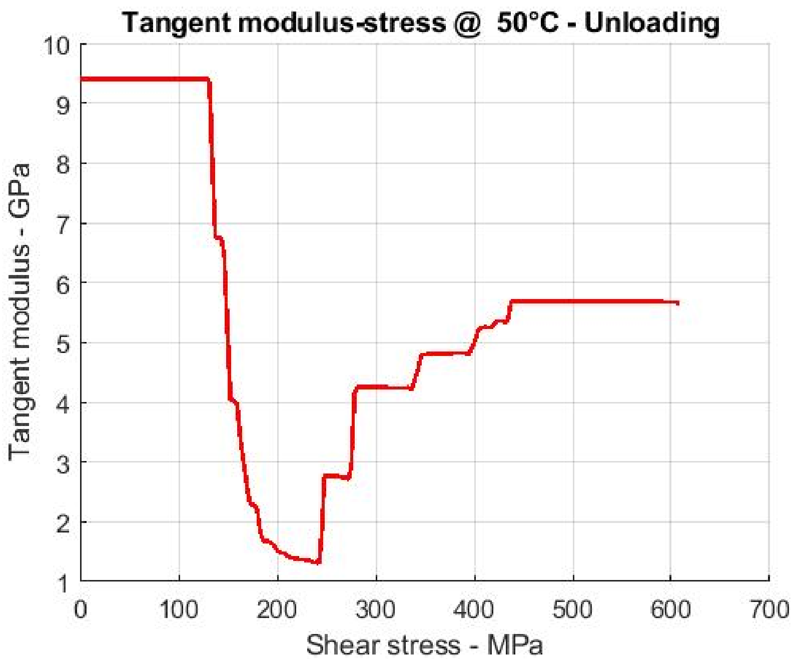

(b)

Figure 4.20: Tangent modulus $(\Delta(stress)/\Delta(strain))$ at 50°C.

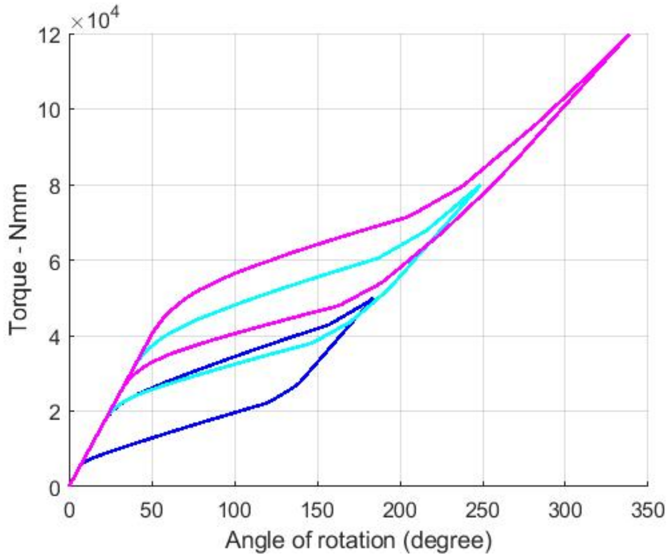

Figure 4.21: Torque-Angle diagram at 24°C 40°C and 50°C.

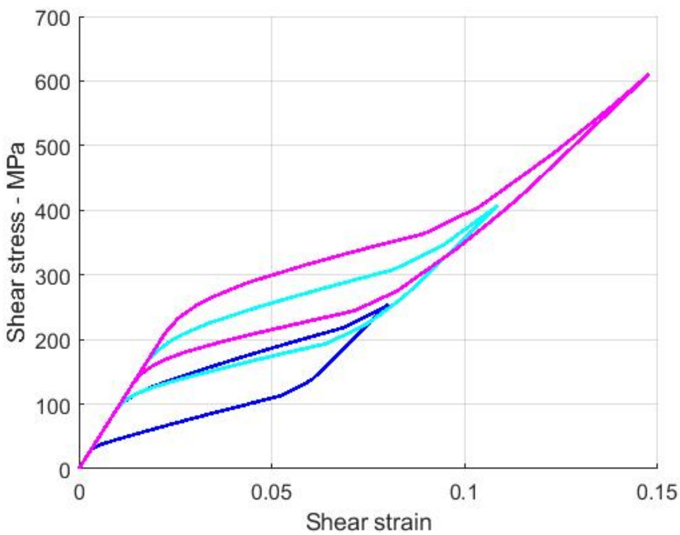

Figure 4.22: Shear stress-strain diagram at 24°C 40°C and 50°C.

4.4.2 Angle-temperature diagrams

Angle-temperature diagrams are helpful to predict the SMA actuator performance similarly to torque-angle graphs. Constant torque FEM simulations have been performed on the rod under investigation, varying temperature over a wider range with respect to that considered in the previous section. Besides the assessments related to the actuator dimensioning, these analyses also verify the physical consistency of the present model. Figure 4.23 shows the rod's behaviour under different torque values separately, while figure 4.24 plots all the cycles in the same diagram.

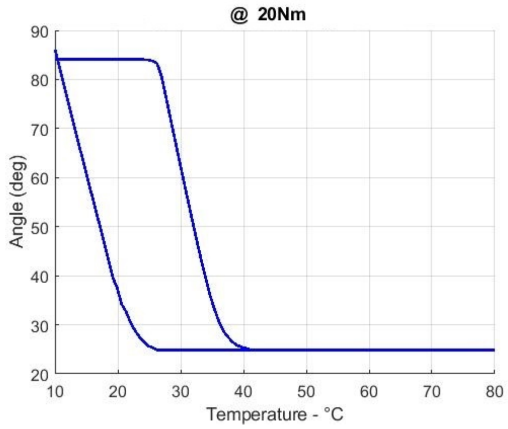

(a) Angle-Temperature diagram under constant $20Nm$ torque.

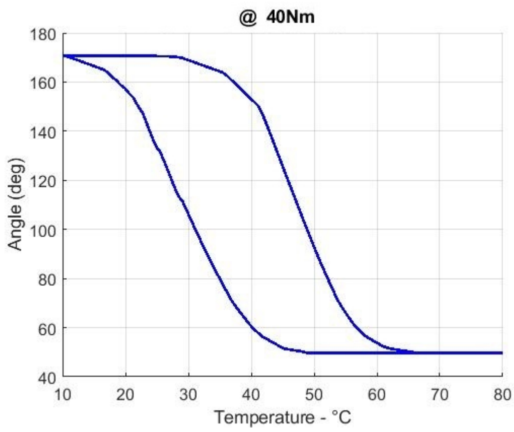

(b) Angle-Temperature diagram under constant $40Nm$ torque.

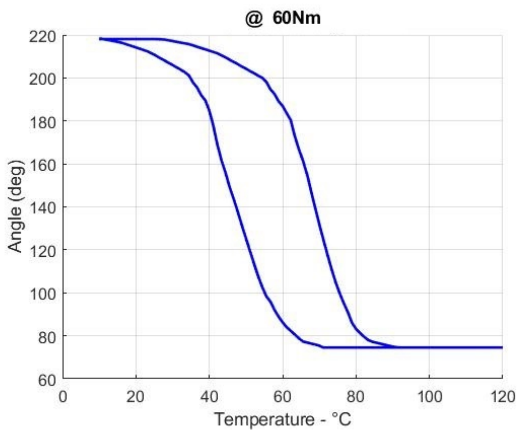

(c) Angle-Temperature diagram under constant $60Nm$ torque.

Figure 4.23: Constant torque thermal cycle response.

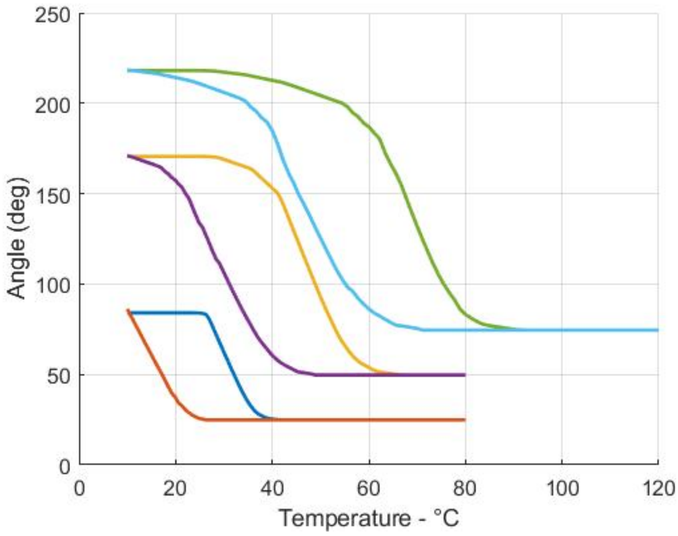

Figure 4.24: Angle-Temperature diagram under constant torque of $20Nm$, $40Nm$ and $60Nm$.

4.5 Actuation

In this section, different actuation paths are examined, accounting for multiple aspects aiming to provide a complete view of the phenomena involved during the operations. Indeed torque angle characteristic is accompanied by the angle-temperature diagram and martensite evolution as a function of radius, all monitored simultaneously during the actuation phases. The actuation scenarios under investigation are the same presented in the conceptual design chapter also to assess the correctness of the assumed paths.

4.5.1 Actuation under constant load

The simplest actuation path is that involving a constant opposite torque. The FEM model under investigation is the same described in the previous sections, used to validate the model response according to experimental data present in the literature. The nonlinear analysis has been set with multiple steps to simulate the real condition loading path. First of all, the initial temperature of 24°C was set, and the specimen was loaded until it reached 172 degrees of rotation, aiming to develop a high amount of stress-induced martensite. At this point, a $21Nm$ torque was applied to partially unload the rod, aiming to bring it on the threshold of martensite to austenite transformation. Afterwards, the temperature was risen to 46°C inducing the shape recovery. Finally, the specimen was cooled to 0°C. The load steps sequence is summarised in table 4.5. Figure 4.26 shows the complete actuation path in the torque angle diagram. In order to monitor all the phenomena involved during the phase transformation, figure 4.27 provides a sequence of snapshots of the torque-angle, angle-temperature and martensite-radius charts. Also, a polar diagram of the angular displacement is reported to visualise the rod's motion. Note that the martensite volume fraction is computed and reported at the element centroid. Although it would be desirable to interpolate a higher number of points, the grid points values subsequently derived are not considered accurate since figures higher than one emerge, which, of course, is physically meaningless. Moreover, to reduce border effects, three elements in the middle of the rod have been considered, as shown in figure 4.25.

STEP 0	Set T=24°C	
STEP 1	Displacement-driven loading to 172°; $T = 24°C$	Blue segment in figure 4.26
STEP 2	Unloading to $21Nm$; $T = 24°C$	Red segment in figure 4.26
STEP 3	Heating 24°C $\rightarrow$ 46°C @$21Nm$	Yellow segment in figure 4.26
STEP 4	Cooling 46°$C \rightarrow 0°C$ @$21Nm$	Purple segment in figure 4.26

Table 4.5: Actuation under constant load - Steps sequence.

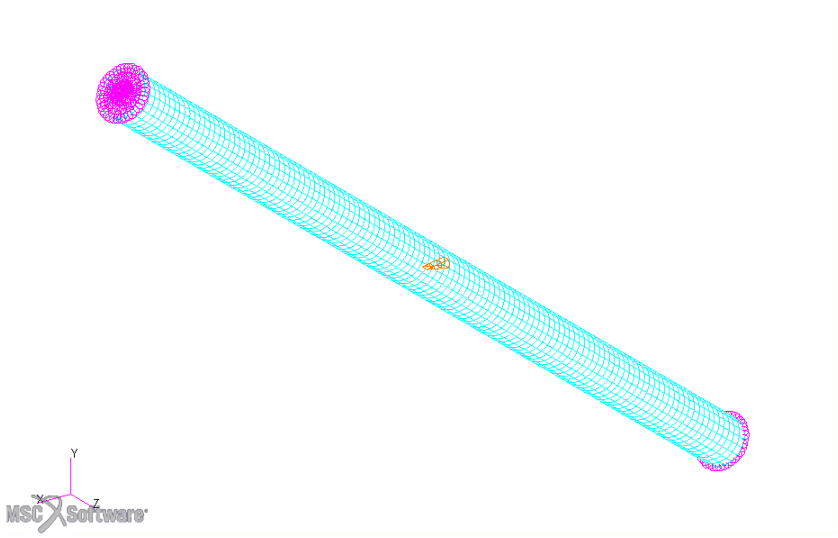

Figure 4.25: Elements considered for martensite volume fraction output.

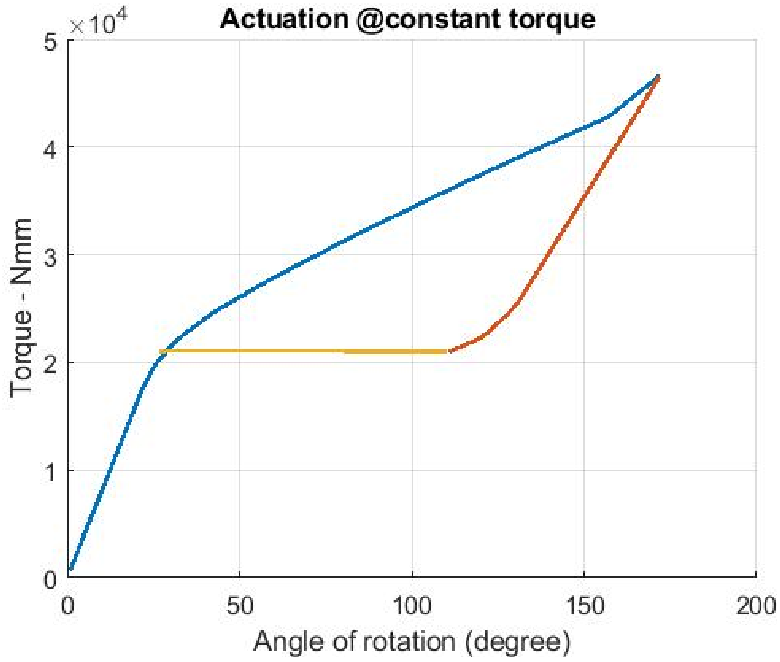

(a) Forward transformation ($M \rightarrow A$).

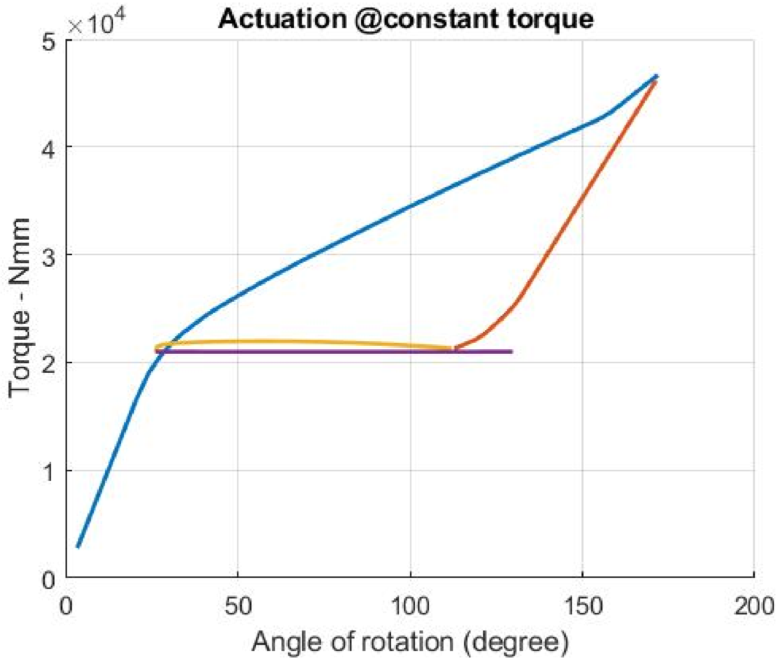

(b) Backward transformation ($A \rightarrow M$).

Figure 4.26: Torque-Angle diagrams - Constant load case.

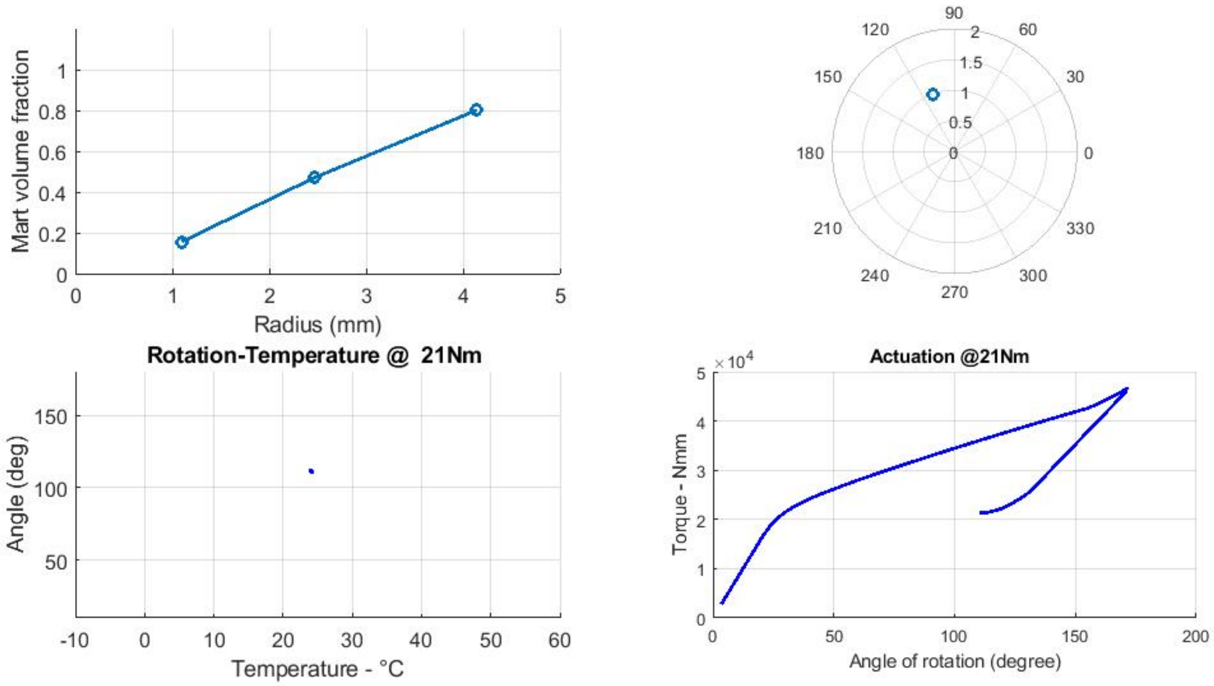

(a)

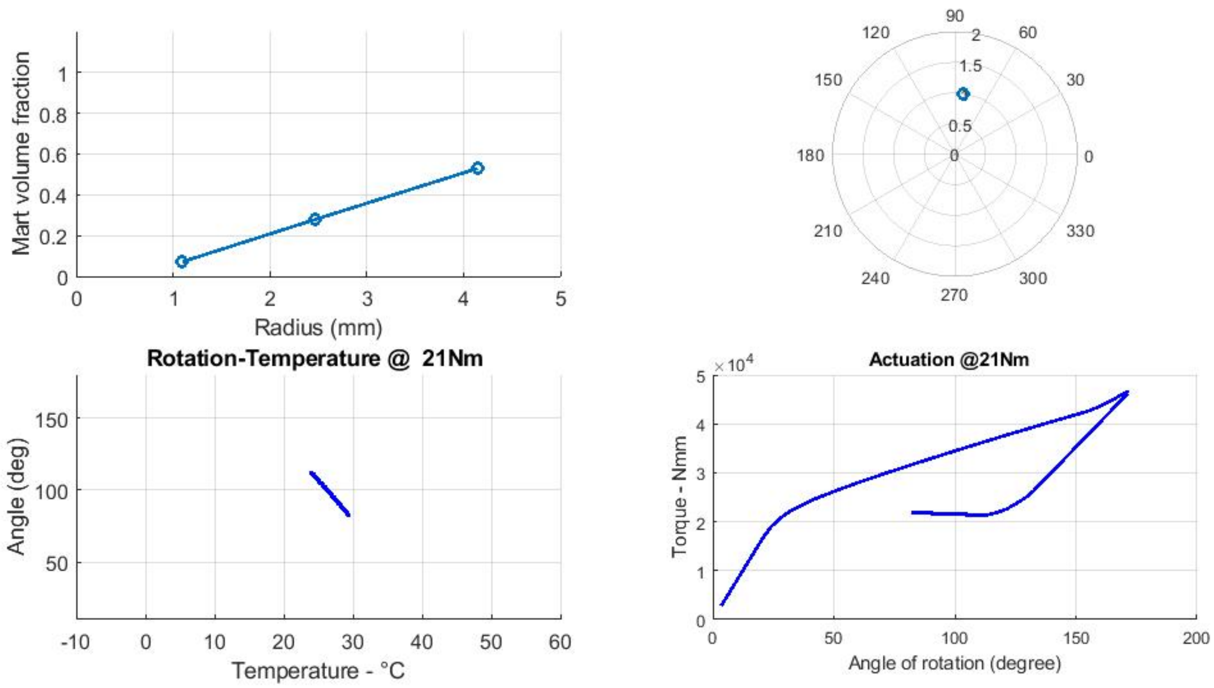

(b)

Figure 4.27: Martensite, displacement, torque and temperature evolution during actuation - Constant load case

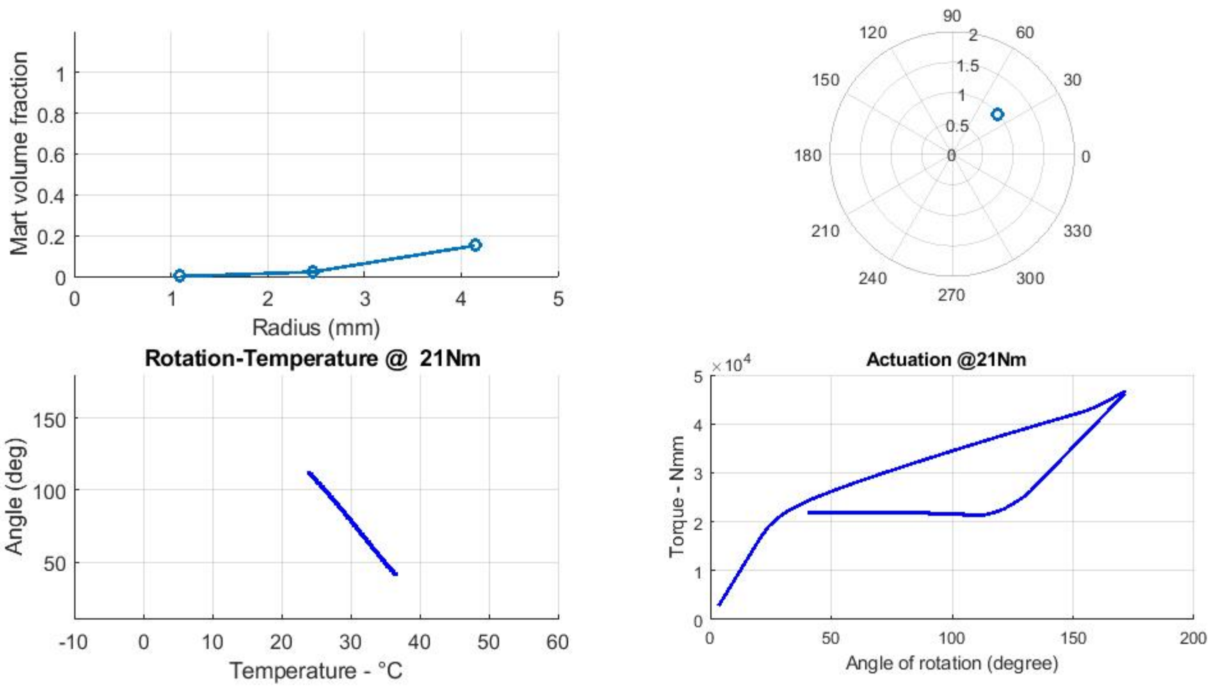

(c)

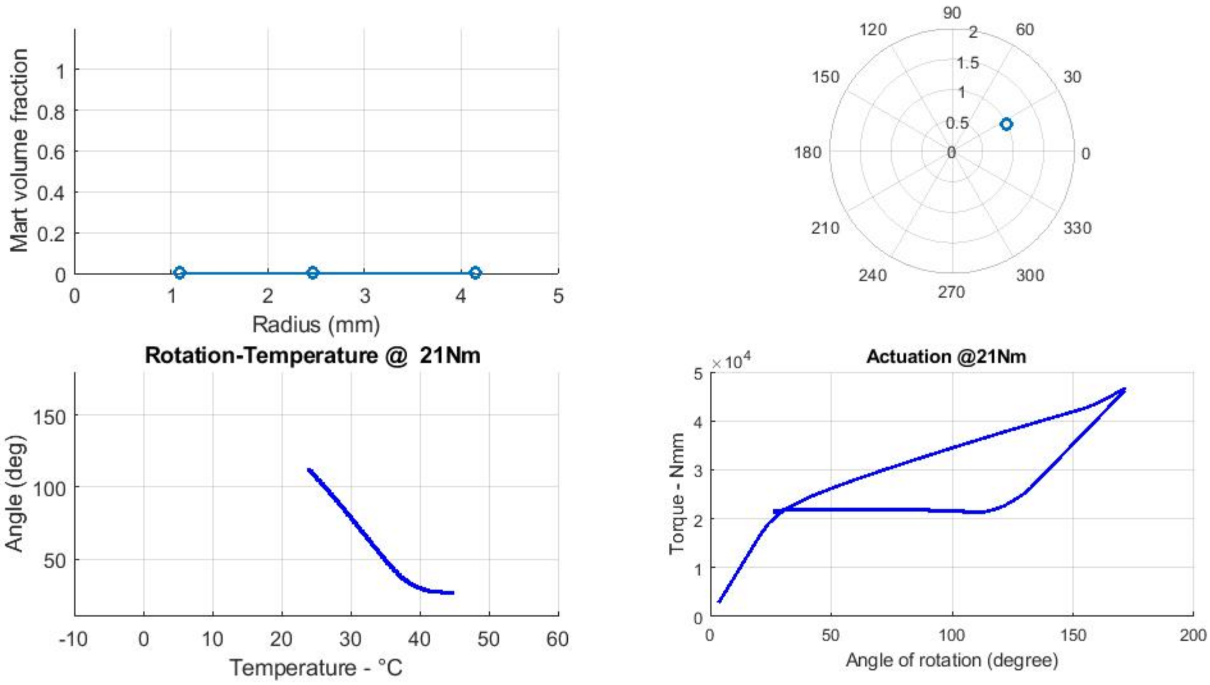

(d)

Figure 4.27: Martensite, displacement, torque and temperature evolution during actuation - Constant load case

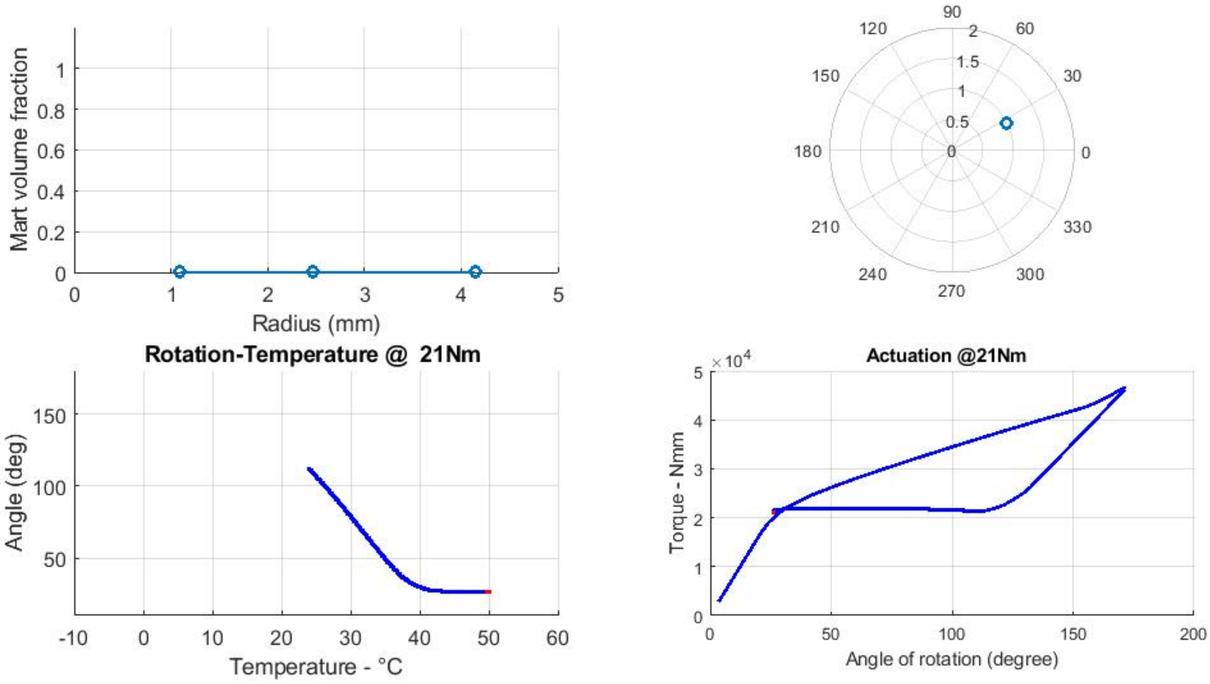

(e)

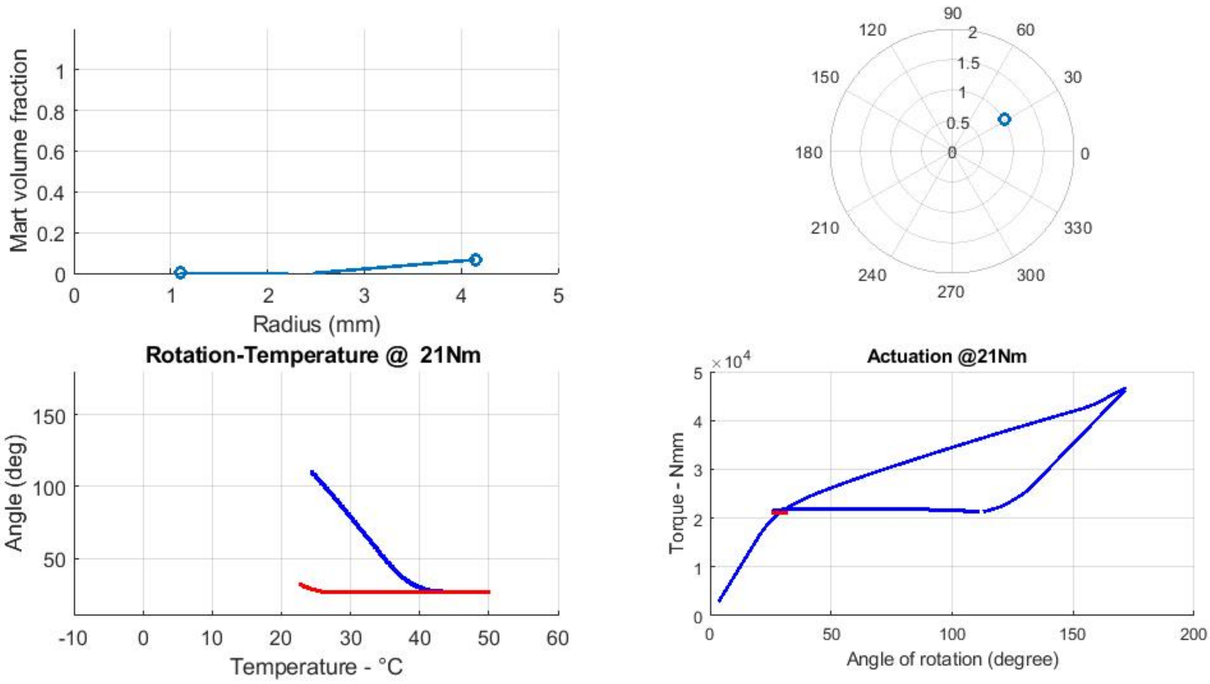

(f)

Figure 4.27: Martensite, displacement, torque and temperature evolution during actuation - Constant load case

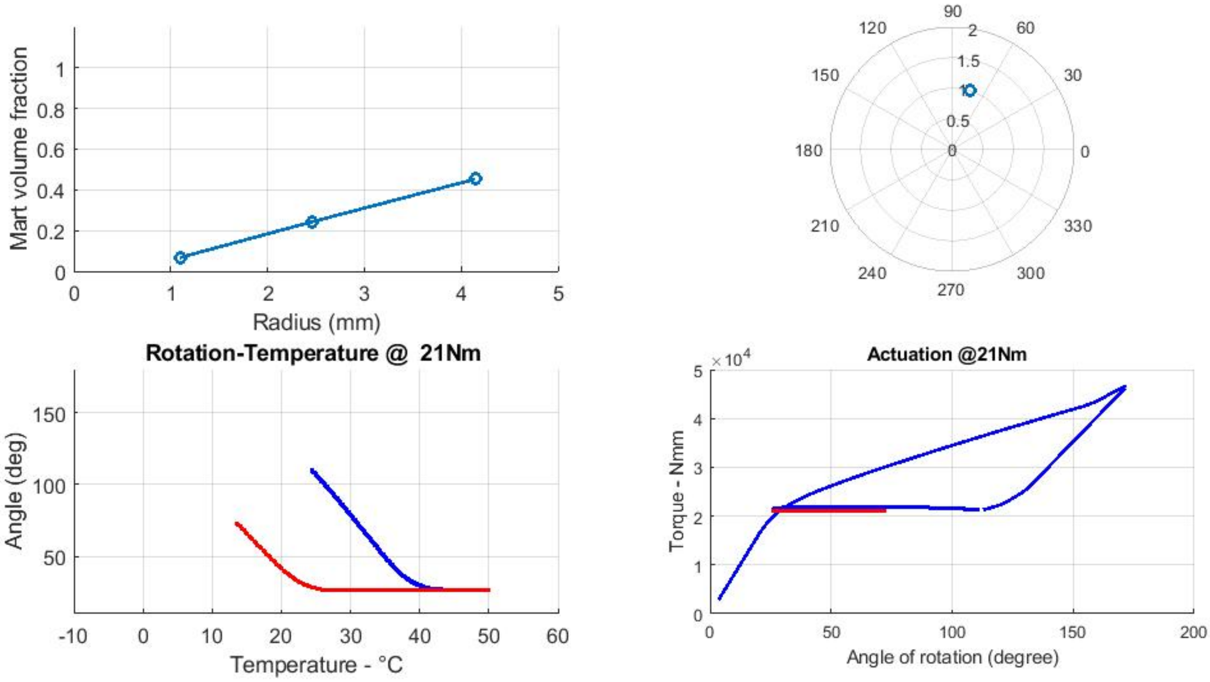

(g)

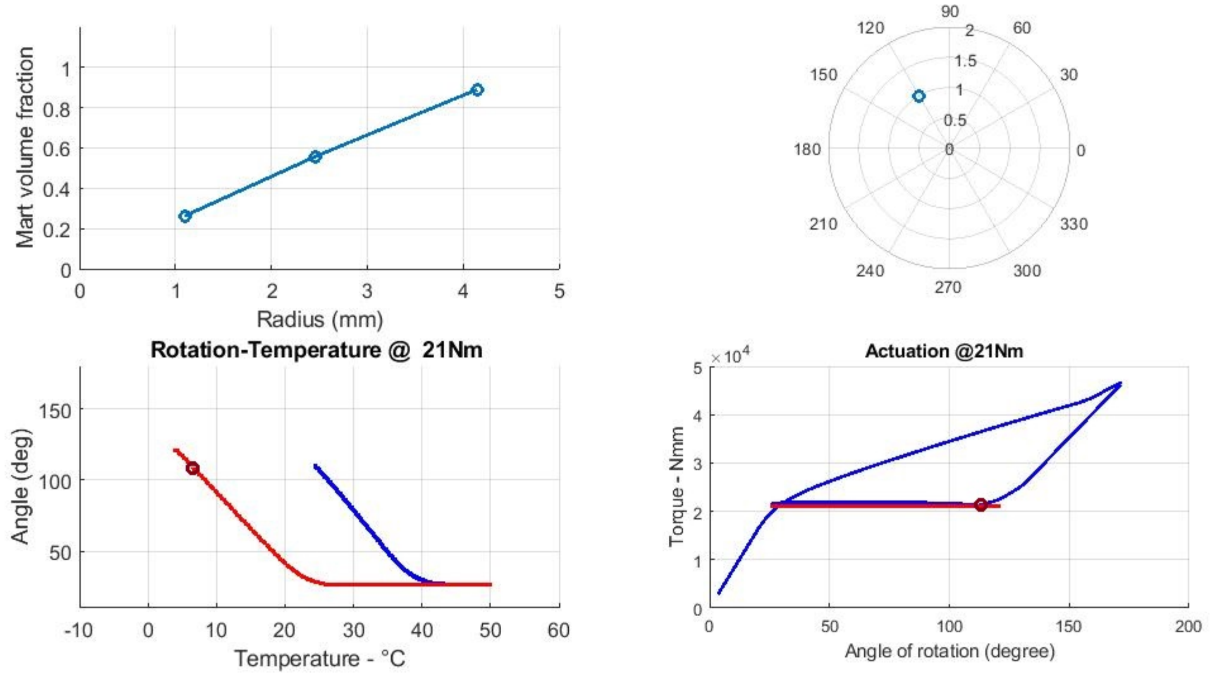

(h)

Figure 4.27: Martensite, displacement, torque and temperature evolution during actuation - Constant load case

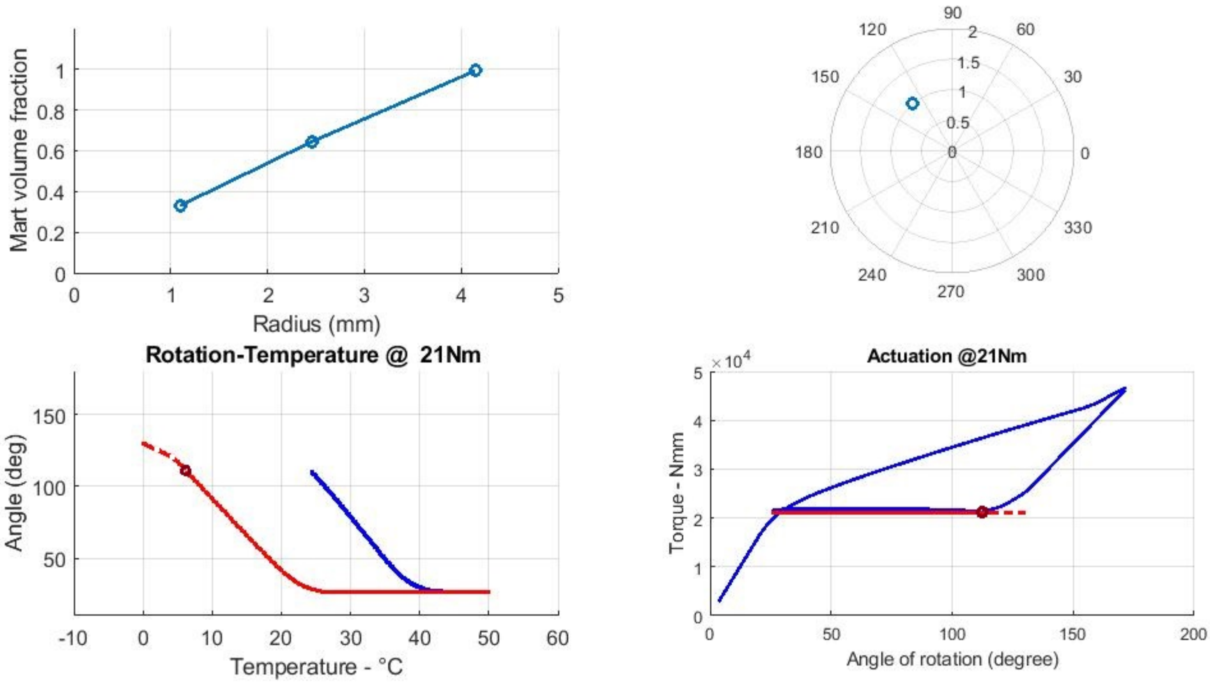

(i)

Figure 4.27: Martensite, displacement, torque and temperature evolution during actuation - Constant load case

4.5.2 Actuation under variable load

The rod model considered for this actuation path is the same presented in the previous sections, as well as the first steps. However, upon unloading to $21Nm$ of torque, a variable load path was introduced using a CBUSH element, which is a generalised spring-damper scalar element. Within this work, it was associated with the PBUSH and the PBUSHT bulk data entries, to define a load-displacement dependency. This way, as the rod recovers its shape, thus inducing an angular displacement, the CBUSH applies a different torque. In this case, a linear loading path was considered; however, the same procedure can be adopted for a generalised loading law acting on the TABLED1 entry. One CBUSH gridpoint was constrained, while the other one was opportunely preloaded. This element was engaged at step three using an MPC that connects the constraint-free CBUSH grid point to the independent node of the moving RBE2, in turn, connected to the SMA rod. Heating and cooling were performed in the same temperature range of the constant-load case. The load steps sequence is summarised in table 4.6, while figures 4.28 and 4.29 show the overall behaviour of the SMA under a variable torque actuation.

STEP 0	Set T=24°C	
STEP 1	Displacement-driven loading to 172°; $T = 24°C$	Blue segment in figure 4.28
STEP 2	Unloading to $21Nm$; $T = 24°C$	Red segment in figure 4.28
STEP 3	Heating 24°C $\rightarrow$ 46°C @ Variable load	Purple segment in figure 4.28
STEP 4	Cooling 46°C $\rightarrow$ 0°C @ Variable load	Green segment in figure 4.28

Table 4.6: Actuation under variable load - Steps sequence.

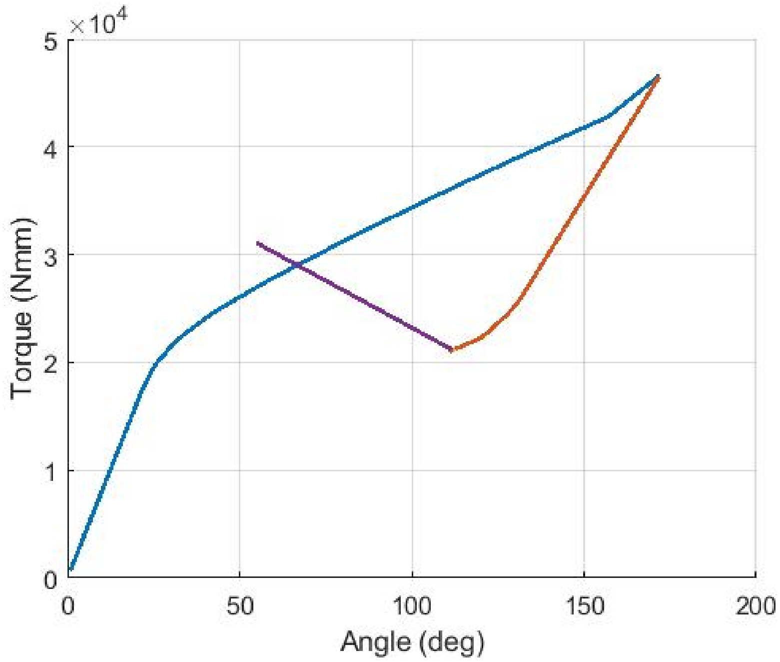

(a) Forward transformation ($M \rightarrow A$).

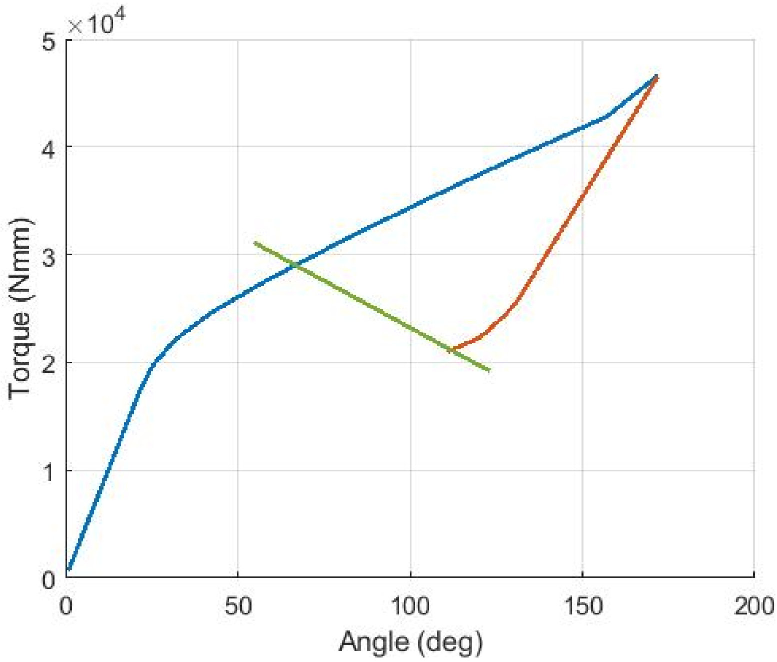

(b) Backward transformation ($A \rightarrow M$).

Figure 4.28: Torque-Angle diagrams - Variable load case.

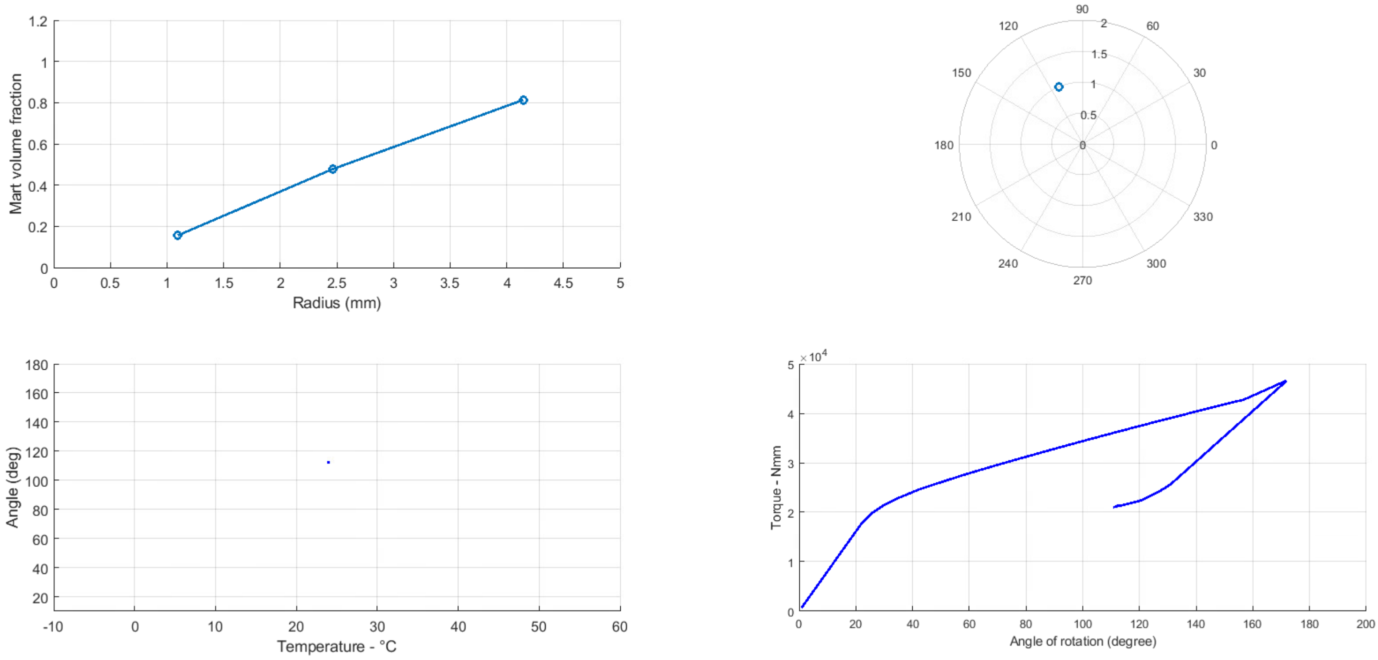

(a)

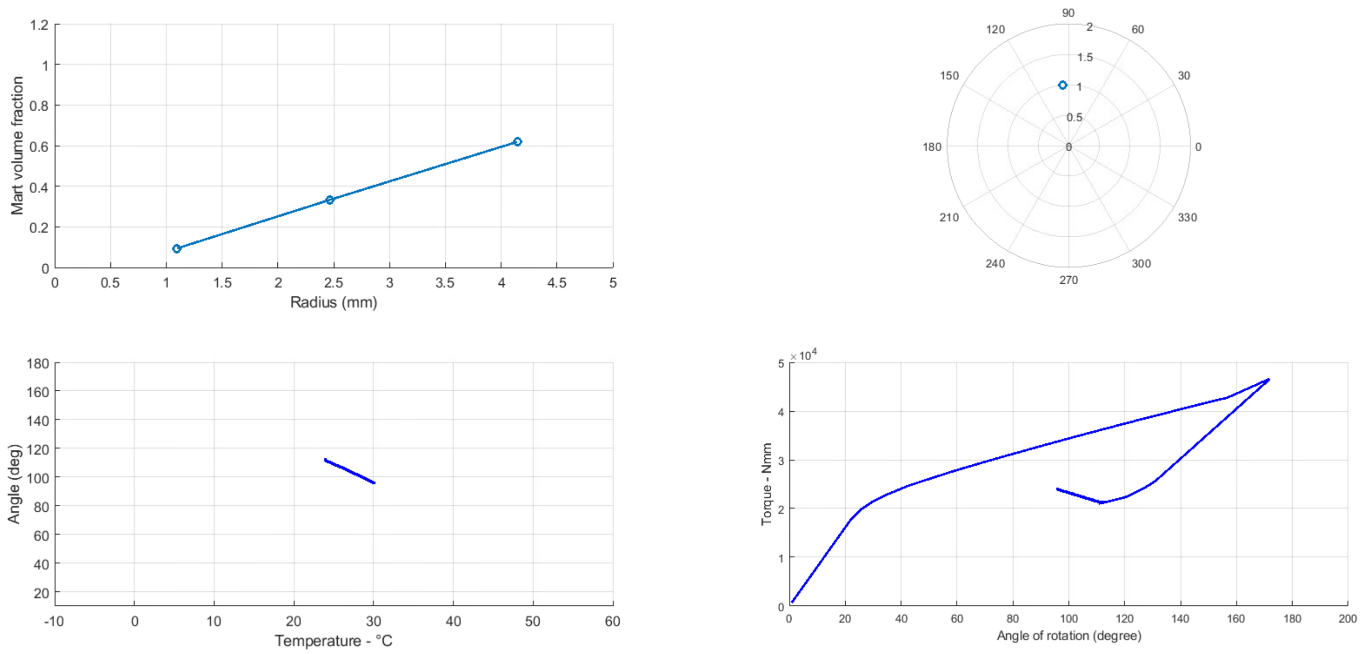

(b)

Figure 4.29: Martensite, displacement, torque and temperature evolution during actuation - Variable load case

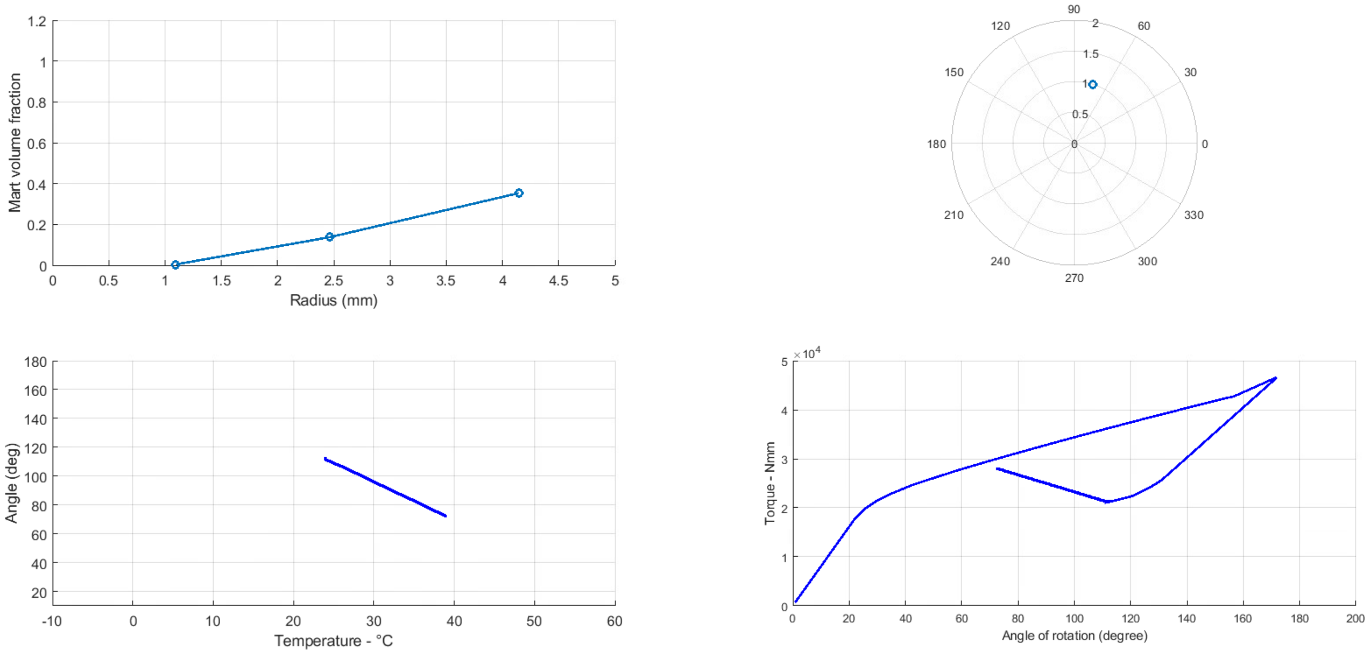

(c)

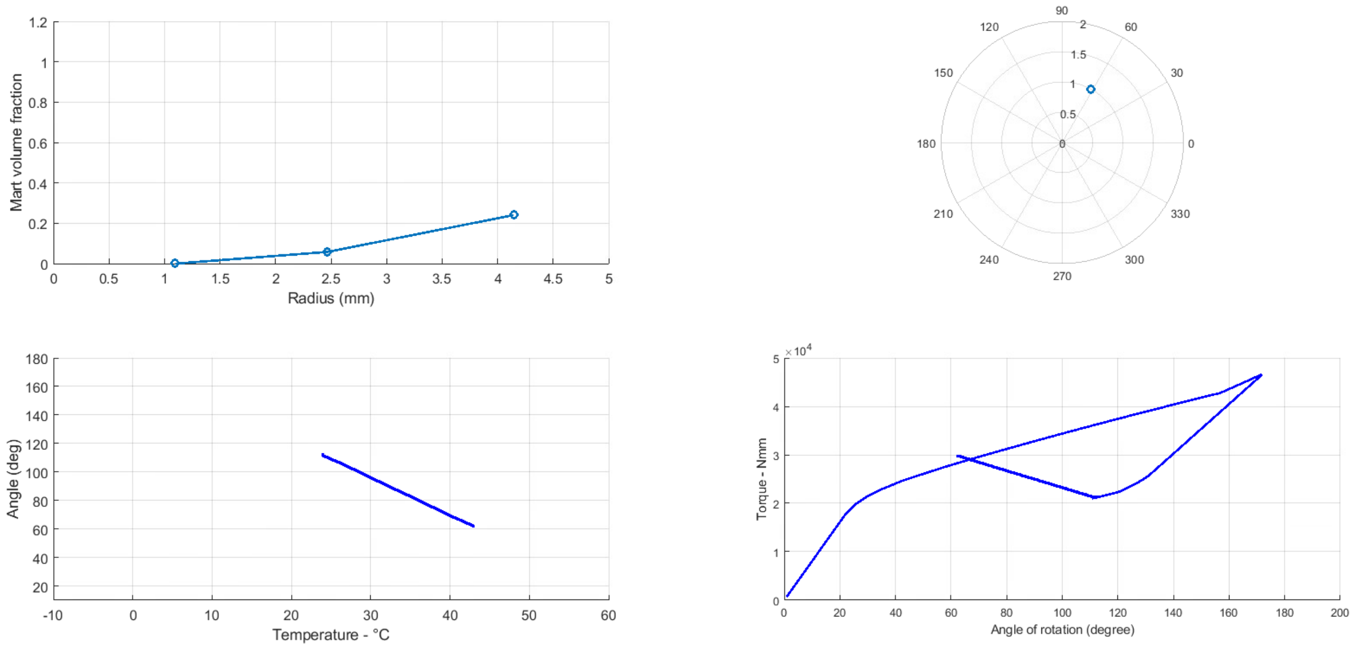

(d)

Figure 4.29: Martensite, displacement, torque and temperature evolution during actuation - Variable load case

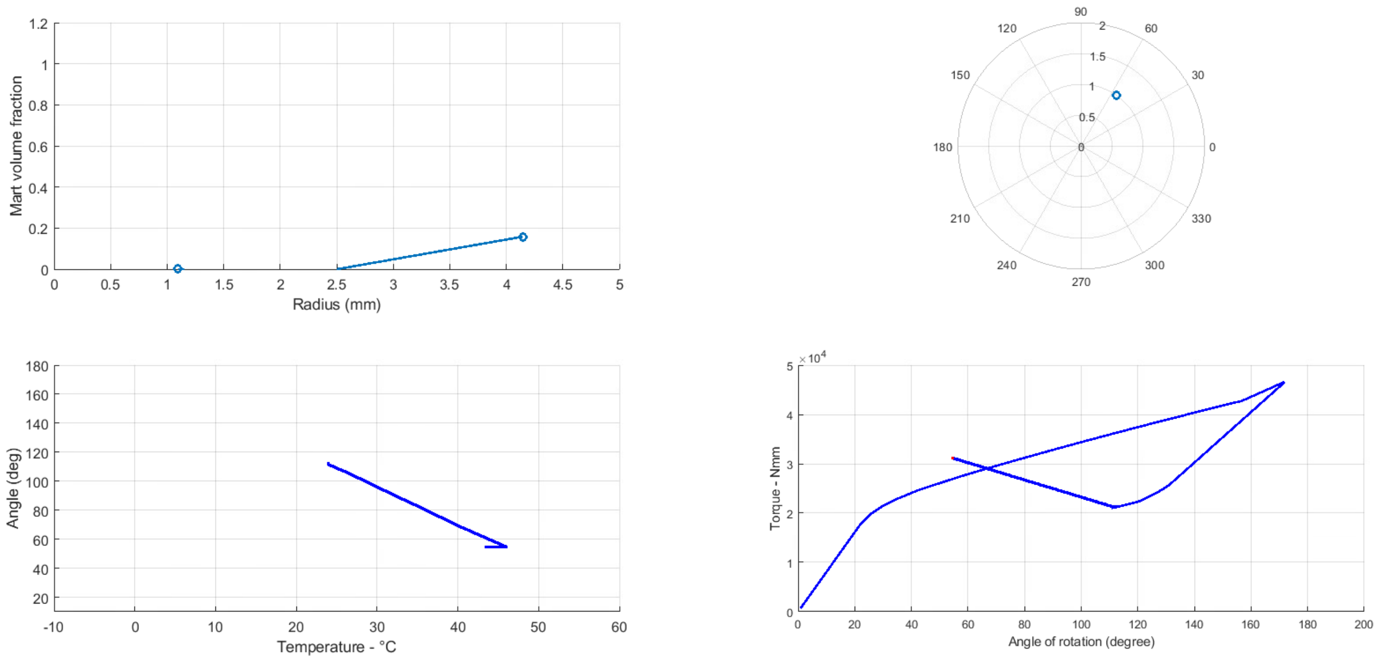

(e)

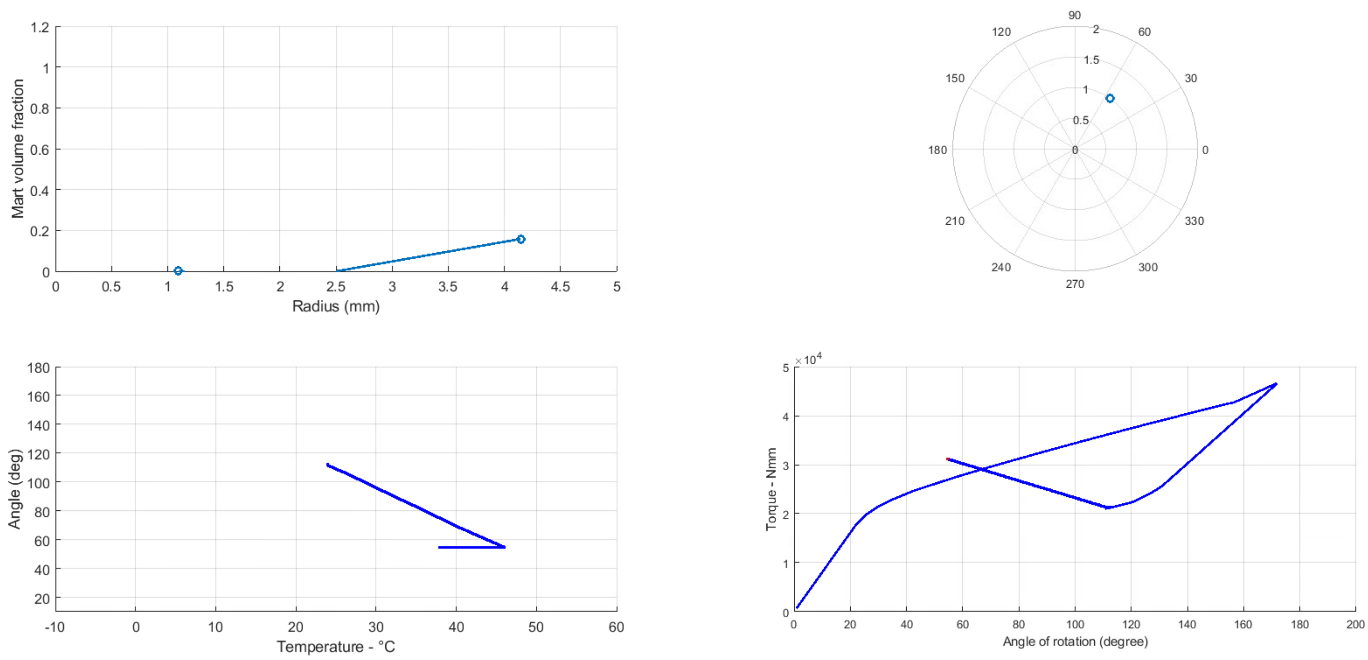

(f)

Figure 4.29: Martensite, displacement, torque and temperature evolution during actuation - Variable load case

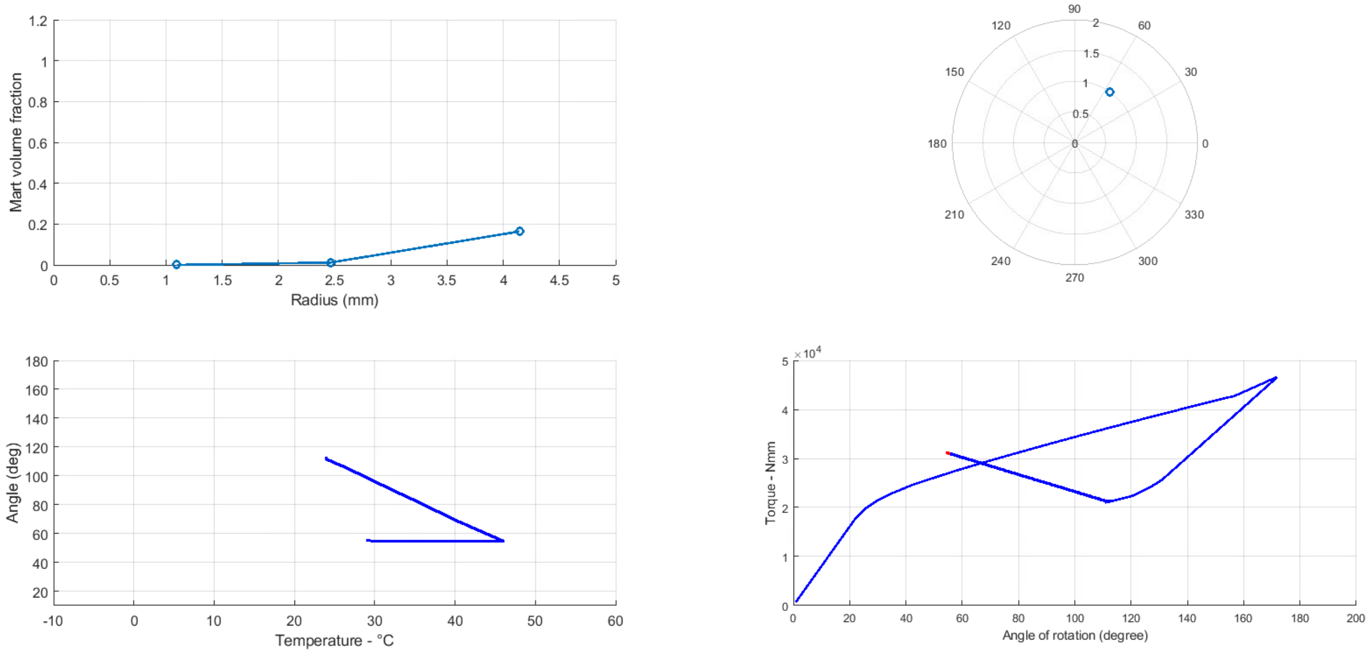

(g)

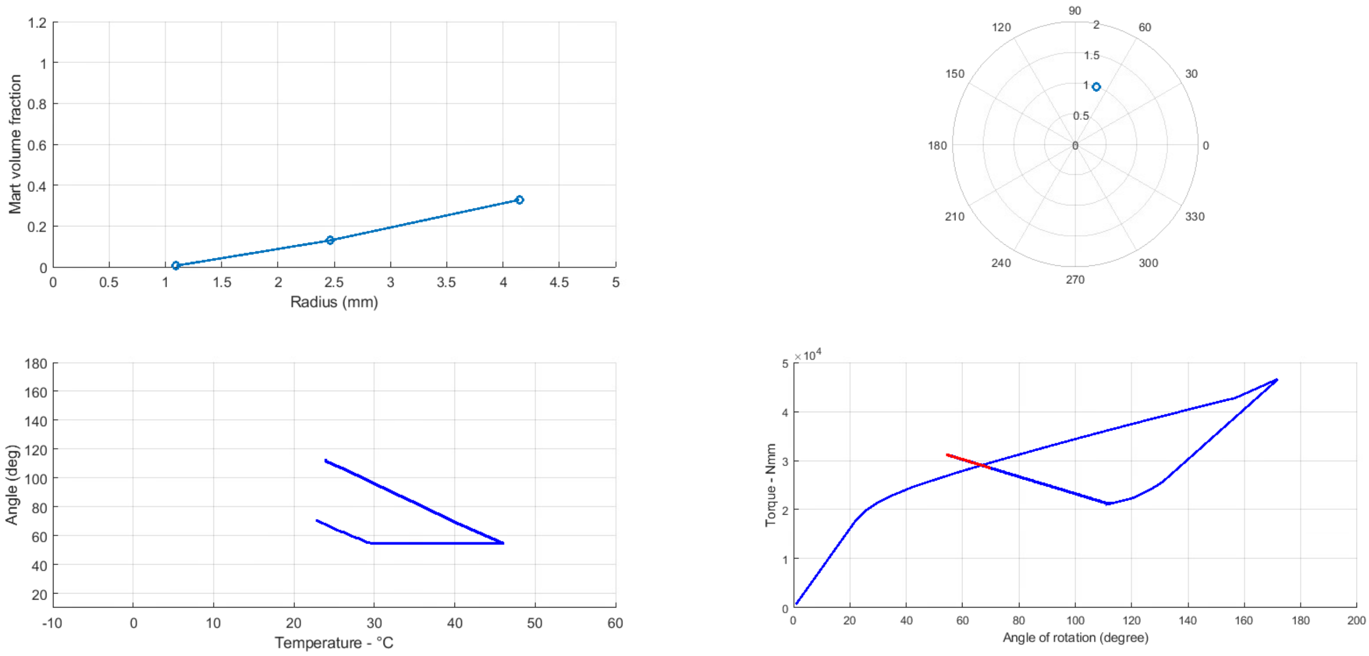

(h)

Figure 4.29: Martensite, displacement, torque and temperature evolution during actuation - Variable load case

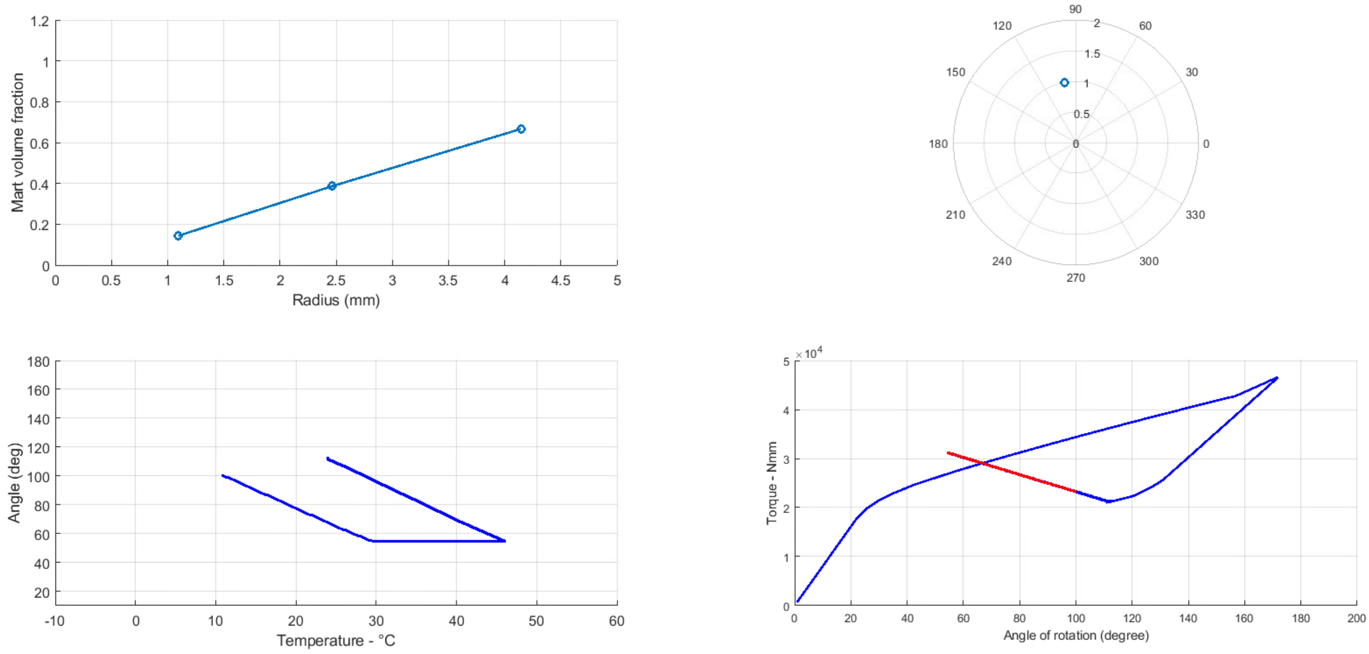

(i)

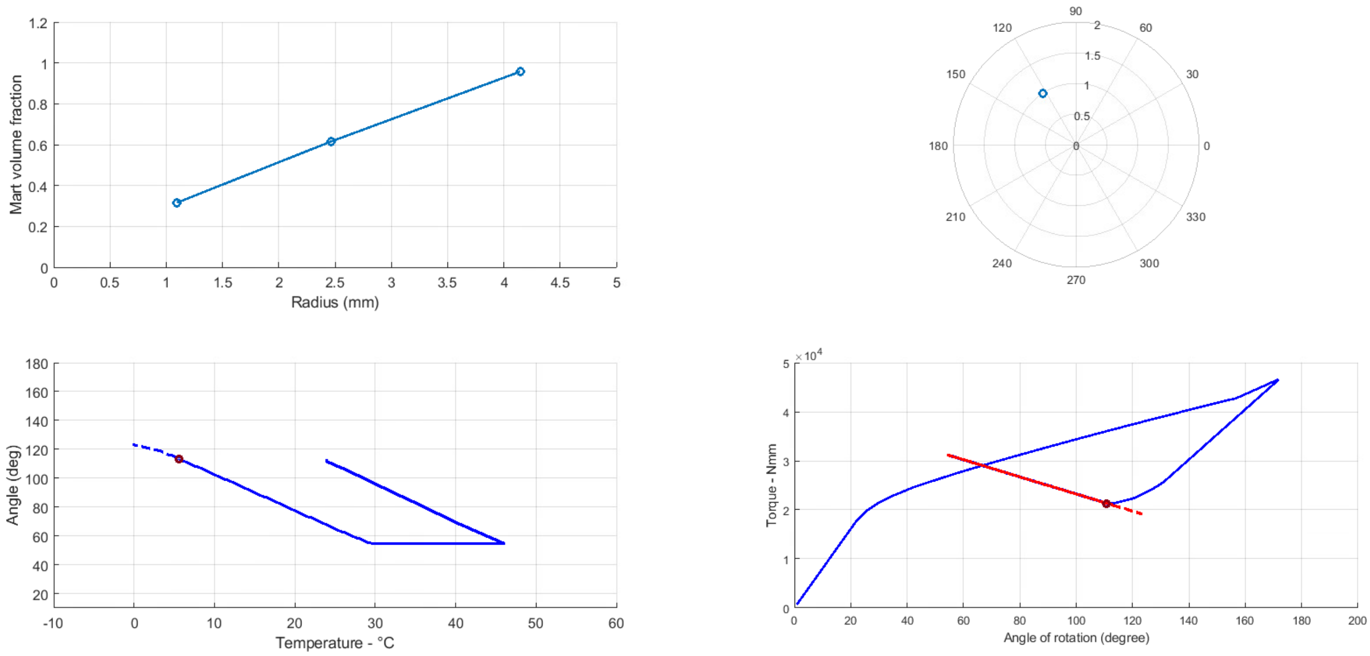

(j)

Figure 4.29: Martensite, displacement, torque and temperature evolution during actuation - Variable load case

4.5.3 Actuator with clutch

In real-world applications, loading and unloading path are often significantly different. For this reason, this section considers a linear loading law and a constant unloading law, as described in the conceptual design chapter. This particular instance illustrates the SMA rod behaviour integrated into an actuator system provided with a clutch. Loading steps from 0 to 3 are the same as mentioned above. At the end of the forward transformation ($M \rightarrow A$) the CBUSH element is disengaged from the SMA, and a constant $21Nm$ torque is applied. Subsequently, the rod is cooled to $0°C$. The load steps sequence is summarised in table 4.7, while figures 4.30 and 4.31 show the overall behaviour of the SMA under the aformentioned conditions.

STEP 0	Set T=24$°C$	
STEP 1	Displacement-driven loading to 172°; $T = 24°C$	Blue segment in figure 4.30
STEP 2	Unloading to $21Nm$; $T = 24°C$	Red segment in figure 4.30
STEP 3	Heating $24°C \rightarrow 46°C$ @ Variable load	Purple segment in figure 4.30
STEP 4	Unloading to $21Nm$; T=46°C	Green segment in figure 4.30
STEP 5	Cooling $46°C \rightarrow 0°C$ @ Constant load	Cyan segment in figure 4.30

Table 4.7: Actuator with clutch - Steps sequence.

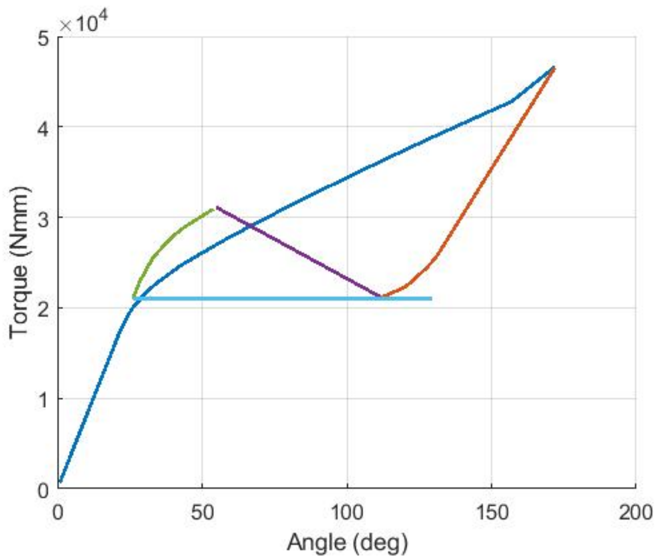

Figure 4.30: Torque-Angle diagrams - Actuator with clutch.

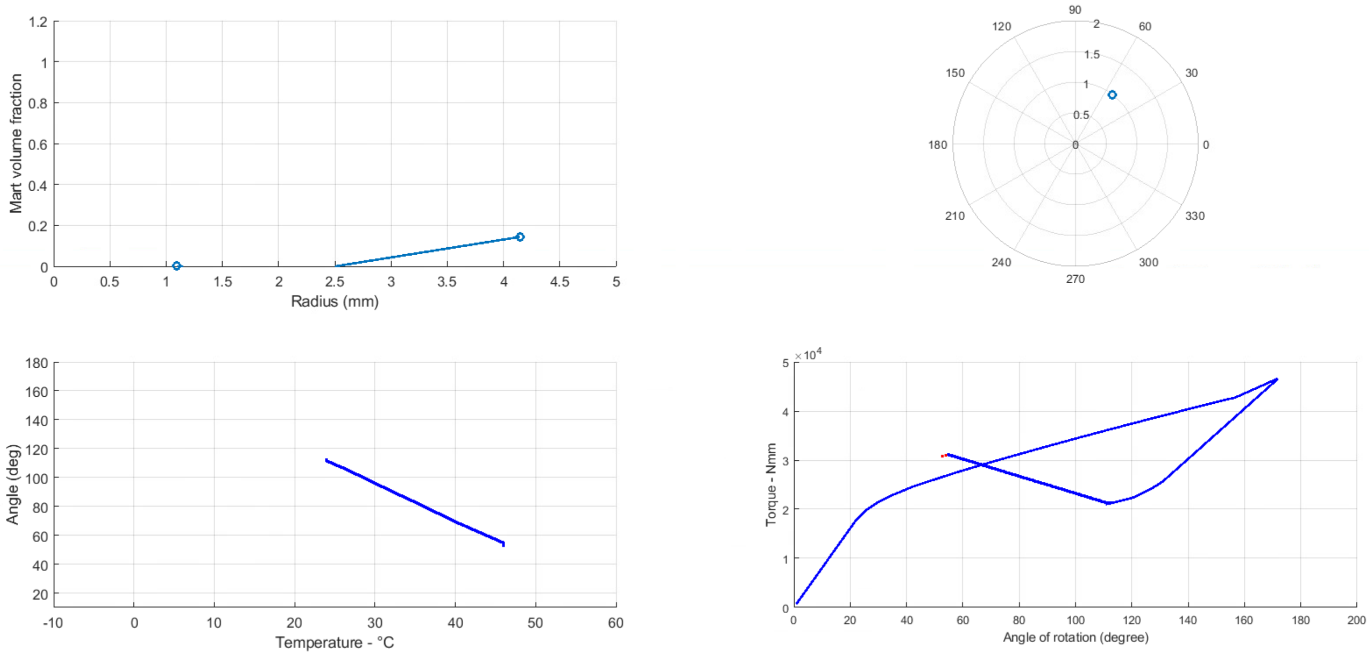

(a)

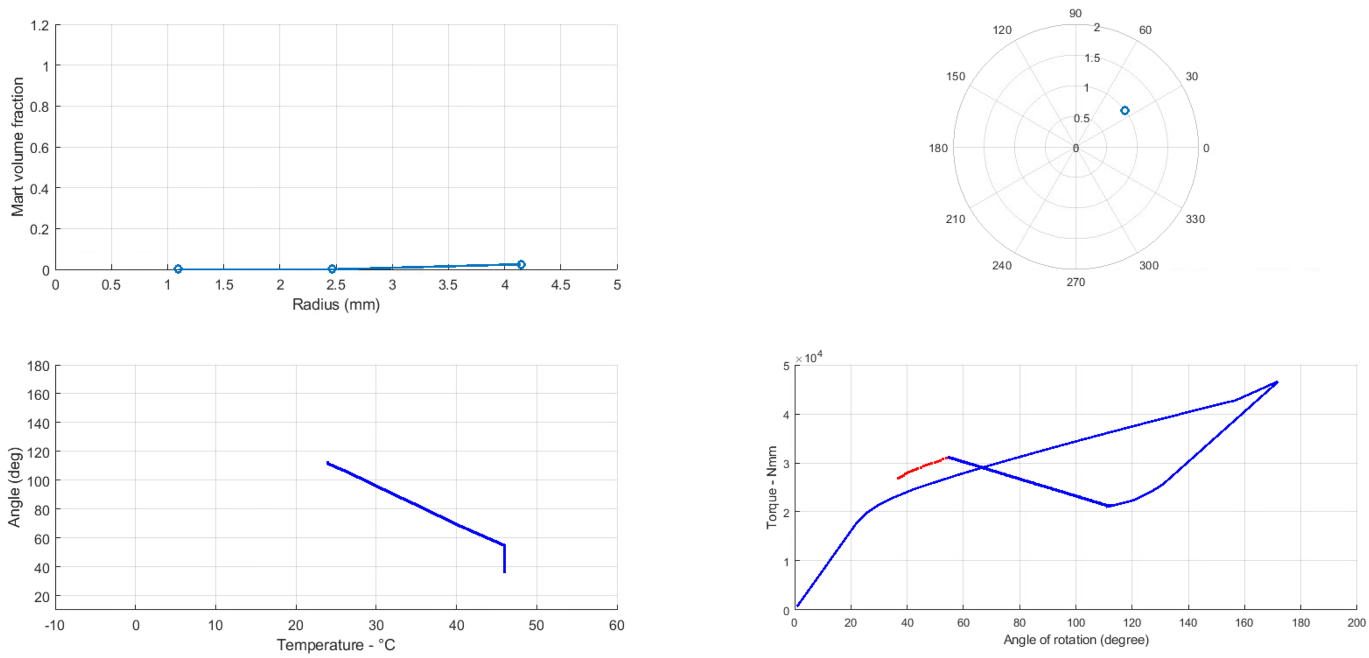

(b)

Figure 4.31: Martensite, displacement, torque and temperature evolution during actuation - Actuator with clutch.

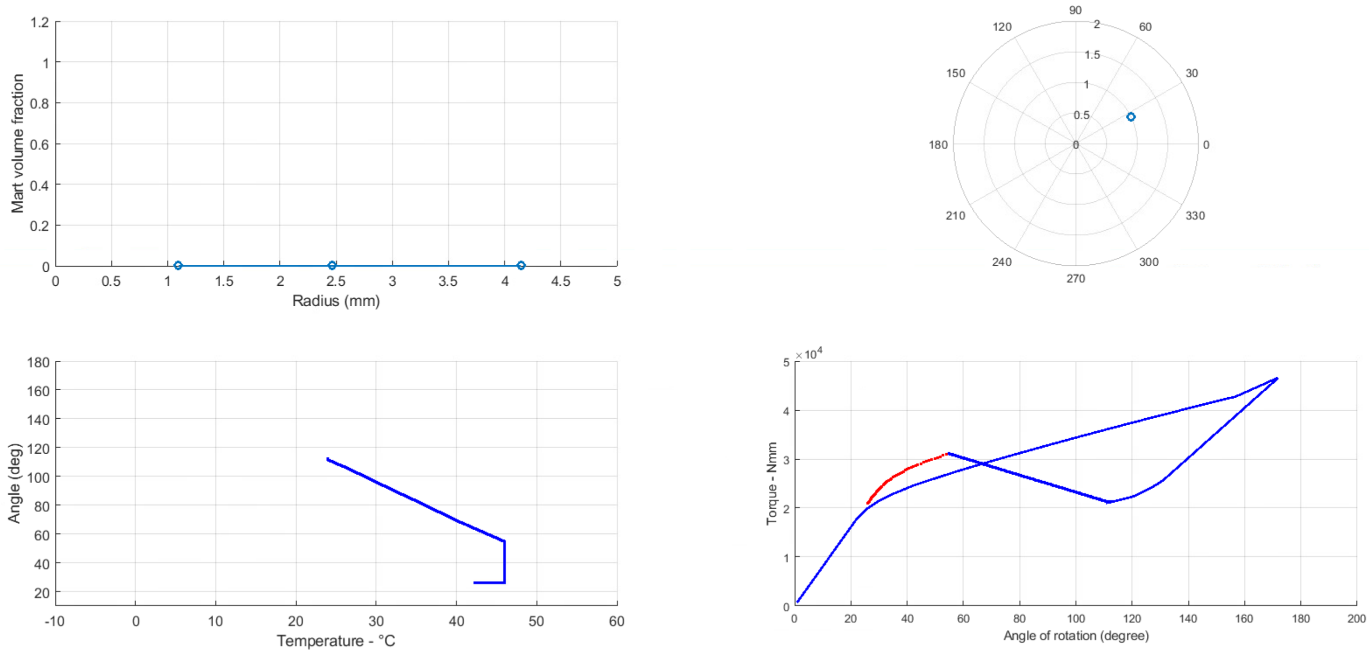

(c)

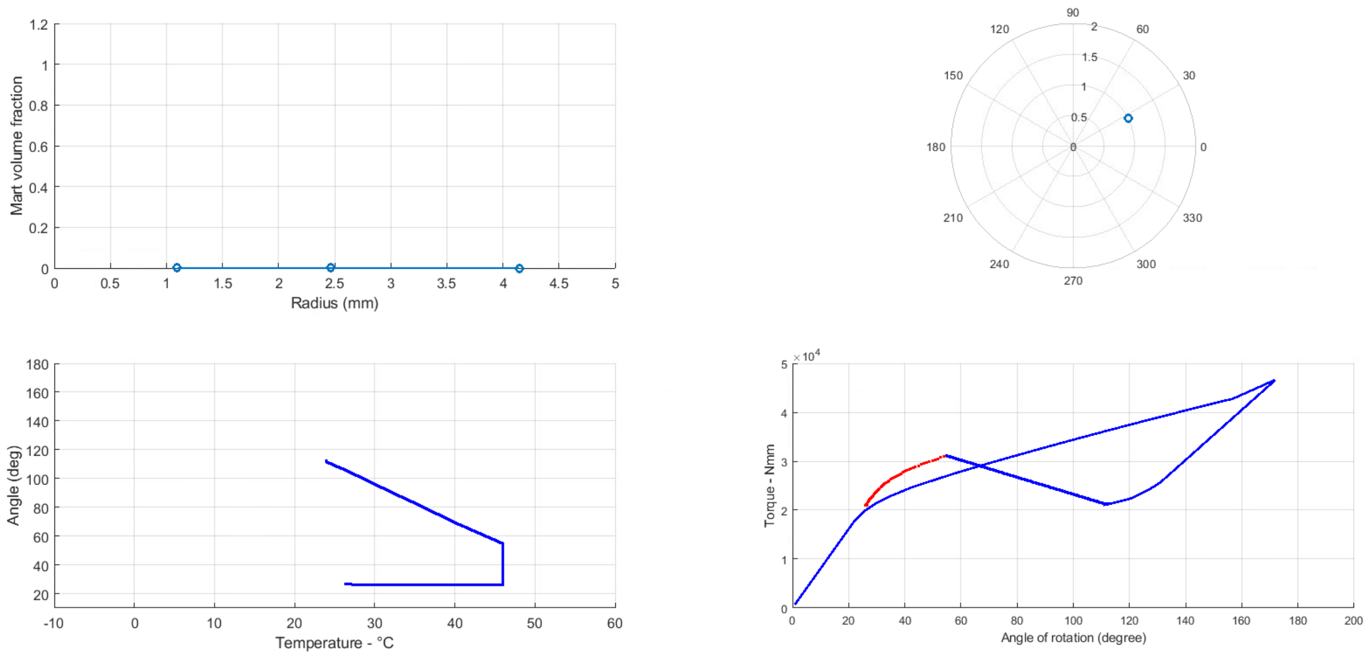

(d)

Figure 4.31: Martensite, displacement, torque and temperature evolution during actuation - Actuator with clutch.

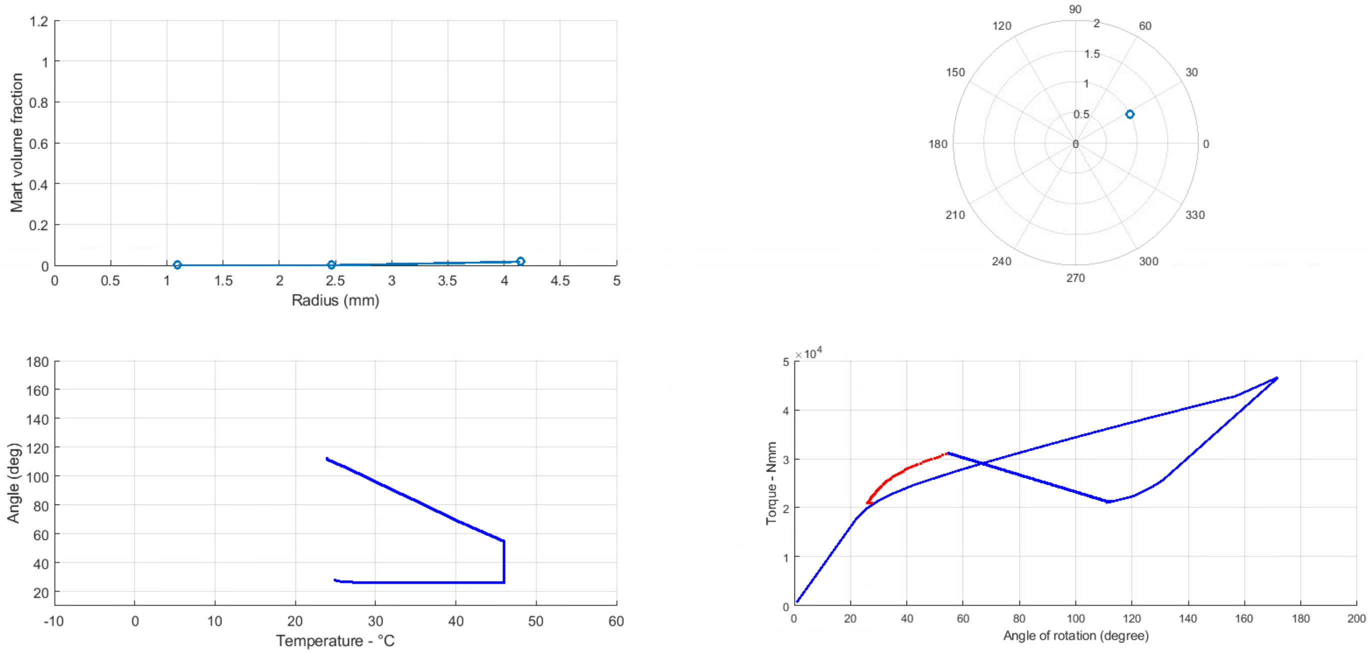

(e)

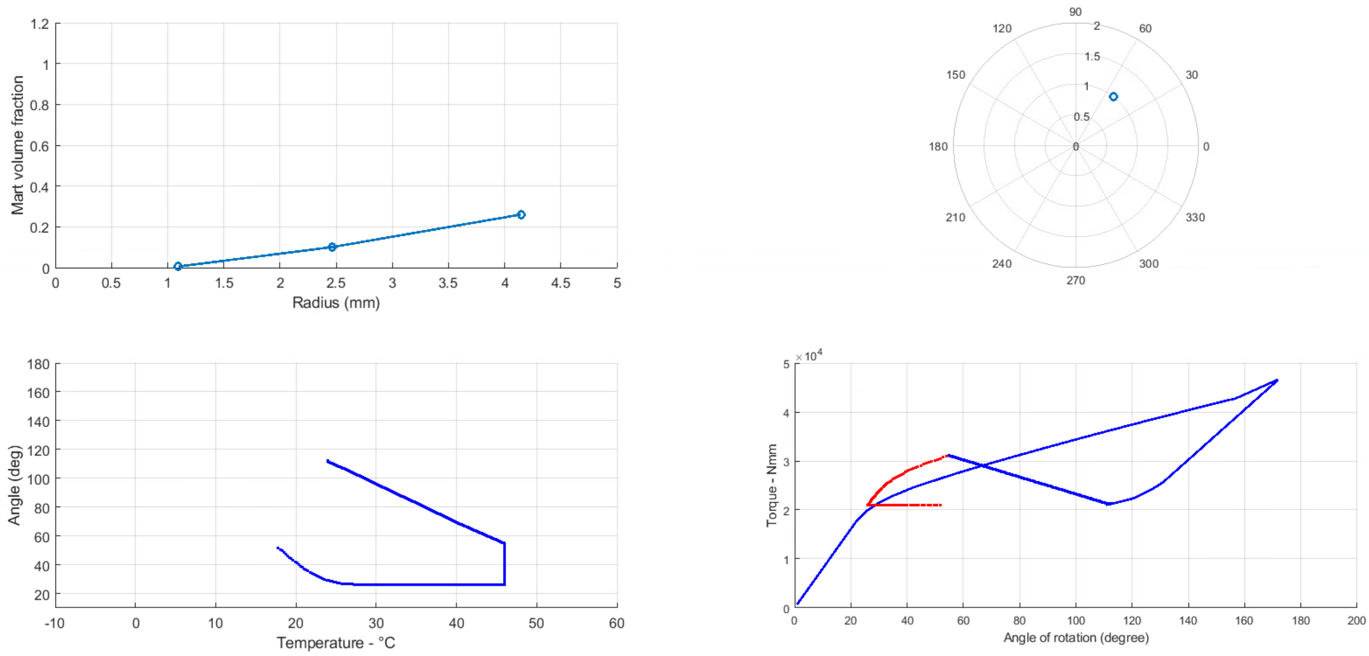

(f)

Figure 4.31: Martensite, displacement, torque and temperature evolution during actuation - Actuator with clutch.

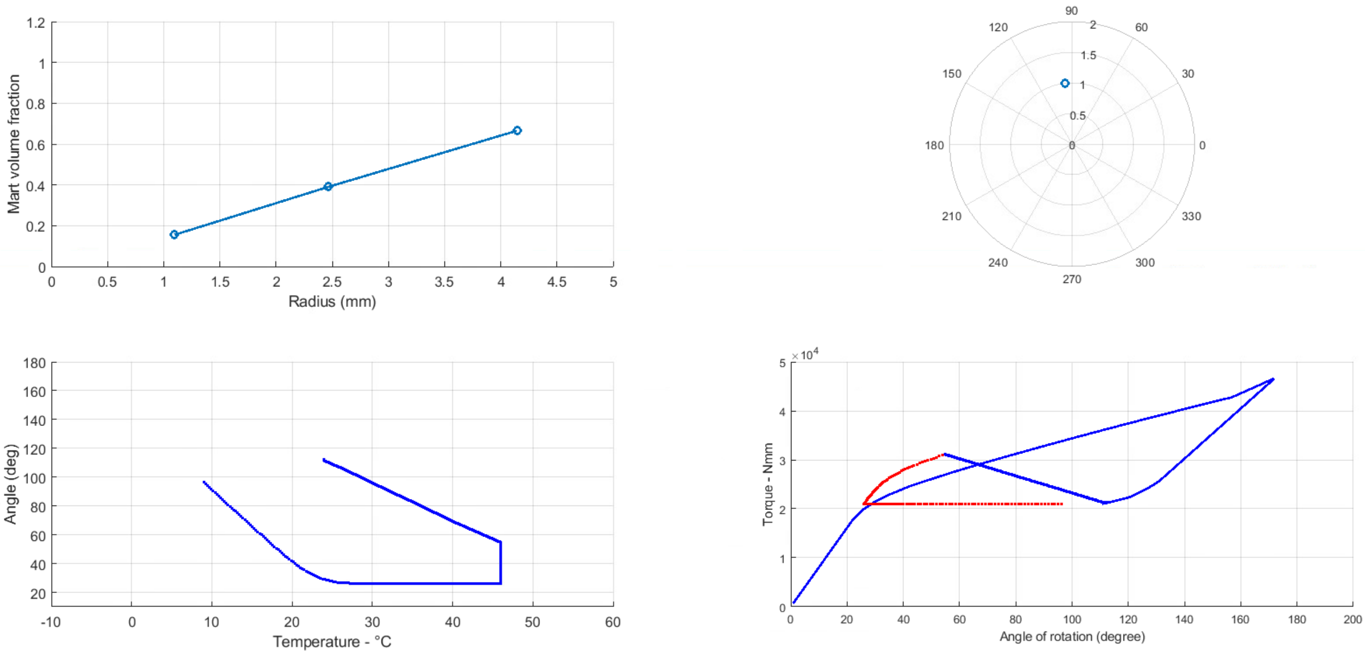

(g)

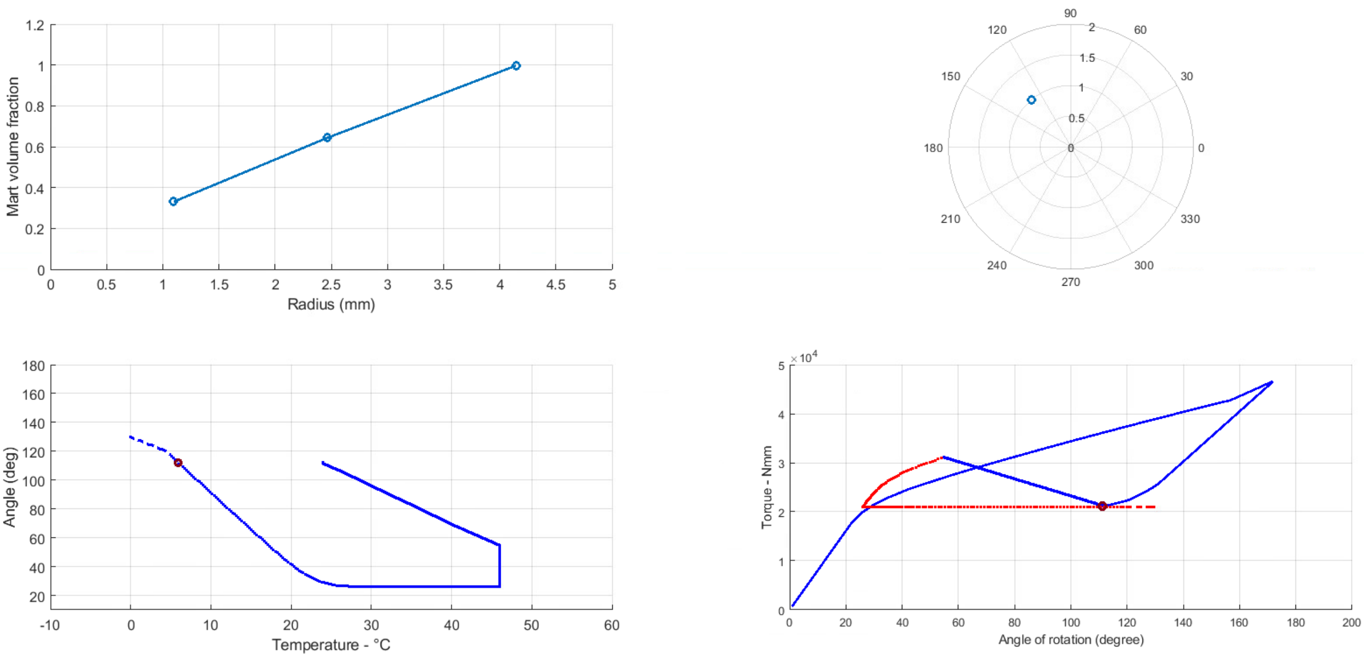

(h)

Figure 4.31: Martensite, displacement, torque and temperature evolution during actuation - Actuator with clutch.

4.5.4 Actuator without clutch

The last scenario investigated in this work concerns an actuator system without the clutch. This means that at the end of the forward actuation, the rod is free to return backward (increasing its deformation toward the martensite phase), but cannot move further in the $M \rightarrow A$ transformation direction because of the spline coupling. Note that forward rotations are retained by the locking mechanism acting on the driven shaft at this point. This particular loading condition requires a one-way rotational contraint which was implemented using an additional CBUSH element described by a strong non-linear law, properly engaged using a second MPC. Thereby, as the end of the forward actuation is reached, the one-way constraint was introduced beside a $21Nm$ torque. The rod is subsequentially cooled to $0°C$ under these boundary conditions. The load steps sequence is summarised in table 4.8, while figures 4.32 and 4.33 show the overall behaviour of the SMA under the aformentioned conditions.

As expected, lowering the temperature under a partial constrain inhibit the austenite-related shape recovery of the rod; however, martensite still generates. This decreases the effective stiffness of the component and thus reduces the perceived stress. As the rod's resisting torque drops to $21Nm$, the specimen is free to recover its martensitic shape. Interestingly, the martensite generated is the same at the end of the SMA transformations considering the same temperature change but different boundary conditions, representing the actuator with and without the clutch. Another fundamental aspect to consider is that Auricchio's formulation does not admit twinned martensite. This means that no arguments can be made on forming multiple-variant martensite in high temperature and stress conditions from this kind of analysis.

STEP 0	Set T=24$°C$	
STEP 1	Displacement-driven loading to 172°; $T = 24°C$	Blue segment in figure 4.32
STEP 2	Unloading to $21Nm$; $T = 24°C$	Red segment in figure 4.32
STEP 3	Heating $24°C \rightarrow 46°C$ @ Variable load	Purple segment in figure 4.32
STEP 4	Constant $21Nm$ torque; $T = 46°C$; One-way constraint	
STEP 5	Cooling $46°C \rightarrow 0°C$ @ Constant load with one-way constraint	Cyan segment in figure 4.32

Table 4.8: Actuator without clutch - Steps sequence.

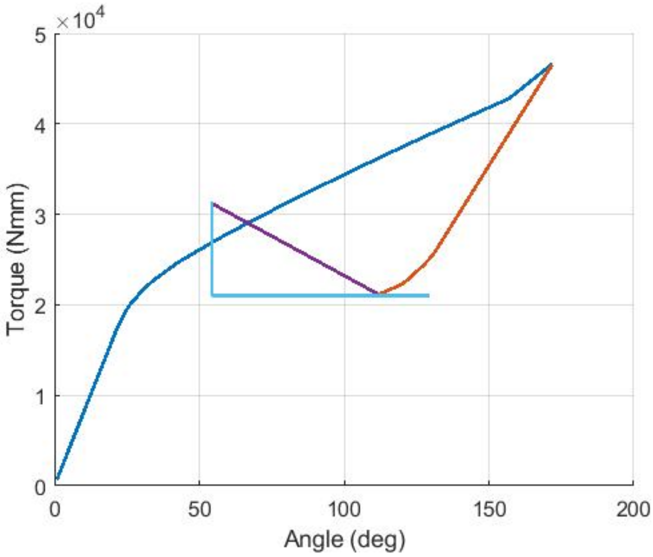

Figure 4.32: Torque-Angle diagrams - Actuator without clutch.

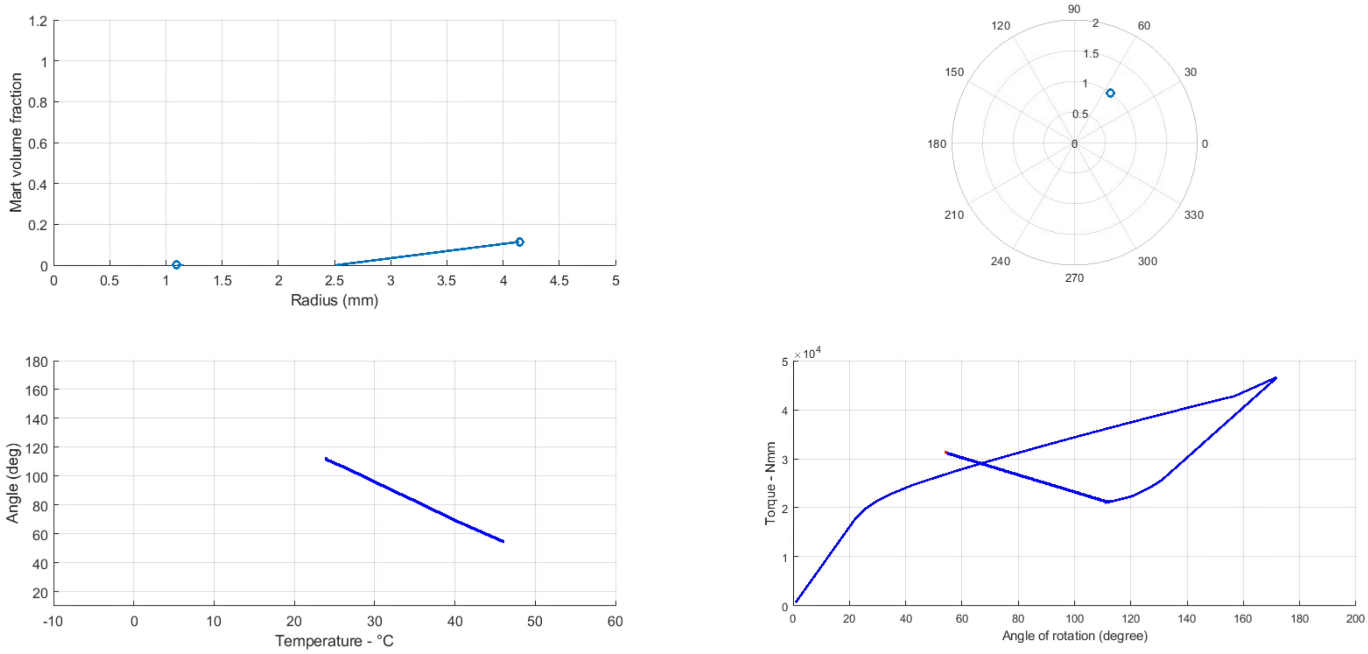

(a)

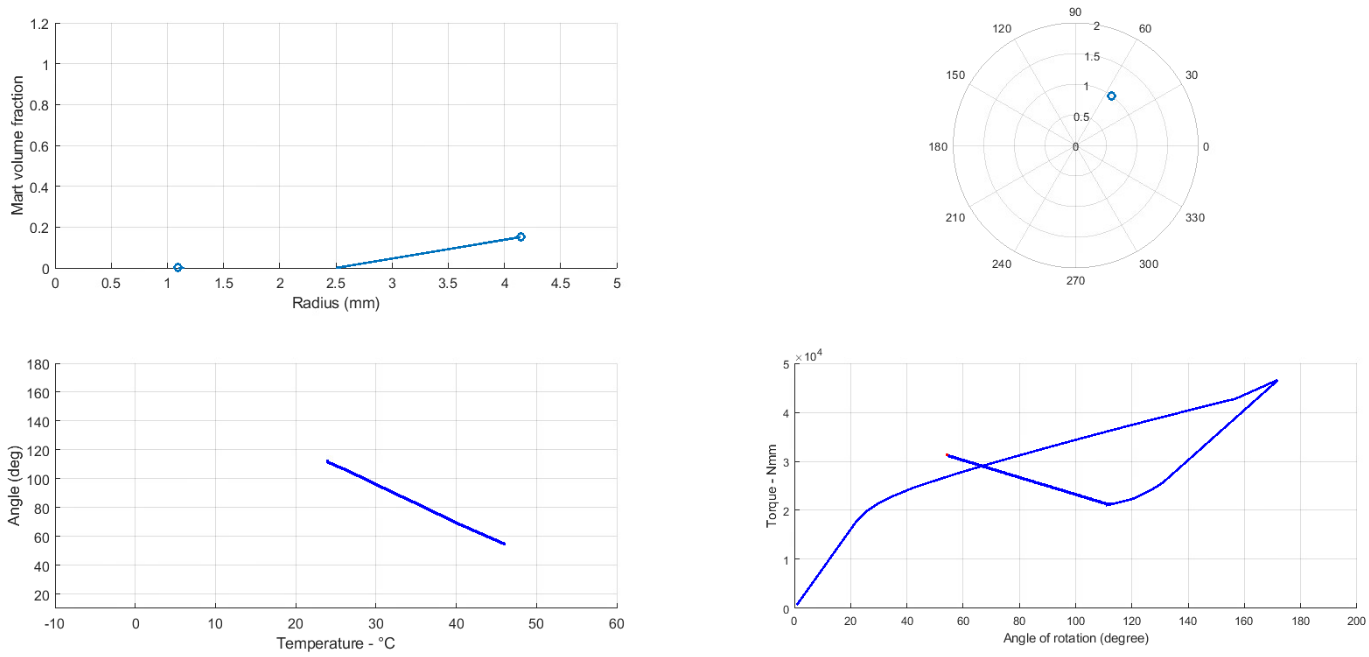

(b)

Figure 4.33: Martensite, displacement, torque and temperature evolution during actuation - Actuator without clutch.

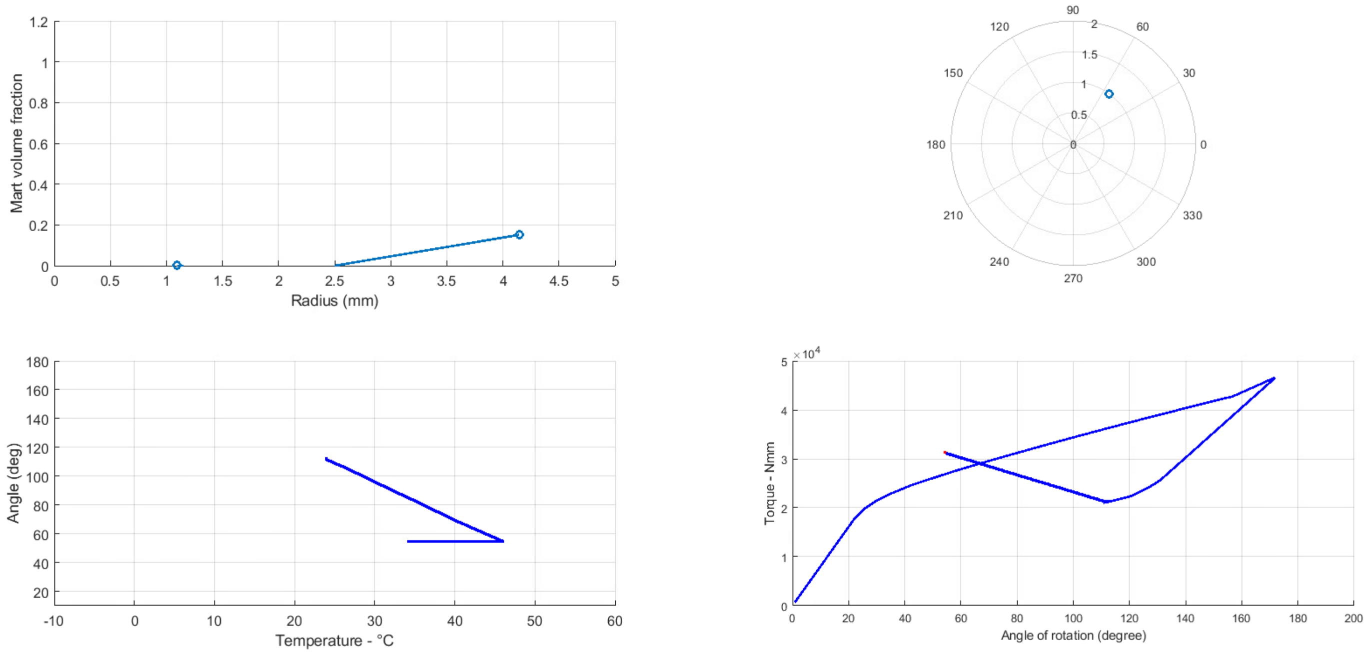

(c)

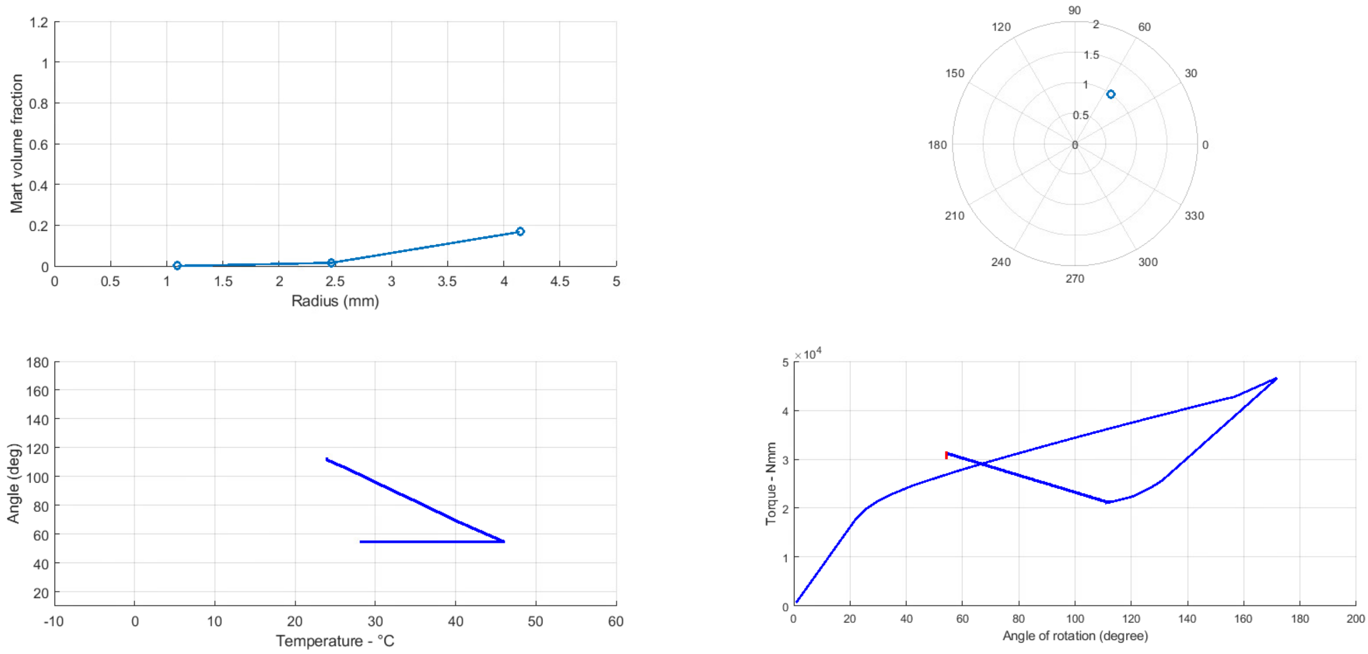

(d)

Figure 4.33: Martensite, displacement, torque and temperature evolution during actuation - Actuator without clutch.

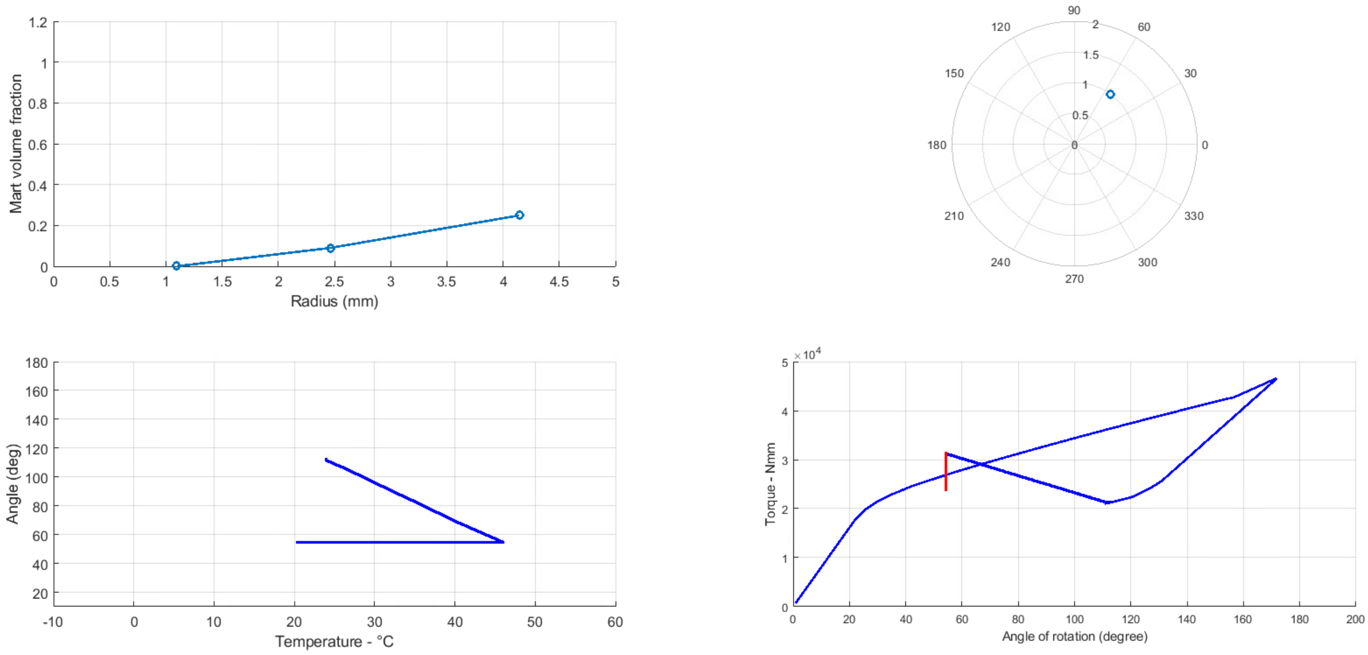

(e)

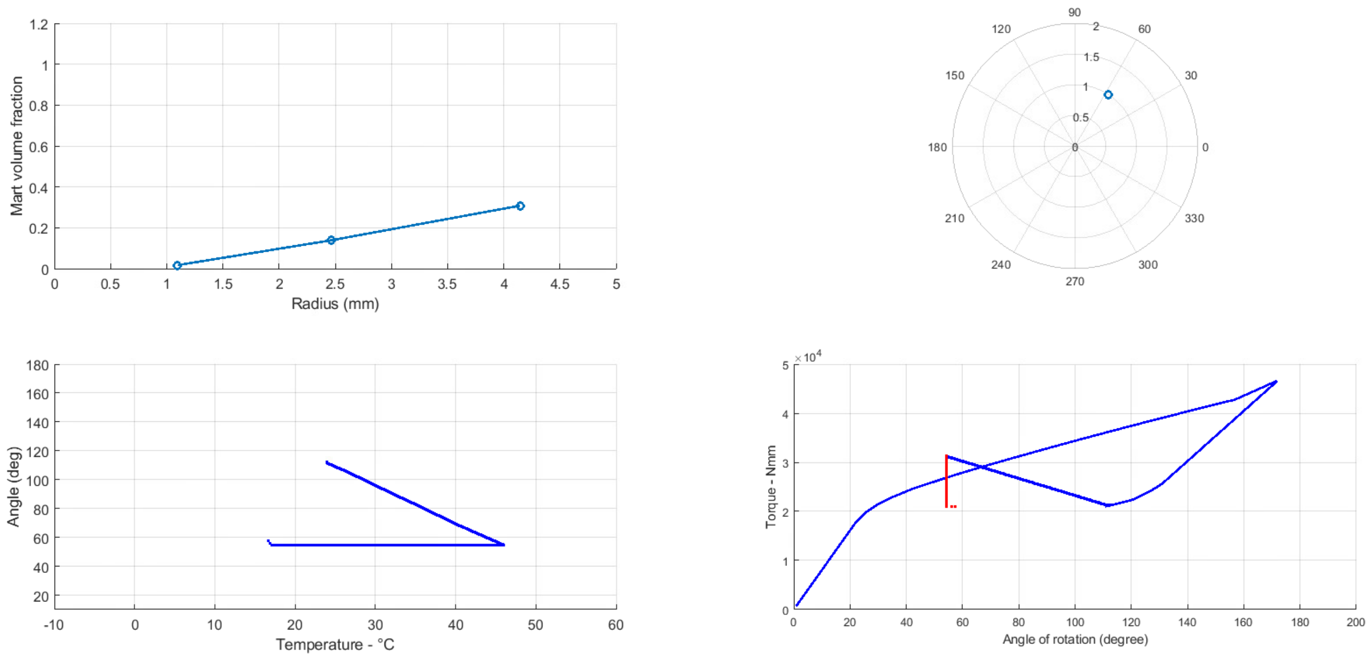

(f)

Figure 4.33: Martensite, displacement, torque and temperature evolution during actuation - Actuator without clutch.

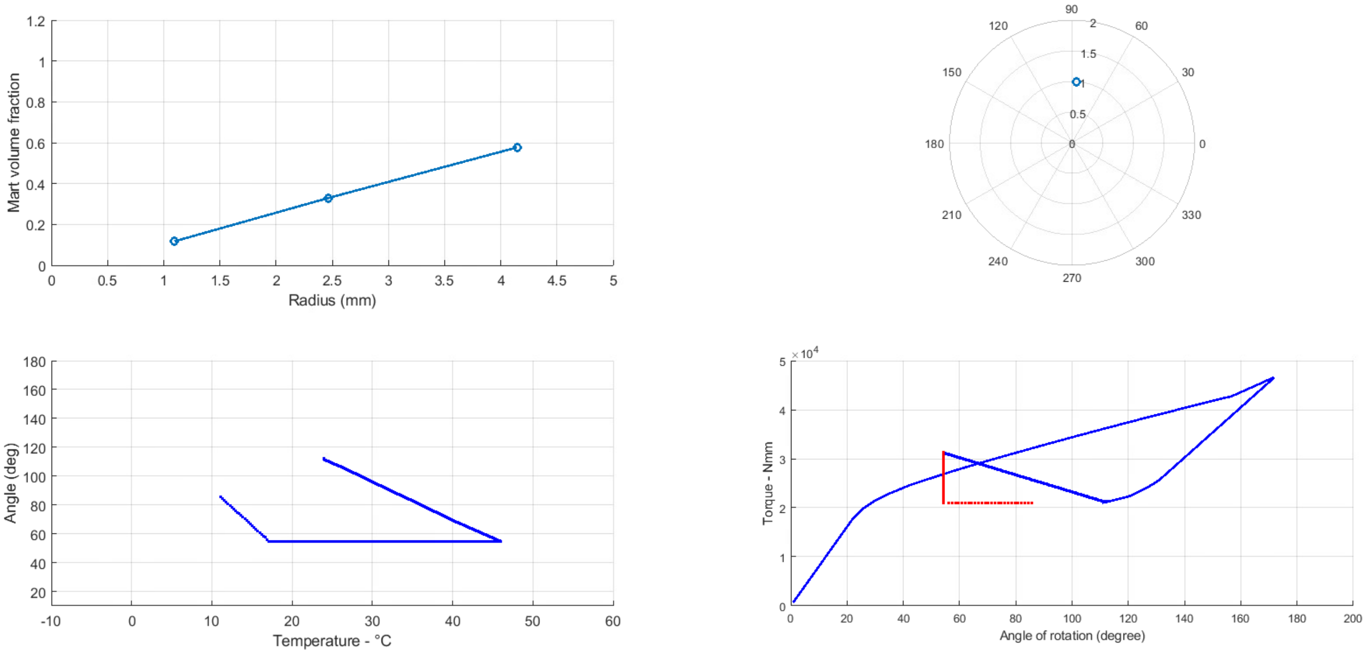

(g)

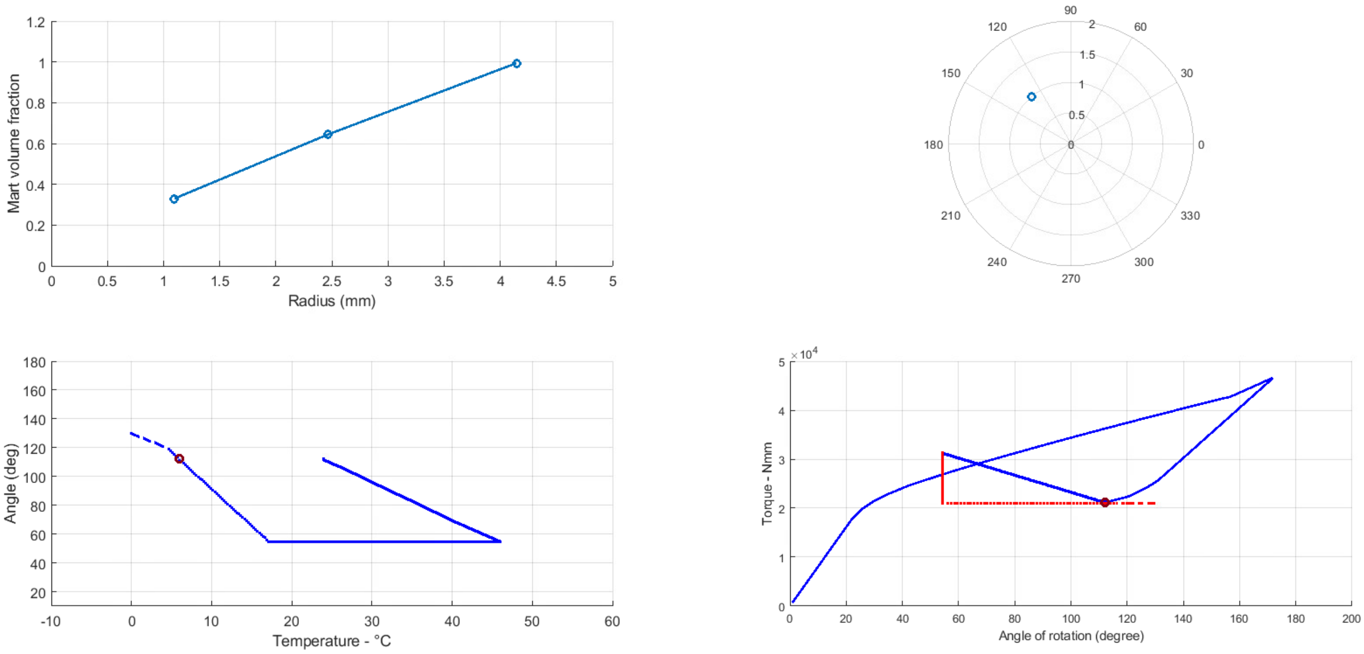

(h)

Figure 4.33: Martensite, displacement, torque and temperature evolution during actuation - Actuator without clutch.

Chapter 5

Observations on SMA rods behaviour under torque loads

This chapter aims to deepen some aspect regarding the SMA rod behaviour under torque loading conditions, discussing inner stress fields, martensite development and multiple cycling effects. All the results are obtained using FEM and material properties as described in the previous section. However, in order to achieve more accurate results, the rod was discretised by a finer mesh. Indeed, five elements along the radius were used, leading to a model with 31000 elements and 124866 nodes. Consequently, the computational cost significantly increased. Figure 5.1 shows the FEM model considered in this section. Again, the mesh includes CPENTA-15 and CHEXA-20 elements.

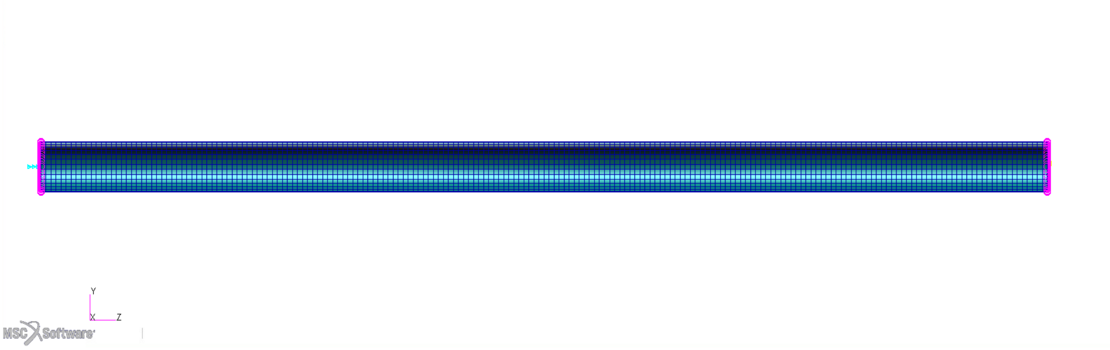

(a)

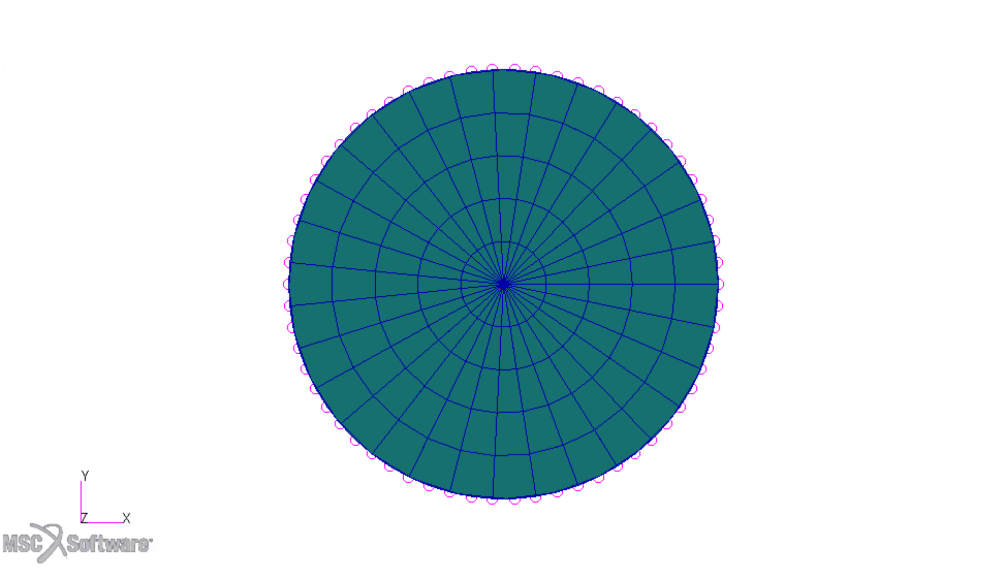

(b)

Figure 5.1: SMA rod's refined mesh.

5.0.1 Torque loading cycle

In the load-driven cycle, constraint and loading conditions are the same as the model considered to validate the model. This means that one end of the rod was constrained, while the other was subjected to an imposed angular displacement, in this case of 180° at $24°C$. Also, RBE2 elements were adopted in order to simplify the output data and the boundary conditions handling. Subsequently, the specimen is set free to recover its austenite shape under zero load condition.

Martensite volume fraction was considered in the element centroid to avoid physically senseless results, as explained in the previous chapter. Also, the stress was considered in the same points to match the radial position of the two quantities involved in this discussion. The overall behaviour of the SMA rod under one torque cycle is displayed in figure 5.2.

Furthermore, figures 5.3, 5.4, 5.5 and 5.6 show the stress-strain cycles which inner nodes are subjected. Note that the axial stress component is about 2.5% of Von Mises stress, which seems reasonable for a system integrated SMA rod.

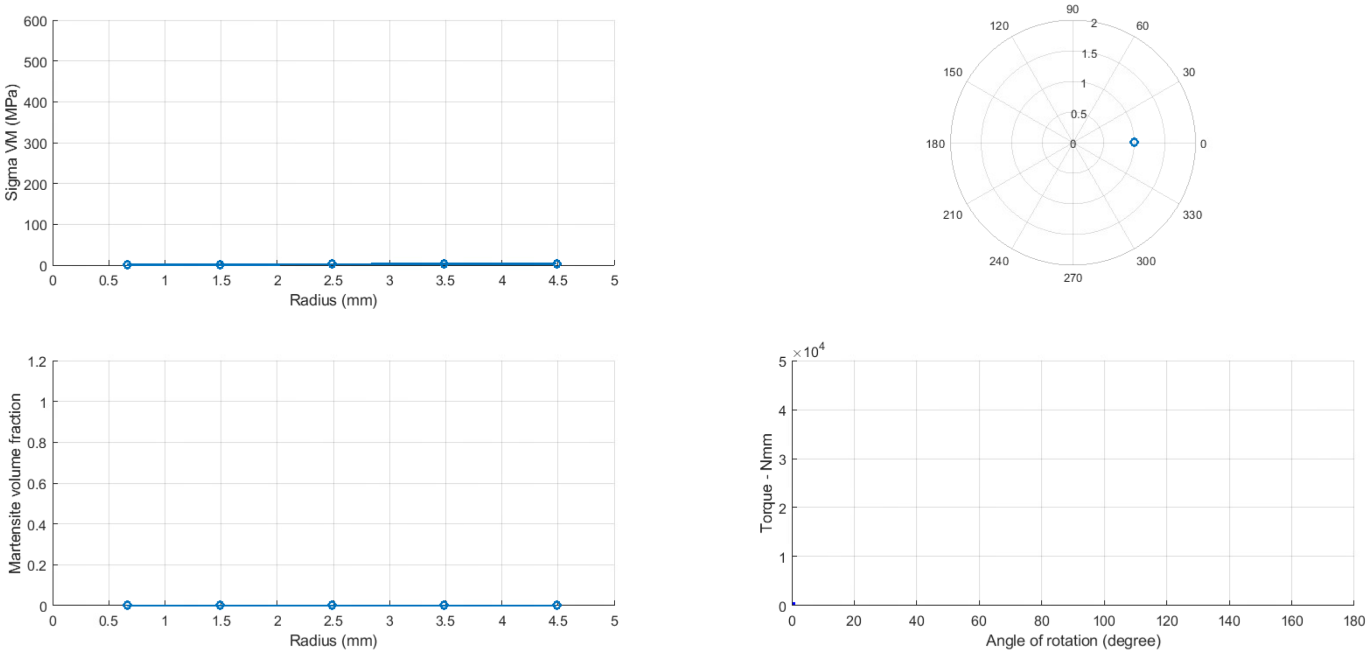

(a)

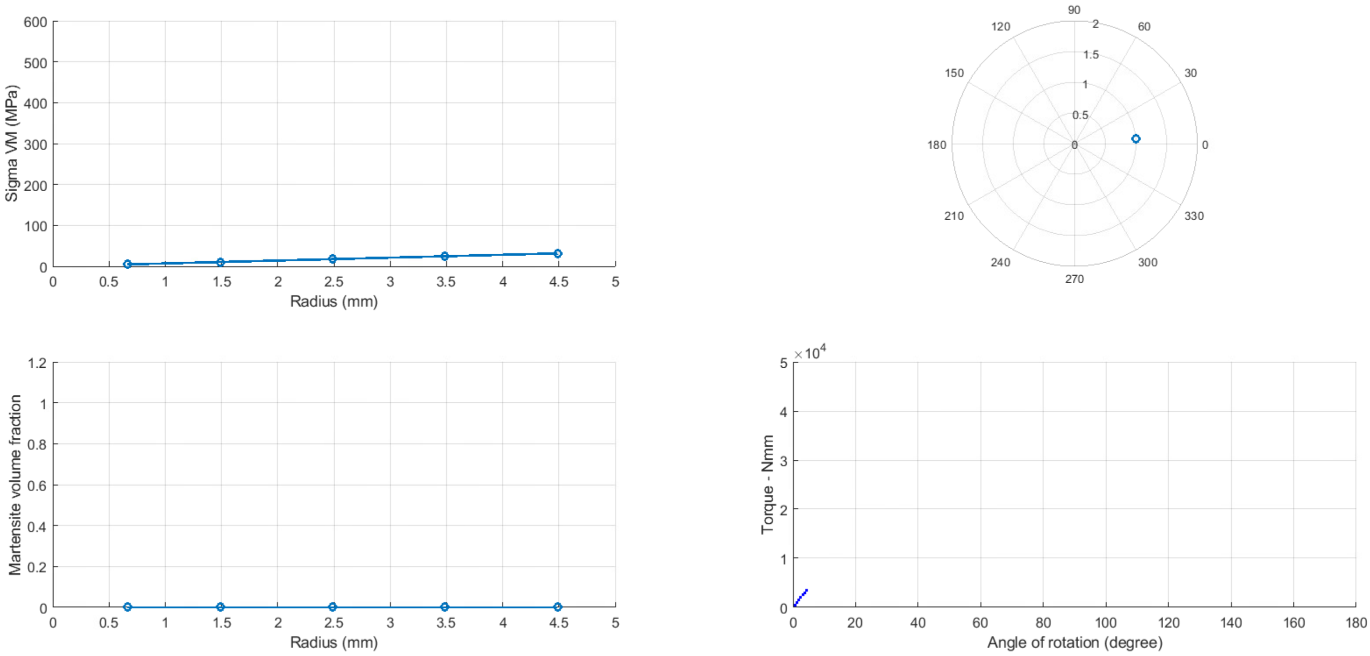

(b)

Figure 5.2: SMA rod behaviour under torque loading cycle @24°C.

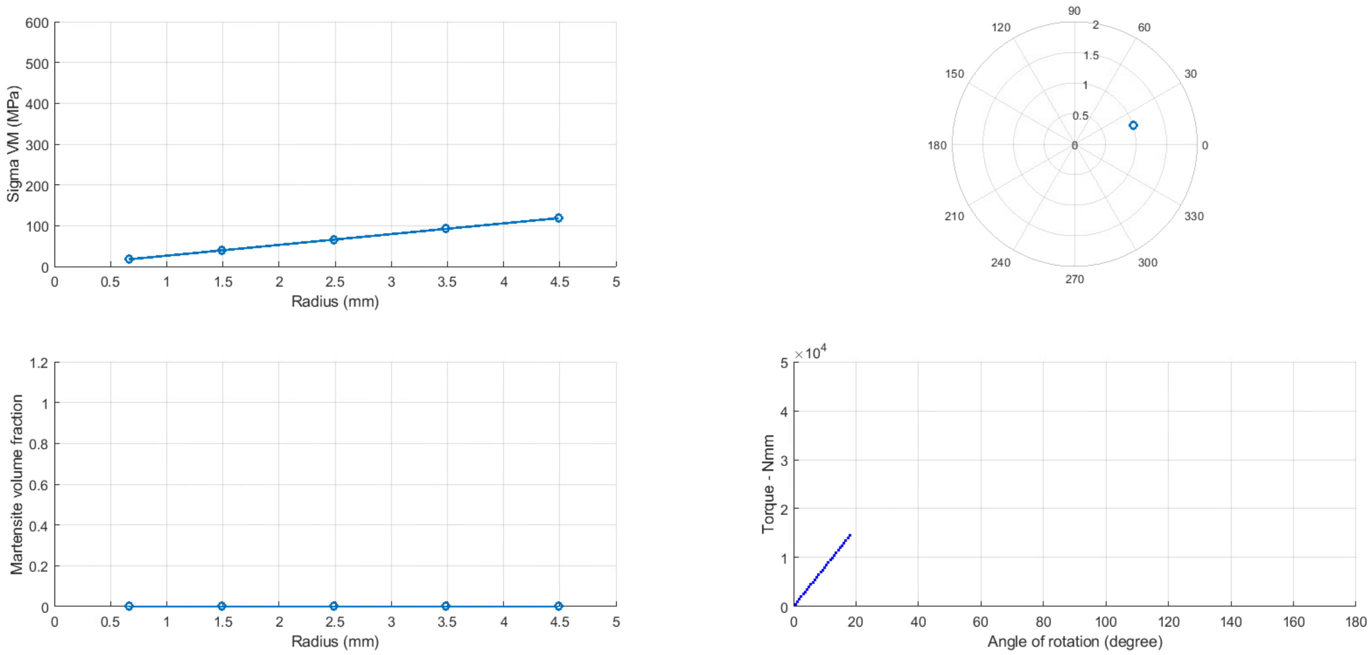

(c)

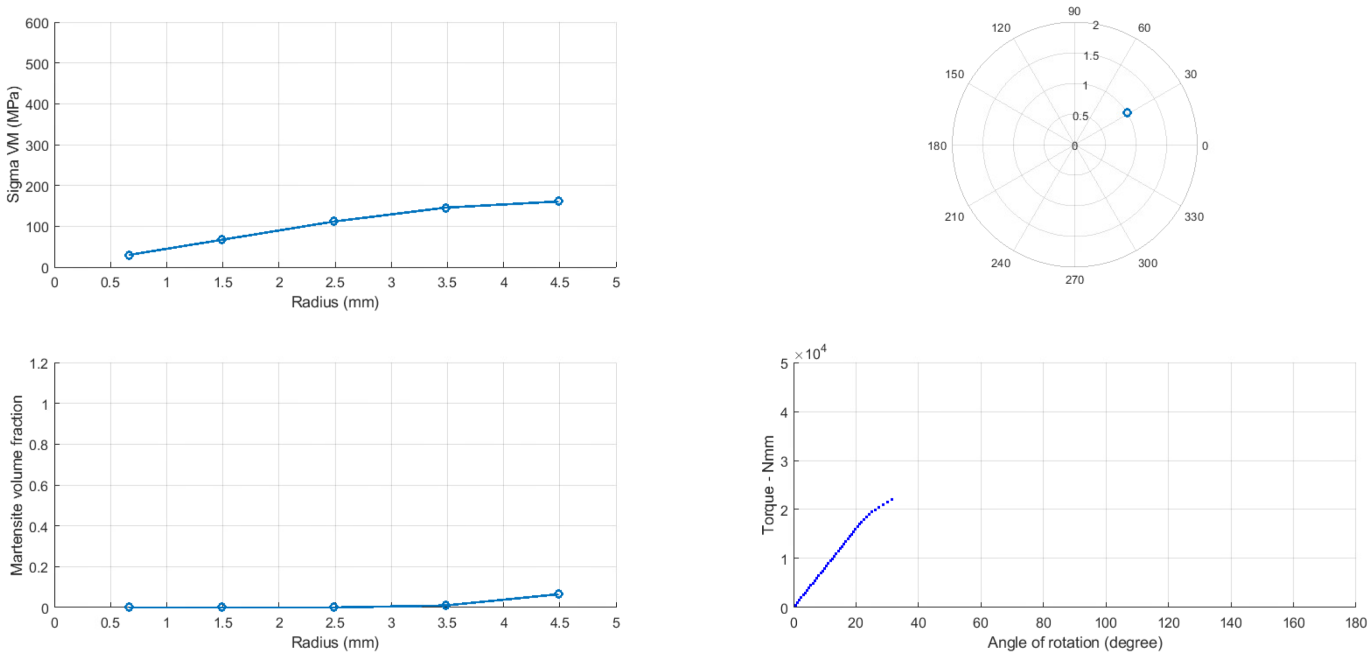

(d)

Figure 5.2: SMA rod behaviour under torque loading cycle @24°C.

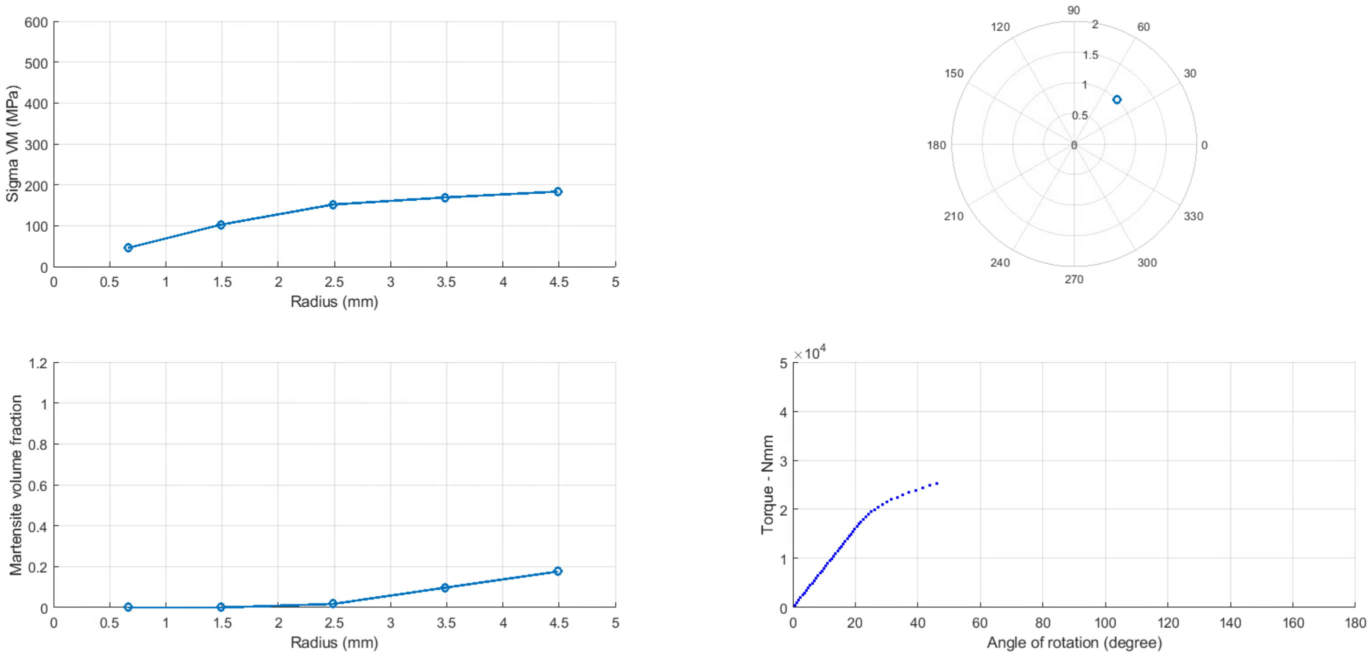

(e)

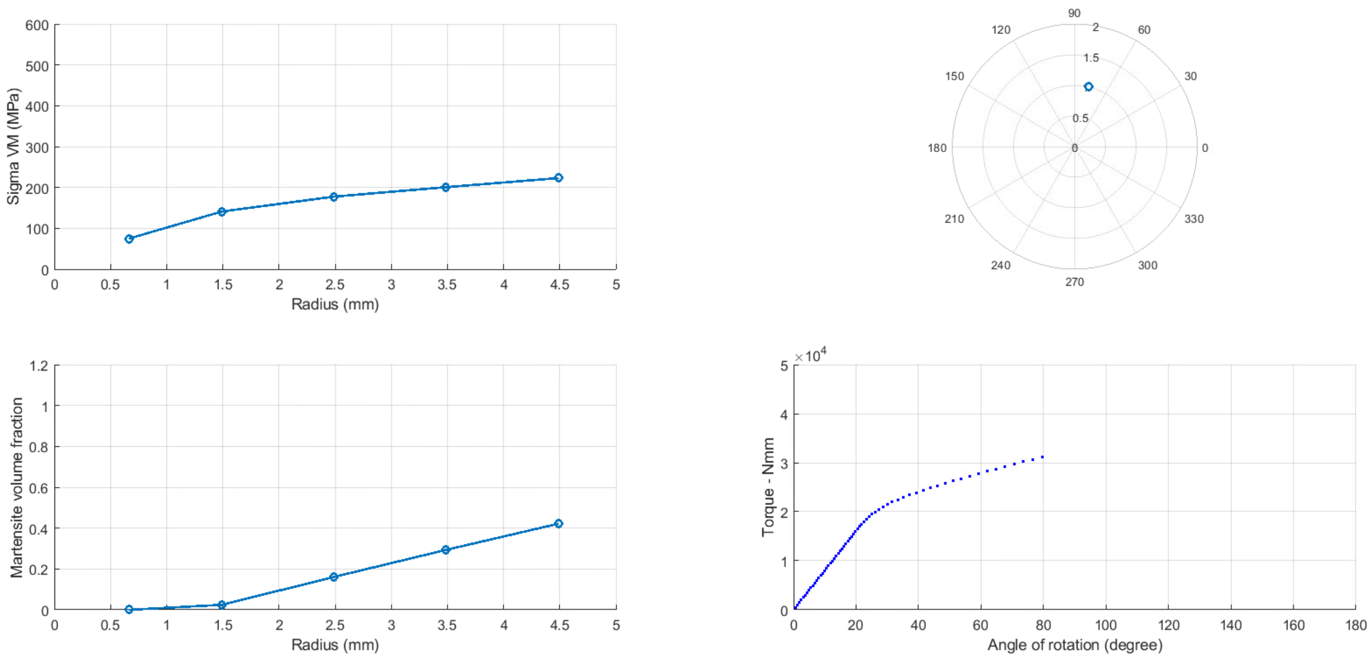

(f)

Figure 5.2: SMA rod behaviour under torque loading cycle @24°C.

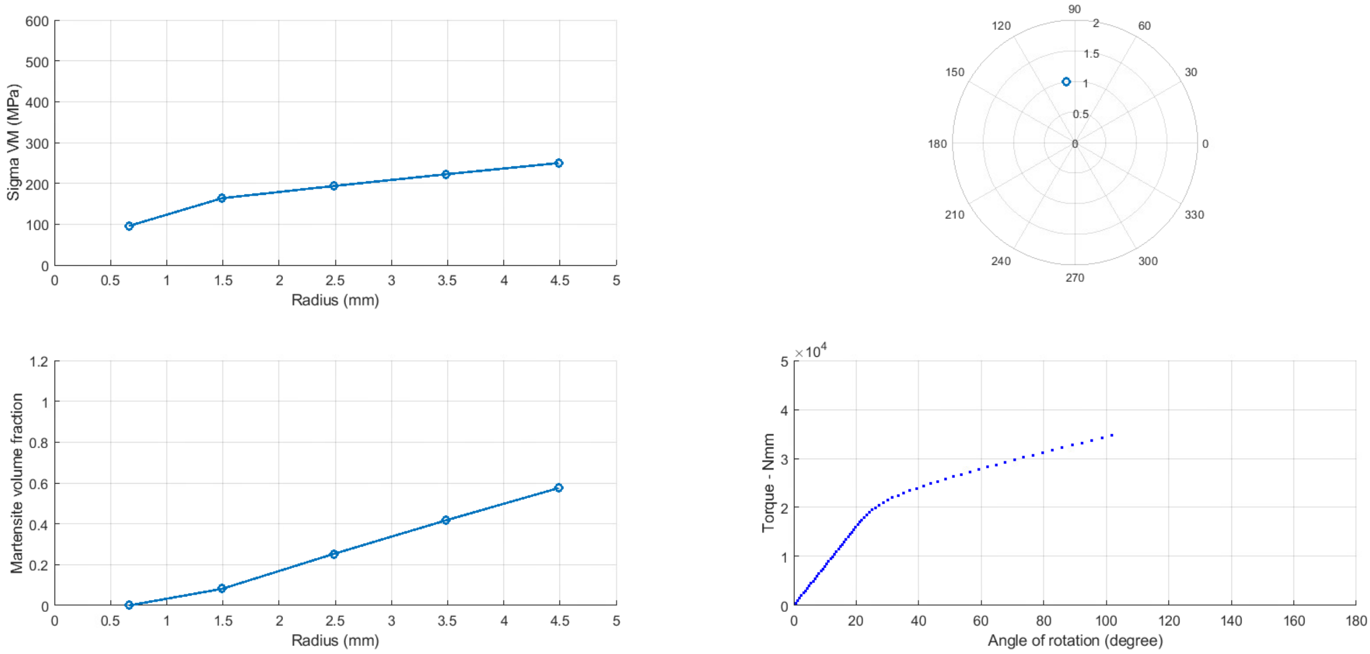

(g)

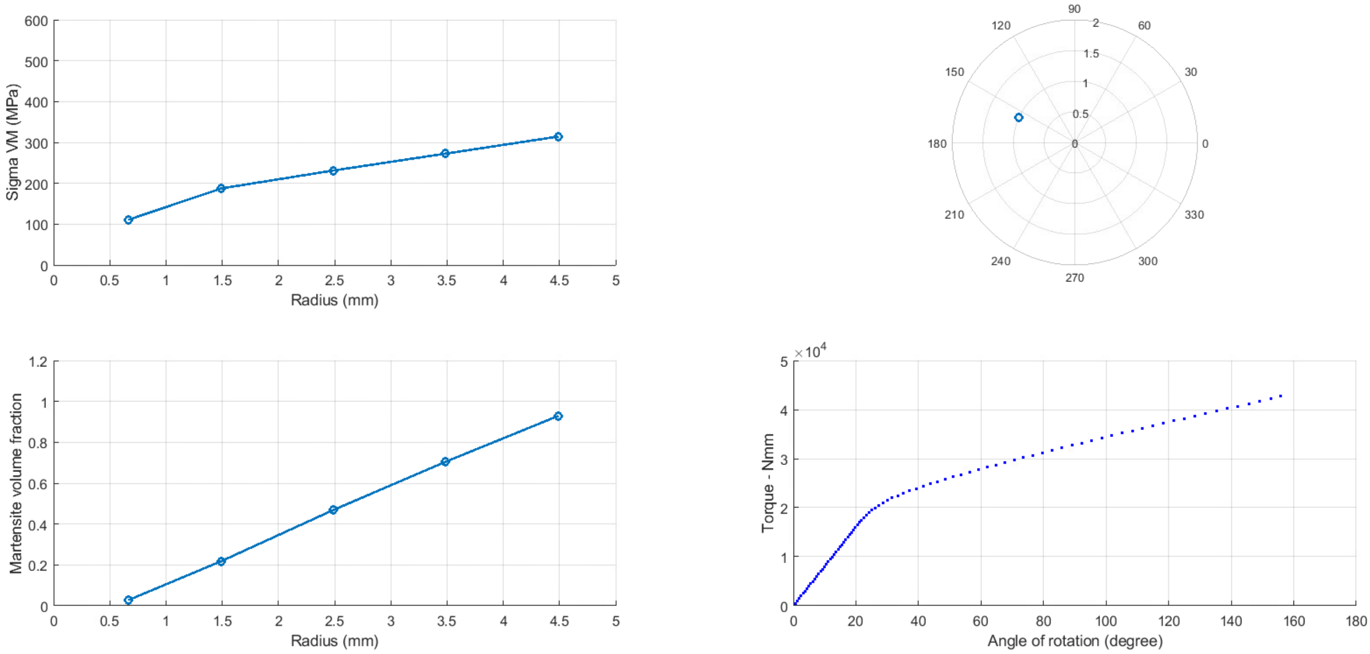

(h)

Figure 5.2: SMA rod behaviour under torque loading cycle @24°C.

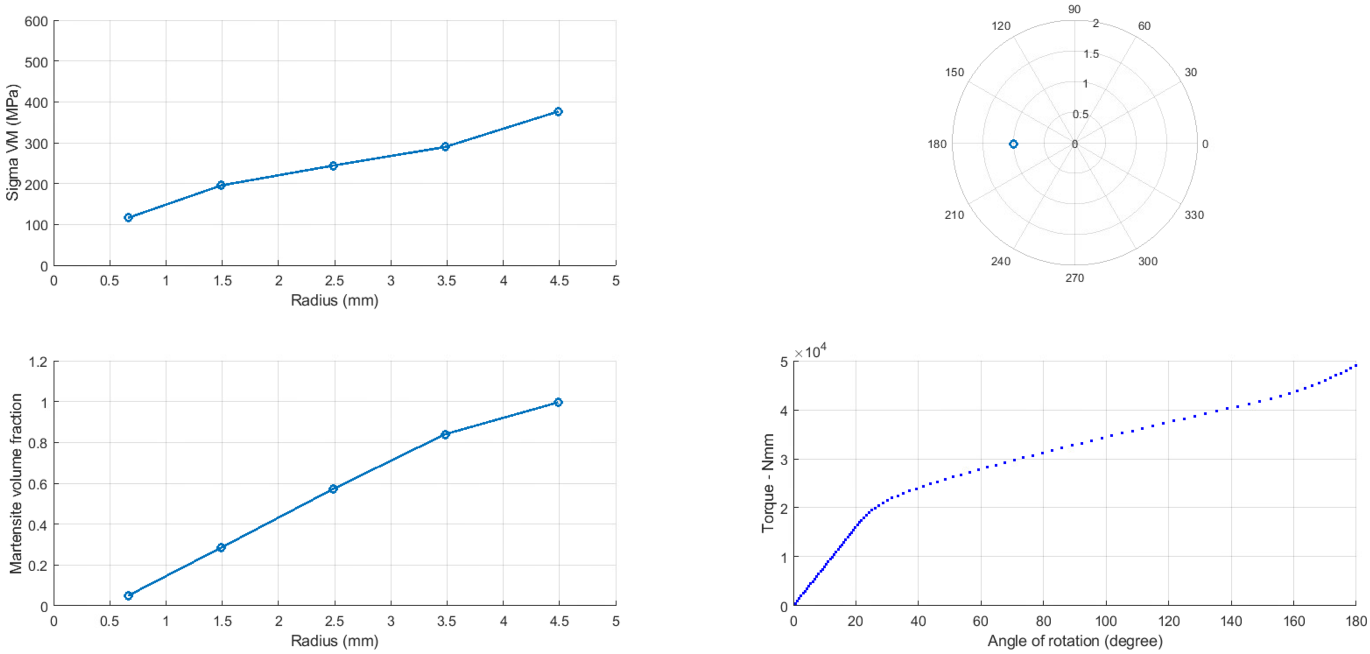

(i)

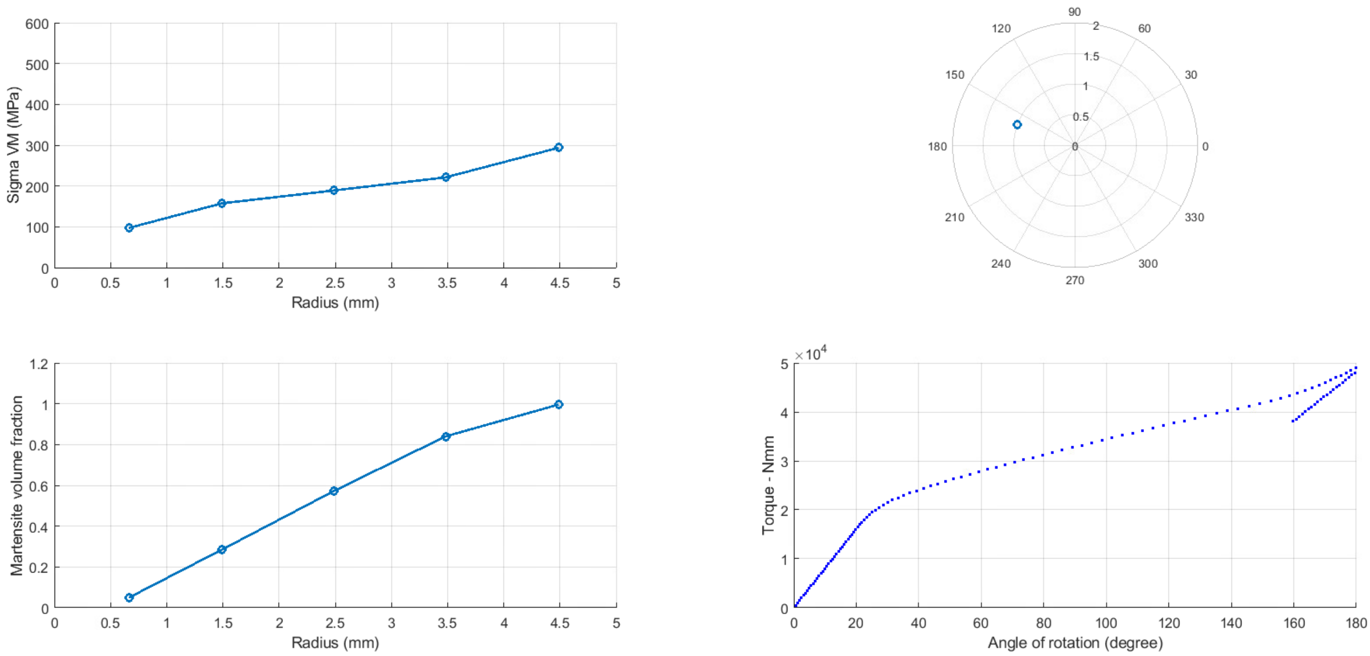

(j)

Figure 5.2: SMA rod behaviour under torque loading cycle @24$^{\circ}C$.

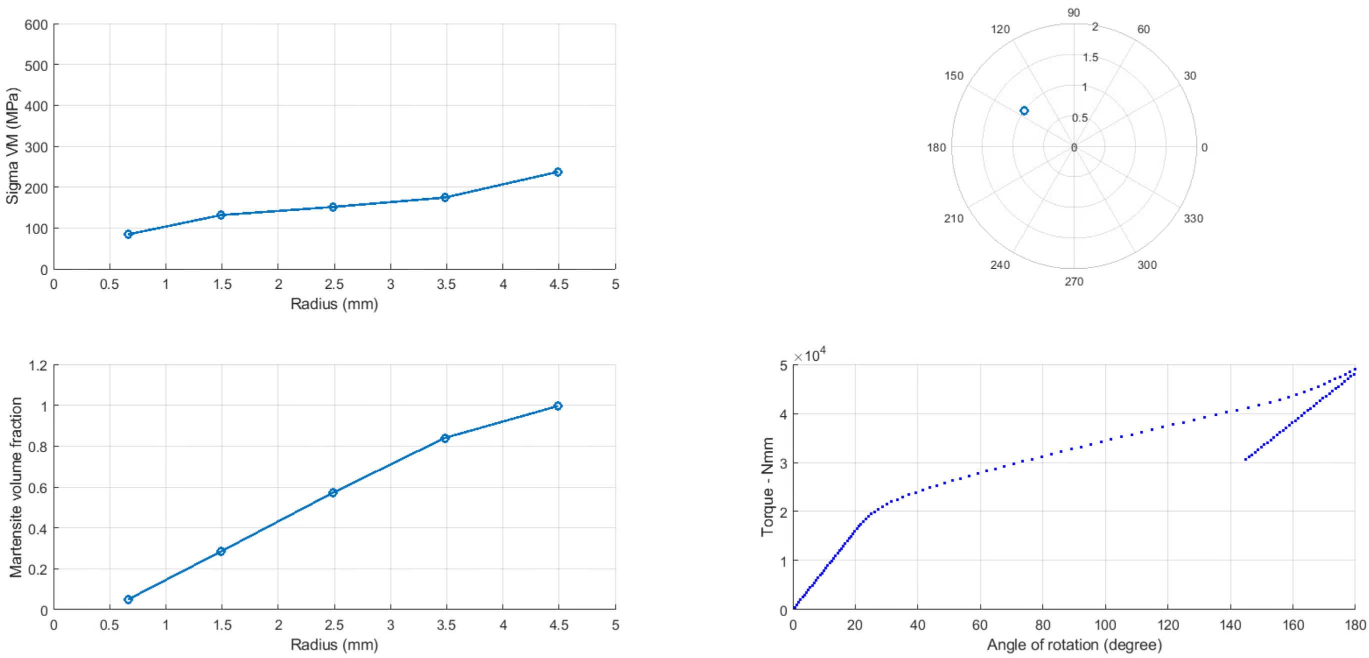

(k)

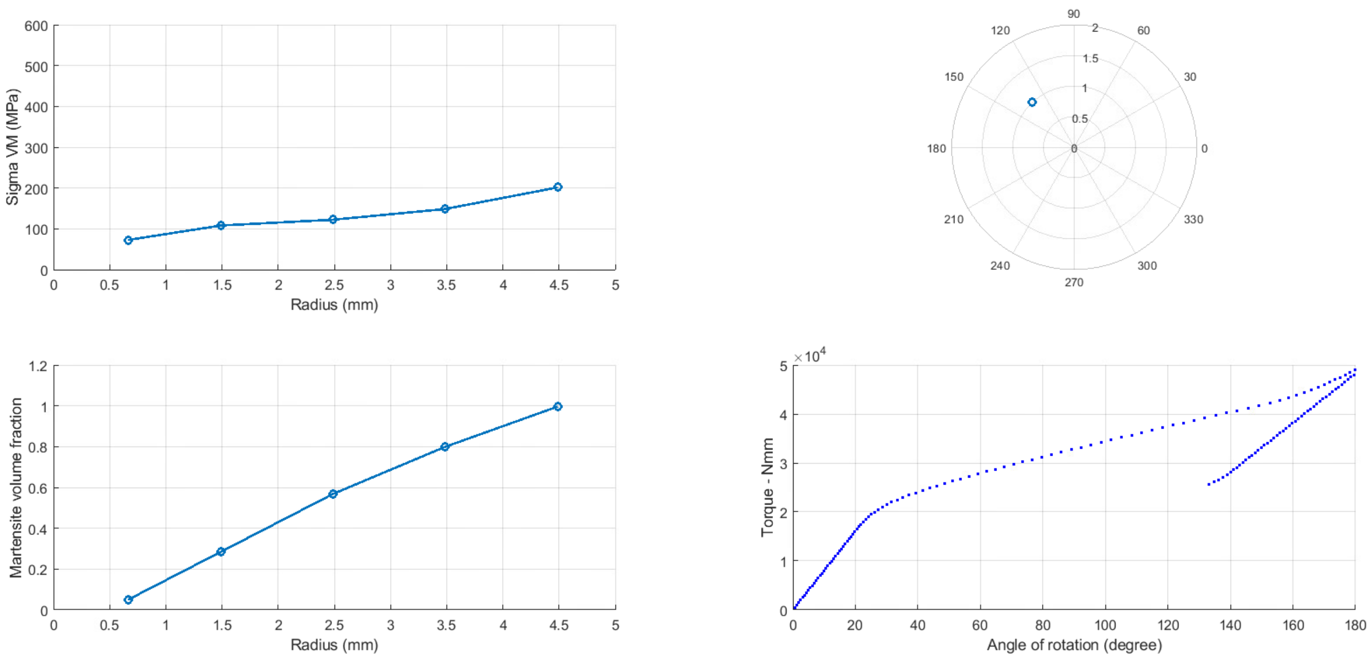

(l)

Figure 5.2: SMA rod behaviour under torque loading cycle @24°C.

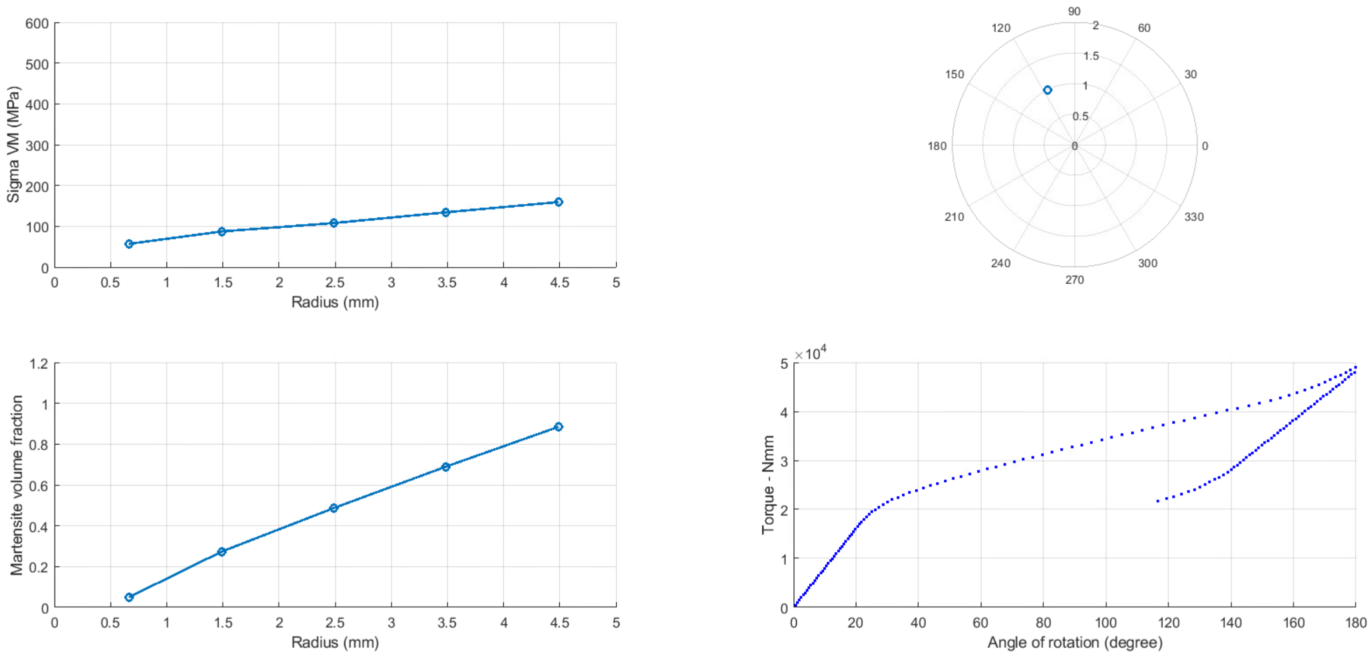

(m)

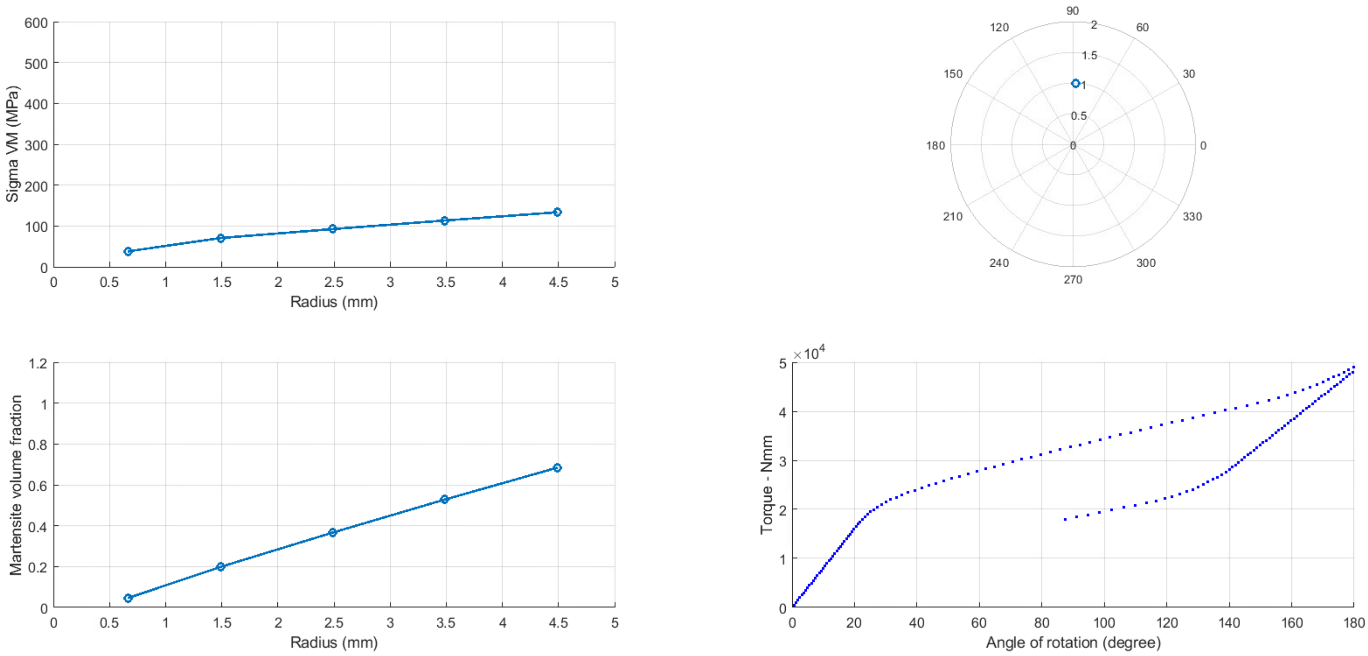

(n)

Figure 5.2: SMA rod behaviour under torque loading cycle @24°C.

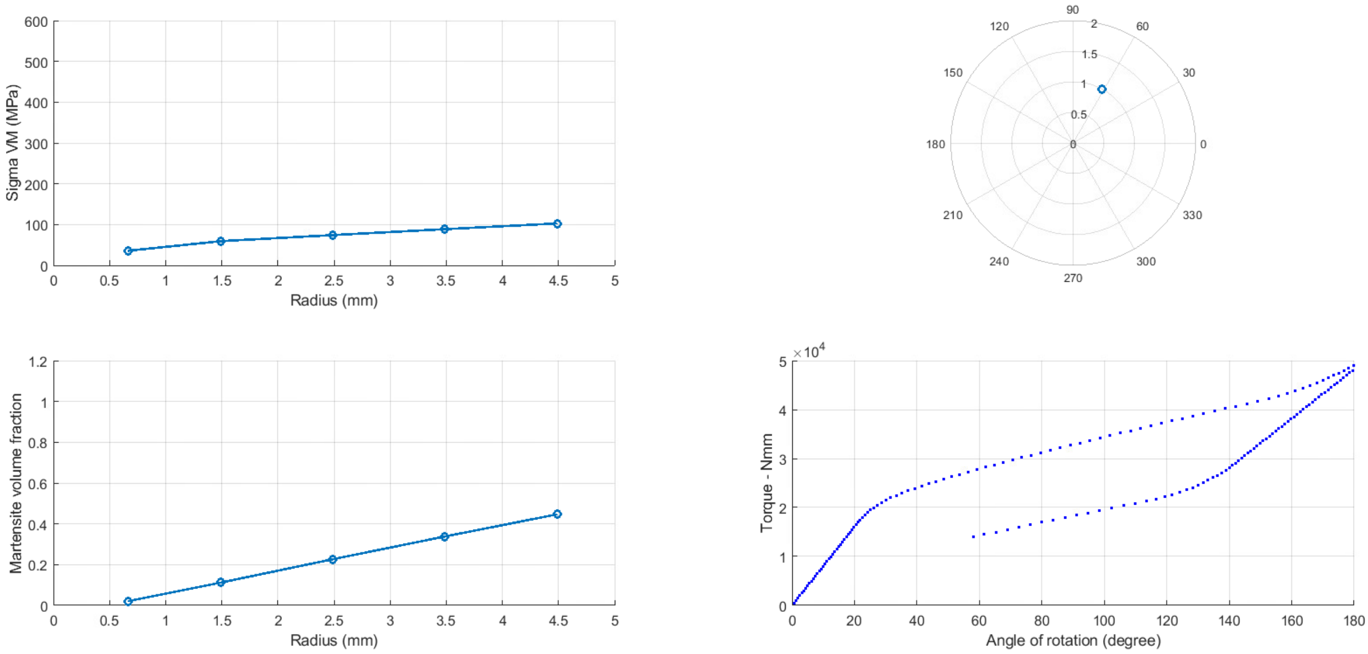

(o)

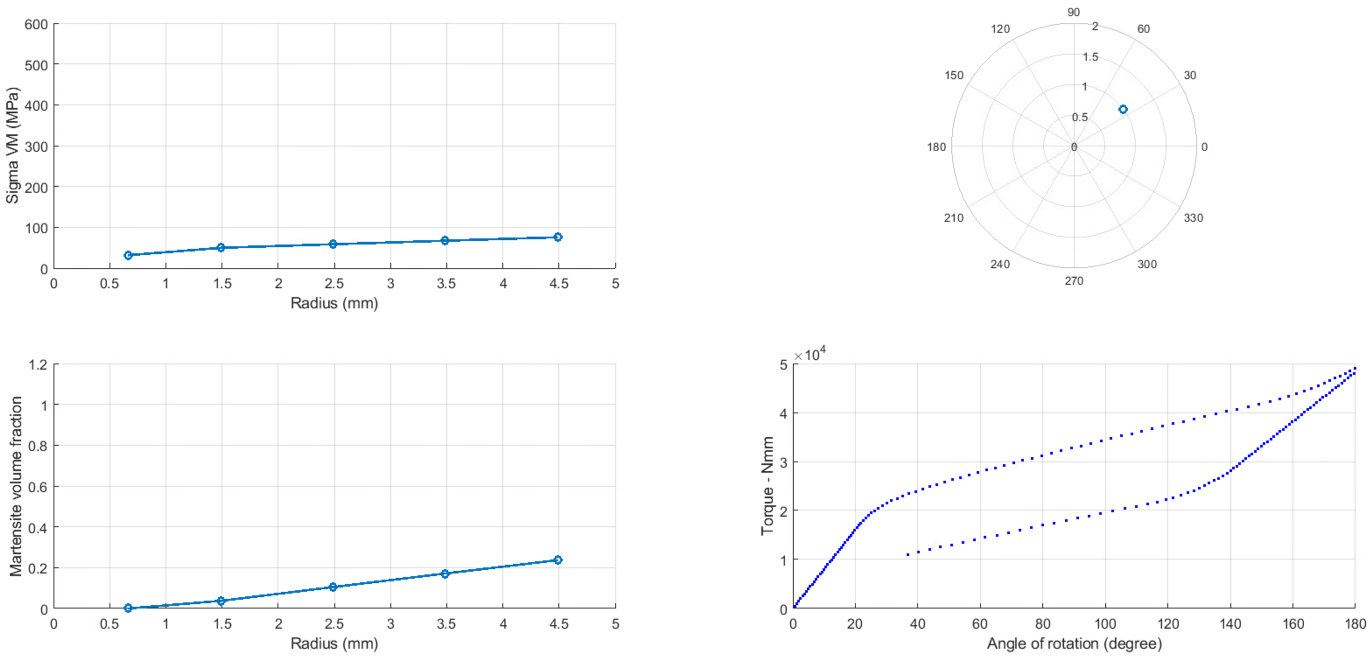

(p)

Figure 5.2: SMA rod behaviour under torque loading cycle @24°C.

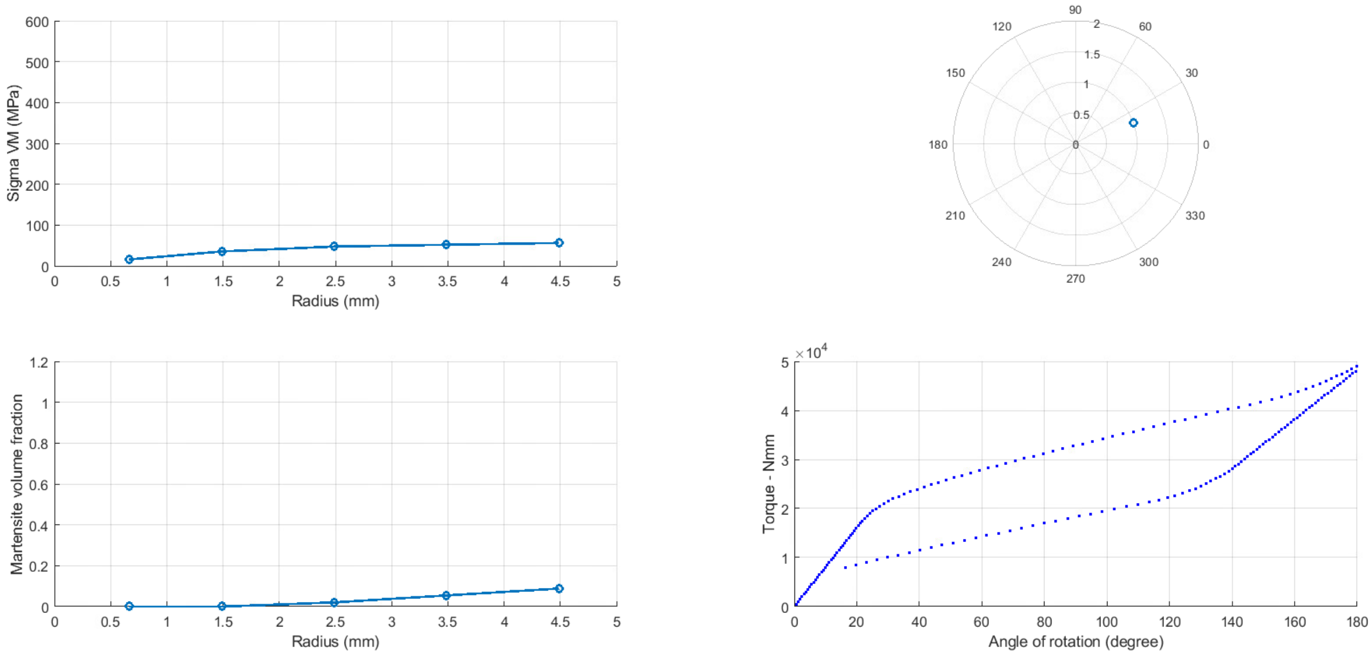

(q)

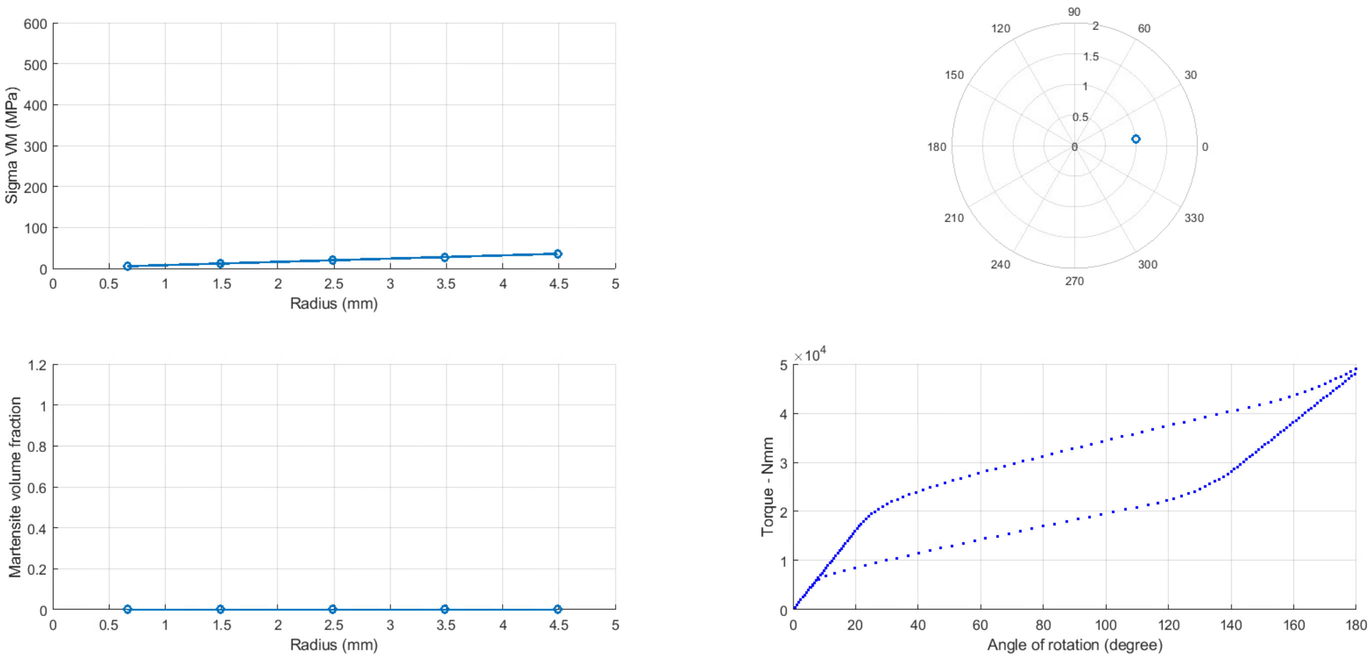

(r)

Figure 5.2: SMA rod behaviour under torque loading cycle @24°C.

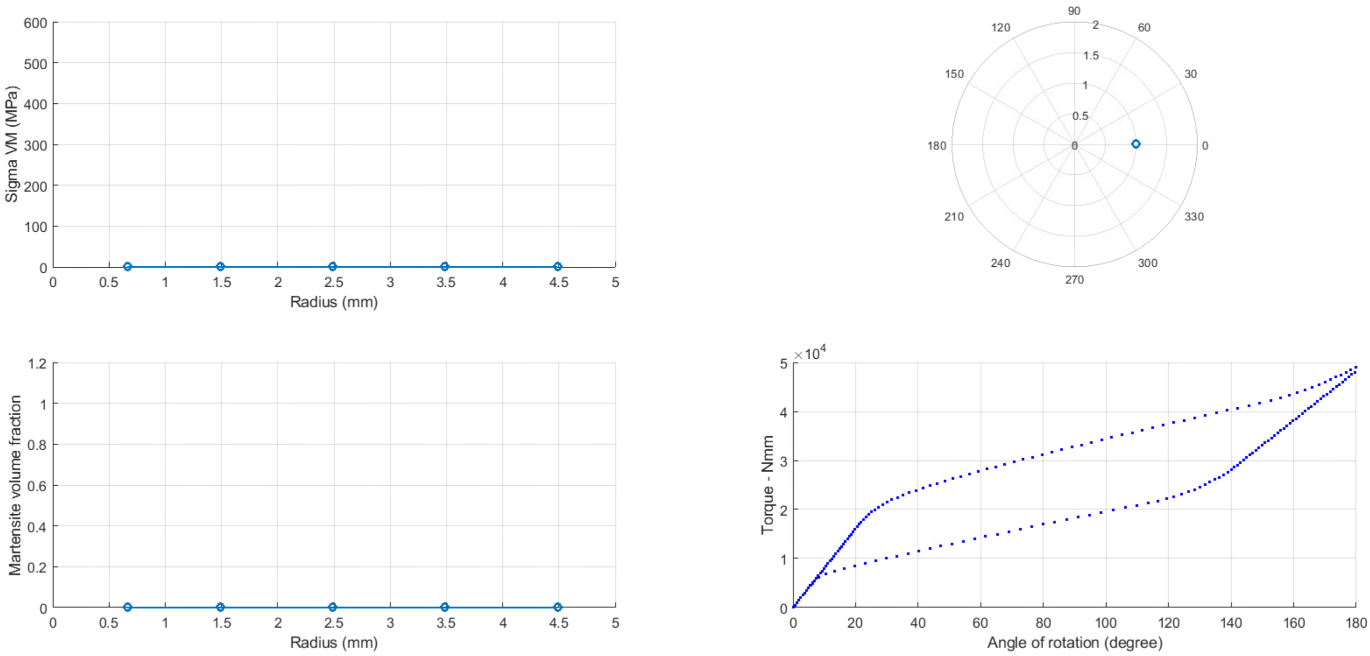

(s)

Figure 5.2: SMA rod behaviour under torque loading cycle @24°C.

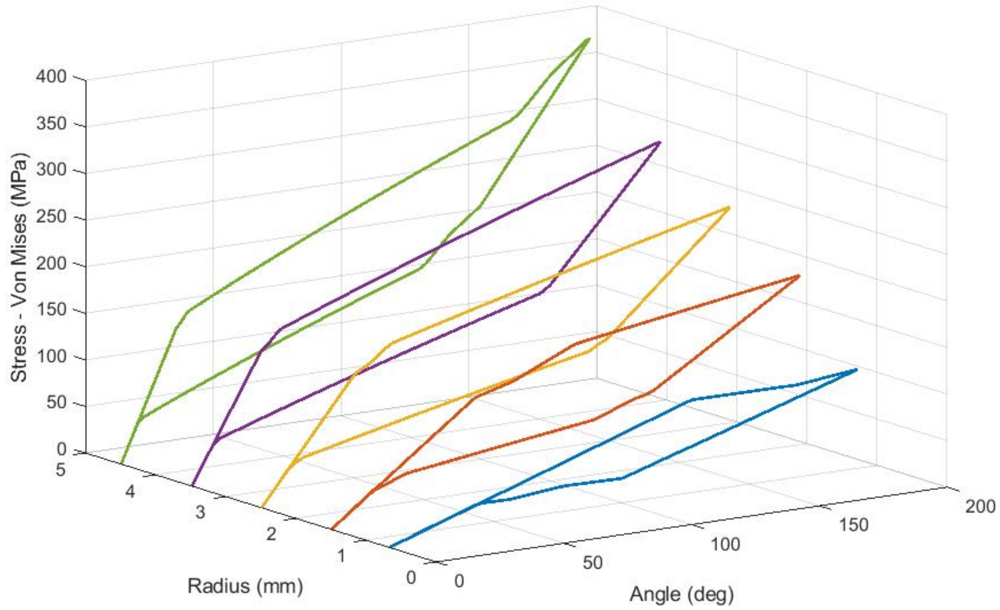

(a)

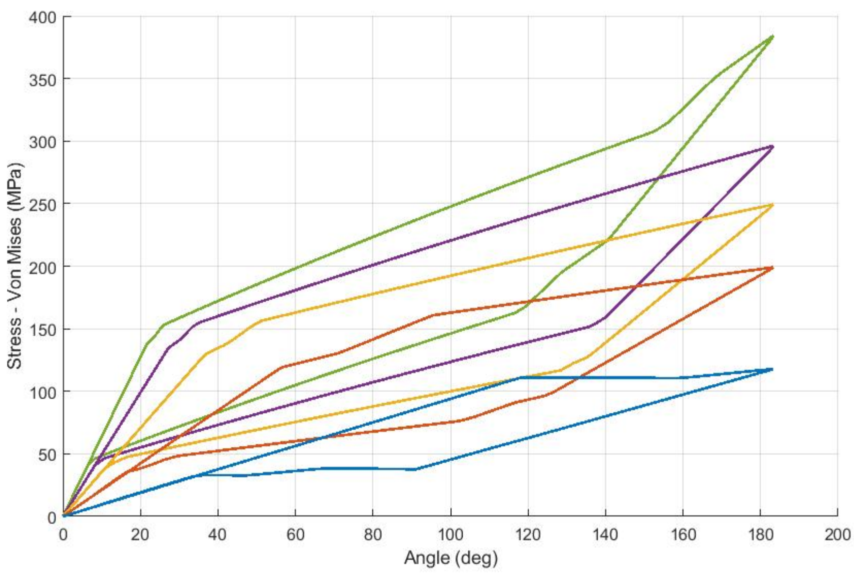

(b)

Figure 5.3: Von Mises Stress cycles.

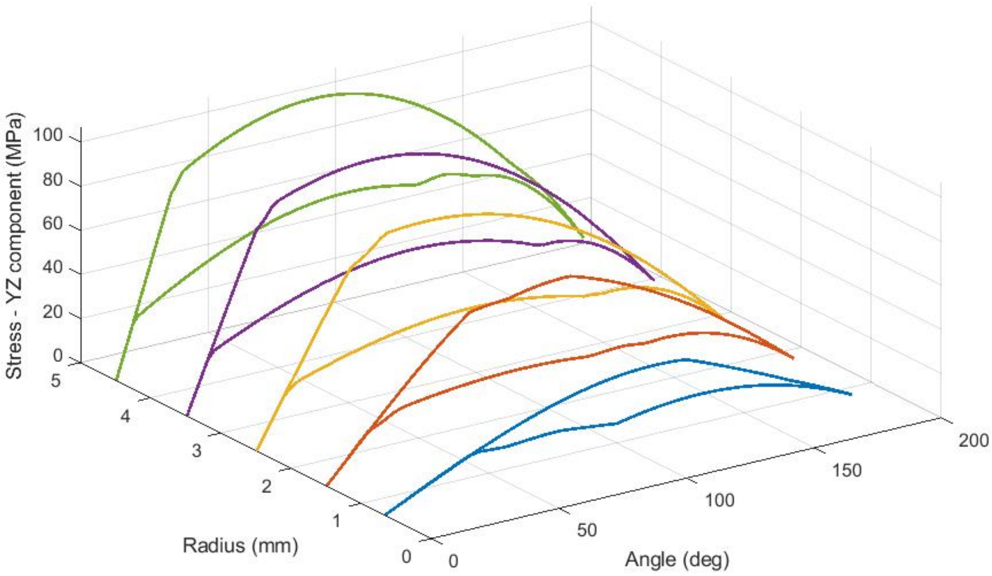

(a)

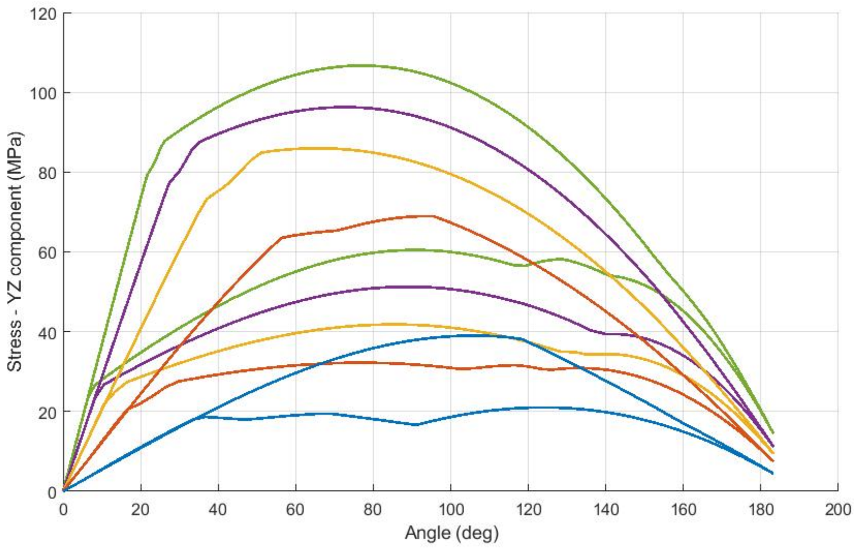

(b)

Figure 5.4: YZ Stress component cycles.

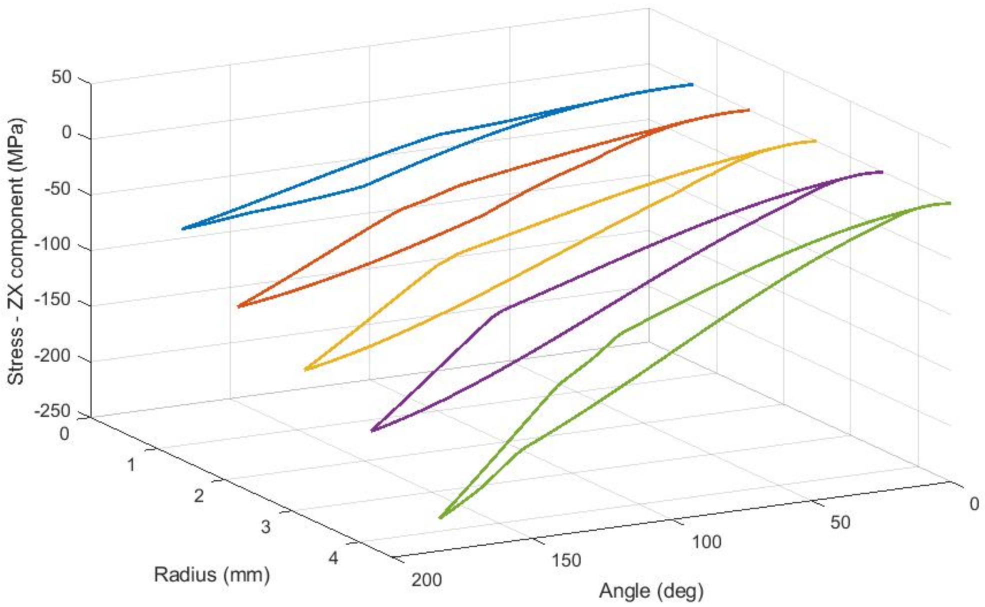

(a)

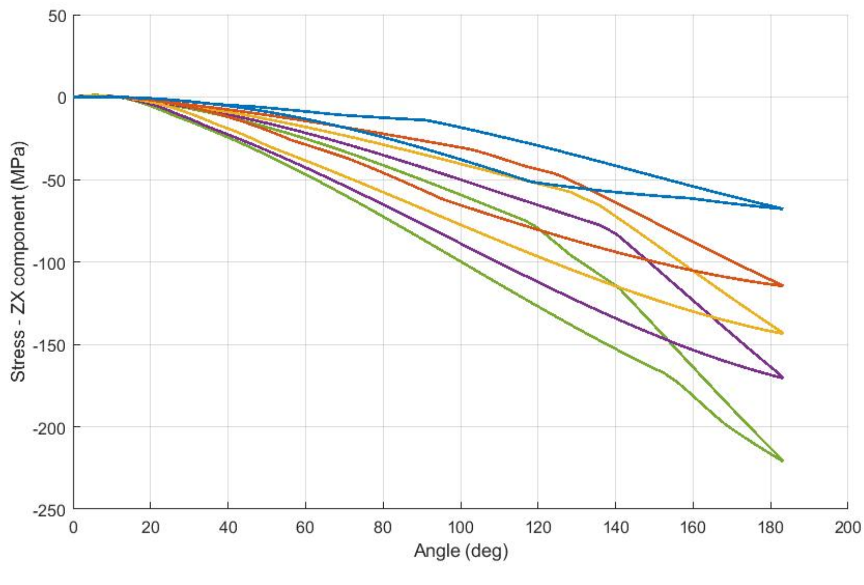

(b)

Figure 5.5: ZX Stress component cycles.

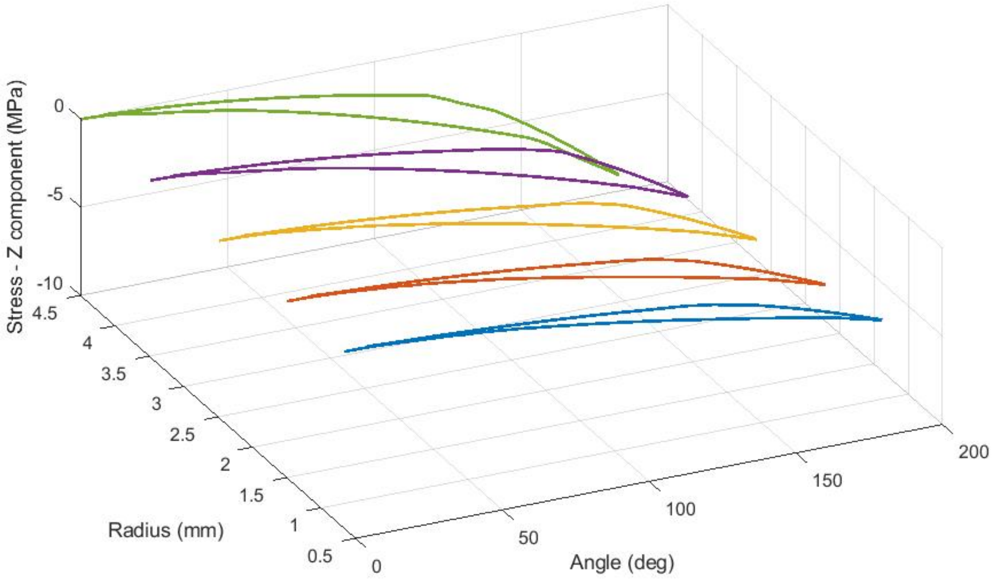

(a)

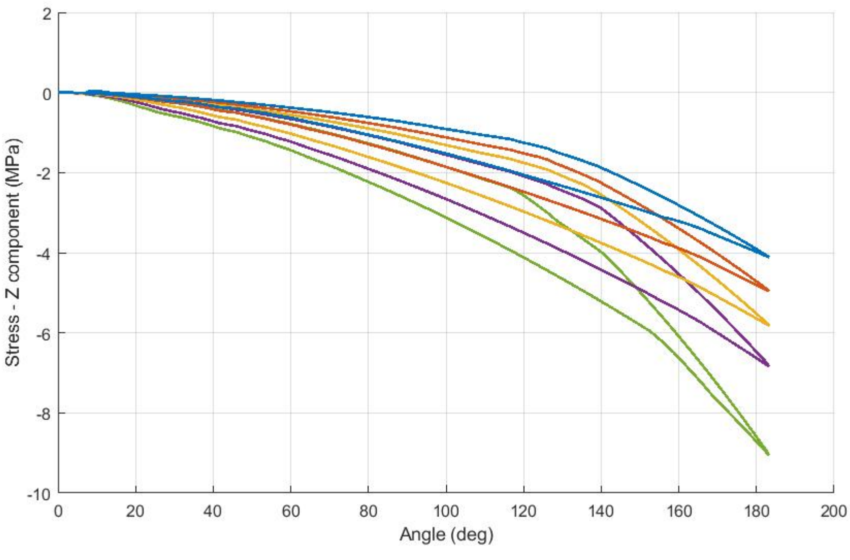

(b)

Figure 5.6: Z Stress component cycles.

5.0.2 Double torque loading cycle

In order to assess the FEM software capability to predict training effects, a two-cycle analysis was performed. The second loop output data exactly matches that of the first one, as shown in figure 5.7. This means that no conclusions can be done on training effects using this model.

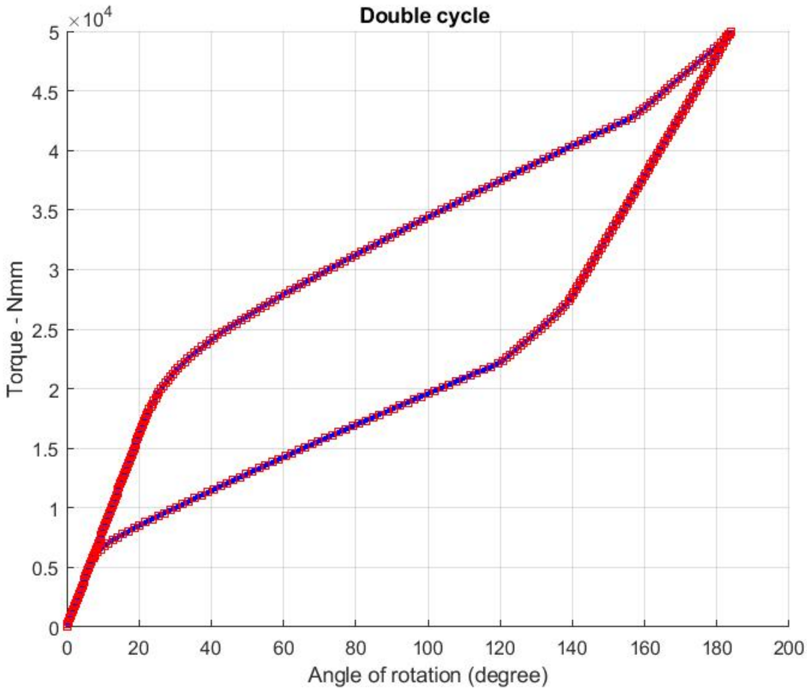

Figure 5.7: Double torque loading cycle @24°C.

5.0.3 Thermal cycle

A thermal cycle is performed on the same model described above. First of all the rod is loaded to $40Nm$ of torque at $10°C$; subsequently, a complete thermal cycle is obtained heating the specimen to $80°C$ and then cooling it back to $10°C$. Martensite, stress and temperature evolution is illustrated in figure 5.8, while figure 5.9 shows the stress cycles at different radial points.

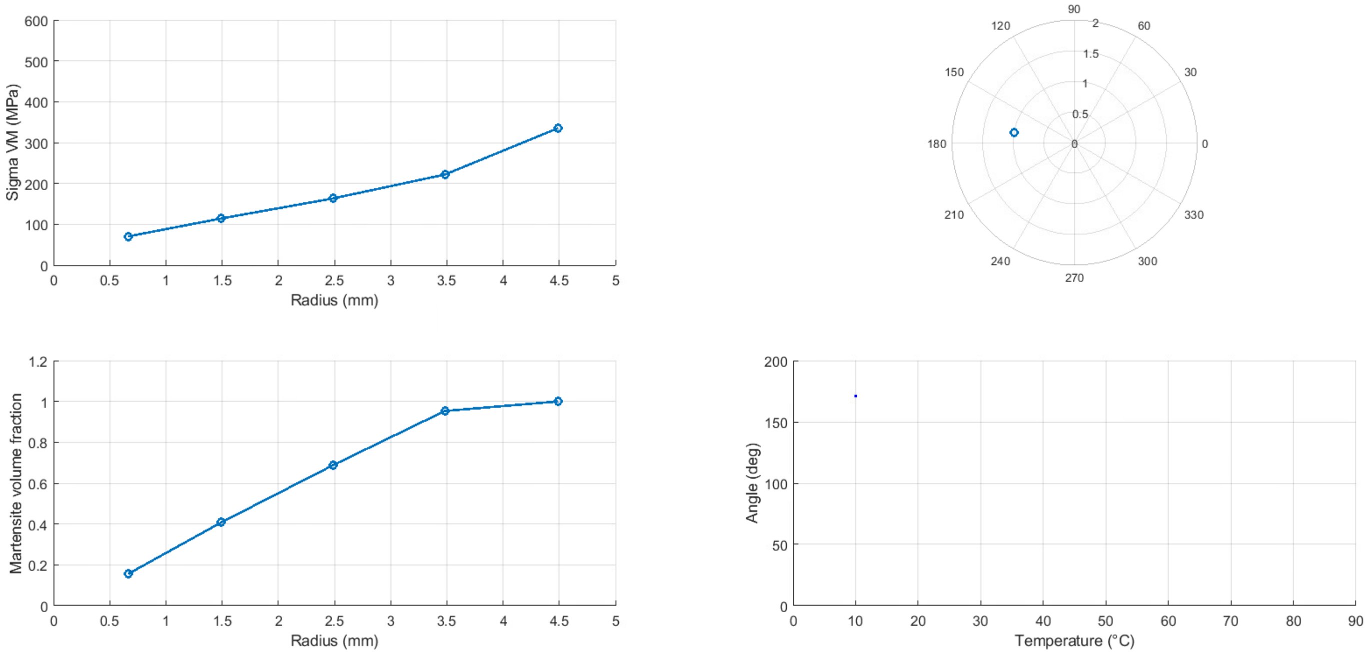

(a)

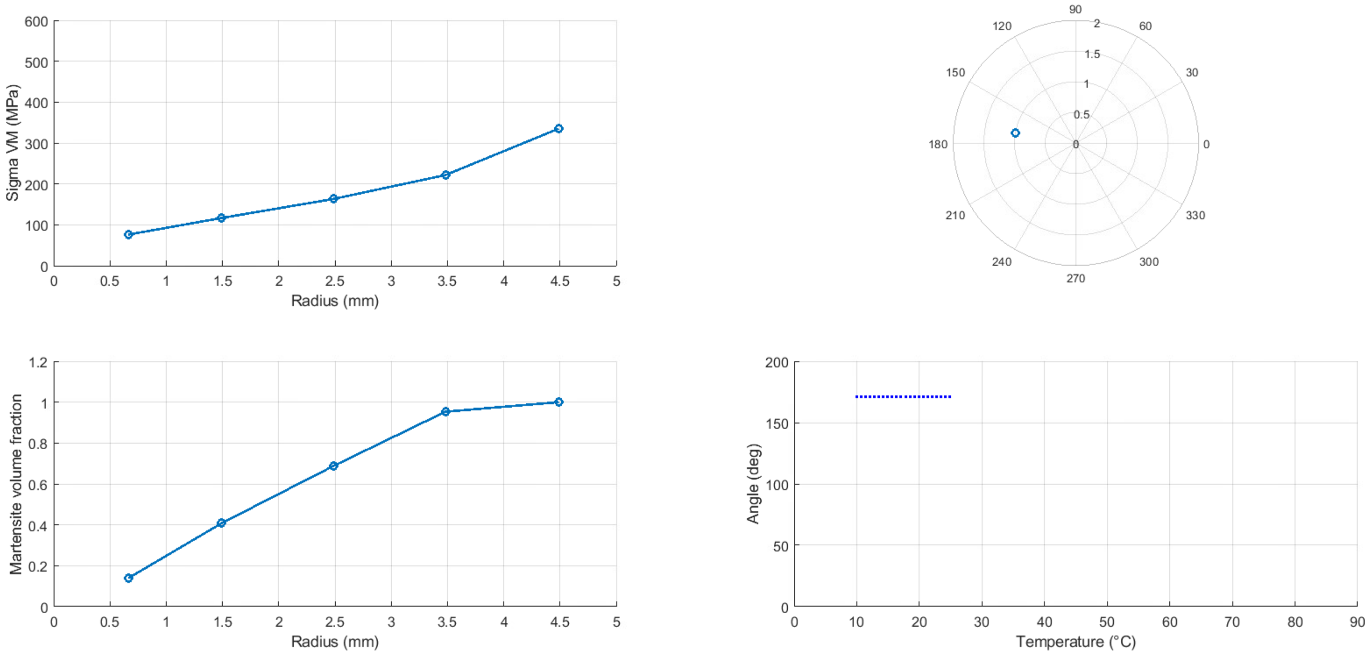

(b)

Figure 5.8: SMA rod behaviour under thermal cycling @40Nm.

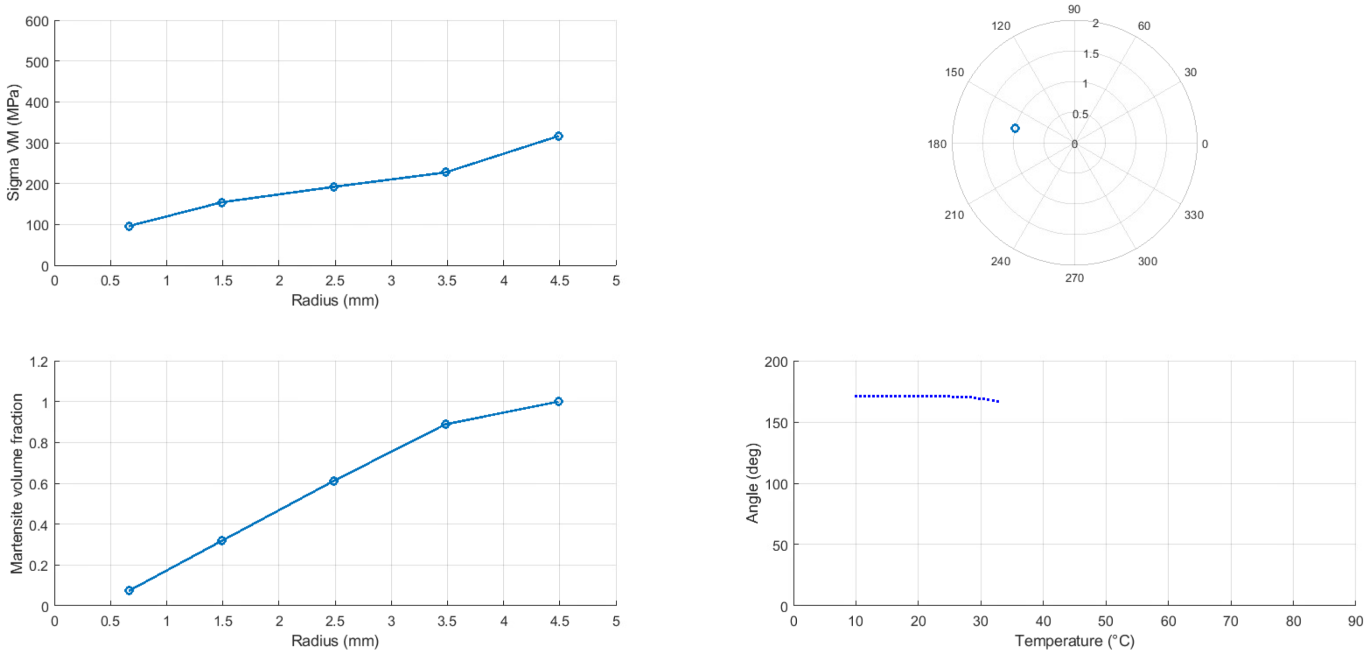

(c)

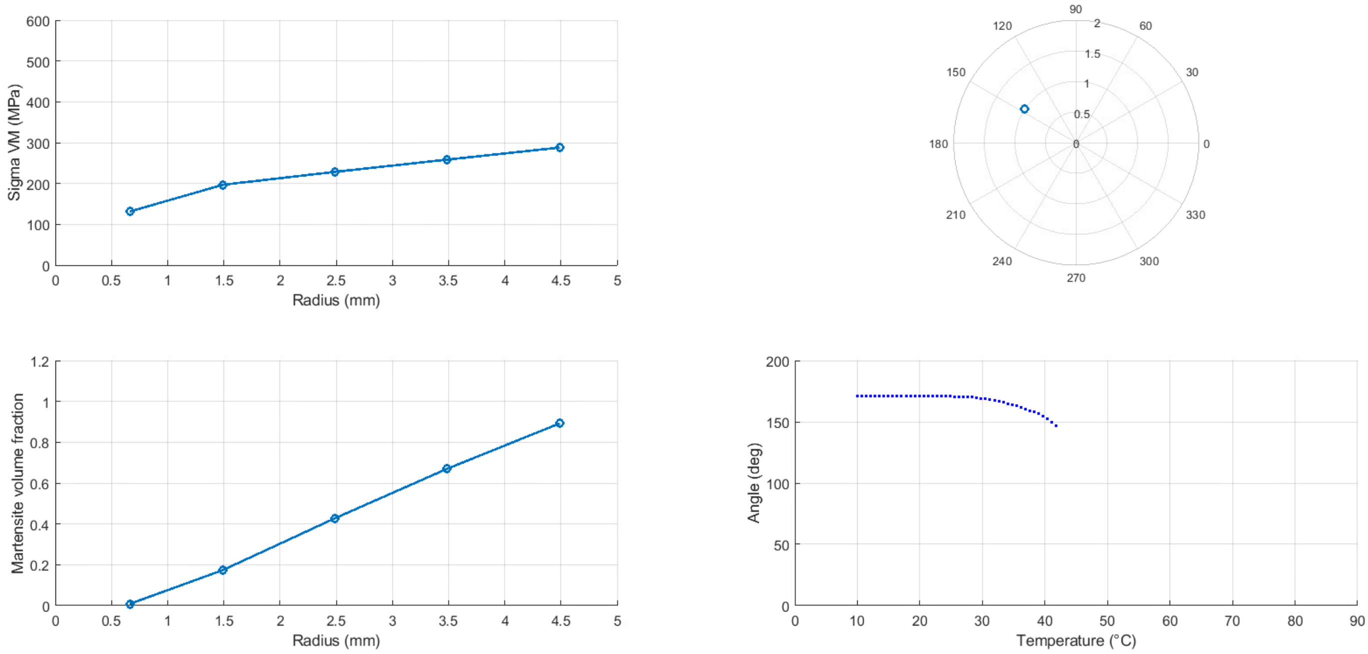

(d)

Figure 5.8: SMA rod behaviour under thermal cycling @40Nm.

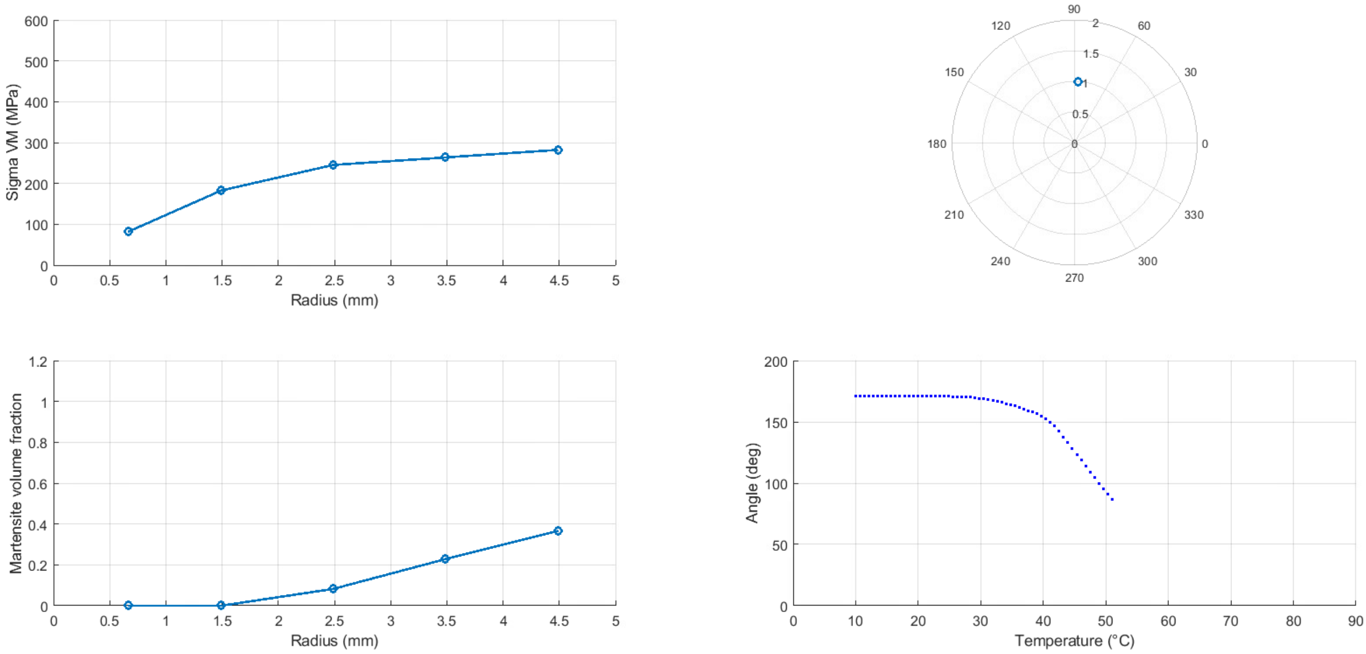

(e)

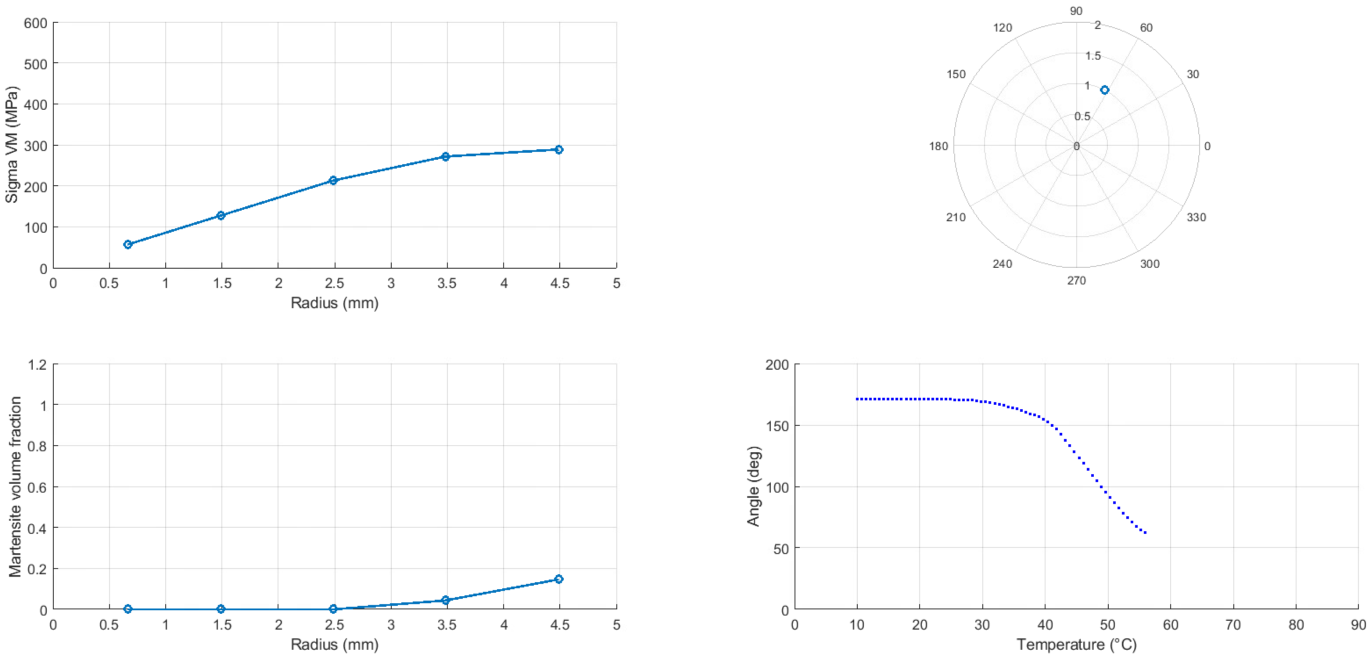

(f)

Figure 5.8: SMA rod behaviour under thermal cycling @40Nm.

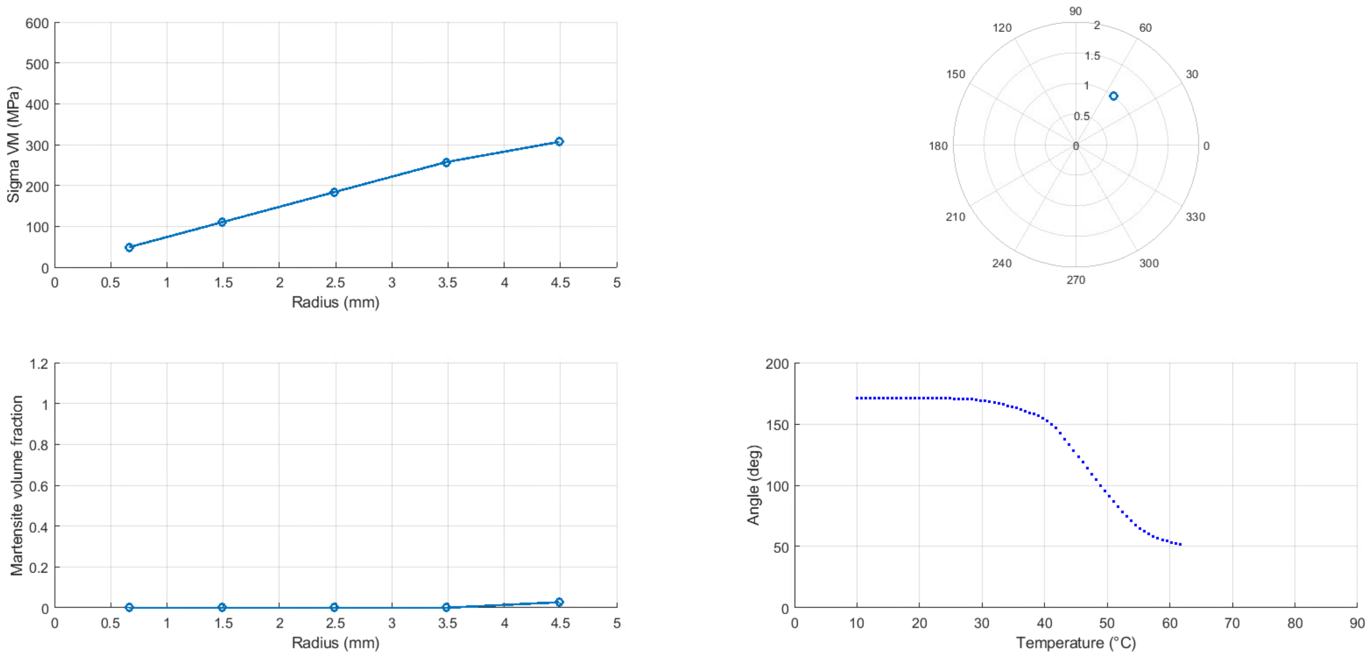

(g)

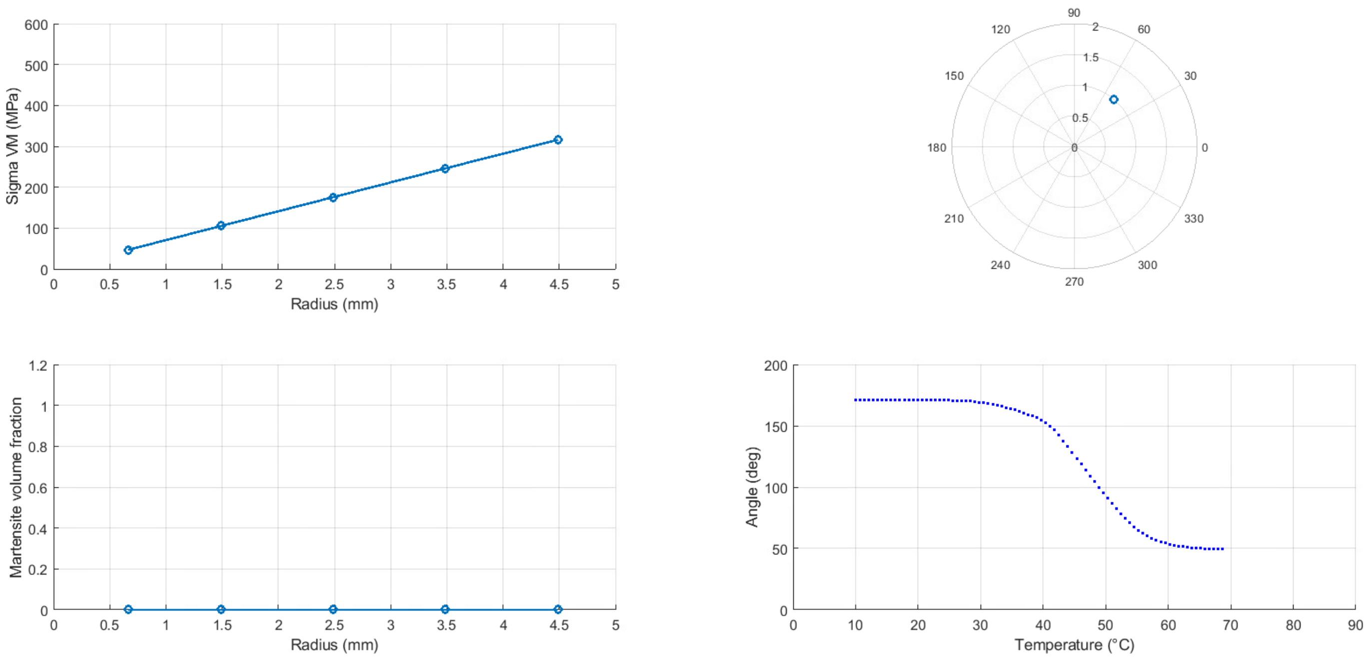

(h)

Figure 5.8: SMA rod behaviour under thermal cycling @40Nm.

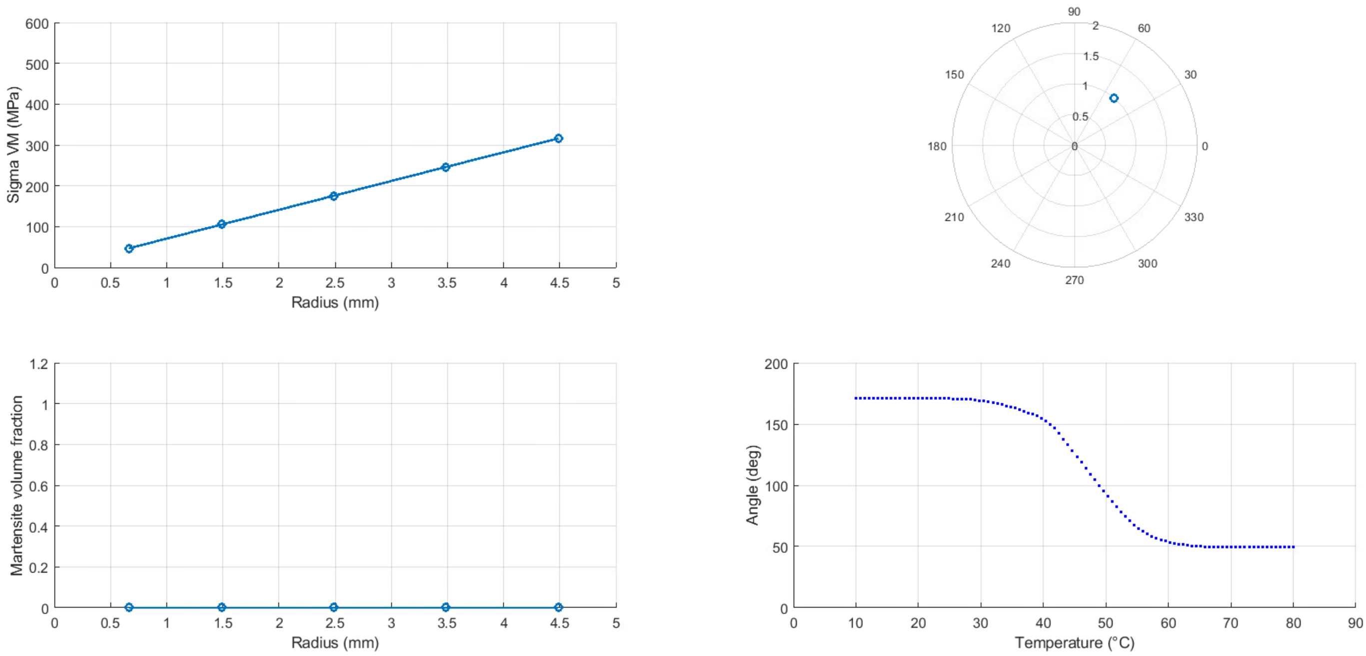

(i)

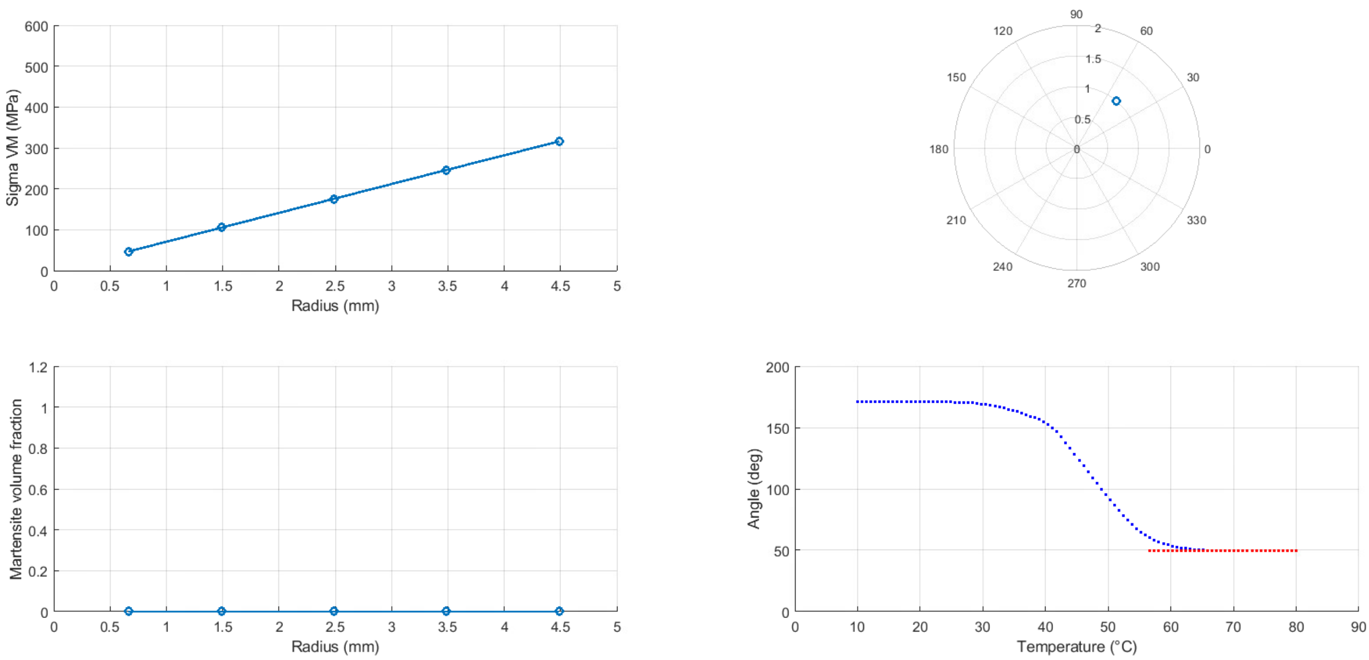

(j)

Figure 5.8: SMA rod behaviour under thermal cycling @40Nm.

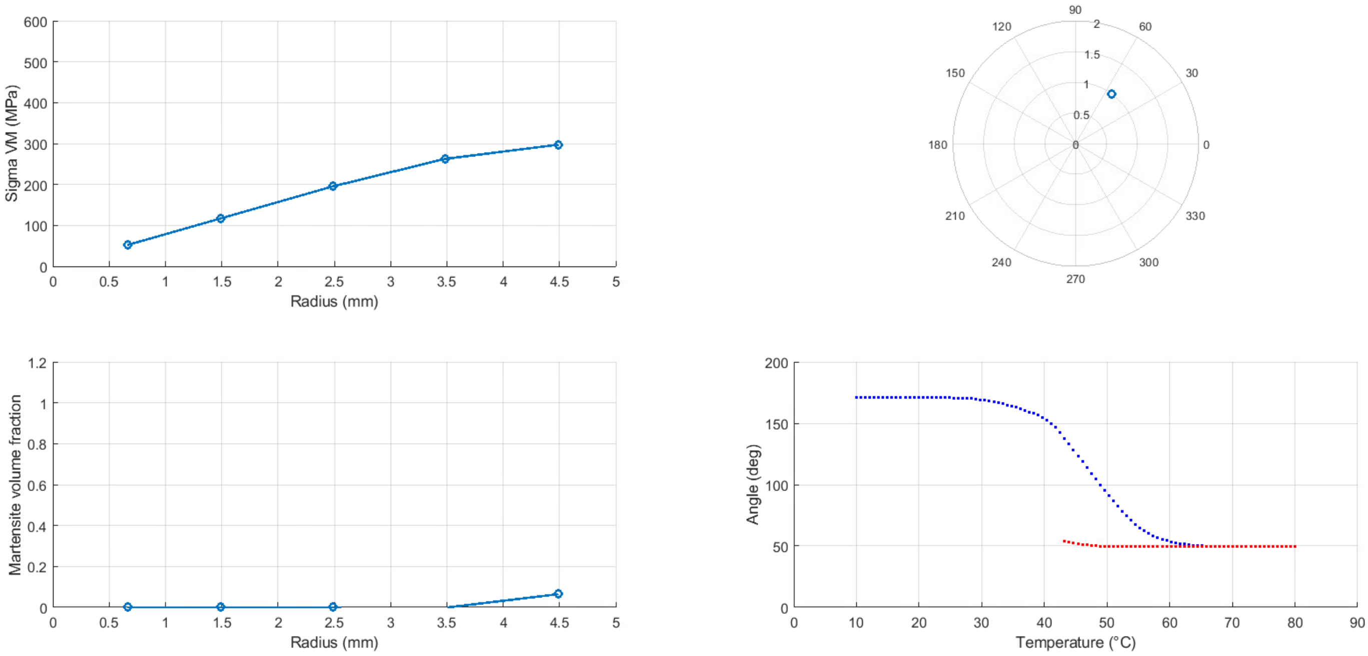

(k)

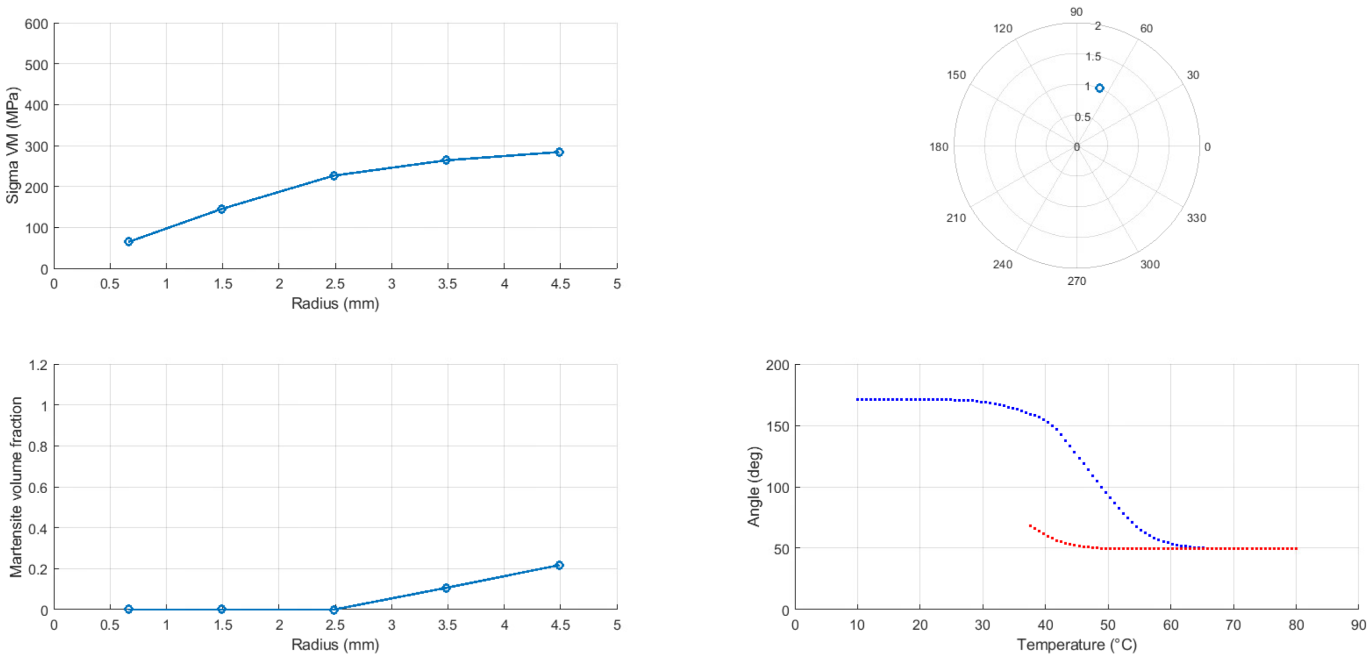

(l)

Figure 5.8: SMA rod behaviour under thermal cycling @40Nm.

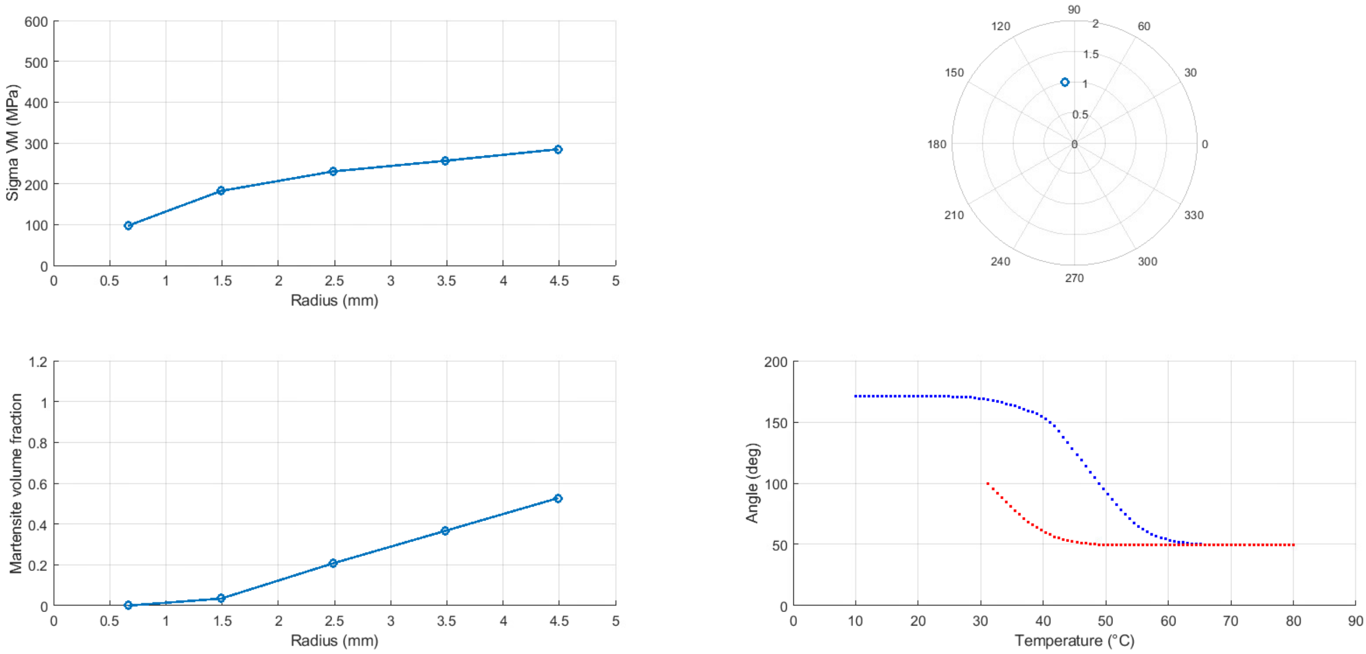

(m)

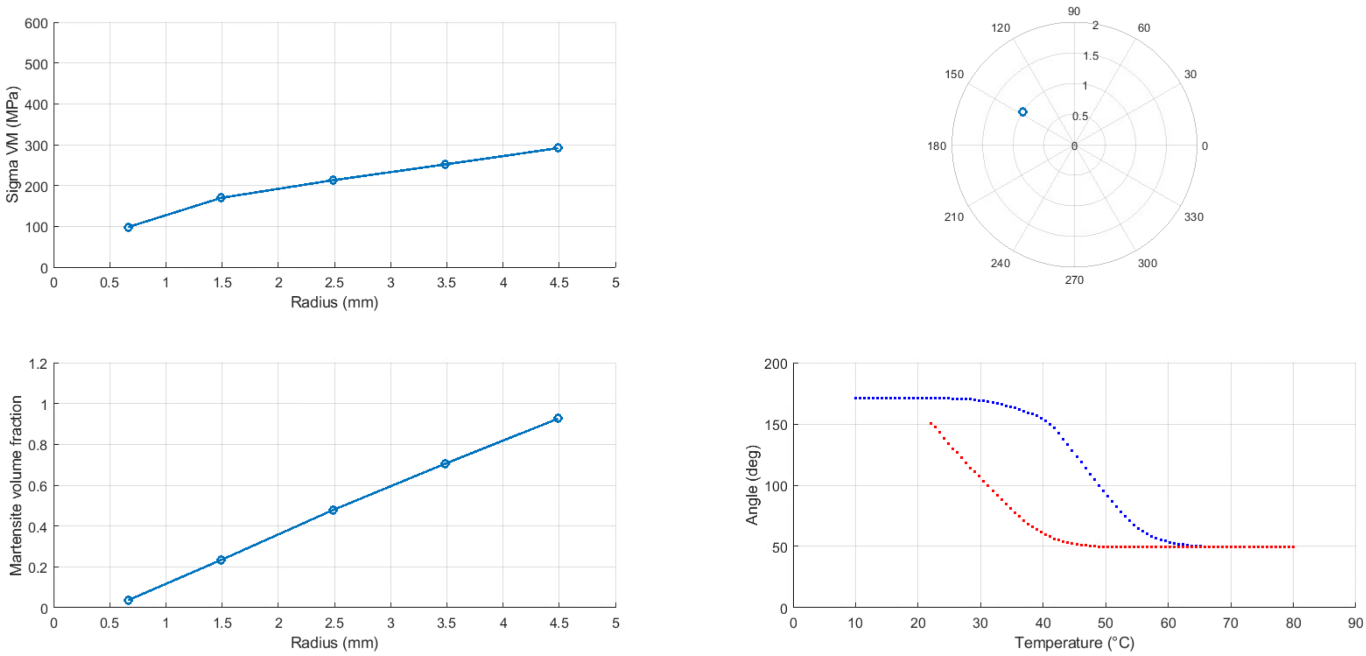

(n)

Figure 5.8: SMA rod behaviour under thermal cycling @40Nm.

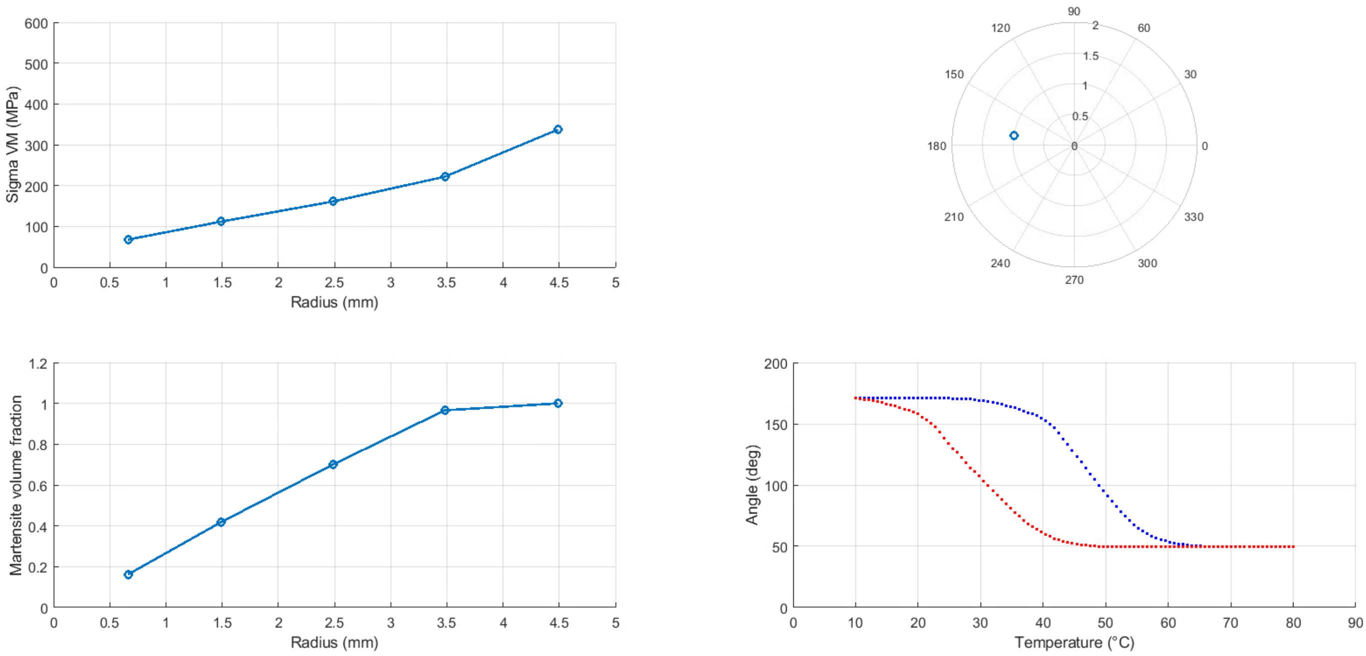

(o)

Figure 5.8: SMA rod behaviour under thermal cycling @$40Nm$.

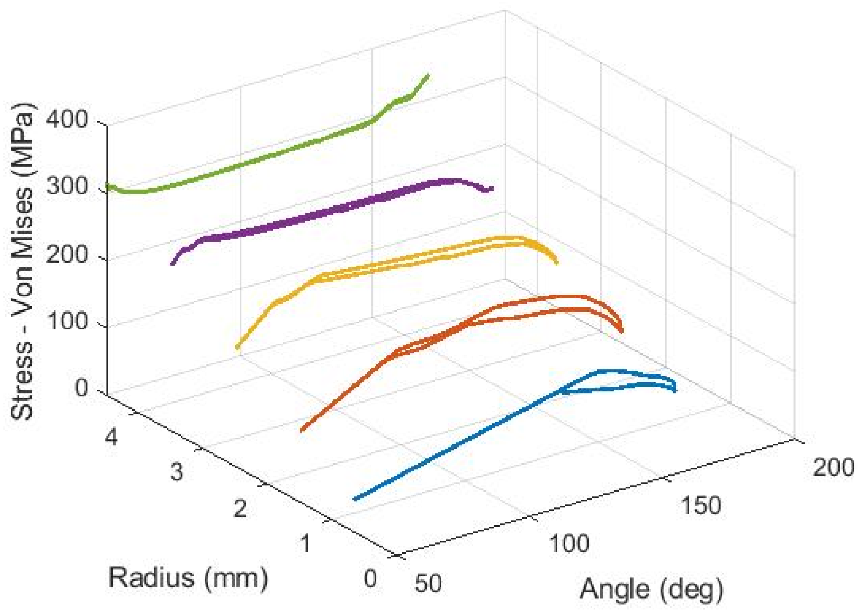

(a)

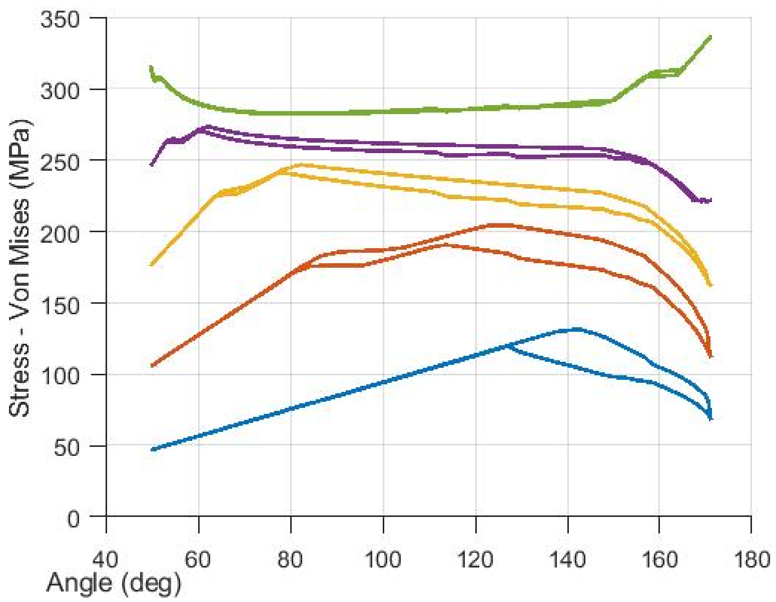

(b)

Figure 5.9: Von Mises Stress under thermal cycling.

Chapter 6

Conclusions and future work

6.1 Summary and conclusions

Shape memory alloy actuators have been studied for more than thirty years. Many experimental tests have been performed, and several patents have been registered. However, designing such devices is still a challenging and tough task. On the one hand, models are not yet able to provide the required accuracy to replace a substantial part of experimental tests; on the other hand, it seems that a gap exists in the literature between the main ideas behind SMA torsional actuators and their actual implementation. Experimental data still remain mandatory for the final draft and are an indispensable source to understand the governing principles of SMAs; this is why a critical review is reported highlighting crucial aspect for the design. Further, this work illustrates a viable path to follow from the conceptual to the preliminary design, considering different actuator configurations in the effort to fill the gap mentioned above.

To get a sense of the torque involved, aerodynamic load predictions are performed using Xfoil for three classes of aircraft (medium size UAV, Four-Seat Aircraft and Regional Transport Aircraft), considering a plain flap and an Adaptive Trailing Edge device. The analysis have been handled using a Matlab script. Also, the obtained data have been compared to those presented in the literature to validate the method adopted.

A FEM model is created in MSC Patran and solved by Nastran which implements Auricchio's formulation. This means provides a holistic vision of the macroscopic phenomena involved during phase transformations, accomplishing either a general method for the preliminary design and a helpful educational tool for those who approach for the first time SMA actuators design. Indeed, SMA rods behaviour under mechanical and thermal loading is thoroughly examined, monitoring stress, temperature, torque and martensite evolution simultaneously.

The main limit of this methodology lies in the fact that the model considered does not admit martensite twinned. Moreover, no conclusions can be done on training effects since performing a second loading cycle does not present any difference with respect to the first one. Also, for the material considered in this dissertation, FEM data overestimates the transformation strain.

6.2 Future work

It is thought that this work has room for improvement concerning three main aspects:

- The SMA component can undergo optimizations starting from the session files already developed, leveraging on the potentialities of Patran Command Language (PCL) and its compatibility with Matlab.
- Thermal aspects can be deepened, also using a non-linear transient solution type to include the time domain and accounting for inertial effects.
- Long term experimental tests can be performed concerning the cooling effect on constrained austenite specimen from high stress and high temperature state, in order to dispel any slightest doubt on twinned martensite formation in these conditions.

Bibliography

[1] https://www.cira.it/en/corporate/about-us.

[2] https://www.cira.it/en/competences/strutture-adattive.

[3] https://aviationsmilitaires.net/v3/kb/picture/7236/aai-rq-7b-shadow-200.

[4] https://www.aeromecanic.com/Skyhawk_DOC_FR_files/spec.pdf.

[5] https://www.atr-aircraft.com/our-aircraft/atr-42-600/.

[6] https://en.wikipedia.org/wiki/AAI_RQ-7_Shadow.

[7] https://en.wikipedia.org/wiki/Cessna_172.

[8] Darin J Arbogast, Robert T Ruggeri, and Richard C Bussom. "Development of a 1/4-scale NiTinol actuator for reconfigurable structures". In: *Industrial and Commercial Applications of Smart Structures Technologies 2008*. Vol. 6930. International Society for Optics and Photonics. 2008, p. 69300L.

[9] Ferdinando Auricchio. "A robust integration-algorithm for a finite-strain shape-memory-alloy superelastic model". In: *International Journal of plasticity* 17.7 (2001), pp. 971–990.

[10] Ferdinando Auricchio and Robert L Taylor. "Shape-memory alloys: modelling and numerical simulations of the finite-strain superelastic behavior". In: *Computer methods in applied mechanics and engineering* 143.1-2 (1997), pp. 175–194.

[11] Ferdinando Auricchio et al. "Theoretical and numerical modeling of shape memory alloys accounting for multiple phase transformations and martensite reorientation". In: *International Journal of Plasticity* 59 (2014), pp. 30–54.

[12] Ian Baker. "Nitinol". In: *Fifty Materials That Make the World*. Springer, 2018, pp. 137–142.

[13] O Benafan and DJ Gaydosh. "Constant-torque thermal cycling and two-way shape memory effect in Ni50. 3Ti29. 7Hf20 torque tubes". In: *Smart Materials and Structures* 27.7 (2018), p. 075035.

[14] O Benafan and DJ Gaydosh. "High temperature shape memory alloy Ni50. 3Ti29. 7Hf20 torque tube actuators". In: *Smart Materials and Structures* 26.9 (2017), p. 095002.

[15] James G Boyd and Dimitris C Lagoudas. "A thermodynamical constitutive model for shape memory materials. Part I. The monolithic shape memory alloy". In: *International Journal of Plasticity* 12.6 (1996), pp. 805–842.

[16] LC Brinson and R Lammering. "Finite element analysis of the behavior of shape memory alloys and their applications". In: *International Journal of solids and structures* 30.23 (1993), pp. 3261–3280.

[17] Glenn S Bushnell, Darin Arbogast, and Robert Ruggeri. "Shape control of a morphing structure (rotor blade) using a shape memory alloy actuator system". In: *Active and Passive Smart Structures and Integrated Systems 2008*. Vol. 6928. International Society for Optics and Photonics. 2008, 69282A.

[18] Frederick T Calkins and James H Mabe. "Flight test of a shape memory alloy actuated adaptive trailing edge flap". In: *ASME 2016 conference on smart materials, adaptive structures and intelligent systems.* American Society of Mechanical Engineers Digital Collection. 2016.

[19] Frederick T Calkins and James H Mabe. "Shape memory alloy based morphing aerostructures". In: *Journal of Mechanical Design* 132.11 (2010).

[20] Josiah Cherian Chekotu et al. "Advances in selective laser melting of nitinol shape memory alloy Part Production". In: *Materials* 12.5 (2019), p. 809.

[21] Dan J Clingman, Robert T Ruggeri, and W Dean Clingman. *Strain energy shuttle apparatus and method.* US Patent 8,347,747. Jan. 2013.

[22] HG Denaci and JD Bird. *Wind-Tunnel Tests of Ailerons at Various Speeds. 2-Ailerons of 0.20 Airfoil Chord and True Contour with 0.60 Aileron-Chord Sealed Internal Balance on the NACA 66, 2-216 Airfoil.* Tech. rep. NATIONAL AERONAUTICS and SPACE ADMIN LANGLEY RESEARCH CENTER HAMPTON VA, 1943.

[23] Ignazio Dimino, Leonardo Lecce, Rosario Pecora, et al. *Morphing wing technologies: Large commercial aircraft and civil helicopters.* Butterworth-Heinemann, 2017.

[24] EASA. *Certification specifications for normal, utility, aerobatic, and commuter category aeroplanes CS-23.* 2003.

[25] CS25 EASA. *Certification Specifications for Large Aeroplanes.* 2009.

[26] Dino Florjancic. "Improved design of a high lift system for general aviation aircraft". In: (2015).

[27] Q Gu et al. "Consistent tangent moduli for multi-yield-surface J 2 plasticity model". In: *Computational Mechanics* 48.1 (2011), pp. 97–120.

[28] Nastran Nonlinear User's Guide. "SOL 400". In: *MSC Software Corporation* (2016).

[29] Ian Gunter et al. *Remotely actuated wind tunnel model rudder using shape memory alloy.* US Patent 8,876,046. Nov. 2014.

[30] Darren J Hartl and Dimitris C Lagoudas. "Aerospace applications of shape memory alloys". In: *Proceedings of the Institution of Mechanical Engineers, Part G: Journal of Aerospace Engineering* 221.4 (2007), pp. 535–552.

[31] Chia-Wen Hou and Chao-Chieh Lan. "Functional joint mechanisms with constant-torque outputs". In: *Mechanism and Machine Theory* 62 (2013), pp. 166–181.

[32] A Dean Jacot. "Shape memory alloy consortium (SMAC)". In: *Smart Structures and Materials 1999: Industrial and Commercial Applications of Smart Structures Technologies.* Vol. 3674. International Society for Optics and Photonics. 1999, pp. 158–165.

[33] A Dean Jacot, Robert T Ruggeri, and Dan J Clingman. *Shape memory alloy device and control method.* US Patent 7,037,076. May 2006.

[34] A Peter Jardine, Jonathan D Bartley-Cho, and John S Flanagan. "Improved design and performance of the SMA torque tube for the DARPA Smart Wing Program". In: *Smart Structures and Materials 1999: Industrial and Commercial Applications of Smart Structures Technologies.* Vol. 3674. International Society for Optics and Photonics. 1999, pp. 260–269.

[35] Andreea Koreanschi, Oliviu Sugar-Gabor, and Ruxandra Mihaela Botez. "Numerical and experimental validation of a morphed wing geometry using Price-Paıdoussis wind tunnel testing". In: *The Aeronautical Journal* 120.1227 (2016), pp. 757–795.

[36] James H Mabe et al. "NiTinol performance characterization and rotary actuator design". In: *Smart Structures and Materials 2004: Industrial and Commercial Applications of Smart Structures Technologies.* Vol. 5388. International Society for Optics and Photonics. 2004, pp. 95–109.

[37] James H Mabe et al. *Shape memory alloy actuator.* US Patent 8,118,264. Feb. 2012.

[38] MSC Marc. "Marc 2013 volume A: theory and user information". In: *MSC Corporation, Newport Beach* (2013).

[39] Reza Mirzaeifar, Reginald DesRoches, and Arash Yavari. "Exact solutions for pure torsion of shape memory alloy circular bars". In: *Mechanics of Materials* 42.8 (2010), pp. 797–806.

[40] S Miyazaki, K Otsuka, and Y Suzuki. "Transformation pseudoelasticity and deformation behavior in a Ti-50.6 at% Ni alloy". In: *Scripta Metallurgica* 15.3 (1981), pp. 287–292.

[41] MSC Nastran et al. "Quick reference guide". In: *MSC. SOFTWARE* 1 (2004).

[42] NX Nastran. "Element library reference". In: *Plano, TX: Siemens PLM Software* (2014).

[43] S. Ameduri, M. Ciminello, A. Concilio, I. Dimino, B. Galasso, M. Guida. *Structural module for fixed and rotary wing.* EP21425028.

[44] P. A. Popov. "Constitutive modelling of shape memory alloys and upscaling of deformable porous media". In: 2005.

[45] Peter Popov and Dimitris C Lagoudas. "A 3-D constitutive model for shape memory alloys incorporating pseudoelasticity and detwinning of self-accommodated martensite". In: *International Journal of Plasticity* 23.10-11 (2007), pp. 1679–1720.

[46] Richard J Re. "Stability and control characteristics: Including aileron hinge moments of a model of a supercritical-wing research airplane". In: (1974).

[47] Mithra MKV Sankrithi and Joshua B Frommer. *Controllable winglets.* US Patent 7,744,038. June 2010.

[48] Robert N Saunders et al. "Modeling and development of a twisting wing using inductively heated shape memory alloy actuators". In: *Active and passive smart structures and integrated systems 2015.* Vol. 9431. International Society for Optics and Photonics. 2015, 94310U.

[49] Junwon Seo, Young Kim, and Jong Hu. "Pilot Study for Investigating the Cyclic Behavior of Slit Damper Systems with Recentering Shape Memory Alloy (SMA) Bending Bars Used for Seismic Restrainers". In: *Applied Sciences* 5 (July 2015), pp. 187–208. DOI: 10.3390/app5030187.

[50] Christopher David Simpson. *Control surface hinge moment prediction using computational fluid dynamics.* The University of Alabama, 2016.

[51] Angela C Souza, Edgar N Mamiya, and Nestor Zouain. "Three-dimensional model for solids undergoing stress-induced phase transformations". In: *European Journal of Mechanics-A/Solids* 17.5 (1998), pp. 789–806.

[52] Hannah Stroud and Darren J Hartl. "Shape memory alloy torsional actuators: a review of applications, experimental investigations, modeling, and design". In: *Smart Materials and Structures* (2020).

[53] Masood Taheri Andani et al. "Modifying the torque–angle behavior of rotary shape memory alloy actuators through axial loading: A semi-analytical study of combined tension–torsion behavior". In: *Journal of Intelligent Material Systems and Structures* 24.12 (2013), pp. 1524–1535.

[54] N Vasudha and K Uma Rao. "Shape memory alloy properties, modelling aspects and potential applications-a review". In: *Journal of Physics: Conference Series.* Vol. 1706. 1. IOP Publishing. 2020, p. 012190.

[55] Kiyohide Wada and Yong Liu. "On the mechanisms of two-way memory effect and stress-assisted two-way memory effect in NiTi shape memory alloy". In: *Journal of alloys and compounds* 449.1-2 (2008), pp. 125–128.

[56] WH Wentz Jr, HC Seetharam, and KA Fiscko. "Force and pressure tests of the GA (W)-1 airfoil with a 20% aileron and pressure tests with a 30% Fowler flap". In: (1977).

[57] David Zaccai, Francesco Bertels, and Roelof Vos. "Design methodology for trailing-edge high-lift mechanisms". In: *CEAS Aeronautical Journal* 7.4 (2016), pp. 521–534.